Norbert Marwan
Michael Riley
Alessandro Giuliani
Charles L. Webber Jr. *Editors*

Translational Recurrences

From Mathematical Theory to Real-World Applications

Springer

Springer Proceedings in Mathematics & Statistics

Volume 103

Springer Proceedings in Mathematics & Statistics

This book series features volumes composed of select contributions from workshops and conferences in all areas of current research in mathematics and statistics, including OR and optimization. In addition to an overall evaluation of the interest, scientific quality, and timeliness of each proposal at the hands of the publisher, individual contributions are all refereed to the high quality standards of leading journals in the field. Thus, this series provides the research community with well-edited, authoritative reports on developments in the most exciting areas of mathematical and statistical research today.

More information about this series at http://www.springer.com/series/10533

Norbert Marwan · Michael Riley
Alessandro Giuliani · Charles L. Webber Jr.
Editors

Translational Recurrences

From Mathematical Theory to Real-World
Applications

Springer

Editors
Norbert Marwan
Potsdam Institute for Climate Impact
    Research
Potsdam
Germany

Michael Riley
Department of Psychology
University of Cincinnati
Cincinnati, OH
USA

Alessandro Giuliani
Istituto Superiore di Sanita
Rome
Italy

Charles L. Webber Jr.
Health Sciences Division, Department
    of Cell and Molecular Physiology
Stritch School of Medicine
Loyola University Chicago
Maywood, IL
USA

Printed on acid-free paper

Preface

Recurrence phenomena are regularly experienced in our daily lives. Recurrences are ubiquitous in the real world and constitute fundamental properties of dynamical systems. Starting with the seminal work of Poincaré in the late nineteenth century (who proved the existence of recurring states in autonomous Hamiltonian systems), the study of recurrences has grown within and across various scientific disciplines. The relatively recent introduction of the recurrence plot (1987) has paved the way for interdisciplinary success stories whereby this simple tool is becoming a unifying force across numerous scientific fields. Indeed, the combined efforts of investigators representing different disciplines are finding common ground with recurrence plots as applied to their specific systems of interest.

On a biannual basis, international symposia on recurrence plots are providing a platform for lively and fruitful debate on both the theoretical and practical domains of recurrence strategies. Unexpected collaborations are being formed that cut across interdisciplinary boundaries. A common vocabulary is being forged which makes "foreign" systems understandable to "strangers" as it were. Starting almost a decade ago, four previous recurrence plot symposia were conducted in Potsdam, Germany (2005); Siena, Italy (2007); Montreal, Canada (2009); and Hong Kong, China (2011).

This volume features 13 selected papers from the Fifth International Symposium on Recurrence Plots in Chicago, Illinois, USA (August 2013). For this particular meeting, special emphases were placed on biological, behavioral, and cognitive systems as well as on the analysis of coupled systems using cross-recurrence methods. These methodological developments and applications highlight the current interest in bivariate and multivariate applications of recurrence analysis to real-world, complex systems.

This book showcases several important examples of the continuing success of recurrence plot strategies across disciplines. Spiegel et al. and Crowley et al. are using recurrence plots to construct novel measures of dissimilarity for multivariate cluster analysis of automotive operational profiles or bivariate detection of dissimilarity between macroeconomic data. Multivariate recurrence-based clustering can also be used to improve the efficiency of brain–computer interfaces as shown by

Uribe et al. and Dos Santos et al. are underscoring the potential of support vector machines based on recurrence quantification measures for the detection of pathological cardiovascular conditions. This strategy is contrasted by Gonzáles et al. who are using traditional recurrence quantifications to compare different variables of the cardiovascular system. Fusaroli et al. are exploring the utility of cross-recurrence analysis to investigate social interactions as well as to delineate crucial challenges and make recommendations for further developments of this approach. Coey et al. and Tolston et al. are studying the complexity of behavioral tasks and examining the coupling of interpersonal coordination by applying cross recurrences. Cross recurrences (besides recurrence networks) are also used by Guhathakurta et al. to study similarities in stock and commodity markets. Sipers et al. are introducing important methodological approaches using recurrence analysis for complex valued signals as well as providing the theoretical foundation for understanding redundancies in recurrence plots. A novel recurrence criterion that can be applied to a special kind of amplitude-varying signals (e.g., for studying transients) is suggested by Ioana et al. Rawald et al. are developing an efficient parallelization scheme for recurrence plot-based calculations, addressing the challenge of recurrence analysis of very long time series.

The papers within this volume represent just a portion of the many other contributions presented at the recurrence plot symposium in Chicago. All such contributions indicate that the applicability of this nonlinear methodology is increasing and that there remains huge potential for interdisciplinary applications, knowledge exchanges, and collaborations. We hope that this volume will encourage the development and application of recurrence plot-based methods in numerous and diverse fields of study.

Potsdam   Norbert Marwan
Cincinnati   Michael Riley
Rome   Alessandro Giuliani
Chicago   Charles L. Webber Jr.

Contents

A Recurrence Plot-Based Distance Measure

Stephan Spiegel, Johannes-Brijnesh Jain and Sahin Albayrak

Abstract Given a set of time series, our goal is to identify prototypes that cover the maximum possible amount of occurring subsequences regardless of their order. This scenario appears in the context of the automotive industry, where the goal is to determine operational profiles that comprise frequently recurring driving behavior patterns. This problem can be solved by clustering, however, standard distance measures such as the dynamic time warping distance might not be suitable for this task, because they aim at capturing the cost of aligning two time series rather than rewarding pairwise recurring patterns. In this contribution, we propose a novel time series distance measure, based on the notion of recurrence plots, which enables us to determine the (dis)similarity of multivariate time series that contain segments of similar trajectories at arbitrary positions. We use recurrence quantification analysis to measure the structures observed in recurrence plots and to investigate dynamical properties, such as determinism, which reflect the pairwise (dis)similarity of time series. In experiments on real-life test drives from Volkswagen, we demonstrate that clustering multivariate time series using the proposed recurrence plot-based distance measure results in prototypical test drives that cover significantly more recurring patterns than using the same clustering algorithm with dynamic time warping distance.

1 Introduction

Clustering of times series data is of pivotal importance in various applications [1] such as, for example, seasonality patterns in retail [2], electricity usage profiles [3], DNA microarrays [4], and fMRI brain activity mappings [5]. A crucial design decision

S. Spiegel (✉) · J.-B. Jain · S. Albayrak
DAI Laboratory, Berlin Institute of Technology, Ernst-Reuter-Platz 7,
10587 Berlin, Germany
e-mail: spiegel@dai-lab.de

J.-B. Jain
e-mail: jain@dai-lab.de

S. Albayrak
e-mail: albayrak@dai-lab.de

of any clustering algorithm is the choice of (dis)similarity function [6, 7]. In many clustering applications, the underlying (dis)similarity function measures the cost of aligning time series to one another. Typical examples of such functions include the DTW and the Euclidean distance [8–10].

Alignment-based (dis)similarity functions, however, seem not to be justified for applications, where two time series are considered to be similar, if they share common or similar subsequences of variable length at arbitrary positions [11–14]. A real-life example for such an application comes from the automotive industry, where test drives of vehicles are considered to be similar, if they share similar driving behavior patterns, i.e. engine behavior or drive maneuvers, which are described by the progression of multiple vehicle parameters over a certain period of time [15, 16]. In this scenario, the order of the driving behavior patterns does not matter [17], but the frequency with which the patterns occur in the contrasted time series.

Recent work [18] on time series distance measures suggests to neglect irrelevant and redundant time series segments, and to retrieve subsequences that best characterize the real-life data. Although subsequence clustering is a tricky endeavor [19], several studies [11–14, 20] have demonstrated that in certain circumstances ignoring sections of extraneous data and keeping intervals with high discriminative power contributes to cluster centers that preserve the characteristics of the data sequences. Related concepts that have been shown to improve clustering results include time series motifs [11, 12], shapelets [13, 14], and discords [20].

In this contribution, we propose to adopt recurrence plots (RPs) [21–23] and related recurrence quantification analysis (RQA) [24–26] to measure the similarity between multivariate time series that contain segments of similar trajectories at arbitrary positions in time [17]. We introduce the concept of joint cross recurrence plots (JCRPs), an extension of traditional RPs, to visualize and investigate multivariate patterns that (re)occur in pairwise compared time series. In dependence on JCRPs and known RQA measures, such as determinism, we define a **R**ecu**RR**ence plot-based (RRR) distance measure, which reflects the proportion of time series segments with similar trajectories or recurring patterns respectively.

In order to demonstrate the practicability of our proposed recurrence plot-based distance measure, we conduct experiments on both synthetic time series and real-life vehicular sensor data [15–17]. The results show that, unlike commonly used (dis)similarity functions, our proposed distance measure is able to (i) determine cluster centers that preserve the characteristics of the data sequences and, furthermore, (ii) identify prototypical time series that cover a high amount of recurring patterns. The rest of the paper is organized as follows. In Sect. 2 we state the general problem being investigated. Subsequently we introduce traditional recurrence plots as well as various extensions in Sect. 3. Recurrence quantification analysis and corresponding measures are discussed in Sect. 4. Our proposed recurrence plot-based distance measure and respective evaluation criteria are introduced in Sect. 5. The experiments results are presented and discussed in Sect. 6. Finally we conclude with future work in Sect. 7.

2 Problem Statement

Car manufacturers aim to optimize the performance of newly developed engines according to operational profiles that characterize recurring driving behavior. To obtain real-life operational profiles for exhaust simulations, Volkswagen (VW) collects data from test drives for various combinations of driver, vehicle and route.

Given a set $\mathscr{X} = \{X_1, X_2, \ldots, X_t\}$ of t test drives, the challenge is to find a subset of k prototypical time series $\mathscr{Y} = \{Y_1, \ldots, Y_k\} \in \mathscr{X}$ that best comprehend the recurring (driving behavior) patterns found in set $\mathscr{X}$. Test drives are represented as multivariate time series $X = (x_1, \ldots, x_n)$ of varying length n, where $x_i \in \mathbb{R}^d$ is a d-dimensional feature vector summarizing the observed measurements at time i. A *pattern* $S = (x_s, \ldots, x_{s+l-1})$ of $X = (x_1, \ldots, x_n)$ is a subsequence of l consecutive time points from X, where $l \le n$ and $1 \le s < s + l - 1 \le n$. Assuming two time series $X = (x_1, ..., x_n)$ and $Y = (y_1, \ldots, y_m)$ with patterns $S = (x_s, \ldots, x_{s+l-1})$ and $P = (y_p, \ldots, y_{p+l-1})$ of length l, we say that S and P are *recurring patterns* of X and Y if $d(S, P) \le \varepsilon$, where and $d : X \times X \to \mathbb{R}^+$ is a (dis)similarity function and ε is a certain similarity threshold. Note that recurring patterns of X and Y may occur at arbitrary positions and in different order.

Since we aim to identify k prototypical time series that (i) best represent the set $\mathscr{X}$ and (ii) are members of the set $\mathscr{X}$, one can employ the k-mediod clustering algorithm.

3 Recurrence Plots

Recurrence plots (RPs) are used to visualize and investigate recurrent states of dynamical systems or rather time series [26, 27]. Even though RPs give very vivid and impressive images of dynamical system trajectories, their implicit mathematical foundation is deceptively simple [21]:

$$R_{i,j}^x(\varepsilon) = \Theta(\varepsilon - ||x_i - x_j||) \quad x_i \in \mathbb{R}^d, i, j = 1 \ldots n \tag{1}$$

where x is a time series of length n, $|| \cdot ||$ a norm and Θ the Heaviside function. One of the most crucial parameters of RPs is the recurrence threshold ε, which influences the formation of line structures [22]. In general, the recurrence threshold should be chosen in a way that noise corrupted observations are filtered out, but at the same time a sufficient number of recurrence structures are preserved. As a rule of thumb, the recurrence rate should be approximately one percent with respect to the size of the plot. For quasi-periodic processes, it has been suggested to use the diagonal line structures to find the optimal recurrence threshold. However, changing the threshold does not preserve the important distribution of recurrence structures [26].

A general problem with standard thresholding methods is that an inappropriate threshold or laminar states cause thick diagonal lines, which basically corresponds to redundant information. Schultz et al. [27] have proposed a local minima-based thresholding approach, which can be performed without choosing any particular threshold and yields in clean RPs of minimized line thickness. But this approach comes with some side-effects, e.g., bowed lines instead of straight diagonal lines.

Furthermore, it is important discuss the definition of recurrences, because distances can be calculated using different norms [21]. Although the L_2-norm is used in most cases, the L_∞-norm is sometimes preferred for relatively large time series with high computational demand [26].

Although traditional RPs only regard one trajectory, we can extend the concept in a way that allows us to study the dynamics of two trajectories in parallel [23]. A cross recurrence plot (CRP) shows all those times at which a state in one dynamical system occurs in a second dynamical system. In other words, the CRP reveals all the times when the trajectories of the first and second time series, x and y, visits roughly the same area in the phase space. The data length, n and m, of both systems can differ, leading to a non-square CRP matrix [22, 24].

$$CR_{i,j}^{x,y}(\varepsilon) = \Theta(\varepsilon - ||x_i - y_j||) \quad x_i, y_j \in \mathbb{R}^d, \ i = 1 \ldots n, \ j = 1 \ldots m \quad (2)$$

For the creation of a CRP, both trajectories, x and y, have to present the same dynamical system with equal state variables because they are in the same phase space. The application of CRPs to absolutely different measurements, which are not observations of the same dynamical system, is rather problematic and requires some data preprocessing with utmost carefulness [22].

In order to test for simultaneously occurring recurrences in different systems, another multivariate extension of RPs was introduced [23]. A joint recurrence plot (JRP) shows all those times at which a recurrence in one dynamical system occurs simultaneously with a recurrence in a second dynamical system. With other words, the JRP is the Hadamard product of the RP of the first system and the RP of the second system. JRPs can be computed from more than two systems. The data length of the considered systems has to be the same [22, 24].

$$JR_{i,j}^{x,y}(\varepsilon^x, \varepsilon^y) = \Theta(\varepsilon^x - ||x_i - x_j||) \cdot \Theta(\varepsilon^y - ||y_i - y_j||) \quad (3)$$
$$x_i \in \mathbb{R}^{d1}, \quad y_j \in \mathbb{R}^{d2}, \quad i, j = 1 \ldots n$$

Such joint recurrence plots have the advantage, that the individual measurements can present different observables with different magnitudes or range. They are often used for the detection of phase synchronization [22, 24].

Since this work aims at clustering test drives, which involves pairwise (dis)similarity comparisons of multivariate time series, we propose a combination of joint and cross recurrence plot, namely (JCRP) joint cross recurrence plot. A JCRP shows all those times at which a multivariate state in one dynamical system occurs

simultaneously in a second dynamical system.

$$JCR_{i,j}^{x,y}(\varepsilon^1, \ldots, \varepsilon^k) = \Theta(\varepsilon^1 - ||x_i^1 - y_j^1||) \cdot \ldots \cdot \Theta(\varepsilon^k - ||x_i^k - y_j^k||) \quad (4)$$

$$x_i, y_j \in \mathbb{R}^d, \quad i = 1 \ldots n, \quad j = 1 \ldots m$$

For the creation of a JRCP both trajectories, x and y, need to have the same dimensionality or number of parameters d, but can have different length, n and m. We shall see that JCRPs are very useful, because they enable us to compare two multivariate systems with the same set of observables that can have different magnitudes. In other words, the introduced *JCR* notation allows us to determine an ε-threshold for each individual parameter, which is advantageous for observables with different variance. A toy example for JCRPs is given in the following:

$$x = \begin{cases} \texttt{dfcghGATHERSPEEDlmknhDECELERATEghfkd} \\ \texttt{rsqtpACCELERATORxywzvBRAKEPEDALtvswr} \end{cases}$$

$$y = \begin{cases} \texttt{kdhfSLOWDOWNglbkchdgfGATHERSPEEDnkml} \\ \texttt{tpsBRAKEPEDALzrysxtwvACCELERATORxtwv} \end{cases}$$

Assume two multivariate time series x and y which comprise the speed and accelerator signal recorded during different car drives. Both time series contain multivariate states or rather string sequences that occur in both systems. The corresponding JCRP of x and y, as illustrated in Fig. 1, shows the times at which a multivariate state occurs simultaneously in both systems. Furthermore, the diagonal line structure in Fig. 1 reveals that both trajectories run through a similar region in phase space for a certain time interval. With other words, both systems contain the same multivariate pattern, which represents that the driver hits the 'ACCELERATOR' pedal and the vehicle simultaneously 'GATHERSPEED'. In Sect. 4 we discuss how to interpret single recurrence points and diagonal line structures, and explain how to use them to define a distance measure for time series with certain distortions or invariance.

4 Recurrence Quantification

Recurrence quantification analysis (RQA) is used to quantify the structures observed in recurrence plots [22]. RQA is grounded in theory, but possesses statistical utility in dissecting and diagnosing nonlinear dynamic systems across multiple fields of science [28]. The explicit mathematical definition to distinct features in recurrence plots enables us to analyze signals that are multivariate, nonlinear, non-stationary and noisy.

The global (large-scale) appearance of a RP can give hints on stationarity and regularity, whereas local (small-scale) patterns are related to dynamical properties, such as determinism [28]. Recent studies have shown that determinism, the percentage
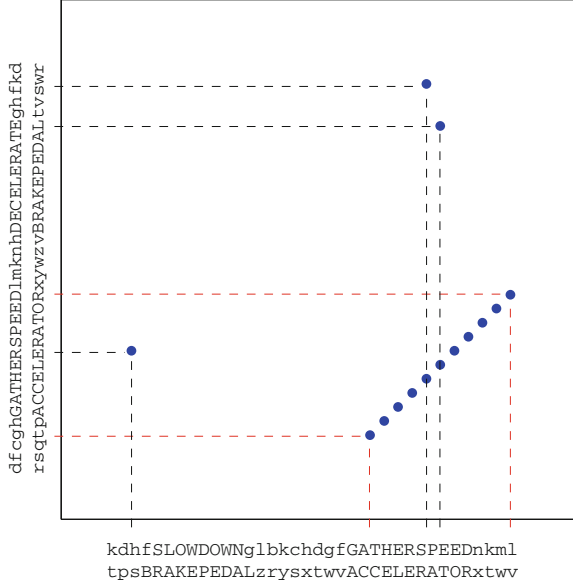
Fig. 1 Joint cross recurrence plot (JCRP) of sample drive x and y from our toy example, with $\varepsilon = 0$

of recurrence points that form lines parallel to the main diagonal, reflects the predictability of a dynamical system [22].

Given a recurrence matrix R with $N \times N$ entries generated by any of the introduced recurrence plot variations, such as our proposed JCRP, we can compute the determinism $DET(\varepsilon, l_{min})$ for a predefined ε-threshold and a minimum diagonal line length l_{min} as followed [22, 24]:

$$DET(\varepsilon, l_{min}) = \frac{\sum_{l=l_{min}}^{N} l \cdot P(\varepsilon, l)}{\sum_{i,j=1}^{N} R_{i,j}(\varepsilon)}$$

$$P(\varepsilon, l) = \sum_{i,j=1}^{N} \left\{ \left(1 - R_{i-1,j-1}(\varepsilon)\right) \cdot \left(1 - R_{i+l,j+l}(\varepsilon)\right) \cdot \prod_{k=0}^{l-1} R_{i+k,j+k}(\varepsilon) \right\} \quad (5)$$

where $P(\varepsilon, l)$ is the histogram of diagonal lines of length l with respect to a certain ε neighborhood.

In general, processes with chaotic behavior cause none or short diagonals, whereas deterministic processes cause relatively long diagonals and less single, isolated recurrence points [22, 29]. In respect to JCRPs, diagonal lines usually occur when the trajectory of two multivariate time series segments is similar according to a certain threshold. Since we aim to measure the similarity between time series that contain segments of similar trajectories at arbitrary positions, which in turn cause diagonal

line structures, we propose to use determinism as a similarity measure. According to the introduced JCRP approach, a high *DET* value indicates high similarity or rather a high percentage of multivariate segments with similar trajectory, whereas a relatively low *DET* value suggests dissimilarity or rather the absence of similar multivariate patterns.

However, data preprocessing like smoothing can introduce spurious line structures in a recurrence plot that cause high determinism value. In this case, further criteria like the directionality of the trajectory should be considered to determine the determinism of a dynamic system, e.g. by using iso-directional and perpendicular RPs [22, 24, 26]. In contrast to traditional recurrence plots, perpendicular recurrence plots (PRPs) consider the dynamical evolution of only the neighborhoods in the perpendicular direction to each phase flow, resulting in plots with lines of the similar width without spreading out in various directions. Removing spurious widths makes it more reasonable to define line-based quantification measures, such as divergence and determinism [30]. Another solution is to estimate the entropy by looking at the distribution of the diagonal lines [26]. The entropy is based on the probability $p(\varepsilon, l)$ that diagonal lines structures with certain length l and similarity ε occur in the recurrence matrix [22, 24].

Recurrence plots (RPs) and corresponding recurrence quantification analysis (RQA) measures have been used to detect transitions and temporal deviations in the dynamics of time series. Since detected variations in RQA measures can easily be misinterpreted, Marwan et al. [25] have proposed to calculate a confidence level to study significant changes. They formulated the hypothesis that the dynamics of a system do not change over times, and therefore the RQA measures obtained by the sliding window technique will be normally distributed. Consequently, if the RQA measures are out of a predefined interquantile range, an observation can be considered significantly. Detecting changes in dynamics by means of RQA measures obtained from a sliding window have been proven to be useful in real-life applications such as comparing traffic flow time series under fine and adverse weather conditions [29].

Since recurrence plot based techniques are still a rather young field in nonlinear time series analysis, systematic research is necessary to define reliable criteria for the selection of parameters, and the estimation of RQA measures [26].

5 Recurrence Plot-Based Distance

According to our formalization of joint cross recurrence (JCR) in Eq. 4 and the denotation of the determinism (DET) in Eq. 5, we can define our RecuRRence Plot-based (RRR) distance measure as follows:

$$RRR(\varepsilon, l_{min}) = 1 - DET(\varepsilon, l_{min}) \tag{6}$$

Since the *DET* value ranges from 0 to 1, depending on the proportion of diagonal line structures found in a *JCR* plot, the *RRR* distance is 0 if the trajectory of both dynamical systems is identical and 1 if there are **no** similar patterns at any position in time.

Although our proposed *RRR* distance measure can be used as a subroutine for various time series mining tasks, this work primarily focuses on clustering. Our aim is to group a set of t unlabeled time series T into k clusters C with centroids Z. In order to evaluate the performance of the time series clustering with respect to our *RRR* distance, we suggest to quantify the number of similar patterns that recur within the established clusters. Therefore, we define the following cluster validation index:

$$E(k) = \frac{1}{t-k} \sum_{z \in \{Z\}} \sum_{c \in \{C_z \setminus z\}} RRR(z, c) \qquad (7)$$

According to our problem setting, the more patterns occur jointly when comparing each centroid $z \in \{Z\}$ with all objects $c \in \{C_z \setminus z\}$ of the corresponding cluster, the lower E, the better our clustering, and the more characteristic are the corresponding prototypes.

Furthermore we are going to evaluate the clustering of time series according to the index I [31], whose value is maximized for the optimal number of clusters:

$$I(k) = \left(\frac{1}{k} \cdot \frac{E(1)}{E(k)} \cdot D_k \right)^p \qquad (8)$$

The index I is a composition of three factors [31], namely $1/k$, $E(1)/E(k)$, and D_k. The first factor will try to reduce index I as the number of clusters k increases. The second factor consists of the ratio of $E(1)$, which is constant for a given dataset, and $E(k)$, which decreases with increase in k. Consequently, index I increases as $E(k)$ decreases, encouraging more clusters that are compact in nature. Finally, the third factor, D_k (which measures the maximum separation between two clusters over all possible pairs of clusters), will increase with the value of k, but is bounded by the maximum separation between two points in the dataset.

$$D_k = \max_{i,j=1}^{k} ||z_i - z_j|| \qquad (9)$$

Thus, the three factors are found to compete with and balance each other critically. The power p is used to control the contrast between the different cluster configurations. Previous work [31] suggests to choose $p = 2$.

The index I has been found to be consistent and reliable, irrespective of the underlying clustering technique and data dimensionality, and furthermore has been shown to outperform the Dunn and David-Bouldin index [31].

6 Evaluation

The goal of our evaluation is to assess how well the RRR distance is suited for: (i) clustering time series that contain similar trajectories at arbitrary positions (in Sect. 6.1), and (ii) identifying prototypical time series that cover as much as possible recurring patterns (in Sect. 6.2).

6.1 Synthetic Data

This controlled experiment aims at visualizing the clustering results of the proposed RRR distance measure compared to the DTW distance.

We generated a labeled dataset, which consists of nine time series from three different categories, called Wave, YoYo and Peak. Each category comprises three time series characterized by multiple occurrence of the same artificial patterns at arbitrary positions. The dataset consists of univariate time series of equal length, as shown in Fig. 2. To visualize the clustering results of the RRR and DTW distance, we applied agglomerative hierarchical clustering with complete linkage on the synthetic dataset.

Figure 3 illustrates the generated hierarchical cluster trees for both examined distance measures on the synthetic time series. The first observation to be made is that RRR perfectly recovers the cluster structure provided by the ground truth, given our knowledge that there are three categories. In contrast, the DTW distance fails and
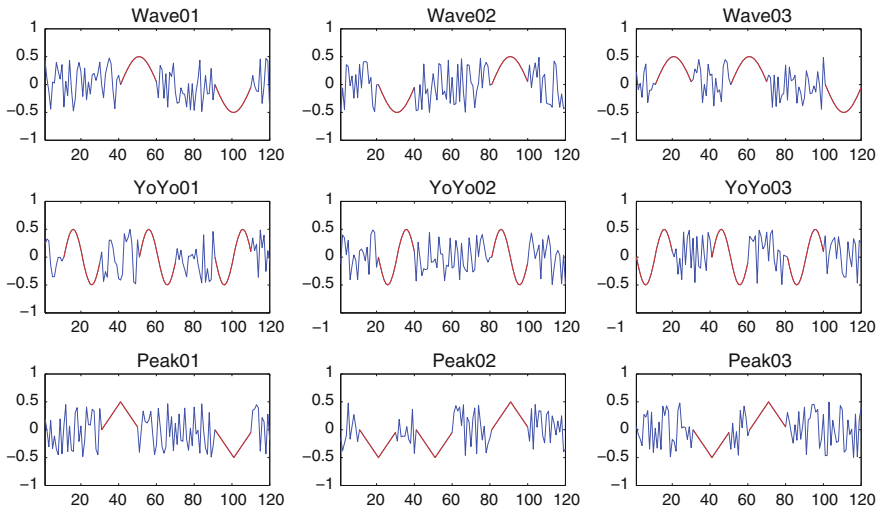
Fig. 2 Univariate synthetic time series with artificially implanted patterns (*red color*) at arbitrary positions, where each time series belongs to one of three groups (Wave, YoYo, and Peak)
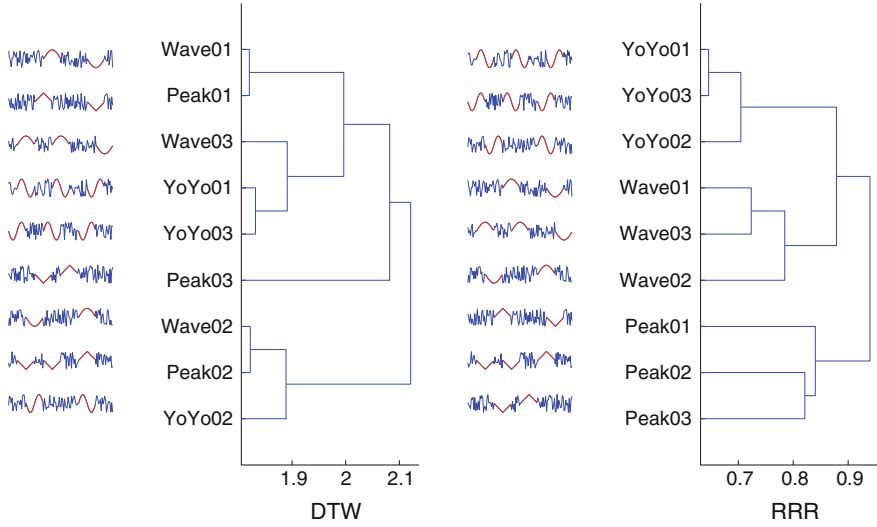
Fig. 3 Cluster tree (dendrogram) of multivariate synthetic time series (introduced in Fig. 2) according to the DTW and RRR distance. The x-axis reveals the distance between the time series being merged and the y-axis illustrates the corresponding name and shape of the time series

assigns time series of different categories to the same cluster at an early stage. The second observation to be made is that RRR is able to recover the ground truth even if a large portion of the time series is noisy. The DTW distance, however, groups time series into the same clusters, if they have globally a similar shape. Therefore, the noisy parts of the time series supersede or superimpose the relevant recurring patterns.

6.2 Real-Life Data

This experiment aims at assessing the time series prototypes identified by the proposed RRR distance measure compared to the DTW distance.

For our evaluation we consider the VW DRIVE dataset, which consists of 124 real-life test drives recorded by one vehicle operated by seven different individuals. Test drives are represented as multivariate time series of varying length and comprise vehicular sensor data of the same observed measurements. Since we aim to identify operations profiles that characterize recurring driving behavior, we exclusively consider accelerator, speed, and revolution measurements, which are more or less directly influenced by the driver. The complete VW DRIVE dataset contains various other measurements, such as airflow and engine temperature, and can be obtained by mailing the first author of this paper.
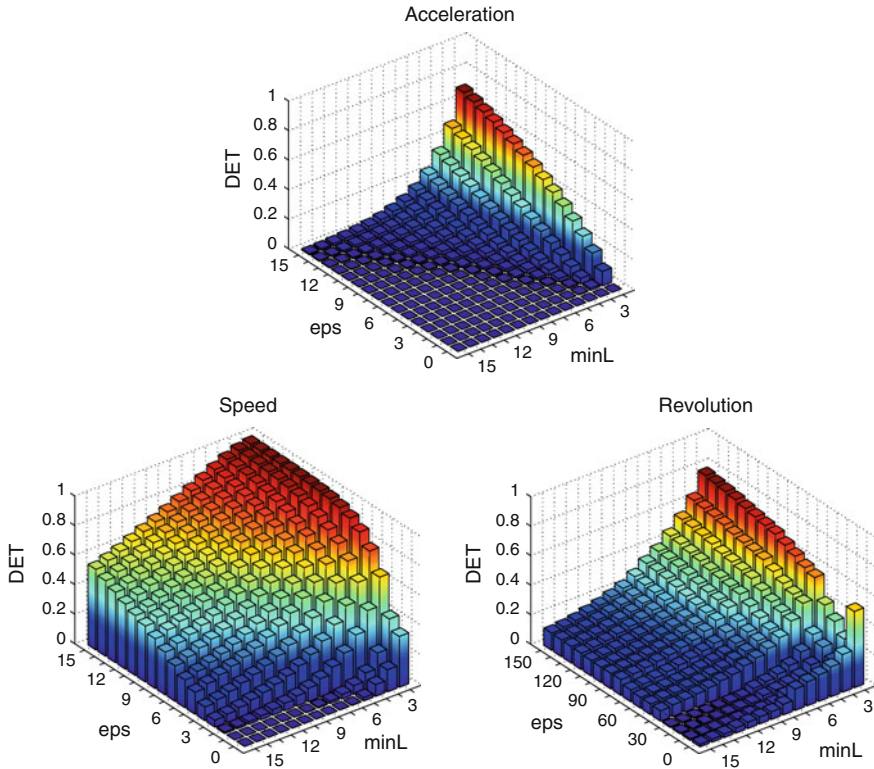
Fig. 4 Determinism (DET) value for changing similarity threshold ε and minimum diagonal *line* length l_{min} for accelerator, speed and revolution signal; based on the cross recurrence plots (CRPs) of 10 randomly selected pairs of tours from our DRIVE dataset. Note that the DET was averaged

To measure the (dis)similarity of the VW DRIVE time series using our proposed RRR distance, we first need to determine the optimal similarity threshold ε and pattern length l_{min} for each of the considered measurements, such that a considerable amount of the recurring patterns is preserved.

Figure 4 shows the determinism value for the accelerator, speed, and revolution signal, in regard to different parameters settings. We can observe that for all considered signals the *DET* value decreases with increasing pattern length l_{min} and decreasing similarity threshold ε. Furthermore, Fig. 4 reveals that the speed signal is highly deterministic, meaning that the same patterns occur frequently, whereas the acceleration and revolution signal are less predictable and show more chaotic behavior.

Since we aim to analyze all signals jointly by means of the proposed joint cross recurrence plot (JCRP) approach, we have to choose a pattern length or rather minimum diagonal line length l_{min} that is suitable for all signals. In general, we are looking for relatively long patterns with high similarity. In other words, we aim to

k	(a) Speed		(a) Speed		(b) Acceleration, Speed, and Revolution		(b) Acceleration, Speed, and Revolution		k
	I RRR	E RRR	I DTW	E DTW	I RRR	E RRR	I DTW	E DTW	
1	-	0.5441	-	0.7041	-	0.7959	-	0.8737	1
2	**1.0000**	**0.5168**	0.1162	0.6794	**1.0000**	**0.7393**	0.7775	0.8622	2
3	0.8778	0.5034	0.6904	0.6602	0.7820	0.7203	0.9088	0.8405	3
4	0.6431	0.4952	0.7548	0.6474	0.5558	0.7064	0.8585	0.8413	4
5	0.4647	0.4924	0.4438	0.6474	0.3883	0.6992	**1.0000**	**0.8407**	5
6	0.3479	0.4909	**1.0000**	**0.6480**	0.2821	0.6934	0.9746	0.8420	6
7	0.2687	0.4888	0.2993	0.6479	0.2141	0.6910	0.2529	0.8452	7
8	0.2151	0.4892	0.1894	0.6493	0.1679	0.6897	0.3100	0.8482	8
9	0.1751	0.4866	0.1189	0.6507	0.1362	0.6855	0.3955	0.8478	9
10	0.1469	0.4862	0.1271	0.6524	0.1131	0.6837	0.2119	0.8534	10
11	0.1254	0.4838	0.3730	0.6530	0.0960	0.6818	0.2624	0.8545	11
12	0.1078	0.4823	0.1184	0.6544	0.0825	0.6784	0.4089	0.8528	12
13	0.0947	0.4817	0.1616	0.6518	0.0717	0.6781	0.2517	0.8576	13
14	0.0838	0.4804	0.2449	0.6531	0.0635	0.6755	0.2453	0.8574	14
15	0.0745	0.4805	0.2988	0.6598	0.0565	0.6746	0.2941	0.8603	15
16	0.0672	0.4803	0.2365	0.6570	0.0508	0.6718	0.2753	0.8588	16
17	0.0609	0.4780	0.1862	0.6507	0.0462	0.6674	0.1106	0.8535	17
18	0.0557	0.4774	0.1761	0.6569	0.0422	0.6687	0.2091	0.8622	18
19	0.0514	0.4751	0.3307	0.6603	0.0387	0.6687	0.1336	0.8596	19
20	0.0473	0.4756	0.0899	0.6579	0.0358	0.6667	0.1036	0.8563	20

Fig. 5 Evaluation of *RRR* and *DTW* distance for clustering **a** univariate and **b** multivariate time series of our DRIVE dataset. We compare the index E for the number of clusters k where the (normalized) index I reaches its maximum. The results are based on 1,000 runs of k-mediods clustering with random initialization

find a parameter setting with preferably large l_{min} and small ε which results in a *DET* value that is above a certain threshold. To preserve the underlying characteristics or rather recurring patterns contained in examined data, at least 20 % of the recurrence points should form diagonal line structures, which corresponds to $DET \geq 0.2$. Based on this criterion we choose $l_{min} = 5$ and $\varepsilon = 14/2/40$ for the accelerator, speed, and revolution signal respectively. Note that the individual signals were not normalized, wherefore the ε-threshold represents the accelerator pedal angle, kilometers per hour, and rotations per minute.

To identify prototypical time series using RRR and DTW distance respectively, we applied k-mediods clustering with random initialization. For evaluation purpose we computed index I and E for a varying number of k prototypes. The results of index I were normalized in a way that the highest value, which indicates the optimal number of clusters, equals one. Since index E is a sum of RRR values (see Eq. 7) and $RRR = 1 - DET$, the lower E, the higher the average *DET* value, and the more recurring (driving behavior) patterns are comprised of the prototypes identified by the respective distance measure.

Figure 5 shows the empirical results for clustering univariate and multivariate time series of the VW DRIVE dataset using RRR and DTW distance respectively. Since the VW DRIVE dataset consists of 'only' 124 test drives recorded by one and the same vehicle, the optimal number of clusters for both RRR and DTW distance is rather small. However, the proposed RRR distance is able to find cluster configurations with lower index E values or rather prototypes with higher amount of recurring patterns than the DTW distance. In case of univariate time series (a), in particular speed measurements, RRR and DTW achieved an index E value of around 0.52 and 0.65 for the optimal number of clusters, which corresponds to a determinism value of 0.48 and 0.35 respectively. In the multivariate case (b), RRR and DTW reached an index E value of around 0.74 and 0.84 for the optimal number of clusters,

which corresponds to determinism value of 0.26 and 0.16 respectively. As might be expected, the results for the univariate time series are better than for the multivariate case, because the search space expands and the probability of recurring patterns decreases with an increasing number of dimensions or measurements respectively. In both cases, however, our RRR distance performs about 10 % better than the compared DTW distance, meaning that the identified prototypes contain 10 % more recurring (driving behavior) patterns.

7 Conclusion

This work is a first attempt to solve time series clustering with nonlinear data analysis and modeling techniques commonly used by theoretical physicists. We adopted recurrence plots (RPs) and recurrence quantification analysis (RQA) to measure the (dis)similarity of multivariate time series that contain segments of similar trajectories at arbitrary positions and in different order.

Strictly speaking, we introduced the concept of joint cross recurrence plots (JCRPs), a multivariate extension of traditional RPs, to visualize and investigate recurring patterns in pairwise compared time series. Furthermore, we defined a recurrence plot-based (RRR) distance measure to cluster time series with order invariance.

The proposed RRR distance was evaluated on both synthetic and real-life time series, and compared with the DTW distance. Our evaluation on synthetic data demonstrates that the RRR distance is able to establish cluster centers that preserve the characteristics of the time series. The results on real-life vehicular data show that, in terms of our cost function, RRR performs about 10 % better than DTW, meaning that the determined prototypes contain 10 % more recurring driving behavior patterns.

Worthwhile future work includes (1) the investigation of RQA measures which quantify recurring patterns with uniform scaling, (2) the application of speed-up techniques for RP computations, and (3) the formalization/analysis of an RP-based distance metric.

References

1. Keogh, E.J., Zhu, Q., Hu, B., Hao, Y., Xi, X., Wei, L., Ratanamahatana, C.A.: The (UCR) time series classification/clustering homepage, www.cs.ucr.edu/eamonn/time_series_data/ (2011)
2. Kumar, M., Patel, N.R., Woo, J.: Clustering seasonality patterns in the presence of errors. In: KDD (2002)

3. Lines, J., Bagnall, A., Caiger-Smith, P., Anderson, S.: Classification of household devices by electricity usage profiles. In: IDEAL, pp. 403–412 (2011)
4. Moeller-Levet, C.S., Klawonn, F., Cho, K.-H., Wolkenhauer, O.: Fuzzy clustering of short time-series and unevenly distributed sampling points. In: IDA, pp. 28–30 (2003)
5. Axel, W., Oliver, L., Dersch, D.R., Leinsinger, G.L., Klaus, H., Benno, P., Dorothee, A.: Cluster analysis of biomedical image time-series. Int. J. Comput. Vision 46(2), 103–128 (2002)
6. Gustavo, E.A., Batista, P.A., Wang, X., Keogh, E.J.: A complexity-invariant distance measure for time series. In: SDM, pp. 699–710 (2011)
7. Liao, T.W.: Clustering of time series data—a survey. J. Pattern Recognit. 38(11), 1857–1874 (2005)
8. Ding, H., Trajcevski, G., Scheuermann, P., Wang, X., Keogh, E.J.: Querying and mining of time series data: experimental comparison of representations and distance measures. PVLDB 1(2), 1542–1552 (2008)
9. Keogh, E.J., Kasetty, S.: On the need for time series data mining benchmarks: a survey and empirical demonstration. Data Min. Knowl. Discov. 7(4), 349–371 (2003)
10. Rakthanmanon, T., Campana, B.J.L., Mueen, A., Batista, G., Westover, M.B., Zhu, Q., Zakaria, J., Keogh, E.J.: Searching and mining trillions of time series subsequences under dynamic time warping. In: KDD, pp. 262–270 (2012)
11. Chiu, B.Y.-c., Keogh, E.J., Lonardi, S.: Probabilistic discovery of time series motifs. In: KDD, pp. 493–498 (2003)
12. Lin, J., Keogh, E.J., Lonardi, S., Patel, P.: Finding motifs in time series. In: KDD (2002)
13. Rakthanmanon, T., Keogh, E.J.: Fast-shapelets: a scalable algorithm for discovering time series shapelets. In: SDM (2013)
14. Zakaria, J., Mueen, A., Keogh, E.J.: Clustering time series using unsupervised-shapelets. In: ICDM, pp. 785–794 (2012)
15. Stephan, S., Johannes, J.B., William, De L.E., Sahin, A.: Pattern recognition in multivariate time series: dissertation proposal. In: PIKM, pp. 27–34 (2011)
16. Stephan, S., Julia, G., Andreas, L., Ernesto, De L., Sahin, A.: Pattern recognition and classification for multivariate time series. In: SensorKDD, pp. 34–42 (2011)
17. Spiegel, S., Albayrak, S.: An order-invariant time series distance measure—Position on recent developments in time series analysis. In: KDIR, pp. 264–268 (2012)
18. Bing, H., Chen, Y., Keogh, E.J.: Time series classification under more realistic assumptions. In: SDM (2013)
19. Keogh, E.J., Lin, J.: Clustering of time-series subsequences is meaningless: implications for previous and future research. Knowl. Inf. Syst. 8(2), 154–177 (2005)
20. Keogh, E.J., Lin, J., Fu, A.W.-C.: HOT SAX: efficiently finding the most unusual time series subsequence. In: ICDM, pp. 226–233 (2005)
21. Marwan, N.: Encounters with neighbours: current developments of concepts based on recurrence plots and their applications. University of Potsdam (2003)
22. Marwan, N., Romano, M., Thiel, M., Kurths, J.: Recurrence plots for the analysis of complex systems. Phys. Rep. 438(5–6), 237–329 (2007)
23. Marwan, N.: A historical review of recurrence plots. Eur. Phys. J. Special Topics 164(1), 3–12 (2008)
24. Marwan, N., Romano, M., Thiel, M.: Recurrence plots and cross recurrence plots. www.recurrence-plot.tk
25. Marwan, N., Schinkel, S., Kurths, J.: Recurrence plots 25 years later—gaining confidence in dynamical transitions. Europhys. Lett., 101(2) (2013)
26. Marwan, N.: How to avoid potential pitfalls in recurrence plot based data analysis. I. J. Bifurcat. Chaos 21(4), 1003–1017 (2011)
27. Schultz, A.P., Zou, Y., Marwan, N., Turvey, M.T.: Local minima-based recurrence plots for continuous dynamical systems. I. J. Bifurcat. Chaos 21(4), 1065–1075 (2011)
28. Webber, C.L., Marwan, N., Facchini, A., Giuliani, A.: Simpler methods do it better: success of recurrence quantification analysis as a general purpose data analysis tool. Phys. Lett. A 373(41), 3753–3756 (2009)

29. Vlahogianni, E.I., Karlaftis, M.G.: Comparing traffic flow time-series under fine and adverse weather conditions using recurrence-based complexity measures. Nonlinear Dyn. **69**(4), 1949–1963 (2012)
30. Choi, J.M., Bae, B.H., Kim, S.Y.: Divergence in perpendicular recurrence plot; quantification of dynamical divergence from short chaotic time series. Phys. Lett. A **263**(4–6), 299–306 (1999)
31. Maulik, U., Bandyopadhyay, S.: Performance evaluation of some clustering algorithms and validity indices. IEEE Trans. Pattern Anal. Mach. Intell. 24(12), 1650–1654 (2002)

Fast Computation of Recurrences in Long Time Series

Tobias Rawald, Mike Sips, Norbert Marwan and Doris Dransch

Abstract   We present an approach to recurrence quantification analysis (RQA) that allows to process very long time series fast. To do so, it utilizes the paradigm *Divide and Recombine*. We *divide* the underlying matrix of a recurrence plot (RP) into sub matrices. The processing of the sub matrices is distributed across multiple graphics processing unit (GPU) devices. GPU devices perform RQA computations very fast since they match the problem very well. The individual results of the sub matrices are *recombined* into a global RQA solution. To address the specific challenges of subdividing the recurrence matrix, we introduce means of synchronization as well as additional data structures. Outperforming existing implementations dramatically, our GPU implementation of RQA processes time series consisting of $N \approx 1,000,000$ data points in about 5 min.

1 Introduction

Many different systems show recurring behavior and its study has attracted attention in almost all scientific fields. The climate system can express recurring behavior due to Milankovich cycles [1], seasonal changes, El Niño/Southern Oscillation, etc. The study of these recurrences allows for a better understanding of the climate system;

T. Rawald (✉) · D. Dransch · M. Sips
German Research Center for GeoSciences GFZ,
Berlin, Germany
e-mail: trawald@gfz-potsdam.de

D. Dransch
e-mail: dransch@gfz-potsdam.de

M. Sips
e-mail: sips@gfz-potsdam.de

N. Marwan
Potsdam Institute for Climate Impact Research, Potsdam, Germany
e-mail: marwan@pik-potsdam.de

its past as well as its future [2–4]. The cardiorespiratory system is investigated by its recurrence properties to get insights in its mechanisms or to measure dysfunctions for diagnosing life threatening conditions [5–9]. Recurrence analysis is promising for investigating brain activity [10] and early detection of epileptic states [11]. Furthermore, it is applied to monitor engines and technological processes, like power generation gas turbines health, cutting processes or crack detection in materials [12–14].

Recurrence plots (RPs) and recurrence quantification analysis (RQA) are powerful methods for analyzing recurrences in measured time series [15]. Their application in many fields have proven their potential for various kinds of analyses [16]. A recurrence plot is a two-dimensional representation of a time series when a m-dimensional phase space trajectory recurs to former (or later) states. Recurrence of a state at time i at a different time j is captured within a two-dimensional squared matrix $\mathbf{r}$ [15]:

$$r_{i,j} = \Theta \left(\varepsilon - \left\| \mathrm{x}_i - \mathrm{x}_j \right\| \right), \quad \mathrm{x}_i \in \mathbb{R}^m, \ i, j = 1 \ldots N. \tag{1}$$

Both of its axes represent the set of states in temporal order. N is the number of considered states x_i (length of phase space trajectory). ε is a threshold distance, $\| \cdot \|$ a norm, and $\Theta(\cdot)$ the Heaviside function. A pair of states that fulfills the threshold condition is assigned with the value 1 (*recurrence point*), whereas a pair that is considered to be dissimilar is assigned with the value 0. Further details about the reconstruction of phase space vectors from a scalar time series, the recurrence parameters, as well as the typical visual characteristics of RPs can be found in [15].

Small scale structures in the RP, like diagonal lines, are used to define measures of complexity establishing the recurrence quantification analysis (RQA) [15, 17, 18]. As an example, we present the RQA measure *percent determinism* (*DET*):

$$DET = \frac{\sum_{l=d_{\min}}^{N} l \, H_{\mathrm{D}}(l)}{\sum_{i,j=1}^{N} r_{i,j}}. \tag{2}$$

It is the fraction of recurrence points that form diagonal lines; $H_{\mathrm{D}}(l)$ is the number of diagonal lines of exactly length l and $d_{\min}$ is a minimal length necessary to be a diagonal line. This measure characterizes the deterministic nature of a dynamical system from a heuristic point of view (further discussions can be found in [15, 19]). Further measures quantify average line lengths or the complexity of the line length frequency distributions $H_{\mathrm{D}}(l)$ (diagonal lines) and $H_{\mathrm{V}}(l)$ (vertical lines).

The time complexity of basic RQA measures is $O(N^2)$, where N denotes the number of data points. This property hampers an efficient computation for very long data. Furthermore, current implementations are limited by the memory these tools can manage. The CRP Toolbox for MATLAB [20] is limited to $N < 10,000$ data points when calculating the entire RP; for standard PC configurations even less, i.e., $N < 5,000$ data points. The RQA software by Webber [21] is capable of processing only up to $N = 5,000$ data points.

We present an algorithm based on the concept of *Divide and Recombine* (D&R) that allows RQA of very long time series in Sect. 2 and evaluate our algorithm in Sect. 3. In Sect. 4 we highlight the utilization of our approach for a concrete application example taken from the climate research domain.

2 Our Approach

2.1 Divide and Recombine

D&R is a very general approach to address large computational problems. The basic idea is to divide a data set into small sub sets allowing the fast computation of analytical results of the subsets. The intermediate results of the sub sets are recombined into a global solution.

The main application of D&R as presented by Guha et al. in [22] is to enable the analysis of big data sets. They use the *MapReduce* [23] framework to distribute the data and analytical computation between several computing nodes. In contrast, the central challenge in the context of RQA is not the amount of data itself but rather that the determination of RQA measures is compute intensive. To meet this challenge, we utilize the paradigm D&R as follows.

We divide the underlying matrix of a RP, the so called *recurrence matrix* [see Eq. 1] into small sub matrices (*Divide*). For each sub matrix, we compute RQA measures in a massively parallel manner on GPU devices. This includes especially the detection of diagonal and vertical lines. The key issue of the divide step is distributing RQA computations of sub matrices between multiple GPU devices. In a final step, the individual results of the sub matrices are recombined into a global RQA solution (*Recombine*).

Having distributed the computational load to several GPU devices using D&R, we further reduce the runtime by exploiting the parallel processing capabilities of a GPU device itself. We subdivide the processing within a sub matrix into a set of subtasks that can be processed concurrently. The underlying workflow of our approach is summarized in Fig. 1.

An important challenge with D&R for RQA is that diagonal and vertical lines may spread over multiple sub matrices (see Fig. 2). To compute a valid global frequency distribution of diagonal and vertical line lengths, we introduce the *carryover buffer*. A carryover buffer is a data structure that allows to share information about the length of diagonal or vertical lines that exceed a sub matrix. In the following, we describe how our approach addresses the challenges of computing valid global frequency distributions of diagonal and vertical line lengths (see Sect. 1).
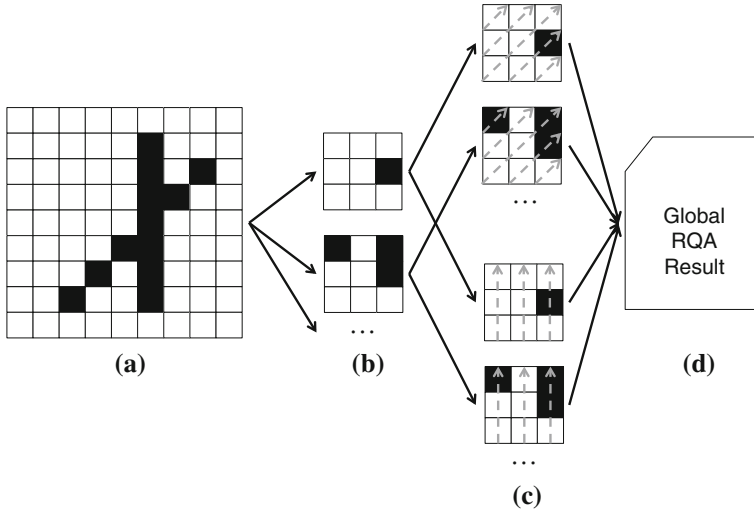
Fig. 1 Our D&R approach. **a** Given a recurrence matrix. **b** We divide the recurrence matrix into a set of sub matrices. **c** We distribute sub matrices to several GPU devices. For each sub matrix, we compute the frequency distributions of *diagonal* and *vertical lines*. The computation of the frequency distributions of a single sub matrix is done in a massively parallel manner on a GPU device by identifying independent sub tasks; depicted as *dotted arrows*. **d** The individual results are recombined into a global RQA solution

2.2 Detection of Vertical and Diagonal Lines

To determine vertical lines within the ith column of the recurrence matrix **r**, the computation starts at element $r_{i,0}$, representing its first element. The index j is increased until the first recurrence point (see Sect. 1) has been found. Assuming the element $r_{i,j}$ is a recurrence point, the counter representing the length of the current vertical line is increased by 1. This counter is initially set to 0. If $r_{i,j+1}$ is also a recurrence point, the counter is increased again. If $r_{i,j+1}$ is not a recurrence point, the vertical line stops at $r_{i,j}$. We then update the frequency distribution of vertical line lengths $H_V(l)$, reset the line length counter to 0 and continue the detection of vertical lines at $r_{i,j+2}$. Note, each column of the recurrence matrix has a separate line length counter attached.

Subdividing **r**, its columns are split into a number of parts belonging to different sub matrices. We introduce the *vertical carryover buffer* to address this challenge. For each column of **r** it stores the length of a vertical line that exceeds the horizontal border of a sub matrix.

Figure 3 compares the detection of vertical lines using (a) the recurrence matrix as a whole with applying (b) the vertical carryover buffer to the set of sub matrices. The states of the carryover buffer element corresponding to the column containing the vertical line after processing a particular sub matrix are shown above the recurrence

(a)   **(b)**
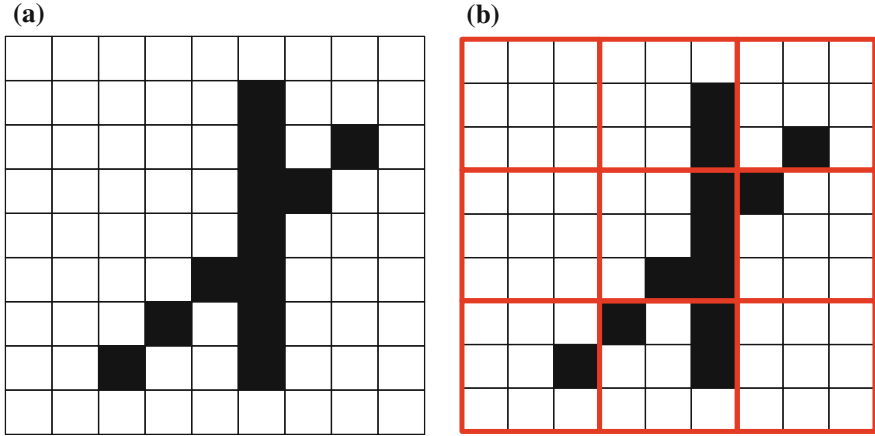
Fig. 2 Challenges of divide and recombine for RQA. The single *diagonal* and *vertical line* in (**a**) are distributed between several sub matrices in (**b**). **a** Full recurrence plot. **b** Divided recurrence plot

plot. If a vertical line reaches the last element of a column of a sub matrix, the carryover buffer element stores its current length. Otherwise its value is 0.

The value of the carryover buffer element is used as input for processing parts of the ith column of **r** that belong to the adjacent sub matrix. To compute valid results, applying the carryover buffer requires a particular order of processing the sub matrices. We present the *vertical execution order rule* that reflects this dependency.

A sub matrix of **r** is referred to as $S_{g,h}$. The sub matrix representing the bottom left corner of the recurrence matrix has the indices $g = 0$ and $h = 0$.

Vertical Execution Order Rule *Suppose a sub matrix $S_{g,h}$ with g being the horizontal index and h being the vertical index. All sub matrices $S_{g,n}$ with $0 \leq n < h$ have to be processed before $S_{g,h}$ is processed.*

Sub matrices which do not share any element of the carryover buffer can be processed concurrently. This allows us to compute the local frequency distribution of vertical line lengths of multiple sub matrices at the same time.

This concept can easily be adapted to the detection of diagonal lines, including the use of a carryover buffer and a particular order of execution concerning the set of sub matrices. The major difference is that a diagonal line may transcend not only the horizontal but also the vertical borders of sub matrices. Furthermore, the size of the carryover buffer is equivalent to the number of diagonals of **r**.

Figure 4 illustrates the detection of diagonal lines. For the purpose of demonstration, the RP contains only a single diagonal line of length 6. Since diagonal lines may cross horizontal as well as vertical sub matrix borders, we define a *diagonal execution order rule* that reflects this property.

Diagonal Execution Order Rule *Suppose a sub matrix $S_{g,h}$ with g being the horizontal index and h being the vertical index. All sub matrices $S_{m,n}$ that fulfill either*

III. | 0

II. | 5

I. | 2

(a)

(b)
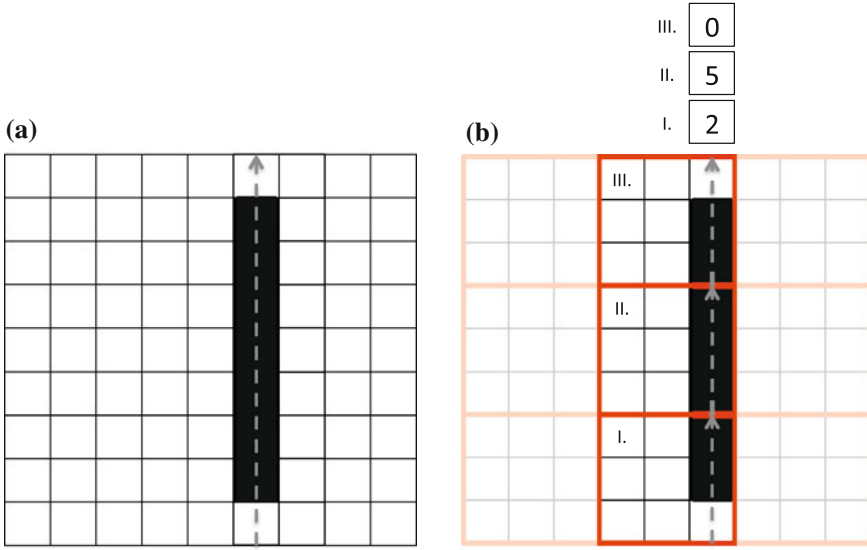
Fig. 3 Detection of vertical lines. Detecting the *vertical line* in (**a**) is straight-forward. Performing the processing on multiple sub matrices in (**b**) requires to preserve the execution order $I. \rightarrow II. \rightarrow III.$ The intermediate states of the carryover buffer element corresponding to the column after processing each sub matrix (2, 5 and 0) are depicted above the recurrence plot. **a** Full recurrence matrix. **b** Multiple sub matrices

(a)

(b)

1 | I.

2 | II.

4 | III.

5 | IV.

0 | V.
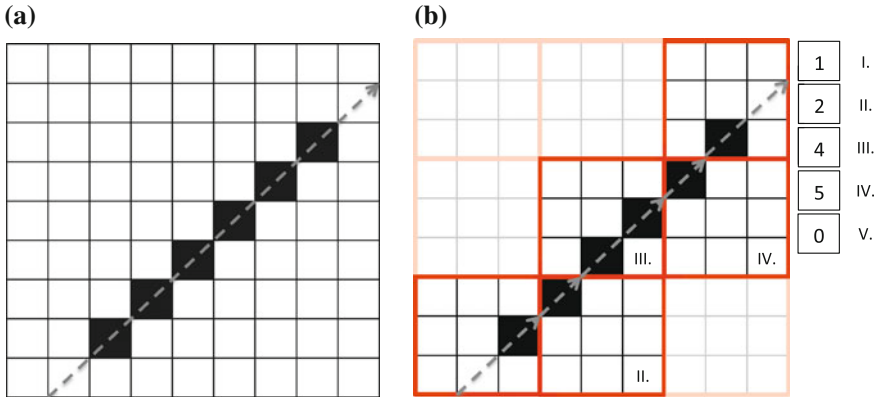
Fig. 4 Detection of diagonal lines. Given a full recurrence matrix in (**a**), the detection of the *diagonal line* is straight-forward. By dividing the recurrence matrix in (**b**), the *diagonal line* stretches over 5 sub matrices. To preserve the validity of the detection result, they must be processed in the order $I. \rightarrow II. \rightarrow III. \rightarrow IV. \rightarrow V.$ The intermediate states of the corresponding carryover buffer element is depicted on the right next to the recurrence plot. **a** Full recurrence matrix. **b** Multiple sub matrices

the condition $(0 \le m \le g) \land (0 \le n < h)$ *or* $(0 \le m < g) \land (0 \le n \le h)$ *have to be processed before* $S_{g,h}$ *is processed.*

3 Performance Evaluation

To evaluate our approach, we compare the performance characteristics of three RQA implementations. We contribute an implementation of our D&R approach using version 1.1 of the *OpenCL* framework for parallel programming of heterogeneous systems [24]. To fulfill the performance requirements, we use the low-level programming language C++ for implementing the host program.

The hardware setup of the experiment consists of an off-the-shelf desktop workstation, containing an Intel i5-3570 quad-core CPU at up to 3.80 GHz and 16 GB of main memory. It also includes a NVIDIA GeForce GTX 690 that provides two GPU processors running at up to 1.019 GHz; each of them is supplied with 2 GB of memory. In the context of heterogeneous computing, each GPU processor is treated as a separate computing device. The workstation runs on a 64-bit version of *OpenSuse* 12.1 with version 4.2.1 of *CUDA*.

To reduce the impact of outliers, we repeat each experiment five times. Measuring the runtime, we rely on the *chrono* package of the *Boost* library [25] with an accuracy up to one millisecond.

As stated in [26], it is important to compare optimized code that is running on the GPU to optimized CPU code. For this reason, we compare the massively parallel GPU implementation approach to two non-distributed, non-D&R CPU implementations. As a baseline we refer to a single-threaded C++ implementation. Additionally, we employ a parallel C++ implementation that is extended with *OpenMP* statements. It executes the detection of diagonal and vertical lines using multiple CPU threads.

Table 1 Runtime for RQA calculation for time series of varying length

Length	OpenCL (1 × GPU) (s)	OpenCL (2 × GPU) (s)	OpenMP (CPU)	Single thread (CPU)
20,000	0.8	0.8	1.1 s	5.6 s
40,000	1.8	1.7	4.4 s	22.3 s
60,000	3.1	2.5	10.0 s	50.2 s
80,000	4.6	3.4	17.7 s	1 min 29.2 s
100,000	6.3	4.5	27.6 s	2 min 19.5 s
120,000	8.4	5.6	39.9	3 min 21.0 s
140,000	10.7	6.7	54.3 s	4 min 33.2 s
160,000	13.3	8.2	1 min 10.9 s	5 min 56.8 s
180,000	16.2	9.7	1 min 29.7 s	7 min 30.9 s
200,000	19.3	11.4	1 min 50.7 s	9 min 16.8 s

Parameters are embedding dimension $m = 2$ and embedding delay $\tau = 2$
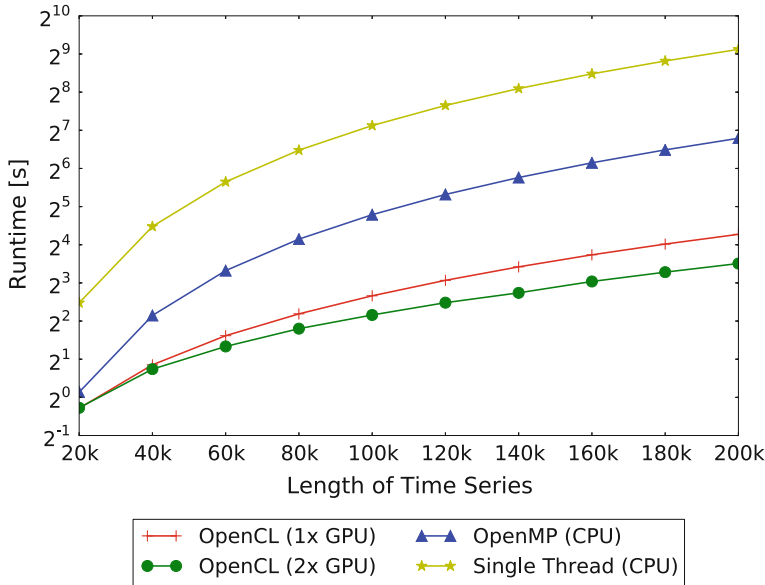
Fig. 5 Runtime comparison. Our GPU implementation (OpenCL) of D&R outperforms both the single-threaded (C++) and multi-threaded (OpenMP) non-D&R CPU implementations. Balancing the work between two GPU processors, the runtime can be reduced additionally up to 40 %

Table 1 and Fig. 5 compare the runtime of the three implementations based on a time series capturing the Sinus wave. We vary the length of the time series between 20,000 and 200,000 data points with a step size of 20,000. For each experiment we use the same parameters for reconstructing the states from the time series (see Sect. 1). Furthermore, we set the size of the sub matrices processed by a GPU processor to 20,000 × 20,000 elements.

In all cases, our OpenCL implementation outperforms the multi-threaded OpenMP implementation (up to a factor >5) and the single-threaded C++ implementation (up to a factor >28) using only one GPU processor. Using both GPU processors available, the runtime can be reduced additionally up to 40 %.

4 Application to Climate Data

In the following we will investigate the hourly temperature dynamics by RQA, which will be applied on a measurement record of hourly air temperature in Potsdam. This record is one of the longest, non-interrupted, hourly climate records in the world. In our analysis it is covering the period from 1893 until 2011 (although the measurements are still ongoing), resulting in 1,043,112 data points (see Fig. 6a). For the period between 1893 and 1974, the warming trend of the annual mean temperature
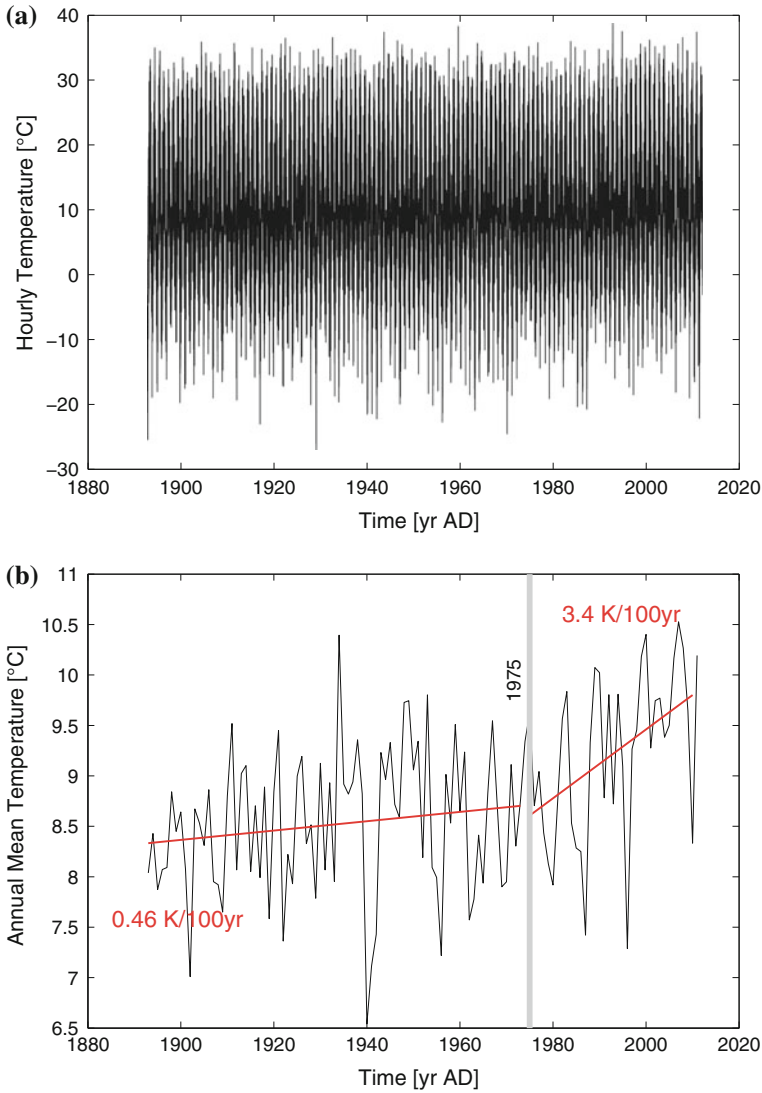
Fig. 6 a Hourly temperature in Potsdam. **b** Annual mean temperature in Potsdam and warming trend for the periods 1893–1974 and 1975–2011

was 0.46 K per century, but after 1974 the trend rose to 3.4 K per century (see Fig. 6b). In the following we will consider the full time period as well as the two periods 1893–1974 (718,776 data points) and 1975–2011 (324,336 data points) separately.

To study the short-term dynamics, we remove the annual trend (seasonal cycle) from the data by phase averaging, resulting in an anomaly temperature record. We use a time delay embedding of dimension $m = 5$ and delay $\tau = 3$, which have

Table 2 RQA results for the full time series of hourly temperature anomaly data of Potsdam as well for the two periods 1893–1974 and 1975–2011

Measure	1893–2011	1893–1974	1975–2011
RR	0.12	0.12	0.13
DET	0.94	0.94	0.94
L	8.4	8.4	8.6
LAM	0.96	0.97	0.96

been found by false nearest neighbors approach for finding m [27] as well as a combined autocorrelation and visual recurrence plot inspection approach for finding an optimal τ [28]. We calculate the four RQA measures (1) recurrence rate RR, (2) determinism DET, (3) average diagonal line length L, and (4) laminartity LAM [15] for a recurrence threshold of $\varepsilon = 1$ (Euclidean norm). These measures reflect different aspects of the short-term dynamics, e.g., predictability. We find that all four measures do not remarkably change for the full period and the sub periods 1893–1974 and 1975–2011 (see Table 2). This result suggests that, in contrast to the longer time-scales, the short-term dynamics, and, thus, the short-term weather predictability, has not (yet) changed due to the climate change.

The calculation of these RQA measures benefits highly from our D&R approach, which makes the calculations possible for these long time series. We apply the same implementations as well as the same experimental environment as described in Sect. 3. Using the single-threaded common RQA software, it takes over six hours to calculate the RQA for the full time period, whereas the OpenMP implementation still needs over one and a half hour. The OpenCL implementation allows to reduce the runtime to about five minutes, using two GPU processors (see Table 3, Fig. 7). This significant runtime improvement of RQA will allow comprehensive investigations of big data collections of weather data, consisting of thousands of time series similar to the present Potsdam temperature record.

Despite its performance improvements, it is of great importance that the GPU implementation computes correct RQA results. Table 4 compares a selection of RQA measures computed by the different implementations for the period between 1893 and 2011. It shows that the GPU implementation calculates the same results as the

Table 3 Runtime for RQA calculation for the full time series of hourly temperature anomaly data of Potsdam as well for the two periods 1893–1974 and 1975–2011

Computation schema	1893–1974	1975–2011	1893–2011
OpenCL (1 × GPU)	4 min 40 s	57 s	10 min 11 s
OpenCL (2 × GPU)	2 min 25 s	30 s	5 min 10 s
OpenMP (CPU)	44 min 38 s	9 min 5 s	1 h 33 min 58 s
Single thread (CPU)	2 h 59 min 25 s	36 min 35 s	6 h 18 min 4 s
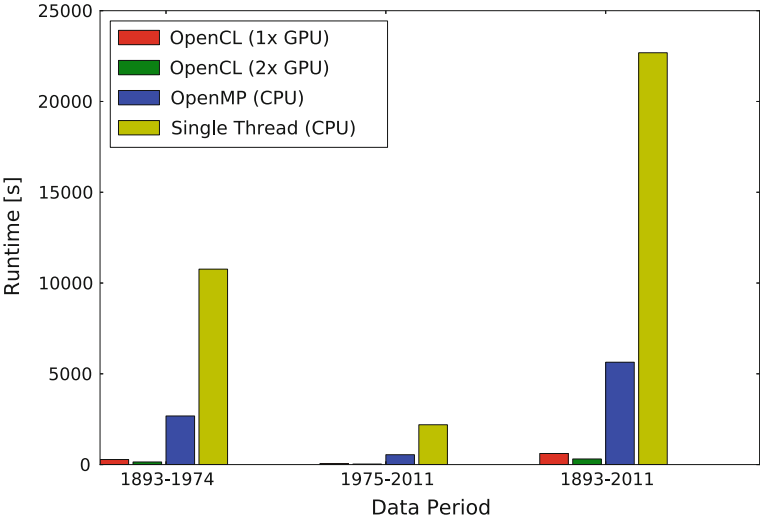
Fig. 7 Runtime for RQA calculation for the full time series of hourly temperature anomaly data of Potsdam as well for the two periods 1893–1974 and 1975–2011

Table 4 Results for the RQA measures recurrence rate RR, determinism DET, average diagonal line length L, and laminarity LAM computed by the different implementations for the period 1893–2011

Measure	OpenCL ($1 \times$ GPU)	OpenCL ($2 \times$ GPU)	OpenMP (CPU)	Single thread (CPU)
RR	0.12	0.12	0.12	0.12
DET	0.94	0.94	0.94	0.94
L	8.4	8.4	8.4	8.4
LAM	0.96	0.96	0.96	0.96

single-threaded C++ and the multi-threaded OpenMP implementation. In addition, distributing the computations between two GPU processors does not influence the results.

5 Conclusion

We present an approach based on the paradigm of D&R that allows to perform RQA on very long time series ($>1{,}000{,}000$ data points) efficiently. By splitting the underlying matrix of a RP into a set of sub matrices, we are able to distribute the computational load between several GPU devices; each sub matrix is processed individually. We address the problem of diagonal and vertical lines transcending the borders of multiple sub matrices by introducing the diagonal and vertical carryover

buffer as global data structures. To preserve the correctness of the RQA measures, we provide specific execution order rules for processing the individual sub matrices.

In comparison to a parallel CPU implementation using OpenMP, we can improve the runtime performance significantly up to factor >9, using two GPU processors. Our experiments have shown that GPU devices are well suited to compute basic RQA measures.

The application of the proposed RQA implementation to a specific problem from climate research has demonstrated its potential for an efficient recurrence study and will allow future RQA investigations of very long time series.

References

1. Muller, R.A., MacDonald, G.J.: Ice Ages and Astronomical Causes. Springer, New York (2002). (Springer Praxis Books/Environmental Sciences)
2. Ponyavin, D.I.: Sol. Phys. **224**(1–2), 465 (2005). doi:10.1007/s11207-005-4979-5
3. Donges, J.F., Donner, R.V., Trauth, M.H., Marwan, N., Schellnhuber, H.J., Kurths, J.: Proc. Nat. Acad. Sci. **108**(51), 20422 (2011). doi:10.1073/pnas.1117052108
4. Goswami, B., Marwan, N., Feulner, G., Kurths, J.: Eur. Phys. J. Special Topics **222**, 861 (2013). doi:10.1140/epjst/e2013-01889-8
5. Zbilut, J.P., Koebbe, M., Loeb, H., Mayer-Kress, G.: pp. 263–266. IEEE Computer Society Press (1990), doi:10.1109/CIC.1990.144211
6. Porta, A., Baselli, G., Montano, N., Gnecchi-Ruscone, T., Lombardi, F., Malliani, A., Cerutti, S.: Biol. Cybern. **75**(2), 163 (1996)
7. Marwan, N., Wessel, N., Meyerfeldt, U., Schirdewan, A., Kurths, J.: Phys. Rev. E **66**(2), 026702 (2002). doi:10.1103/PhysRevE.66.026702
8. Van Leeuwen, P., Geue, D., Thiel, M., Cysarz, D., Lange, S., Romano, M.C., Wessel, N., Kurths, J., Grönemeyer, D.H.W.: Proc. Nat. Acad. Sci. **106**(33), 13661 (2009). doi:10.1073/pnas.0901049106
9. Marwan, N., Zou, Y., Wessel, N., Riedl, M., Kurths, J.: Philos. Trans. R. Soc. A **371**(1997), 20110624 (2013). doi:10.1098/rsta.2011.0624
10. Carrubba, S., Frilot II, C., Chesson Jr, A.L., Marino, A.A.: Med. Eng. Phys. **32**(8), 898 (2010). doi:10.1016/j.medengphy.2010.06.006
11. Acharya, U.R., Sree, S.V., Chattopadhyay, S., Yu, W., Ang, P.C.A.: Int. J. Neural Syst. **21**(3), 199 (2011). doi:10.1142/S0129065711002808
12. Bassily, H., Wagner.: **10**, 629–635 (2008)
13. Litak, G., Sen, A.K., Syta, A.: Chaos, Solitons Fractals **41**(4), 2115 (2009). doi:10.1016/j.chaos.2008.08.018
14. Iwaniec, J., Uhl, T., Staszewski, W.J., Klepka, A.: Nonlinear Dyn. **70**(1), 125 (2012). doi:10.1007/s11071-012-0436-9
15. Marwan, N., Romano, M.C., Thiel, M., Kurths, J.: Phys. Rep. **438**(5–6), 237 (2007). doi:10.1016/j.physrep.2006.11.001
16. Marwan, N.: Eur. Phys. J. Special Topics **164**(1), 3 (2008). doi:10.1140/epjst/e2008-00829-1
17. Zbilut, J.P., Webber Jr, C.L.: Phys. Lett. A **171**(3–4), 199 (1992). doi:10.1016/0375-9601(92)90426-M
18. Webber Jr, C.L., Zbilut, J.P.: J. Appl. Physiol. **76**(2), 965 (1994)

19. Marwan, N., Schinkel, S., Kurths, J.: Europhys. Lett. **101**, 20007 (2013). doi:10.1209/0295-5075/101/20007
20. Marwan, N.: CRP Toolbox 5.17 (2013). Platform independent (for Matlab). http://tocsy.pik-potsdam.de/CRPtoolbox
21. Webber, C.L. Jr.: RQA Software 14.1 (2013). Only for DOS. http://homepages.luc.edu/~decwebber
22. Guha, S., Hafen, R., Rounds, J., Xia, J., Li, J., Xi, B., Cleveland, W.S.: Stat. 1(1), 53 (2012). doi:10.1002/sta4.7. http://dx.doi.org/10.1002/sta4.7
23. Dean, J., Ghemawat, S.: Commun. ACM **51**(1), 107 (2008)
24. OpenCL 1.1 Specification (2010). http://www.khronos.org/registry/cl/specs/opencl-1.1.pdf
25. Dawes, B., Abrahams, D., Rivera, R.: Boost—C++ libraries (2013). http://www.boost.org
26. Lee, V.W., Kim, C., Chhugani, J., Deisher, M., Kim, D., Nguyen, A.D., Satish, N., Smelyanskiy, M., Chennupaty, S., Hammarlund, P., Singhal, R., Dubey, P.: In: Proceedings of the 37th Annual International Symposium on Computer Architecture, ISCA'10, pp. 451–460 (2010)
27. Kennel, M.B., Brown, R., Abarbanel, H.D.I.: Phys. Rev. A **45**(6), 3403 (1992). doi:10.1103/PhysRevA.45.3403
28. Marwan, N.: Int. J. Bifurcat. Chaos **21**(4), 1003 (2011). doi:10.1142/S0218127411029008

Unthresholded Recurrence Plots
for Complex-Valued Representations
of Narrow Band Signals

Aloys Sipers, Paul Borm and Ralf Peeters

Abstract We address the information content of unthresholded recurrence plots for complex-valued signals admitting a Fourier series representation (including periodic and sampled signals). Unthresholded recurrence plots of complex-valued signals contain the information of two real-valued signals simultaneously and can therefore be used to study the relationship between these signals. The graph theoretic procedure in our recent work [1], which was developed to characterize the uniqueness conditions for real-valued signals, is extended to the class of complex-valued signals. The special properties of complex signal representations provide alternative ways to employ unthresholded recurrence plots on narrow band signals. Examples and an application from EEG analysis clarify the results.

1 Introduction

Recurrence plots (RPs) are a signal analysis method that was initially introduced to visualize characteristics of a trajectory in a phase space [2]. Later, to go beyond the visual impression, different measures of quantification of RPs were introduced, see [3, 4]. These techniques have been applied in a variety of different disciplines, such as finance, economy, earth sciences, biology, neuroscience, physiology, engineering, physics and chemistry. In the last decade an impressive increase of the application

A. Sipers (✉) · P. Borm
Centre of Expertise in Life Sciences, Zuyd University,
Nieuw Eyckholt 300, 6419 DJ Heerlen, The Netherlands
e-mail: aloys.sipers@zuyd.nl

P. Borm
e-mail: paul.borm@zuyd.nl

R. Peeters
Department of Knowledge Engineering, Universiteit Maastricht,
Bouillonstraat 8-10, 6200 MD Maastricht, The Netherlands
e-mail: ralf.peeters@maastrichtuniversity.nl

of methods based on RPs can be observed, see the bibliography collected on the website [5]. Some of the pitfalls which can occur during the application of RPs are highlighted in [6].

Given a finite-interval continuous-time real-valued signal $x(t)$, with $t \in [0, 1)$ say, its corresponding recurrence plot is constructed with the time-delay embedding method (cf. [7]) in three steps:

(1) An embedding dimension M and a time-delay $\tau \in (0, 1)$ are chosen, and an associated M-dimensional vector trajectory $X(t)$ is constructed as:

$$X(t) = \begin{pmatrix} x(t) \\ x(t + \tau) \\ \vdots \\ x(t + (M-1)\tau) \end{pmatrix}, t \in [0, 1). \tag{1}$$

Here, for technical convenience (to avoid having to take finite interval effects explicitly into account), the signal $x(t)$ is *periodically extended* from the interval $[0, 1)$ to all of $\mathbb{R}$.

(2) The *unthresholded* recurrence plot (URP) is defined as (the graph of) the intra-trajectory distance function $\text{URP}_X(u, v)$, given by

$$\text{URP}_X(u, v) = \|X(u) - X(v)\|, \quad u, v \in [0, 1), \tag{2}$$

in which $\| \cdot \|$ denotes the Euclidean norm.

(3) For a given positive threshold ε, the *binary* (thresholded) recurrence plot is defined as

$$\text{RP}_X^\varepsilon(u, v) = \begin{cases} 1 & \text{if } \text{URP}_X(u, v) \leq \varepsilon, \\ 0 & \text{if } \text{URP}_X(u, v) > \varepsilon. \end{cases} \tag{3}$$

In this paper we study the information content of URPs of complex-valued signals. They are defined in a similar manner, with the Euclidean norm $\| \cdot \|$ in step (2) generalized to trajectories that are now in $\mathbb{C}^M$. This theoretical study on URPs of complex-valued signals is new and may serve as a starting point for applications of URPs and RPs on complex-valued signals which are constructed from real world data. Furthermore, the special properties of *complex signal representation* are used to employ URPs in alternative ways on signals with a narrow band power spectrum. The information content of URPs and RPs of real-valued signals has been studied in [1, 8–13], respectively.

In Sect. 2, we study the information content of URPs of zero mean continuous-time complex-valued signals on [0, 1) which admit a Fourier series representation. We build upon our recent work of [1] where real-valued signals were analyzed. As in that case, we show that for any complex-valued signal its power spectrum is entirely determined by its URP, regardless of the choice of M and τ. It is easily seen that a URP does not carry information on the mean of a signal (hence the zero mean assumption), nor on a unimodular scaling factor, nor on complex conjugation. We provide sufficient

conditions on M and τ which guarantee that a zero mean complex-valued signal $w(t)$ can be *uniquely* recovered from its URP, up to conjugacy and a unimodular factor. They extend the necessary and sufficient conditions for real-valued signals given in [1]. In general, when these conditions are not satisfied, it depends on M, τ, and the frequency content of the actual signal $w(t)$ itself, which information can be recovered from its URP. These results have implications for real-valued signals too, because recurrence plots of complex-valued signals relate to *joint recurrence plots* for two real-valued signals; see [14].

In Sect. 3, we address another application of complex-valued signal representations by studying signals with a narrow band power spectrum. Then, in Sect. 4, the information content and the structure of URPs for narrow band signals are illustrated by two examples. First, we investigate four different settings for M and τ, which cause complex signals with magnitudes having different morphology to exhibit identical URPs. Second, an application with real measurement data from EEG analysis involving an alpha rhythm is presented, to illustrate the use of URPs on complex-valued narrow band signals in alternative ways. We compare the frequency content on horizontal (or vertical) and on diagonal lines in a URP, and we illustrate how this information can be used to approximate the envelope of the underlying signal.

Section 5 concludes the paper. All the proofs are collected in the Appendix.

2 Unique Reconstruction of a Complex-Valued Signal from Its Unthresholded Recurrence Plot

In this section we extend the results of [1] for real-valued signals, to the class of complex-valued signals $w(t) = x(t) + iy(t)$. Here, $x(t)$ and $y(t)$ denote the real and the imaginary part of $w(t)$, respectively. For a given embedding dimension and time-delay the corresponding trajectories relate similarly as $W(t) = X(t) + iY(t)$. For all time instances u and v it holds that $W(u) \approx W(v)$, i.e., a near recurrence occurs, if and only if both $X(u) \approx X(v)$ and $Y(u) \approx Y(v)$. Therefore, recurrence plots of complex-valued signals are closely related to joint recurrence plots (JRPs), see [14]. To be precise, a *binary* (thresholded) joint recurrence plot is defined as the product of the RPs of the signals $x(t)$ and $y(t)$, which may be constructed for different embedding dimensions, different time-delays and different thresholds:

$$\mathrm{JRP}_{X,Y}^{\varepsilon_X, \varepsilon_Y}(u, v) := \mathrm{RP}_X^{\varepsilon_X}(u, v)\mathrm{RP}_Y^{\varepsilon_Y}(u, v).$$

Note that $\mathrm{URP}_W(u, v)^2 = \|W(u) - W(v)\|^2 = \|X(u) - X(v)\|^2 + \|Y(u) - Y(v)\|^2$. Therefore $\mathrm{RP}_W^{\varepsilon}(u, v) = 1$ if and only if $(\|X(u) - X(v)\|^2 + \|Y(u) - Y(v)\|^2)/\varepsilon^2 \leq 1$, while $\mathrm{JRP}_{X,Y}^{\varepsilon_X, \varepsilon_Y}(u, v) = 1$ if and only if $\max\{\|X(u) - X(v)\|/\varepsilon_X, \|Y(u) - Y(v)\|/\varepsilon_Y\} \leq 1$. This makes clear that the RP of a complex-valued signal employs the 2-norm, while the JRP of two real-valued signals employs a mixture of the

(a)   **(b)**

x $\mathrm{JRP}_{X,Y}$

y RP_{X+iY}
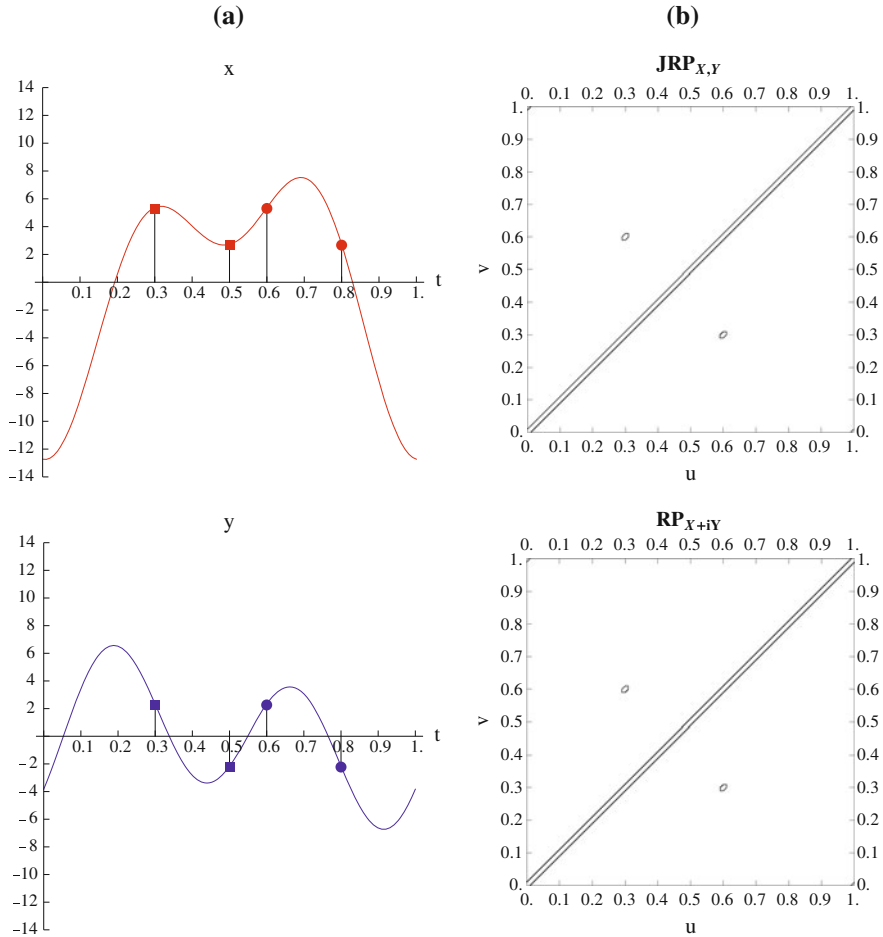
Fig. 1 **a** Real-valued signals $x(t)$ and $y(t)$ with joint recurrences. **b** Joint recurrence plot of $x(t)$ and $y(t)$ (*top*) recurrence plot of the complex-valued signal $w(t) = x(t) + iy(t)$ (*bottom*)

2-norm and the maximum-norm. However, topologically these norms are equivalent (i.e., they define the same families of open sets), so that small distances for one norm correspond to small distances for the other norm. An example of a joint recurrence plot of two real-valued signals and the recurrence plot of the corresponding complex-valued signal for equal embedding dimensions $M = 2$, equal time delays $\tau = 0.2$ and equal thresholds $\varepsilon = 0.1$, is displayed in Fig. 1b. The signal values giving rise to the joint recurrence in $\mathrm{JRP}_{X,Y}(u, v)$ and the recurrence in $\mathrm{RP}_{X+iY}(u, v)$, are indicated by squares and circles in Fig. 1a. The corresponding time instants are $u = 0.3$, $u + \tau = 0.5$, $v = 0.6$ and $v + \tau = 0.8$. This demonstrates that a recurrence plot of a complex-valued signal contains *joint* information on two real-valued signals.

We shall investigate to which extent a recurrence plot of a complex-valued signal also contains *individual* information about the two real-valued signals.

As a URP does not contain information on the mean of a signal, without loss of generality we focus attention on the class of complex-valued zero mean signals $w(t)$. We restrict to signals on $[0, 1)$ which admit a Fourier series representation which converges pointwise almost everywhere and has finite energy:

$$w(t) = \sum_{k \in \mathbb{Z}} w_k e^{2\pi kti}, \quad \text{with } w_0 = 0, \text{ and } \sum_{k \in \mathbb{Z}} |w_k|^2 < \infty. \tag{4}$$

Then for such a signal $w(t)$, for a given embedding dimension M and time-delay τ, the trajectory $W(t)$ is:

$$W(t) = \sum_{k \in \mathbb{Z}} w_k e^{2\pi kti} T_k, \tag{5}$$

in which (for all $k \in \mathbb{Z}$)

$$T_k = \begin{pmatrix} 1 \\ z^k \\ \vdots \\ z^{(M-1)k} \end{pmatrix}, \quad \text{with } z = e^{2\pi \tau i}. \tag{6}$$

When considering the inner product $\langle W(u), W(v) \rangle$ (with linearity in the first argument) as a two-variable function of $u, v \in [0, 1)$, it is obtained that

$$\langle W(u), W(v) \rangle = \sum_{p \in \mathbb{Z}} \sum_{q \in \mathbb{Z}} w_p \overline{w_q} e^{2\pi (pu - qv)i} \langle T_p, T_q \rangle. \tag{7}$$

This constitutes a 2-dimensional Fourier series representation of $\langle W(u), W(v) \rangle$, with 2D-Fourier coefficients $w_p \overline{w_{-q}} \langle T_p, T_{-q} \rangle$. Note that $\langle T_p, T_q \rangle = \langle T_{p+r}, T_{q+r} \rangle$ for all integers p, q, r. An explicit expression for the inner product $\langle T_p, T_q \rangle$ is provided by [1, Lemma 3.1]. It holds that $\langle T_p, T_q \rangle \neq 0$ if and only if $[(p - q)\tau \in \mathbb{Z}] \vee [(p - q)M\tau \notin \mathbb{Z}]$. Also, $\langle T_0, T_0 \rangle = M$.

The 2D-Fourier coefficients of $\langle W(u), W(v) \rangle$ enable the computation of the 2D-Fourier coefficients of $\mathrm{URP}_W(u, v)^2$, which are given by the following proposition.

Proposition 1 *Let $w(t) = \sum_{k \in \mathbb{Z}} w_k e^{2\pi kti}$ be a complex-valued zero mean signal from our class. Let $W(t)$ be its trajectory for the embedding dimension M and time-delay τ. Then a 2D-Fourier representation of its squared URP is given by*

$$\mathrm{URP}_W(u, v)^2 = \sum_{p \in \mathbb{Z}} \sum_{q \in \mathbb{Z}} \mathscr{W}_{p,q} e^{2\pi (pu + qv)i}, \tag{8}$$

in which the 2D-Fourier coefficients are given by

$$\mathscr{W}_{0,0} = 2M \sum_{k \in \mathbb{Z}} |w_k|^2 \tag{9}$$

$$\mathscr{W}_{p,0} = \langle T_p, T_0 \rangle \sum_{k \in \mathbb{Z}} w_{k+p} \overline{w_k} \quad (p \neq 0) \tag{10}$$

$$\mathscr{W}_{0,q} = \langle T_q, T_0 \rangle \sum_{k \in \mathbb{Z}} w_{k+q} \overline{w_k} \quad (q \neq 0) \tag{11}$$

$$\mathscr{W}_{p,q} = -\langle T_{p+q}, T_0 \rangle \left(w_p \overline{w_{-q}} + \overline{w_{-p}} w_q \right) \quad (p, q \neq 0). \tag{12}$$

Note that $\mathscr{W}_{p,q} = \mathscr{W}_{q,p}$ and $\mathscr{W}_{-p,-q} = \overline{\mathscr{W}_{p,q}}$ for all integers p and q. By choosing $q = -p \neq 0$, it follows that $\mathscr{W}_{p,-p} = -M(|w_p|^2 + |w_{-p}|^2)$. Therefore, when the URPs (for the same time-delay embedding) of two signals with Fourier coefficients $\{w_k\}_{k \in \mathbb{Z}}$ and $\{v_k\}_{k \in \mathbb{Z}}$ happen to coincide, it holds that $|w_p|^2 + |w_{-p}|^2 = |v_p|^2 + |v_{-p}|^2$ for all $p \in \mathbb{Z}^+$. Observe that $|w_p|^2 + |w_{-p}|^2$ denotes contribution of the frequency p to the power of $w(t)$. Because the 2D-Fourier coefficients of a URP characterize it uniquely, this proves the following result.

Corollary 1 *Let $w(t) = \sum_{k \in \mathbb{Z}} w_k e^{2\pi k t i}$ and $v(t) = \sum_{k \in \mathbb{Z}} v_k e^{2\pi k t i}$ be two complex-valued zero mean signals from our class. Let $W(t)$ and $V(t)$ be their trajectories, respectively, for the same time-delay embedding. If their URPs coincide, then also the power spectra of the signals $w(t)$ and $v(t)$ coincide. i.e., for all $k \in \mathbb{Z}$ it holds that $|w_k|^2 + |w_{-k}|^2 = |v_k|^2 + |v_{-k}|^2$.*

Sufficient conditions for the reconstruction of a complex-valued signal $w(t)$ from its URP can also be given, in terms of the following associated graph G_W.

Definition 1 Let $w(t) = \sum_{k \in \mathbb{Z}} w_k e^{2\pi k t i}$ be a complex-valued zero mean signal from our class. Let $W(t)$ be its trajectory for the embedding dimension M and time-delay τ. Then define the associated graph G_W as the simple undirected graph for which:

(1) the nodes are labeled by positive indices from the set

$$K_W = \{k \in \mathbb{Z}^+ \mid w_k \neq 0 \vee w_{-k} \neq 0\},$$

(2) two distinct nodes labeled $p, q \in K_W$ are adjacent if and only if both $\langle T_p, T_q \rangle \neq 0$ and $\langle T_p, T_{-q} \rangle \neq 0$.

The following theorem contains the main reconstruction result of this section. Note that we will call a graph complete if all nodes are connected to all nodes, including self-loops.

Theorem 1 *Let $w(t) = \sum_{k \in \mathbb{Z}} w_k e^{2\pi k t i}$ and $v(t) = \sum_{k \in \mathbb{Z}} v_k e^{2\pi k t i}$ be two complex-valued zero mean signals from our class. Let $W(t)$ and $V(t)$ be their trajectories, respectively, for the same time-delay embedding. If the unthresholded recurrence plots URP_W and URP_V coincide and the associated graph G_W is complete, then the signal $v(t)$ is determined by $w(t)$ up to conjugacy and a unimodular factor, i.e., there exists a unimodular constant α such that $v(t) = \alpha w(t)$ or $v(t) = \alpha \overline{w(t)}$.*

Recall that the graph G_W has positively labeled nodes $k \in K_W$ which in fact correspond to the *pairs* of indices $(k, -k)$. Also, adjacency requires both $\langle T_p, T_q \rangle$ and $\langle T_p, T_{-q} \rangle$ to be nonzero. These are more restrictive conditions than what we have used for real-valued signals in [1], where we were able to give necessary and sufficient conditions for the unique reconstruction of a signal from its URP (up to a sign). It is still an open question to find necessary and sufficient conditions for the reconstruction of complex-valued signals.

In the case of a complete graph G_W, Theorem 1 implies that the magnitudes $|v(t)|$ and $|w(t)|$ coincide. This means that a URP with a complete graph uniquely determines the magnitude of the underlying complex-valued signal. On the other hand, if the graph G_W is not complete then signals with magnitudes of different morphology can exhibit identical URPs. The first example of Sect. 4 demonstrates this.

3 Unthresholded Recurrence Plots for Narrow Band Signals

Motivated by practical applications, we now focus on real-valued signals with a *narrow band* power spectrum. A narrow band signal can be considered as an amplitude modulated sinusoid. Due to the special properties of an associated complex signal representation, the well-known 'analytic signal', the results of the previous section can be used to employ unthresholded recurrence plots an alternative way.

Definition 2 For a given real-valued zero mean signal $x(t) = \sum_{k \in \mathbb{Z}} x_k e^{2\pi kti}$, the complex-valued analytic signal $z(t)$ is defined as follows:

$$z(t) = 2 \sum_{k>0} x_k e^{2\pi kti}. \tag{13}$$

Consequently: $x(t) = Re\,(z(t))$.

The trajectory $Z(t)$ of the analytic signal $z(t)$ associated with $x(t)$ is given by:

$$Z(t) = 2 \sum_{k>0} x_k e^{2\pi kti} T_k. \tag{14}$$

Proposition 2 *Let $z(t) = 2 \sum_{k>0} x_k e^{2\pi kti}$ be an analytic signal. Suppose that the squared unthresholded recurrence plot $URP_Z(u, v)^2 = \|Z(u) - Z(v)\|^2$ can be expressed as a 2D-Fourier series:*

$$URP_Z(u, v)^2 = \sum_{p \in \mathbb{Z}} \sum_{q \in \mathbb{Z}} \mathscr{Z}_{p,q} e^{2\pi (pu+qv)i}.$$

Then the 2D-Fourier coefficients $\mathscr{Z}_{p,q}$ can be expressed through the coefficients x_k of the real-valued signal $x(t)$ as:

$$\mathscr{Z}_{m,n} = \begin{cases} -4\langle T_{m+n}, T_0\rangle x_m \overline{x_{-n}} & \text{for } m > 0, n < 0, \\ -4\langle T_{m+n}, T_0\rangle \overline{x_{-m}} x_n & \text{for } m < 0, n > 0, \\ 0 & \text{otherwise.} \end{cases} \tag{15}$$

An analytic signal is a special case of zero mean complex-valued signal $w(t) = \sum_{k\in\mathbb{Z}} w_k e^{2\pi kti}$, with $w_k = 0$ for $k \leq 0$, i.e.: $w(t) = \sum_{k>0} w_k e^{2\pi kti}$. For the class of analytic signals, Corollary 1 therefore reduces to the following result.

Corollary 2 *Let $w(t) = \sum_{k>0} w_k e^{2\pi kti}$ and $v(t) = \sum_{k>0} v_k e^{2\pi kti}$ be two zero mean analytic signals from our class. Let $W(t)$ and $V(t)$ be their trajectories, respectively, for the same time-delay embedding. If their URPs coincide, then also the power spectra of the signals $w(t)$ and $v(t)$ coincide: for all $k > 0$ it holds that $|w_k| = |v_k|$.*

Because the complex conjugate of a nontrivial analytic signal is not itself an analytic signal, Theorem 1 reduces to the following result.

Theorem 2 *Let $w(t) = \sum_{k>0} w_k e^{2\pi kti}$ and $v(t) = \sum_{k>0} v_k e^{2\pi kti}$ be two zero mean analytic signals from our class. Let $W(t)$ and $V(t)$ be their trajectories, respectively, for the same time-delay embedding. If the unthresholded recurrence plots URP_W and URP_V coincide and the associated graph G_W is complete, then the signal $v(t)$ is determined by $w(t)$ up to a unimodular factor, i.e., there exists a unimodular constant α such that $v(t) = \alpha w(t)$.*

We now turn to narrow band analytic signals $z(t)$ which can be regarded as a *amplitude modulated carrier* signals:

$$z(t) = e^{2\pi cti} (2x_c + w(t)), \tag{16}$$

where $c \in \mathbb{Z}^+$ denotes the index of the corresponding Fourier coefficient x_c and also the *carrier* frequency (which is integer because we consider periodic signals with period 1). The complex-valued signal $w(t) = \sum_{k\in\mathbb{Z}} w_k e^{2\pi kti}$ is referred as the *modulating* signal, which has:

$$w_k = \begin{cases} 2x_{c+k} & \text{for } k > -c \wedge k \neq 0, \\ 0 & \text{for } k \leq -c \text{ or } k = 0. \end{cases} \tag{17}$$

A geometric interpretation of Eq. (16) is given in Fig. 2. There, the narrow band signal $z(t)$ is represented as a rotating vector $\overrightarrow{OQ} = \overrightarrow{OP} + \overrightarrow{PQ}$. The vector $\overrightarrow{OP}$ represents the constant signal $2x_c$ and the vector $\overrightarrow{PQ}$ represents the modulating signal $w(t)$, both rotating at a constant angular velocity $2\pi c$.

The following proposition interrelates the trajectories, the URPs, and the graphs of the analytic signal $z(t)$ and the modulating signal $w(t)$.

Proposition 3 *Let $c \in \mathbb{Z}^+$ be a carrier frequency and $x(t)$ a zero-mean periodic signal from our class. Then:*
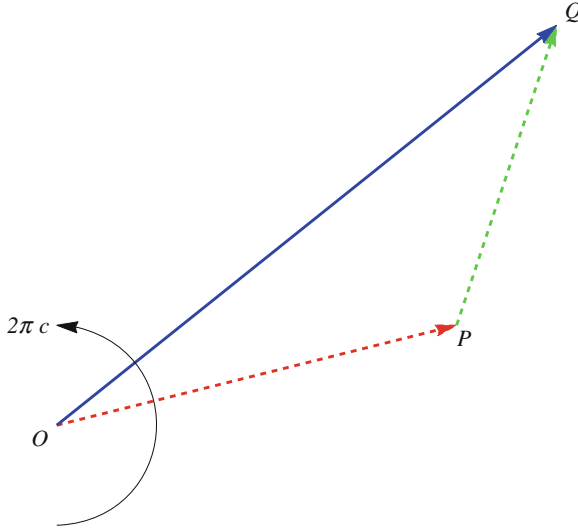
Fig. 2 Geometric interpretation of a narrow band signal $z(t)$ or its trajectory $Z(t)$ as a rotating resultant $\overrightarrow{OQ}$ of a constant vector $\overrightarrow{OP}$ and a modulating vector $\overrightarrow{PQ}$, all rotating at angular velocity $2\pi c$

(1) *The trajectory $Z(t)$ of the analytic signal $z(t)$ can be expressed trough the trajectory $W(t)$ of the modulating signal $w(t)$ as:*

$$Z(t) = e^{2\pi c t i} \, diag\,(T_c)\,(2x_c T_0 + W(t))\,. \tag{18}$$

in which $diag(T_c)$ denotes the diagonal matrix having the entries of the vector T_c along its main diagonal.

(2) *Let URP_Z and URP_W be the unthresholded recurrence plots of the analytic signal $z(t)$ and the modulating signal $w(t)$, respectively. If $c(u - v) \in \mathbb{Z}$ then:*

$$|Z(u) - Z(v)| = |W(u) - W(v)|\,, \tag{19}$$
$$URP_Z(u, v) = URP_W(u, v), \tag{20}$$

in which $|\cdot|$ denotes the entry-wise absolute value.

(3) *The 2D-Fourier coefficients $\mathcal{W}_{p,q}$ of $URP_W(u, v)^2$ can be expressed through the 2D-Fourier coefficients $\mathcal{Z}_{p,q}$ of $URP_Z(u, v)^2$ as:*

$$\mathcal{W}_{p,q} = \mathcal{Z}_{p+c,q-c} + \mathcal{Z}_{q+c,p-c}. \tag{21}$$

(4) *The nodes of the graph G_W can be obtained from the nodes of the graph G_Z as:*

$$K_W = \{k \in \mathbb{Z}^+ \,|\, x_{c+k} \neq 0 \vee x_{c-k} \neq 0\}. \tag{22}$$

Figure 2 also provides a geometric interpretation of part (1) of this proposition. Now, the trajectory $Z(t)$ is represented as a rotating vector $\overrightarrow{OQ} = \overrightarrow{OP} + \overrightarrow{PQ}$, rotating at a constant angular velocity $2\pi c$. The vectors $\overrightarrow{OP}$ and $\overrightarrow{PQ}$ now represent the constant vector diag $(T_c) (2x_c T_0) = 2x_c T_c$ and the modulating trajectory diag $(T_c) W(t)$, respectively.

In order to go beyond the visual impression yielded by RPs, several measures which quantify structures in RPs, have been proposed in [3] and are known as recurrence quantification analysis (RQA). These measures are based on *horizontal* (or *vertical*) and on *diagonal* lines of an RP. An important difference between the unthresholded recurrence plots URP_X^2 and URP_Z^2 for narrow band signals lies in the frequency content of their restrictions to these lines.

Since we consider complex-valued periodic signals with period $T = 1$ it holds that $f_k = \frac{k}{T} = k$. Therefore, for convenience we shall call the indices k also frequencies.

Proposition 4 *Let $x(t)$ be a zero-mean real periodic signal with period* 1*, which has a finite Fourier series with the frequency range $\{c - d, \ldots, c + d\}$. Then:*

(1) *The restrictions of $URP_X(u, v)^2$ to horizontal, vertical and diagonal lines, have the frequency ranges:*

$\quad v \qquad$ *is constant* : $\{0, \ldots, 2d\} \cup \{c - d, \ldots, c + d\} \cup \{2c - 2d, \ldots, 2c + 2d\}$;
$\quad u \qquad$ *is constant* : $\{0, \ldots, 2d\} \cup \{c - d, \ldots, c + d\} \cup \{2c - 2d, \ldots, 2c + 2d\}$;
$\quad u - v$ *is constant* : $\{0, \ldots, 2d\} \cup \{2c - 2d, \ldots, 2c + 2d\}$.

(2) *The restrictions of $URP_Z(u, v)^2$ to horizontal, vertical and diagonal lines, have the frequency ranges:*

$$\quad v \qquad \text{is constant} : \{0, \ldots, 2d\} \cup \{c - d, \ldots, c + d\};$$
$$\quad u \qquad \text{is constant} : \{0, \ldots, 2d\} \cup \{c - d, \ldots, c + d\};$$
$$\quad u - v \text{ is constant} : \{0, \ldots, 2d\}.$$

(3) *The frequency ranges $\{0, \ldots, 2d\}$, $\{c - d, \ldots, c + d\}$ and $\{2c - 2d, \ldots, 2c + 2d\}$ are mutually disjoint if and only if $c > 3d$.*

Note that, contrary to $\text{URP}_X(u, v)^2$, the restrictions of $\text{URP}_Z(u, v)^2$ to horizontal, vertical and diagonal lines, have no frequencies in the range $\{2c - 2d, \ldots, 2c + 2d\}$. Also note that the frequency range of the restriction of $\text{URP}_Z(u, v)^2$ to diagonal lines only depends on the bandwidth $2d$ of the signal $x(t)$. These properties appear as *elongated* contours along the diagonal lines in URP_Z.

To illustrate this result, we here present an example. We consider a real signal $x(t) = \sum_{k=-22}^{-18} x_k e^{2\pi k t i} + \sum_{k=18}^{22} x_k e^{2\pi k t i}$, involving just five different frequencies, for which the Fourier coefficients are given by:

(a)

(b)

(c)

(d)
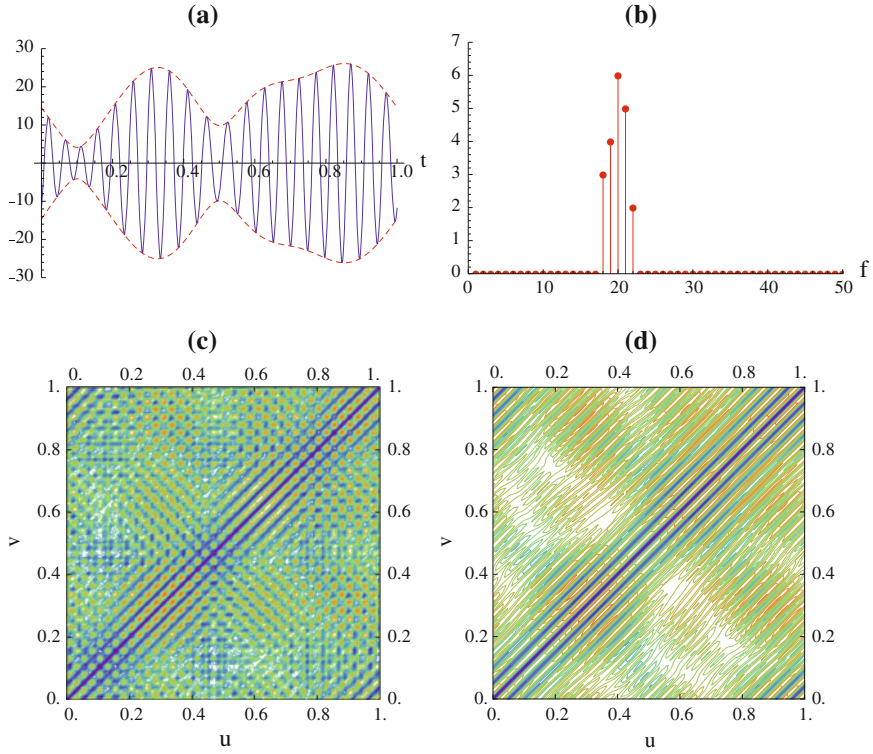
Fig. 3 **a** Signal $x(t)$ and its envelope $\pm|z(t)|$, **b** magnitude spectrum of $x(t)$, **c** URP of the real signal $x(t)$, **d** URP of the analytic signal $z(t)$

$$x_{18} = \overline{x_{-18}} = 3e^{-5i},$$
$$x_9 = \overline{x_{-9}} = 4e^{3i},$$
$$x_{10} = \overline{x_{-10}} = 6e^{4i},$$
$$x_{11} = \overline{x_{-11}} = 5e^{-2i},$$
$$x_{22} = \overline{x_{-22}} = 2e^{-6i}.$$

The signal $x(t)$ and its analytic signal $z(t)$ have the frequency range $\{c-d, \ldots, c+d\}$ for the settings $c = 20$ and $d = 2$. The signal $x(t)$ and its *envelope* $\pm|z(t)|$ are displayed in Fig. 3a. The magnitude spectrum of $x(t)$ is displayed in Fig. 3b. The unthresholded recurrence plots URP_X and URP_Z are computed for the settings $M = 4$ and $\tau = \frac{1}{3}$ and are displayed in Fig. 3c and d, respectively. The magnitude spectra of $\text{URP}_X(u, v)^2$ and $\text{URP}_Z(u, v)^2$ on the horizontal lines $(u, v) = (t, 0.625)$, the vertical lines $(u, v) = (0.625, t)$ and on the diagonal lines $(u, v) = (t + 0.125, t)$, with $t \in [0, 1)$, are displayed in Fig. 4a and b, respectively. These figures demonstrate that different parts of the spectrum can be investigated in isolation, by studying appropriately selected lines in the URPs of either $x(t)$ or $z(t)$.
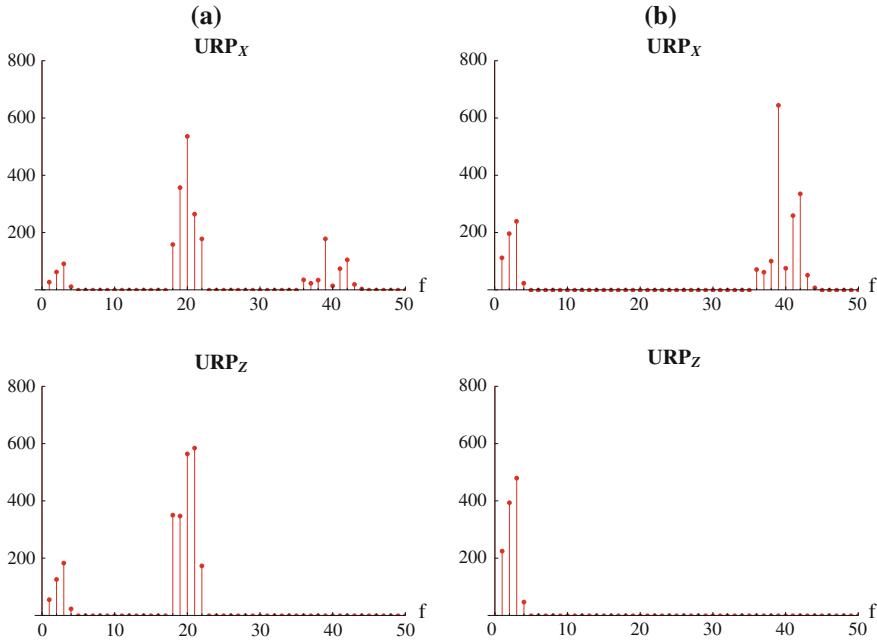
Fig. 4 Magnitude spectra along selected lines [**a** $u = 0.625$ or $v = 0.625$, **b** $u - v = 0.125$] in the squared URPs of the signal $x(t)$ (*top*) and its analytic signal $z(t)$ (*bottom*)

4 Examples, Including an Application in EEG Analysis

To illustrate the main results and techniques of the previous sections, we here present two more examples.

In the first example we investigate four different settings for M and τ, which may cause complex-valued signals with morphologically different magnitudes still to exhibit identical URPs. This example serves to demonstrate the limitations that apply to the interpretation of a URP, emanating from the choice of embedding dimension and time-delay.

In the second example we consider an application in EEG analysis, which concerns a digitally sampled measurement signal featuring a so-called alpha rhythm. The measured alpha rhythm is band-pass filtered to obtain the so-called alpha band signal. We investigate the unthresholded recurrence plots of the associated analytic signal and the modulating signal for a given choice of the carrier frequency.

Example 1 Different complex-valued signals exhibiting identical URPs. For four different settings of M and τ we give pairs of complex-valued signals $v(t) = \sum_{k=-2}^{2} v_k e^{2\pi k t i}$, $w(t) = \sum_{k=-2}^{2} w_k e^{2\pi k t i}$ with morphologically different magnitudes but identical URPs. In accordance with Corollary 1 it holds that $|v_{-k}|^2 + |v_k|^2 = |w_{-k}|^2 + |w_k|^2$, for $k \in 1, 2$.
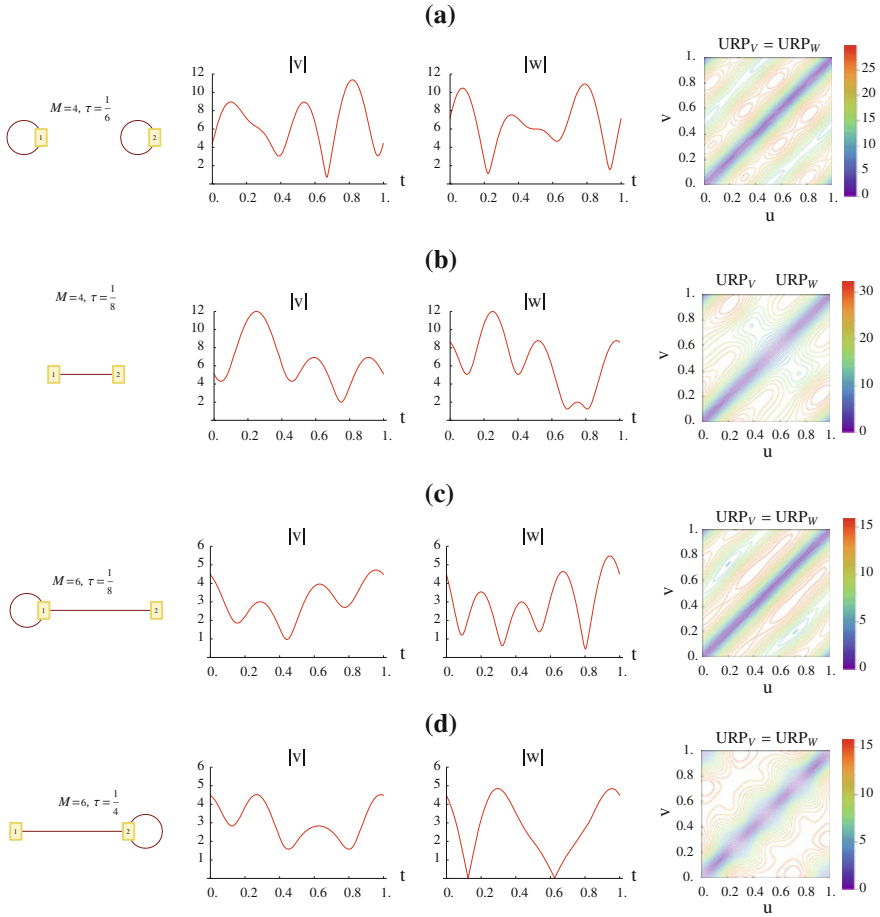
Fig. 5 Graphs, magnitudes and URPs for different settings of embedding dimension M and time-delay τ, for four different pairs of signals $v(t)$ and $w(t)$ specified in the text

The associated graphs G_V and G_W in all cases have exactly 2 nodes, labeled 1 and 2. Adjacency of those nodes depends on the values of M and τ. Recall that two distinct nodes $p, q \in K_W$ are adjacent if and only if both $\langle T_p, T_q \rangle \neq 0$ and $\langle T_p, T_{-q} \rangle \neq 0$.

(i) $M = 4$ and $\tau = \frac{1}{6}$, see Fig. 5a.

$$v_{-2} = 6, \quad v_{-1} = 1, \quad v_1 = -3, \ v_2 = -2i,$$
$$w_{-2} = 6i, \ w_{-1} = -1, \ w_1 = 3, \quad w_2 = 2.$$

The graph is not complete, since the nodes 1 and 2 are not adjacent.

(ii) $M = 4$ and $\tau = \frac{1}{8}$, see Fig. 5b.

$$v_{-2} = 0, \ v_{-1} = 3, \ v_1 = -4, \ v_2 = 5i,$$
$$w_{-2} = 3, \ w_{-1} = 0, \ w_1 = 5i, \ w_2 = 4.$$

The graph is not complete, since the nodes 1 and 2 both have no self-loops.

(iii) $M = 6$ and $\tau = \frac{1}{8}$, see Fig. 5c.

$$v_{-2} = 0, \quad v_{-1} = 1, \ v_1 = 1, \ v_2 = 2 + 2i,$$
$$w_{-2} = -2i, \ w_{-1} = 1, \ w_1 = 1, \ w_2 = 2.$$

The graph is not complete, since the node 2 has no self-loop.

(iv) $M = 6$ and $\tau = \frac{1}{4}$, see Fig. 5d.

$$v_{-2} = 1, \ v_{-1} = 0, \quad v_1 = 2 + 2i, \ v_2 = 1,$$
$$w_{-2} = 1, \ w_{-1} = -2i, \ w_1 = 2, \quad w_2 = 1.$$

The graph is not complete, since the node 1 has no self-loop.

This example demonstrates that for certain 'unfortunate' choices of M and τ the magnitude of the underlying complex-valued signal cannot be uniquely retrieved from the URP. In such cases, in view of Theorem 1, the graphs associated with the URPs are incomplete.

Example 2 EEG analysis featuring an alpha rhythm. In EEG analysis an EEG signal is decomposed into five band signals corresponding to the delta (0.1–4 Hz), theta (4–8 Hz), alpha (8–12 Hz), beta (12–30 Hz), and gamma (30–100 Hz) frequency bands, see [15]. These basic EEG frequency bands are understood to reflect different functional processes in the brain.

From a digitally sampled EEG measurement signal we consider an excerpt of $N = 500$ samples, exhibiting an alpha rhythm, with a duration of $T = 2$ s. Alpha rhythms are characterized by a clear peak in their magnitude spectrum for a frequency in the alpha band (8–12 Hz), see Fig. 6a. The alpha band signal $x(t)$, see Fig. 6b, is obtained from the alpha rhythm by selecting the coefficients with frequencies $f_k = \frac{k}{T}$ in the alpha frequency band, i.e. $k \in \{16, \ldots, 24\}$. For the setting $c = 20$ (i.e. $f_c = \frac{c}{T}$ $= 10$ Hz), the modulating signal $w(t)$ is constructed from the analytic signal $z(t)$ using Eq. (16). The URPs of the signal $z(t)$ and the signal $w(t)$, for the settings $M = 3$ and $\tau = \frac{1}{50}T = 0.04$ s, are both displayed in Fig. 7. Note that τ is an integer multiple of the sampling time $\Delta t := \frac{T}{N} = 0.004$ s.

The graph G_Z has 9 nodes: $k \in K_Z = \{16, \ldots, 24\}$. The graph G_W has 4 nodes: $k \in K_W = \{1, \ldots, 4\}$ which are obtained from K_Z by using part (4) of Proposition 3. Since M and the denominator of $\frac{\tau}{T}$ are co-prime, it follows from Part (2) of [1, Corollary 3.5] that the graphs G_Z and G_W are complete. Consequently, the signal $z(t)$ is determined up to a unimodular factor by URP$_Z$, and the signal $w(t)$ is determined up to conjugacy and a unimodular factor by URP$_W$.
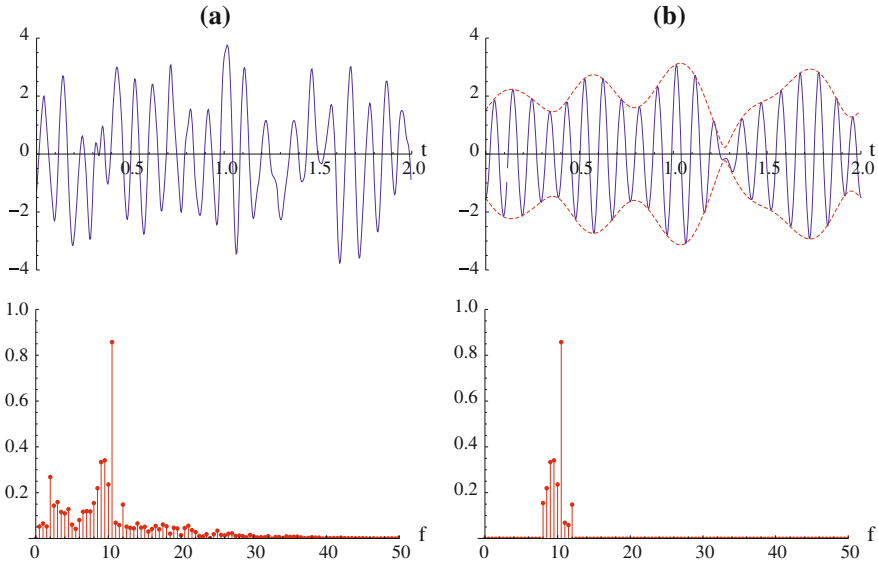
Fig. 6 **a** Measured alpha rhythm signal (*top*), **b** selected alpha band signal (*top*), and their corresponding magnitude spectra (*bottom*)

According to part (1) of Proposition 3 it holds that $\mathrm{URP}_Z(u, v)$ an $\mathrm{URP}_W(u, v)$ coincide on the diagonal lines $10(u - v) \in \mathbb{Z}$, but they are different between these lines. Some of these diagonal lines are indicated by dashed black lines in the upper triangular part of URP_W, see in Fig. 7. In view of part (2) of Proposition 4 it holds that the signals $z(t)$ and $w(t)$ have frequency ranges $\{\frac{k}{T} \mid |k| \in \{c - d, \ldots, c + d\}\}$ and $\{\frac{k}{T} \mid |k| \in \{1, \ldots, d\}\}$, respectively, for the settings $c = 20$ and $d = 4$. Therefore the restrictions of $\mathrm{URP}_W(u, v)^2$ to horizontal, vertical and diagonal lines, all have the frequency range $\{\frac{k}{T} \mid |k| \in \{0, \ldots, 2d\}\} = \{\frac{k}{2} \mid |k| \in \{0, \ldots, 8\}\}$. The restriction of $\mathrm{URP}_Z(u, v)^2$ diagonal lines has the latter frequency range too, whereas the restrictions to horizontal and vertical lines also have *higher* frequencies in the range $\{\frac{k}{T} \mid |k| \in \{c - d, \ldots, c + d\}\} = \{\frac{k}{2} \mid |k| \in \{16, \ldots, 24\}\}$.

In EEG amplitude modulation analysis, the envelopes of EEG band signals are studied, see e.g. [16–20]. In this example, the envelope $\pm|z(t)|$ of the alpha band signal $x(t)$ is displayed in Fig. 6b. The horizontal and vertical lines in URP_Z provide information about the magnitude $|z(t)|$. To illustrate this, we approximate $|z(t)|$ by $\sqrt{\frac{|z(t-\tau)|^2 + |z(t)|^2 + |z(t+\tau)|^2}{3}} = \frac{\|Z(t - \frac{1}{2}(M-1)\tau)\|}{\sqrt{M}}$. The norm $\|Z(t - \frac{1}{2}(M - 1)\tau)\|$ in the latter term can be computed by using an identity provided by [1, Proposition 5.1]:

$$T^2 \|Z(t)\|^2 = T \int_0^T \mathrm{URP}_Z(u, t)^2 du - \frac{1}{2} \int_0^T \int_0^T \mathrm{URP}_Z(u, v)^2 du \, dv. \quad (23)$$
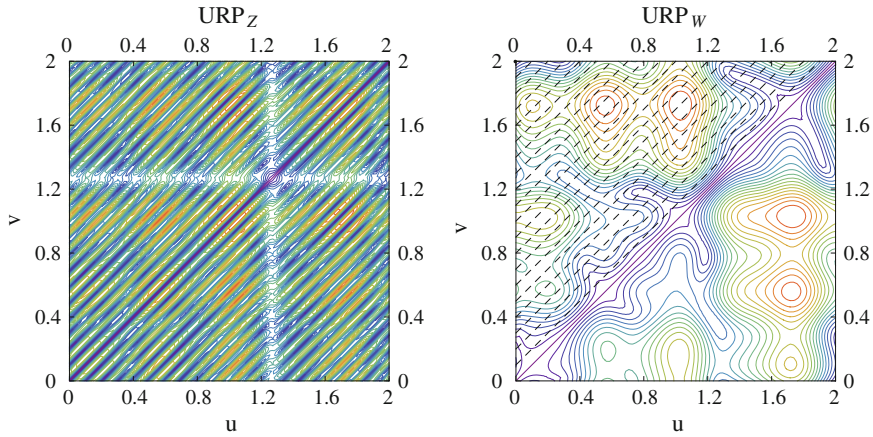
Fig. 7 URPs of the analytical signal $z(t)$ and the modulating signal $w(t)$
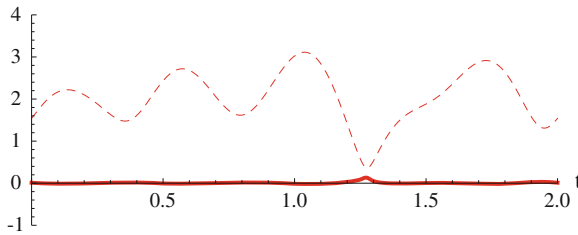
Fig. 8 Approximation for the envelope $|z(t)|$ (*dashed*) constructed from horizontal lines in URP$_Z$, and the corresponding approximation error (*solid*)

The integrand in the single integral term is a restriction of URP$_Z$ to the horizontal line corresponding to a given time instance t. The double integral has a constant value which is independent of t. The approximation $\frac{\|Z(t-\frac{1}{2}(M-1)\tau)\|}{\sqrt{M}}$ (dashed graph) and the approximation error $\frac{\|Z(t-\frac{1}{2}(M-1)\tau)\|}{\sqrt{M}} - |z(t)|$ (solid graph) are displayed in Fig. 8. This example shows how the frequency range of the complex-valued modulating signal $w(t)$ can be determined from the frequency range of the restrictions of URP$_Z^2$ to diagonal lines. It also demonstrates how the envelope of the real-valued narrow band signal $x(t)$ is related to the information content of the horizontal and vertical lines in URP$_Z$. As a new alternative method for EEG amplitude modulation analysis one could study URP$_W$ instead.

5 Conclusions and Discussion

When considering URPs as a tool to extract information from complex-valued signals, we have argued in this paper that it is important to first establish which information can or cannot be recovered from URPs.

In Sect. 2 we extended our work [1], concerning URPs of real-valued signals, to complex-valued signals. There we focused on computing the Fourier coefficients w_k of $w(t)$ from the 2D-Fourier coefficients $\mathscr{W}_{p,q}$ of URP$_W$. We showed that a signal $w(t)$, with a complete associated graph G_W, can be uniquely recovered from its URP up to conjugacy and a unimodular factor, see Theorem 1. If the graph G_W is not complete then signals with morphologically different magnitudes can exhibit identical URPs. The first example of Sect. 4 demonstrates this. We also related recurrence plots of complex-valued signals to *joint recurrence plots* which allows studying the relationship between two real-valued signals, see [14]. It is found that recurrence plots of complex-valued signals can be used to locate joint recurrences in a pairs of real-valued signals.

In Sect. 3, we used the special properties of *complex signal representation* to study signals with a narrow band power spectrum. For a given choice of the carrier frequency, a corresponding modulating signal can be computed from the analytic signal. Modulating signals provide an alternative way to employ URPs for studying narrow band signals. The trajectories, URPs and the graphs of the analytic signal and the modulating signal are related in Proposition 3. The frequency ranges of restrictions of a URP on horizontal, vertical and diagonal lines are investigated to explain the elongated contours along the diagonal lines in the URP of the analytic signal. It is shown how the frequency range of restrictions on horizontal and vertical lines differs from that on diagonal lines. It is found how the frequency ranges of these restrictions for a real-valued signal differ from those of the corresponding analytic signal. We also illustrated how the information content on horizontal and vertical lines in a URP can be used to approximate the envelope of the underlying narrow band signal. These results are demonstrated by the second example of Sect. 4.

A couple of research questions still remain open. (1) One important question concerns redundancy in the URP, being a 2-dimensional representation of a 1-dimensional signal, which is currently under investigation. The question arises to which extent a selected part of a URP may still contain all the information contained in the entire URP. This is of importance for relating subpatterns in a unthresholded recurrence plot URP$_W$ to localized (morphological) properties of the underlying complex-valued signal $w(t)$. (2) To quantify patterns that occur in RPs, several measures have been proposed in the literature, see e.g. [3], that are used in recurrence quantification analysis (RQA). An important question concerns the generalization of these measures to RPs of complex-valued signals.

Appendix

Proof of Proposition 1 Observe that

$$\|W(u) - W(v)\|^2 = \|W(u)\|^2 - \langle W(u), W(v)\rangle - \langle W(v), W(u)\rangle + \|W(v)\|^2.$$

For arbitrary t we have:

$$\|W(t)\|^2 = \sum_{p\in\mathbb{Z}}\sum_{q\in\mathbb{Z}} w_p\overline{w_q}\langle T_p, T_q\rangle e^{2\pi(p-q)ti} = \sum_{k\in\mathbb{Z}}\sum_{q\in\mathbb{Z}} w_{q+k}\overline{w_q}\langle T_k, T_0\rangle e^{2\pi kti}$$

$$= \sum_{k\in\mathbb{Z}}\langle T_k, T_0\rangle e^{2\pi kti} \sum_{q\in\mathbb{Z}} w_{k+q}\overline{w_q}.$$

For $t = u$ and $t = v$ this specializes to:

$$\|W(u)\|^2 = \sum_{p\in\mathbb{Z}}\langle T_p, T_0\rangle e^{2\pi pui} \sum_{k\in\mathbb{Z}} w_{k+p}\overline{w_k},$$

$$\|W(v)\|^2 = \sum_{q\in\mathbb{Z}}\langle T_q, T_0\rangle e^{2\pi qvi} \sum_{k\in\mathbb{Z}} w_{k+q}\overline{w_k}.$$

For $\langle W(u), W(v)\rangle$ we have already presented the expression

$$\langle W(u), W(v)\rangle = \sum_{p\in\mathbb{Z}}\sum_{q\in\mathbb{Z}} w_p\overline{w_q}\langle T_p, T_q\rangle e^{2\pi(pu-qv)i}$$

$$= \sum_{p\in\mathbb{Z}}\sum_{q\in\mathbb{Z}} w_p\overline{w_{-q}}\langle T_{p+q}, T_0\rangle e^{2\pi(pu+qv)i}.$$

It follows that

$$\langle W(u), W(v)\rangle + \langle W(v), W(u)\rangle = \sum_{p\in\mathbb{Z}}\sum_{q\in\mathbb{Z}}\langle T_{p+q}, T_0\rangle \left(w_p\overline{w_{-q}} + \overline{w_{-p}}w_q\right) e^{2\pi(pu+qv)i}.$$

Using $w_0 = 0$, it follows for $p = q = 0$ that:

$$\mathscr{W}_{0,0} = 2M\sum_{k\in\mathbb{Z}}|w_k|^2.$$

For $p \neq 0, q = 0$:

$$\mathscr{W}_{p,0} = \langle T_p, T_0\rangle \sum_{k\in\mathbb{Z}} w_{k+p}\overline{w_k}.$$

For $p = 0, q \neq 0$:

$$\mathscr{W}_{0,q} = \langle T_q, T_0 \rangle \sum_{k \in \mathbb{Z}} w_{k+q} \overline{w_k}.$$

And for $p \neq 0, q \neq 0$:

$$\mathscr{W}_{p,q} = -\langle T_{p+q}, T_0 \rangle (w_p \overline{w_{-q}} + \overline{w_{-p}} w_q). \tag{24}$$

$\square$

Proof of Theorem 1 First observe that the URPs for $w(t)$ and $v(t)$ coincide if and only of their 2D-Fourier representations coincide. This requires that

$$\sum_{k \in \mathbb{Z}} |w_k|^2 = \sum_{k \in \mathbb{Z}} |v_k|^2,$$

$$\langle T_p, T_0 \rangle \sum_{k \in \mathbb{Z}} w_{k+p} \overline{w_k} = \langle T_p, T_0 \rangle \sum_{k \in \mathbb{Z}} v_{k+p} \overline{v_k}, \quad \text{for all } p \neq 0,$$

$$\langle T_{p+q}, T_0 \rangle (w_p \overline{w_{-q}} + \overline{w_{-p}} w_q) = \langle T_{p+q}, T_0 \rangle (v_p \overline{v_{-q}} + \overline{v_{-p}} v_q), \quad \text{for all } p, q \neq 0.$$

As we have seen, choosing $q = -p \neq 0$ in the third of these conditions implies that: $|w_p|^2 + |w_{-p}|^2 = |v_p|^2 + |v_{-p}|^2$ for all $p \in \mathbb{Z}^+$. Summation over all p then implies the first of these conditions. Likewise, choosing $p = k + \tilde{p}$ and $q = -k$ in the third of these conditions gives: $\langle T_{\tilde{p}}, T_0 \rangle (w_{k+\tilde{p}} \overline{w_k} + \overline{w_{-k+\tilde{p}}} w_{-k}) = \langle T_{\tilde{p}}, T_0 \rangle (v_{k+\tilde{p}} \overline{v_k} + \overline{v_{-k+\tilde{p}}} v_{-k})$. Summation over all $k \in \mathbb{Z}$ now implies the second of these conditions. Therefore, the two URPs coincide if and only if the third condition holds.

To address this condition, a special subclass of 2×2 complex matrices is introduced. For all $\alpha, \beta \in \mathbb{C}$ define the associated matrices $S(\alpha, \beta)$ as:

$$S(\alpha, \beta) = \begin{pmatrix} \alpha & \overline{\beta} \\ \beta & \overline{\alpha} \end{pmatrix}.$$

For this subclass, note that $S(\alpha, \beta)S(\gamma, \delta) = S(\alpha\gamma + \overline{\beta}\delta, \overline{\alpha}\delta + \beta\gamma)$ and $\det S(\alpha, \beta) = |\alpha|^2 - |\beta|^2$. It follows that the subclass of invertible matrices $S(\alpha, \beta)$ forms a multiplicative group (under ordinary matrix multiplication), with $S(\alpha, \beta)^{-1} = S(\dfrac{\overline{\alpha}}{|\alpha|^2 - |\beta|^2}, \dfrac{-\beta}{|\alpha|^2 - |\beta|^2})$. The intersection of this group with the group of unitary matrices (for which inversion coincides with Hermitian transposition) consists of the matrices $S(\alpha, \beta)$ with $|\alpha|^2 + |\beta|^2 = 1$ and $\alpha\beta = 0$ (i.e., either $\alpha = 0$ and $|\beta| = 1$, or $|\alpha| = 1$ and $\beta = 0$).

The usefulness of this matrix group lies in the observation that two identities

$$\mathscr{W}_{p,-q} = -\langle T_{p-q}, T_0 \rangle (w_p \overline{w_q} + \overline{w_{-p}} w_{-q})$$
$$\mathscr{W}_{-p,-q} = -\langle T_{-p-q}, T_0 \rangle (w_{-p} \overline{w_q} + \overline{w_p} w_{-q})$$

are jointly captured by the matrix identity

$$S(w_p, w_{-p})S(w_q, w_{-q})^* = -S\left(\frac{\mathscr{W}_{p,-q}}{\langle T_{p-q}, T_0\rangle}, \frac{\mathscr{W}_{-p,-q}}{\langle T_{-p-q}, T_0\rangle}\right), \qquad (25)$$

provided that $\langle T_{p-q}, T_0\rangle$ and $\langle T_{-p-q}, T_0\rangle$ are both nonzero. When p and q are adjacent nodes in the graph G_W, this condition holds; this is implied by the completeness assumption for the graph G_W. Then the corresponding 2D-Fourier coefficients $\mathscr{W}_{p,-q}$ and $\mathscr{W}_{-p,-q}$ coincide with their counterparts $\mathscr{V}_{p,-q}$ and $\mathscr{V}_{-p,-q}$, respectively, if and only if

$$S(w_p, w_{-p})S(w_q, w_{-q})^* = S(v_p, v_{-p})S(v_q, v_{-q})^*.$$

We consider two different cases.

(a) Suppose that $|w_p| \neq |w_{-p}|$ for some $p \in K_W$. Then $S(w_p, w_{-p})$ is invertible. Upon choosing $q = p$, we have that $S(w_p, w_{-p})S(w_p, w_{-p})^* = S(v_p, v_{-p})$ $S(v_p, v_{-p})^*$ can be rewritten as $S(w_p, w_{-p})^{-1}S(v_p, v_{-p})S(v_p, v_{-p})^*$ $S(w_p, w_{-p})^{-*} = I$. Therefore: $S(v_p, v_{-p}) = S(w_p, w_{-p})S(\alpha, \beta)$ for some unitary matrix $S(\alpha, \beta)$. For the choice $q \neq p$, we then have that $S(w_p, w_{-p})$ $S(w_q, w_{-q})^* = S(v_p, v_{-p})S(v_q, v_{-q})^*$ becomes equivalent to $S(v_q, v_{-q}) = S(w_q, w_{-q})S(\alpha, \beta)$, involving the same unitary matrix $S(\alpha, \beta)$. Now it is easily verified that if $\alpha = 0$ then $v_q = \beta w_{-q}$ for all $q \in K_W$, i.e.: $v(t) = \beta\overline{w(t)}$ for a unimodular constant β. Alternatively, if $\beta = 0$ then $v_q = \alpha w_q$ for all $q \in K_W$, i.e.: $v(t) = \alpha w(t)$ for a unimodular constant α.

(b) Suppose that $|w_p| = |w_{-p}|$ for all $p \in K_W$. Then for the choices $p = -q = k$ and $p = q = k$ we obtain the two conditions:

$$|w_k|^2 + |w_{-k}|^2 = |v_k|^2 + |v_{-k}|^2,$$
$$w_k\overline{w_{-k}} = v_k\overline{v_{-k}}.$$

It follows that $v_k = u_k w_k$ and $v_{-k} = u_k w_{-k}$ for some unimodular factor u_k. Then the normalized (unimodular) quantities $V_k := \frac{v_k}{|v_k|}$ and $W_k := \frac{w_k}{|w_k|}$ satisfy $V_k = u_k W_k$, $V_{-k} = u_k W_{-k}$ and $V_p\overline{V_{-q}} + \overline{V_{-p}}V_q = W_p\overline{W_{-q}} + \overline{W_{-p}}W_q$. Hence: $\left(\frac{u_p}{u_q} - 1\right)\left(\frac{u_p}{u_q} - \frac{W_q W_{-q}}{W_p W_{-p}}\right) = 0$ if and only if $u_p = u_q$ or $u_p W_p W_{-p} = u_q W_q W_{-q}$.

First, suppose $W_m W_{-m} \neq W_n W_{-n}$ and $u_m = u_n$ for some $m, n \in K_W$. For $k \in K_W$ we have $u_k = u_m$ or $u_k W_k W_{-k} = u_m W_m W_{-m}$. Similarly, it holds that $u_k = u_n$ or $u_k W_k W_{-k} = u_n W_n W_{-n}$. Since $u_k W_k W_{-k} = u_m W_m W_{-m}$ and $u_k W_k W_{-k} = u_n W_n W_{-n}$ cannot both hold true, it follows that $u_k = u_m$ or $u_k = u_n$. This implies that for all $k \in K_W$: $u_k = \alpha$ for some unimodular constant α. Hence $V_k = \alpha W_k$ for all k if and only if $v_k = \alpha w_k$ for all k, which holds if and only if $v(t) = \alpha w(t)$.

Otherwise, suppose $u_m \neq u_n$. Again, for $k \in K_W$ we have $u_k = u_m$ or $u_k W_k W_{-k} = u_m W_m W_{-m}$. Similarly, it holds that $u_k = u_n$ or $u_k W_k W_{-k} = u_n W_n W_{-n}$. Since $u_k = u_m$ and $u_k = u_n$ cannot both hold true it follows that $u_k W_k W_{-k} = u_m W_m W_{-m}$ or $u_k W_k W_{-k} = u_n W_n W_{-n}$. This implies that for all $k \in K_W$: $u_k W_k W_{-k} = u_m W_m W_{-m} = u_n W_n W_{-n} = \beta$ for some unimodular constant β. Hence $u_k W_k W_{-k} = u_p W_p W_{-p} = u_q W_q W_{-q} = \beta$ for some unimodular

constant β. Therefore $V_k = \beta\overline{W_{-k}}$ for all k if and only if $v_k = \beta\overline{w_{-k}}$ for all k, if and only if $v(t) = \beta\overline{w(t)}$.

Finally, suppose $W_m W_{-m} = W_n W_{-n}$ for all $m, n \in K_W$. Then $u_k = u_n$ or $u_k W_k W_{-k} = u_n W_n W_{-n}$ implies $u_k = u_n$. Hence, for all $k \in K_W$: $u_k = \alpha$ for some unimodular constant α. Therefore $V_k = \alpha W_k$ for all k if and only if $v_k = \alpha w_k$ for all k, if and only if $v(t) = \alpha w(t)$.

$\square$

Proof of Proposition 3

(1) From Eq. (16) we have that:

$$z(t + m\tau) = e^{2\pi c(t+m\tau)i} (2x_c + w(t + m\tau)) = e^{2\pi cti} e^{2\pi cm\tau i} (2x_c + w(t + m\tau))$$

In this expression, the factor $e^{2\pi cm\tau i}$ is the $(m + 1)$-th diagonal entry of the matrix $diag(T_c)$. The factor $2x_c + w(t + m\tau)$ is the $(m+1)$-th entry of the vector $2x_c T_0 + W(t)$.

(2) Suppose $c(u - v) \in \mathbb{Z}$, then $e^{2\pi cui} = e^{2\pi cvi}$. Hence $Z(u) - Z(v) = e^{2\pi cui} diag(T_c) (Z(u) - Z(v))$, which implies that $|Z(u) - Z(v)| = |W(u) - W(v)|$ and $\|Z(u) - Z(v)\| = \|W(u) - W(v)\|$.

(3) First, suppose $m = c + p > 0$ and $n = q - c < 0$. Then, from Proposition 2 and Eq. (17) it follows that:

$$\mathscr{Z}_{c+p,q-c} = -4x_{c+p}\overline{x_{c-q}}\langle T_{p+q}, T_0\rangle = -w_p\overline{w_{-q}}\langle T_{p+q}, T_0\rangle,$$

Second, suppose $m = p - c < 0$ and $n = c + q > 0$. Then, from Proposition 2 and Eq. (17) it follows that:

$$\mathscr{Z}_{p-c,c+q} = -4\overline{x_{c-p}}x_{c+q}\langle T_{p+q}, T_0\rangle = -\overline{w_{-p}}w_q\langle T_{p+q}, T_0\rangle,$$

Then, for $p < c$ and $q < c$:

$$\mathscr{W}_{p,q} = -\langle T_{p+q}, T_0\rangle \left(w_p\overline{w_{-q}} + \overline{w_{-p}}w_q\right) = \mathscr{Z}_{p+c,q-c} + \mathscr{Z}_{q+c,p-c}.$$

(4) The result follows immediately from Definition 1 and Eq. (17). $\square$

Proof of Proposition 4

Write $Z(t) = e^{2\pi cti} V(t)$.

(1) Horizontal, vertical and diagonal lines in URP_X. Horizontal lines $(u, v) = (t, t_0)$ and vertical lines $(u, v) = (t_0, t)$:

$$\text{URP}_X(u, v)^2 = \|X(t) - X(t_0)\|^2$$
$$= \left(\|X(t_0)\|^2 + \frac{1}{2}\|V(t)\|^2\right)$$
$$-2Re\left(e^{2\pi cti}\langle V(t), X(t_0)\rangle\right)$$
$$+\frac{1}{2}Re\left(e^{4\pi cti}\langle V(t), \overline{V(t)}\rangle\right).$$

The first, second and third term have frequencies in the ranges $\{0, \ldots, 2d\}$, $\{c - d, \ldots, c + d\}$ and $\{2c - 2d, \ldots, 2c + 2d\}$, respectively. Diagonal lines $(u, v) = (t + \tau_0, t)$:

$$\text{URP}_X(u, v)^2 = \|X(t + \tau_0) - X(t)\|^2$$
$$= \frac{1}{2}\left\|e^{2\pi c\tau_0 i}V(t + \tau_0) - V(t)\right\|^2$$
$$+\frac{1}{2}Re\left(e^{4\pi cti}\langle e^{2\pi c\tau_0 i}V(t + \tau_0) - V(t), e^{-2\pi c\tau_0 i}\overline{V(t + \tau_0)} - \overline{V(t)}\rangle\right).$$

The first and second term have frequencies in the ranges $\{0, \ldots, 2d\}$ and $\{2c - 2d, \ldots, 2c + 2d\}$, respectively.

(2) Horizontal, vertical and diagonal lines in URP$_Z$. Horizontal lines $(u, v) = (t, t_0)$ and vertical lines $(u, v) = (t_0, t)$:

$$\text{URP}_Z(u, v)^2 = \|Z(t) - Z(t_0)\|^2$$
$$= \left(\|Z(t_0)\|^2 + \|V(t)\|^2\right)$$
$$-2Re\left(e^{2\pi cti}\langle V(t), Z(t_0)\rangle\right).$$

The first and second term have frequencies in the ranges $\{0, \ldots, 2d\}$ and $\{c - d, \ldots, c + d\}$, respectively.

Diagonal lines $(u, v) = (t + \tau_0, t)$:

$$\text{URP}_Z(u, v)^2 = \|Z(t + \tau_0) - Z(t)\|^2 = \left\|e^{2\pi c\tau_0 i}V(t + \tau_0) - V(t)\right\|^2.$$

The latter term has frequencies in the range $\{0, \ldots, 2d\}$.

(3) The maximum of the first frequency range is lower than the minimum of the second frequency range if and only if $c > 3d$. Similarly, the maximum of the second frequency range is lower than the minimum of the third frequency range if and only if $c > 3d$.

References

1. Sipers, A., Borm, P., Peeters, R.: On the unique reconstruction of a signal from its unthresholded recurrence plot. Phys. Lett. A **375**(24), 2309–2321 (2011)
2. Eckmann, J.P., Oliffson Kamphorst, S., Ruelle, D.: Recurrence plots of dynamical systems. Europhys. Lett. **4**(9), 973–977 (1987)
3. Marwan, N., Romano, M.C., Thiel, M., Kurths, J.: Recurrence plots for the analysis of complex systems. Phys. Rep. **438**(5), 237–329 (2007)
4. Webber, C.L., Zbilut, J.P.: Dynamical assessment of physiological systems and states using recurrence plot strategies. J. Appl. Physiol. **76**(2), 965–973 (1994)
5. Website on recurrence plots and cross recurrence plots (2013). http://www.recurrence-plot.tk. Accessed 1 Nov 2013
6. Marwan, N.: How to avoid potential pitfalls in recurrence plot based data analysis. Int. J. Bifurcat. Chaos **21**(04), 1003–1017 (2011)
7. Takens, F.: Detecting strange attractors in turbulence. In: Rand, D., Young, L. (eds.) Dynamical Systems and Turbulence. Lecture Notes in Mathematics, pp. 366–381. Springer, Berlin (1981)
8. Chen, Y., Yang, H.: Multiscale recurrence analysis of long-term nonlinear and nonstationary time series. Chaos, Solitons Fractals **45**(7), 978–987 (2012)
9. McGuire, G., Azar, N.B., Shelhamer, M.: Recurrence matrices and the preservation of dynamical properties. Phys. Lett. A **237**(1), 43–47 (1997)
10. Hirata, Y., Horai, S., Aihara, K.: Reproduction of distance matrices and original time series from recurrence plots and their applications. European Phys. J., Special Topics **164**(1), 13–22 (2008)
11. Jie, L., Shu-Ting, S., Jun-Chan, Z.: Comparison study of typical algorithms for reconstructing time series from the recurrence plot of dynamical systems. Chin. Phys. B **22**(1), 010–505 (2013)
12. Robinson, G., Thiel, M.: Recurrences determine the dynamics. Chaos **19**(2), 023–104 (2009)
13. Thiel, M., Romano, M.C., Kurths, J.: How much information is contained in a recurrence plot? Phys. Lett. A **330**(5), 343–349 (2004)
14. Romano, M.C., Thiel, M., Kurths, J., von Bloh, W.: Multivariate recurrence plots. Phys. Lett. A **330**(3–4), 214–223 (2004)
15. Krauss, G.L., Fisher, R.S.: The Johns Hopkins Atlas of Digital EEG, chap. 2, pp. 58–61. Johns Hopkins University Press, Baltimore (2006)
16. Bajaj, V., Pachori, R.: Classification of seizure and nonseizure EEG signals using empirical mode decomposition. Inf. Technol. Biomed. IEEE Trans. **16**(6), 1135–1142 (2012)
17. Bajaj, V., Pachori, R.: EEG signal classification using empirical mode decomposition and support vector machine. In: Proceedings of the International Conference on Soft Computing for Problem Solving (SocProS 2011), vol. 131, pp. 623–635. Springer, India (2012), 20–22 Dec 2011
18. Etévenon, P., Lebrun, N., Clochon, P., Perchey, G., Eustache, F., Baron, J.C.: High temporal resolution dynamic mapping of instantaneous EEG amplitude modulation after tone-burst auditory stimulation. Brain Topogr. **12**(2), 129–137 (1999)
19. Falk, T.H., Fraga, F.J., Trambaiolli, L., Anghinah, R.: EEG amplitude modulation analysis for semi-automated diagnosis of Alzheimer's disease. EURASIP J Adv. Signal Process. **2012**(1), 192 (2012)
20. Pachori, R.B., Bajaj, V.: Analysis of normal and epileptic seizure EEG signals using empirical mode decomposition. Comput. Methods Programs Biomed. **104**(3), 373–381 (2011)

Quantifying Redundancy and Information Content of Lines in Recurrence Plots Using the Theory of Framework Rigidity

Aloys Sipers, Paul Borm and Ralf Peeters

Abstract We address redundancy in the information content of unthresholded recurrence plots (URPs). The theory of framework rigidity is employed to explain and analyze this redundancy geometrically. First we show that the domain of a URP can be restricted to just a finite number of vertical or horizontal lines without loss of information. Then we construct a globally rigid framework to demonstrate a similar property for diagonal lines. This result gives theoretical support to recurrence quantification analysis (RQA), which analyzes and extracts features from an RP along such lines. Third, we construct a finite set of curves, one of which is a contour line, for which it again holds that the URP contains all information along them. This links the information content of lossy (thresholded) recurrence plots to that of URPs. This study is also a starting point in employing redundancy to improve existing recurrence plots based methods and algorithms, and to develop new ones. Several examples clarify the methods and an application from EEG artifact detection shows some of their practical potential.

1 Introduction

Recurrence plots (RPs), see [1], are a popular tool for the visualization of the behavior of dynamical systems, in particular for their phase space trajectories. Recurrence quantification analysis (RQA), see [2, 3], provides RP based methods to further

A. Sipers (✉) · P. Borm
Centre of Expertise in Life Sciences, Zuyd University,
Nieuw Eyckholt 300, 6419 DJ Heerlen,
The Netherlands
e-mail: aloys.sipers@zuyd.nl

P. Borm
e-mail: paul.borm@zuyd.nl

R. Peeters
Department of Knowledge Engineering, Universiteit Maastricht,
Bouillonstraat 8-10, 6200 MD
Maastricht, The Netherlands
e-mail: ralf.peeters@maastrichtuniversity.nl

analyze and quantify RPs and the underlying dynamical behavior. RQA proceeds by selecting horizontal, vertical and diagonal lines in recurrence plots and computing various quantities from them. Potential problems and pitfalls related to different aspects of the application of RPs are pointed out in [4]. The methods based on RPs have been successfully applied to various fields in the natural sciences as well as in engineering and in economy. See, for instance, the bibliography collected on the recurrence plot website [5], which shows an impressive increase of such applications over the last decade.

Recurrence plots can also be used to analyze scalar signals $x(t)$ by first embedding them in an M-dimensional trajectory space. Given a finite-interval continuous-time real-valued signal $x(t)$, with $t \in [0, 1)$ say, the time-delay embedding method of [6] constructs such a trajectory $X(t)$ as:

$$X(t) = \begin{pmatrix} x(t) \\ x(t + \tau) \\ \vdots \\ x(t + (M - 1)\tau) \end{pmatrix}, \quad t \in [0, 1). \tag{1}$$

The embedding dimension M and the time-delay $\tau \in (0, 1)$ are specified by the user, for which some techniques are available in the literature, e.g. involving the average mutual information (AMI) [7] for M, or the false nearest neighbors fraction (FNNF) [8] for τ. Next, the *unthresholded* recurrence plot (URP) is defined as (the graph of) the intra-trajectory distance function for $X(t)$:

$$\text{URP}_X(u, v) = \|X(u) - X(v)\|, \quad u, v \in [0, 1), \tag{2}$$

in which $\| \cdot \|$ denotes a norm. While several other norms are also popular in the literature, such as the 1-norm and the maximum norm, we will exclusively use the Euclidean norm here. Also, to avoid having to take finite interval effects explicitly into account, the signal $x(t)$ and its trajectory $X(t)$ are periodically extended from the interval $[0, 1)$ to all of $\mathbb{R}$. Finally, for a given positive threshold ε, the *binary* (thresholded) recurrence plot is defined as

$$\text{RP}_X^\varepsilon(u, v) = \Theta \left(\varepsilon - \|X(u) - X(v)\| \right), \quad u, v \in [0, 1), \tag{3}$$

in which Θ denotes the Heaviside function (i.e. $\Theta(x) = 1$ for $x \geq 0$ and $\Theta(x) = 0$ otherwise). Recurrence plots can likewise be defined for discrete-time signals and trajectories in an obvious way, by restricting t, u and v to a discrete set of time instants (and choosing τ accordingly).

For a proper understanding of the information content of a recurrence plot, we have previously addressed the relationship between the URP and its underlying signal $x(t)$ using Fourier analysis and graph theory; see [9]. Generically it holds that URP_X determines $x(t)$ up to a sign and an additive constant, but more information from $x(t)$ may sometimes be lost, depending on the frequency content of $x(t)$ and

on the choice of the embedding parameters M and τ. Earlier work in this area is found in [10, 11], while the relationship between the RP and $x(t)$ was previously investigated in [12–15]. In the present paper we study redundancy of information in URPs themselves. One obvious aspect of URPs and RPs is their symmetry with respect to the diagonal $u = v$. Since URPs are a 2-dimensional representation of a 1-dimensional object (the trajectory in M-dimensional space), it should also not come as a surprise that it carries much more redundant information. We first address the joint information content of horizontal and vertical lines in a URP and we show how this determines the (redundant) information in other parts of that URP. As an example, we show how our results on redundancy in URPs can be employed for the detection of similar signal segments. (Other detection methods based on RPs can also be found in [16–18].) For further studies on lines structures in RPs, see e.g. [2, 19, 20]. We shall also briefly address the information in diagonals and in contour lines of a URP. This aims to better understand the information which is preserved in an RP, as an RP is obtained from a URP by thresholding.

Because a URP captures distance information between pairs of points on the trajectory $X(t)$, it is natural to employ the theory of framework rigidity, see [21–23], to explain geometrically the redundant distance information in a URP. Following [23], we introduce some preliminary definitions and notation. A *configuration* P in $\mathbb{R}^M$ is a finite set of N points $P = \{P_1, P_2, \ldots, P_N\}$. Let G be a simple graph on the nodes $1, 2, \ldots, N$, then a *bar-and-joint framework* (or simply a *framework*) in $\mathbb{R}^M$, denoted by $G(P)$, is the graph G together with the configuration P, where each node n of G is located at the point P_n. Each edge (m, n) in G is viewed as a rigid bar of length equal to $\|P_m - P_n\|$, and each node in G as a joint – with full rotational freedom for all its adjacent bars. Two frameworks $G(P)$ and $G(Q)$ are said to be *equivalent* if $\|P_m - P_n\| = \|Q_m - Q_n\|$ for all edges (m, n) of G. They are said to be *congruent* if $\|P_m - P_n\| = \|Q_m - Q_n\|$ for all pairs of nodes m and n in the graph G. This is the same as saying that $G(Q)$ can be obtained from $G(P)$ by an isometry. A framework $G(P)$ is called *rigid* if there is an $\epsilon > 0$ such that every framework $G(Q)$ which is equivalent to $G(P)$ and for which $\|P_n - Q_n\| < \epsilon$ for all $n = 1, 2, \ldots, N$, is also congruent to $G(P)$. A framework is called *globally rigid* if this holds for every $\epsilon > 0$, i.e. if every framework $G(Q)$ which is equivalent to $G(P)$ is congruent to $G(P)$. A complete graph always gives a globally rigid framework for every embedding dimension M. See Fig. 1 for an example of four frameworks in $\mathbb{R}^2$ illustrating these concepts, where the nodes (joints) are represented by dots and the edges (bars) by straight lines.

In this paper we consider frameworks $G(\mathcal{X})$ which involve a configuration of points $\mathcal{X} = \{\mathcal{X}_1, \ldots, \mathcal{X}_N\}$ located on a trajectory $X(t)$. i.e. for all nodes $n = 1, \ldots, N$ of G: $\mathcal{X}_n = X(t_n)$ for some set of time instants $t_1, \ldots, t_N$. Note that global rigidity of $G(\mathcal{X})$ then expresses the property that all the values of $\text{URP}_X(u, v)$ with $u, v \in \{t_1, \ldots, t_N\}$ are determined by the subset of such values with (u, v) corresponding to the edges of G.
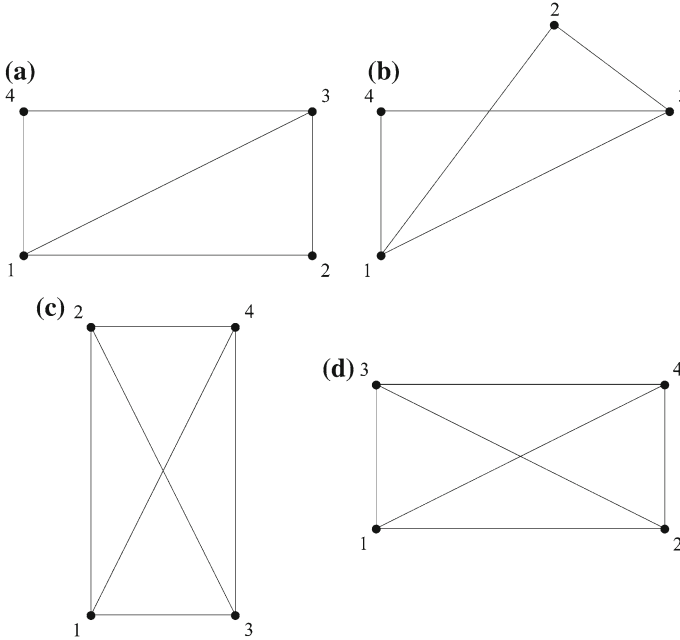
Fig. 1 The frameworks in **a** and **b** are equivalent. When embedded in $\mathbb{R}^2$, both are rigid. They are not congruent, therefore they are both not globally rigid. When embedded in $\mathbb{R}^3$ they are both also no longer rigid. The frameworks in **c** and **d** are congruent and both are globally rigid. The graph G is complete; therefore global rigidity holds for arbitrary embedding dimensions ≥ 2

The paper is structured as follows. In Sect. 2, we show that the whole URP can be reconstructed from the information content of a set of selected horizontal or vertical lines in a URP. The geometrical interpretation and the use of redundancy in recurrence plot analysis is demonstrated and evaluated by three examples. First, redundant distance information in a trajectory and in its URP is illustrated geometrically. Second, we show that the choice of the embedding parameters M and τ may influence the number of lines needed in the URP to capture all the information. Third, an application in EEG analysis involving eye blink artifact detection is presented, to demonstrate how redundancy can be employed to reduce the analysis region for the URP. In Sect. 3, we construct globally rigid frameworks with points which relate to diagonals of a URP, and then we extend that approach to (approximate) contour lines. This aims to better understand the information which is (and which is not) preserved in RPs. Section 4 concludes the paper. All the proofs are collected in the Appendix.

2 Redundancy in URPs and the Information Contained in Vertical Lines

In this section we show with basic geometry how an entire URP can be reconstructed from the information it carries in a few well selected horizontal or vertical lines. Because URP_X is constructed from the intra-trajectory distances of $X(t)$ in the embedding space $\mathbb{R}^M$, it is clear that it is invariant under isometric transformation of $X(t)$, which makes it natural to employ affine geometric tools. To formalize this we have the following basic results.

Lemma 1 *Let V_X be the smallest affine subspace of $\mathbb{R}^M$ which contains the trajectory $X(t)$. Denote $k = dim(V_X)$. Let $\mathbb{T}_b = \{t_0, t_1, \ldots, t_k\}$ be a set of time instants such that $\{X(t_0), X(t_1), \ldots, X(t_k)\}$ constitutes an affine basis for V_X. Each point $X(t)$ can then be written in a unique way as $X(t) = \sum_{m=0}^{k} \alpha_m(t) X(t_m)$ with affine coordinates $\alpha_m(t) \in \mathbb{R}$, satisfying $\sum_{m=0}^{k} \alpha_m(t) = 1$.*
Relative to the point $X(t_0)$, let the trajectory be represented by $\widetilde{X}(t) := X(t) - X(t_0)$, so that a basis for the linear space $V_X - X(t_0)$ is given by the columns of the matrix $B := \left(\widetilde{X}(t_1) | \ldots | \widetilde{X}(t_k) \right)$. Note that for this basis, the coordinate vector of $\widetilde{X}(t)$ is the unique vector $\alpha(t)$ satisfying $\widetilde{X}(t) = B\alpha(t)$. Its entries coincide with the affine coordinates: $\alpha(t) = (\alpha_1(t), \ldots, \alpha_k(t))^T$. We then have that:

(1) The coordinate vector $\alpha(t)$ of $\widetilde{X}(t)$ is given by

$$\alpha(t) = (B^T B)^{-1} B^T \widetilde{X}(t). \tag{4}$$

(2) The values $URP_X(u, v)$ of the unthresholded recurrence plot satisfy:

$$URP_X(u, v)^2 = (A(u) - A(v))^T \left(B^T B \right)^{-1} (A(u) - A(v)), \tag{5}$$

where
$$A(t) := B^T \widetilde{X}(t) = B^T B \alpha(t). \tag{6}$$

(3) For $m = 1, \ldots, k$, the entries $A_m(t)$ of $A(t)$ are given in terms of URP_X by:

$$A_m(t) = \frac{1}{2} \left(URP_X(t_0, t_m)^2 + URP_X(t_0, t)^2 - URP_X(t_m, t)^2 \right). \tag{7}$$

(4) For $m, n = 1, \ldots, k$, the entries $\left(B^T B \right)_{m,n}$ of the Gram matrix $B^T B$ are given by:
$$\left(B^T B \right)_{m,n} = A_m(t_n) = A_n(t_m). \tag{8}$$

Combining parts (2), (3) and (4) of this lemma, it follows that $URP_X(u, v)$ can be computed from the joint information stored at certain other locations in the URP. We have the following theorem.

Theorem 1 *Let V_X be the smallest affine subspace of $\mathbb{R}^M$ containing the trajectory $X(t)$. Denote $k = dim(V_X)$. Let $\mathbb{T}_b := \{t_0, t_1, \ldots, t_k\}$ be a set of time instants such that $\{X(t_0), X(t_1), \ldots, X(t_k)\}$ is an affine basis for V_X. Then:*
(1) The entire unthresholded recurrence plot $URP_X(u, v)$ can be computed from the restriction of $URP_X(u, v)$ to the $k + 1$ vertical lines of points (u, v) with $u \in \mathbb{T}_b$.
(2) Let $\mathbb{T}_a \subseteq [0, 1)$ be an arbitrary subset of time instants. Then the restriction of $URP_X(u, v)$ to $\mathbb{T}_a \times \mathbb{T}_a$ can be computed from the restriction of $URP_X(u, v)$ to $\mathbb{T}_b \times (\mathbb{T}_b \cup \mathbb{T}_a)$.

According to part (1) of this theorem, the dimension k of the affine subspace V_X determines how many vertical lines jointly carry all the information in a URP. (By symmetry, this likewise holds for horizontal lines.) The value of k is bounded from above by the embedding dimension M, but it may also vary with the choice of time-delay τ. We can make this precise for time-delay embeddings of real periodic signals $x(t)$ which have a Fourier series representation $x(t) = \sum_{p \in \mathbb{Z}} c_p e^{2\pi pti}$. For such signals it holds that the complex Fourier coefficients c_p satisfy $c_{-p} = \overline{c_p}$ for all $p \in \mathbb{Z}$. The corresponding trajectory $X(t)$ is given by $X(t) = \sum_{p \in \mathbb{Z}} c_p e^{2\pi pti} T_p$, in which the complex-valued vectors $T_p \in \mathbb{C}^M$ are given by:

$$T_p = \begin{pmatrix} 1 \\ z^p \\ \vdots \\ z^{(M-1)p} \end{pmatrix}, \quad \text{with } z = e^{2\pi \tau i}. \tag{9}$$

See also [9], where this class was used extensively. We then have the following result.

Proposition 1 *Let $x(t)$ be a real periodic signal with a Fourier series representation $x(t) = \sum_{p \in \mathbb{Z}} c_p e^{2\pi pti}$. Let k be the dimension of the smallest affine subspace V_X of $\mathbb{R}^M$ containing the trajectory $X(t) = \sum_{p \in \mathbb{Z}} c_p e^{2\pi pti} T_p$. Define the set $K_X := \{p \in \mathbb{Z} \setminus \{0\} \mid c_p \neq 0\}$ and define the linear subspace $\mathcal{V}$ of $\mathbb{C}^M$ as the span of the set of vectors T_p with $p \in K_X$. Then:*
(1) $k = dim(\mathcal{V})$.
(2) Let r be the cardinality of the set $\{p\tau (mod\ 1) \mid p \in K_X\}$, i.e. the total number of different fractional parts of the quantities $p\tau$ with $p \in K_X$. Then $k = \min\{M, r\}$.

For values of τ that are not rational, all the quantities $p\tau (mod\ 1)$ with $p \in K_X$ are different. Then part (2) of this proposition shows that $k = \min\{M, |K_X|\}$ and the dimension k of V_X attains its maximal value (i.e. for the situation where τ is varied but M and the signal $x(t)$ are fixed). Because the vectors T_p all depend continuously on τ, it follows from part (1) that the same maximal value of k is also attained in open neighborhoods of such irrational values for τ and hence it is attained generically. However, for some special rational choices of τ (e.g. in combination with finite sets K_X), the value of k may drop.

To further clarify the findings of this section, we now give three examples. In the first example we explain geometrically the redundant distance information contained in a URP. In the second example we investigate the impact of different choices of τ, which may lead to different values of the dimension $k = \dim(V_X)$. In the third example we investigate an application in EEG analysis. It concerns a digitally sampled measurement signal containing eye blink artifacts. We demonstrate how the set of time instants $\mathbb{T}_b$ in Theorem 1 can be chosen to reduce the analysis region from the entire URP to only a part.

Example 1 Parts of a URP constructed from vertical lines in that URP

To illustrate Theorem 1 and the underlying Lemma 1, we consider a trajectory $X(t)$ in $\mathbb{R}^2$ and a set of time instants $\mathbb{T}_b = \{t_0, t_1, t_2\}$, for three different choices of $\mathbb{T}_a$.
(i) Let $\mathbb{T}_a = \{u_0, v_0\}$.
From Lemma 1 we have that $\mathrm{URP}_X(u_0, v_0)$ is determined by the entries of $A(u_0)$, $A(v_0)$ and $B^T B$. The entries of $B^T B$ are in turn given by the entries of $A(t_1)$ and $A(t_2)$. The entries of a vector $A(t)$ are determined by $\mathrm{URP}_X(t_0, t)$, $\mathrm{URP}_X(t_1, t)$, $\mathrm{URP}_X(t_2, t)$, $\mathrm{URP}_X(t_0, t_1)$ and $\mathrm{URP}_X(t_0, t_2)$. With $t \in \{t_1, t_2, u_0, v_0\}$, it therefore follows that $\mathrm{URP}_X(u_0, v_0)$ is determined by:

(1) The values $\mathrm{URP}_X(t_0, t_1)$, $\mathrm{URP}_X(t_0, t_2)$ and $\mathrm{URP}_X(t_1, t_2)$, which equal the lengths of the three black solid lines in Fig. 2a. Note that this constitutes the complete graph for the affine basis of trajectory points $\{X(t_0), X(t_1), X(t_2)\}$ for $\mathbb{T}_b$.
(2) The values $\mathrm{URP}_X(t_0, u_0)$, $\mathrm{URP}_X(t_1, u_0)$ and $\mathrm{URP}_X(t_2, u_0)$, which equal the lengths of the three red solid lines in Fig. 2a. These values fix the position of the point $X(u_0)$ relative to the affine basis under (1).
(3) The values $\mathrm{URP}_X(t_0, v_0)$, $\mathrm{URP}_X(t_1, v_0)$ and $\mathrm{URP}_X(t_2, v_0)$, which equal the lengths of the three green solid lines in Fig. 2a. These values fix the position of the point $X(v_0)$ relative to the affine basis under (1).

The key geometric observation is that the framework $G(P)$ with P consisting of the trajectory points for the time instants $\mathbb{T}_a \cup \mathbb{T}_b$ and which has all the possible edges except for the edge between $X(u_0)$ and $X(v_0)$ (represented by the blue dashed line in Fig. 2a), is a *globally rigid* framework. Therefore the value of $\mathrm{URP}_X(u_0, v_0)$ is fixed. In Fig. 2b, the corresponding points in the recurrence plot URP_X are indicated: the blue dot for (u_0, v_0), three black dots for (t_0, t_1), (t_0, t_1), (t_1, t_2), three red dots for (t_0, u_0), (t_1, u_0), (t_2, u_0), and three green dots for (t_0, v_0), (t_1, v_0), (t_2, v_0). Because of symmetry, and because the values of any URP along the diagonal $u = v$ are all zero, the statements of Theorem 1 follow (also for horizontal lines).
(ii) Let $\mathbb{T}_a = [\alpha, \beta]$ be a subinterval of $[0, 1]$.
The restriction of $\mathrm{URP}_X(u, v)$ to the grid points $\mathbb{T}_b \times \mathbb{T}_b$ again corresponds to the complete graph for the affine basis of points $X(t_0)$, $X(t_1)$ and $X(t_2)$, previously indicated by the solid black triangle in Fig. 2a. The restriction of $\mathrm{URP}_X(u, v)$ to the
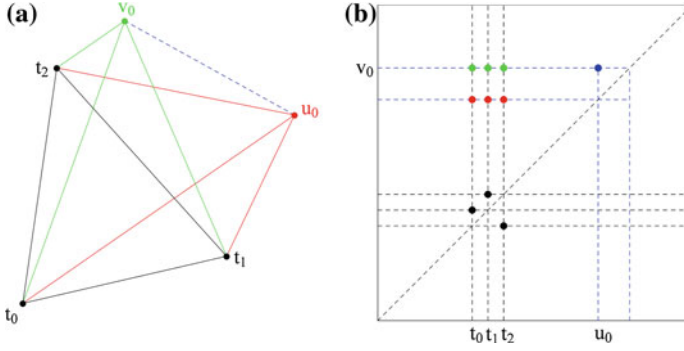
Fig. 2 Geometric representation of redundant distance information: **a** in a trajectory; **b** in its URP

three vertical line segments with coordinates in $\mathbb{T}_b \times [\alpha, \beta]$, captures the distances between the points $X(t)$ with $t \in [\alpha, \beta]$ and the three points of the affine basis; it fixes the position of these points $X(t)$ relative to the basis. Taking $u_0, v_0 \in [\alpha, \beta]$, the restriction of $\mathrm{URP}_X(u, v)$ to the square area $[\alpha, \beta] \times [\alpha, \beta]$ can then be constructed in a point-by-point manner as described under (i).

(iii) Suppose $\mathbb{T}_a = [0, 1]$. This is case (ii) for the special choice $\alpha = 0$ and $\beta = 1$. Then from the restriction of $\mathrm{URP}_X(u, v)$ to the three vertical lines with (u, v) in $\{t_0, t_1, t_2\} \times [0, 1]$, see Fig. 2b, all of $\mathrm{URP}_X(u, v)$ can be constructed.

Example 2 Influence of the embedding parameters M and τ on redundancy

Consider a zero-mean real-valued signal of the form $x(t) = \sum_{p=-2}^{2} c_p e^{2\pi p t i}$ with $c_{-p} = \overline{c_p} \neq 0$ for $p \in K_X = \{-2, -1, 1, 2\}$ and $c_0 = 0$. Let the embedding dimension be chosen as $M = 4$. The corresponding trajectory $X(t)$ is contained in a smallest affine subspace V_X of $\mathbb{R}^4$, which is in fact a linear subspace because of the zero-mean property. It therefore coincides with the intersection of $\mathbb{R}^4$ and the space $\mathcal{V}$ spanned by the four vectors $T_p \in \mathbb{C}^4$ with $p \in K_X$. According to Proposition 1(1) we have that: $k = \dim(V_X) = \dim(\mathcal{V}) = \mathrm{rank}\left(T_{-2}|T_{-1}|T_1|T_2\right)$. The latter matrix is a Vandermonde matrix for the 4 complex numbers in the set $\{\overline{z}^2, \overline{z}, z, z^2\}$ with $z = e^{2\pi \tau i}$. These are numbers on the complex unit circle and depend on τ. To find the value of k we must count how many different values are contained in this set. From Proposition 1(2) (and since $M = 4$) we have that k also equals the cardinality r of $\{p\tau (\mathrm{mod}\ 1) \mid p \in K_X\}$. We compute k for four different rational values of τ.

(1) $\tau = \frac{1}{2}$. Then $z = e^{\pi i} = -1$ and $|\{\overline{z}^2, \overline{z}, z, z^2\}| = |\{-1, 1\}| = 2$. Alternatively, $r = |\{p\tau (\mathrm{mod}\ 1) \mid p \in K_X\}| = |\{0, \frac{1}{2}\}| = 2$. Both approaches give $k = 2$.

(2) $\tau = \frac{1}{3}$. Now $z = e^{2\pi i/3}$ and $|\{\overline{z}^2, \overline{z}, z, z^2\}| = |\{e^{2\pi i/3}, e^{4\pi i/3}\}| = 2$. Also, $r = |\{p\tau (\mathrm{mod}\ 1) \mid p \in K_X\}| = |\{\frac{1}{3}, \frac{2}{3}\}| = 2$. It again follows that $k = 2$.

(3) $\tau = \frac{1}{4}$. Here $z = e^{\pi i/2} = i$ and $|\{\bar{z}^2, \bar{z}, z, z^2\}| = |\{i, -1, -i\}| = 3$. Likewise, $r = |\{p\tau \,(\text{mod } 1) \mid p \in K_X\}| = |\{\frac{1}{4}, \frac{1}{2}, \frac{3}{4}\}| = 3$, whence $k = 3$.

(4) $\tau = \frac{1}{5}$. In this case
$z = e^{2\pi i/5}$ and $|\{\bar{z}^2, \bar{z}, z, z^2\}| = |\{e^{2\pi i/5}, e^{4\pi i/5}, e^{6\pi i/5}, e^{8\pi i/5}\}| = 4$. Similarly, $r = |\{p\tau \,(\text{mod } 1) \mid p \in K_X\}| = |\{\frac{1}{5}, \frac{2}{5}, \frac{3}{5}, \frac{4}{5}\}| = 4$. Now k attains its maximal possible value (for the given choice of M and $x(t)$): $k = 4$.

This example shows that different choices of τ may sometimes produce different values of k. Recall that the number $k + 1$ gives the number of vertical lines to which a URP can be restricted without loss of information. Note also that it follows from the results of [9] that for the given values of M, τ and K_X, the URP determines the underlying zero-mean signal $x(t)$ up to a sign choice in each of the cases (2) and (4), whereas in case (1) it determines $x(t)$ up to two sign choices, and in case (3) up to one sign choice and one complex unimodular factor. Therefore it does not generally hold that a URP which is less informative on $x(t)$ will have fewer lines that still contain all its information.

Example 3   Reduction of the region of analysis for eye blink artifact detection

We present an application in EEG analysis to illustrate how redundancy in a URP can be used to reduce the search region for the detection of morphologically similar signal segments. From a digitally sampled EEG measurement signal (with sampling frequency 250 Hz) we took an excerpt of $N = 2,500$ samples with a total duration of $T = 10$ s, containing 7 eye blink artifacts. From this discrete-time measurement signal a continuous-time signal $x(t)$ was constructed, interpolating the measurement values to let $x(t)$ have a finite Fourier series. It is shown in Fig. 3a. The eye blink artifacts are clearly visible, as they occur as upward peaks having a significantly higher amplitude than the rhythmic brain activity contained in the signal. The corresponding URP was computed for the time-delay embedding parameters $M = 55$ and $\tau = 0.004$ with u and v ranging over the interval $[0, 10]$; it is displayed in Fig. 3b. It has distinctly yellow strips which mark the location of the onset of eye blinks in the signal $x(t)$. The choice of a high embedding dimension helps to locate the eye blinks, as it induces corresponding maxima in the URP, plotted in red.

For testing purposes, a second signal $y(t)$ was generated by adding Gaussian zero-mean white noise $w(t)$ with variance $\sigma^2 = 25$ to the signal $x(t)$ at the sample times, i.e. before interpolation. The high variance of the noise makes that the eye blink artifacts are no longer easily observed in the signal by mere inspection and simple thresholding does not allow their detection. This noise corrupted signal $y(t)$ is shown in Fig. 3c and its URP (for the same embedding parameters as before) is given in Fig. 3d.

The theory of this section indicates that all the information of the URP is also still contained in a limited number of vertical lines of the URP, which can be bounded above by $M + 1$. One may for instance focus attention on vertical lines which are close to each other, i.e. on a vertical strip of the URP. Note that a vertical strip which
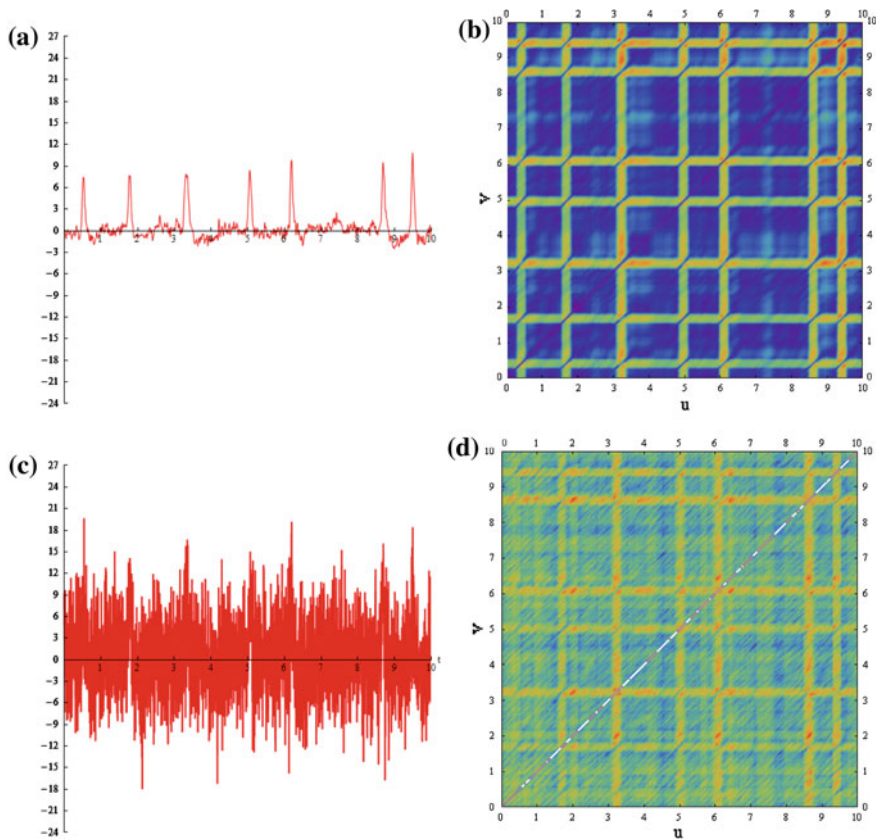
Fig. 3 **a** The interpolated EEG signal $x(t)$, containing 7 eye blink artifacts. **b** The URP of $x(t)$. **c** The noise corrupted signal $y(t) = x(t) + w(t)$ with Gaussian zero-mean white noise $w(t)$ with variance 25. **d** The URP of $y(t)$

aligns with an eye blink artifact allows one to locate the other artifacts in the URP for the clean signal $x(t)$ by searching for the local maxima in the URP. However, the same result can still be obtained for vertical strips which do not align with eye blink artifacts. In fact, for the URP of the noisy signal $y(t)$, the strips which do not align with eye blinks seem to be more promising for avoiding false positive detections (which for instance might occur near the vertical line with $u = 6.3$).

3 Distance Information Carried by Diagonals and Contour Lines

In the previous section we have demonstrated that a URP can be restricted without loss of information to just $k + 1$ of its vertical (or horizontal) lines, corresponding to an affine basis of V_X. We took a geometric approach, constructing a globally rigid graph

connecting any two points $X(u)$ and $X(v)$ to all of the affine basis $\{X(t) \mid t \in \mathbb{T}_b\}$. The distance information contained in the selected vertical lines of the URP then admits the computation of $\text{URP}_X(u, v)$.

In the present section we investigate the information content of different sets of lines or curves in a URP, also involving the construction of a globally rigid graph. We first study the situation for diagonals, which like vertical and horizontal lines are also used for RQA. In the discussion that follows we assume that the periodic trajectory $X(t)$ is nontrivial and sufficiently smooth (i.e. continuous or continuously differentiable with respect to t). For such $X(t)$ and its URP, a graph G and an associated framework $G(\mathcal{X})$ are now constructed in the following way.

- Choose an initial time instant $t_0 \in [0, 1)$, a time step $\Delta t > 0$, and an integer N. Let k be the dimension of the affine trajectory space V_X.
- For $n = 1, 2, \ldots, N$, define the time instants t_n by:

$$t_n = t_{n-1} + \Delta t \ (\text{mod } 1). \tag{10}$$

  i.e. t_n increases linearly with n with fixed increments Δt, but the time instants are 'wrapped around' from 1 back to 0 in view of periodicity of $X(t)$.
- Let G have the nodes $\{0, 1, \ldots, N\}$ and the edge set $\{(i, j) \mid 1 \leq j - i \leq k + 1\}$.
- Let $\mathcal{X} = \{\mathcal{X}_0, \mathcal{X}_1, \ldots, \mathcal{X}_N\}$ with $\mathcal{X}_n = X(t_n)$ for $n = 0, 1, \ldots, N$ be a configuration consisting of trajectory points, and $G(\mathcal{X})$ the corresponding framework.

If N is sufficiently large, then periodicity of the sequence of time instants will occur if and only if Δt is rational. If Δt is irrational, the sequence will be dense and any two points $u, v \in [0, 1)$ will be approximated arbitrarily closely by some time instants t_i and t_j in the sequence. Now suppose that $k + 1$ consecutive points $X(t_n), \ldots, X(t_n + k)$ always constitute an affine basis for V_X. Then the framework $G(\mathcal{X})$ is globally rigid: by construction, any $k + 2$ consecutive points form a clique (i.e. a complete subgraph) which is globally rigid and fixes the position of its first (last) point relative to the last (first) $k + 1$ points. Any $k + 3$ consecutive points are then covered by two such overlapping cliques, of which the overlap consists of an affine basis of $k + 1$ consecutive points, fixing the relative positions of the first and last points and hence their distance.

The points (t_n, t_{n+1}) all lie on the diagonal line D_1 described by $v = u + \Delta t \ (\text{mod } 1)$ in the domain of a URP. Because of the periodic nature of the URP, we will identify opposite sides of a URP and allow curves and lines to be continued across them. Likewise, the points (t_n, t_{n+2}) all lie on the diagonal line D_2 described by $v = u + 2\Delta t \ (\text{mod } 1)$. Continuing in a similar fashion, we have for $\ell = 3, \ldots, k + 1$ that the points $(t_n, t_{n+\ell})$ all lie on the diagonal line D_ℓ described by $v = u + \ell \Delta t \ (\text{mod } 1)$. If the value of the URP is known along the diagonal lines $D_1, \ldots, D_{k+1}$, then the lengths of the bars in the framework $G(\mathcal{X})$ are all known, and by global rigidity the distance between any two points $X(t_i)$ and $X(t_j)$ can be computed. Continuity of $X(t)$ makes that such points can be used to approximate $X(u)$ and $X(v)$ arbitrarily closely. This gives the following theorem.

Theorem 2 *Let $X(t) \in \mathbb{R}^M$ be a continuous periodic trajectory with period $T = 1$. Let $k = \dim(V_X)$, where V_X is the smallest affine subspace of $\mathbb{R}^M$ containing $X(t)$ for all $t \in [0, 1)$. Let $\Delta t \in (0, 1)$ be irrational and consider the $k + 1$ diagonal lines $D_1, \ldots, D_{k+1}$ given by $D_\ell : u \mapsto v = u + \ell \Delta t \pmod 1$. If an initial point t_0 exists such that for all $n \in \mathbb{N}$, with $t_n = t_0 + n \Delta t \pmod 1$, the subset of $k + 1$ consecutive trajectory points $X(t_n), \ldots, X(t_{n+k})$ gives an affine basis for V_X, then the domain of $URP_X(u, v)$ can be restricted to the diagonals $D_1, \ldots, D_{k+1}$ without loss of information.*

This theorem strongly suggests that, generically, the information of a URP is not only contained along $k + 1$ of its vertical lines, but also along $k + 1$ suitably chosen diagonals. The remaining open issue concerns the existence of an initial time instant t_0 with the properties required by the theorem, for a suitable large class of trajectories $X(t)$.

We proceed to study the information content of $k+1$ curves in the URP, one of which is a contour line. To fix terminology, the *level set* L_d of a URP for a given value $d > 0$ is defined to consist of all the points (u, v) for which $URP_X(u, v) = d$. A level set typically consists of one or several curves which are *contour lines* of the URP; they make up the connected components of the level set L_d. Again we identify opposite sides of a URP so that contour lines can continue across them. Note that a (binary, thresholded) RP is basically obtained from a URP by determining the level set for a specified value $d = \varepsilon$. This study aims to better understand the loss of information that occurs when thresholding a URP to produce an RP.

We now construct a graph G and an associated framework $G(\mathcal{X})$ largely as before when studying diagonals, but with the following adaptations.

- We choose an additional distance value $d > 0$, but the time step Δt is no longer needed.
- For $n = 1, 2, \ldots, N$, the time instants t_n are no longer generated according to Eq. (10), but instead by:

$$t_n = \min\{\tilde{t} > t_{n-1} \mid \mathrm{URP}_X(\tilde{t} \pmod 1, t_{n-1}) = d\} \pmod 1. \tag{11}$$

  i.e. t_n is the earliest time instant after t_{n-1} for which $\|X(t_n) - X(t_{n-1})\| = d$, where time instants are 'wrapped around' from 1 back to 0 in view of periodicity of $X(t)$.

For the construction to produce a valid sequence $\{t_0, t_1, \ldots, t_N\}$, a sufficient condition that we will assume to hold is $0 < d < D/2$, where $D = \max_{u,v} \mathrm{URP}_X(u, v)$. (Continuity of the periodic trajectory $X(t)$ guarantees D to exist and to have a finite value.) As before, we again assume that any subsequence of $k + 1$ consecutive trajectory points $X(t_n), \ldots, X(t_{n+k})$ gives an affine basis of V_X. Then the graph G is again globally rigid.

We have that $\|X(t_n) - X(t_{n-1})\| = d$ for all $n = 1, 2, \ldots, N$, which shows that the corresponding points (t_{n-1}, t_n) in the domain of URP_X are all located, by construction, on the level set L_d. Equation (11) defines t_n as a function of t_{n-1},

which we denote by C_1. The graph of this function may be a single contour line for the value d, or be composed of parts of one or several contour lines of L_d. The points (t_{n-2}, t_n) with $n = 2, 3, \ldots, N$ in general do not lie on a single level set. The function which generates t_n from t_{n-1} is denoted by C_2. It is obtained by applying two steps of the recursion of Eq. (11), showing that $C_2 = C_1 \circ C_1$. When d is small and $X(t)$ continuously differentiable, which admits local linearization, this curve approximates a subset of the level set L_{2d}. This subset may consist of a single contour line, or of various parts of one or several contour lines. This depends on the curvature of the trajectory and on how nearby different sections of the trajectory can be. Likewise, the points (t_{n-3}, t_n) with $n = 3, \ldots, N$ lie on the graph of the function $C_3 = C_1 \circ C_1 \circ C_1$, which, for small d, approximates a subset of L_{3d}. Continuing in a similar fashion, we construct $k + 1$ curves C_ℓ which pass through the sets of points $\{(t_{n-\ell}, t_n) \mid n = \ell, \ell + 1, \ldots, N\}$ for $\ell = 1, 2, \ldots, k + 1$, respectively, and which, for small d, approximate subsets of the level sets $L_d, L_{2d}, ..., L_{(k+1)d}$. These curves C_ℓ are characterized recursively by $C_\ell = C_1 \circ C_{\ell-1}$. They have a continuous graph if and only if C_1 is continuous.

We now sketch how, if C_1 happens to be continuous and for a well chosen value of d, the values of the URP along the curves $C_1, \ldots, C_{k+1}$ can be used to compute the distance between two points $X(u_0)$ and $X(v_0)$. Let $t_0 = u_0$ and construct the sequence of time instants $u_1, u_2, \ldots, u_N$ as described above. Then, by construction, the points $(u_n, u_{n+\ell})$ are located on the curve C_ℓ for all $n = 0, 1, \ldots, N - \ell$. Because of global rigidity of the graph G, the information in the URP along the curves $C_1, \ldots, C_{k+1}$ fixes the distance between any two points $X(u_i)$ and $X(u_j)$. For sufficiently large N, exploiting periodicity of the trajectory $X(t)$, we aim for a situation in which the sequence of time instants u_n becomes dense in the interval $[0, 1)$. Before, for the diagonals D_ℓ, this required Δt to be irrational. For the current situation this requires the distance value d to be chosen such that the sequence of time instants u_n again does not become periodic. It also requires that the range of C_1, and hence the range of each curve C_ℓ, is dense in $[0, 1)$. In this way, the time instant v_0 can be approximated arbitrarily closely by a subsequence of time points u_{n_j}. Consequently, also the value of $\text{URP}_X(u_0, v_0)$ can be obtained with arbitrary precision from the values $\text{URP}_X(u_0, u_{n_j})$.

If C_1 is continuous and describes a contour line then, even though this procedure has numerical drawbacks and is not advocated from a practical point of view, it strongly suggests that, for a suitably selected value of d, the information contained in the URP along the curves $C_1, \ldots, C_{k+1}$ determines $\text{URP}_X(u, v)$ completely. More generally, if C_1 is discontinuous and in particular if its range is not dense in $[0, 1)$, then a similar statement holds if instead of using the curve C_1, one uses the multi-valued function of which the graph is the level set L_d. Along with this, the curves C_ℓ should then be replaced by the graphs of the multi-valued functions obtained by

composing L_d with itself multiple times. This level set L_d determines the recurrence plot $\mathrm{RP}_X^d(u, v)$. Thresholding is a lossy operation and for an RP it is well known that it contains in general less information than the URP. The above discussion makes clear that by adding the information along another k well selected curves or level sets of the URP, loss of information can be avoided.

Example 4 Information along curves in the URP

To illustrate the constructions of this section, we consider a zero-mean periodic signal $x(t)$ which is specified by

$$x(t) = 8\sin(2\pi t) + 2\cos(4\pi t + \frac{1}{5}) + \sin(6\pi t + 1). \qquad (12)$$

It is shown in Fig. 4a. It has a finite power spectrum with the corresponding index set $K_X = \{-3, -2, -1, 1, 2, 3\}$. We choose the embedding parameters $M = 2$ and $\tau = \frac{1}{5}$, for which the 2-dimensional periodic trajectory $X(t)$ is given in Fig. 4b. Note that $V_X = \mathbb{R}^2$ and $k = \dim(V_X) = 2$. A contour plot of the resulting URP is shown in Fig. 4c, while the RP for the threshold value $\varepsilon = 5$ is displayed in Fig. 4d. Three specific level sets, consisting of contour lines for the URP values $d = 5$, $2d = 10$, and $3d = 15$, are presented in Fig. 4e.

In Fig. 4f the three curves C_1, C_2, and C_3 for $d = 5$ are given. These are closed curves when opposite sides of the square plot area are identified, consistent with the periodicity of $X(t)$. The curve C_1 coincides with a contour line of the URP (and also of the RP) for $d = 5$. The curves C_2 and C_3 are approximations of contour lines for the URP values $2d = 10$ and $3d = 15$, respectively. (They are not very close approximations, since d is not really small.)

Starting from an initial time $t_0 = u_0 = 0.05$, the corresponding points $X(u_n)$ generated with $d = 5$ for $n = 0, 1, \ldots, 13$ are shown on the trajectory in Fig. 4b. By definition, these are such that $\|X(u_n) - X(u_{n-1})\| = 5$ for $n = 1, \ldots, 13$. The curve C_2 in the URP captures the distances $\|X(u_n) - X(u_{n-2})\|$, while the curve C_3 captures the distances $\|X(u_n) - X(u_{n-3})\|$. The globally rigid graph G has all the edges corresponding to these distances and is also displayed in Fig. 4b. It follows that the curves C_1, C_2, and C_3 jointly carry sufficient information to compute $\mathrm{URP}_X(u_0, u_n)$ for all n. The corresponding locations in the URP are also displayed in Fig. 4f. Note that the points $X(u_{11})$, $X(u_{12})$ and $X(u_{13})$ are located on $X(t)$ in between the pairs of points $X(u_0)$ and $X(u_1)$, $X(u_1)$ and $X(u_2)$, and $X(u_2)$ and $X(u_3)$, respectively. If n is increased further, this eventually produces many more points in these intervals, which can then be used to approximate any given point $X(v)$ and the value $\mathrm{URP}_X(u_0, v)$.
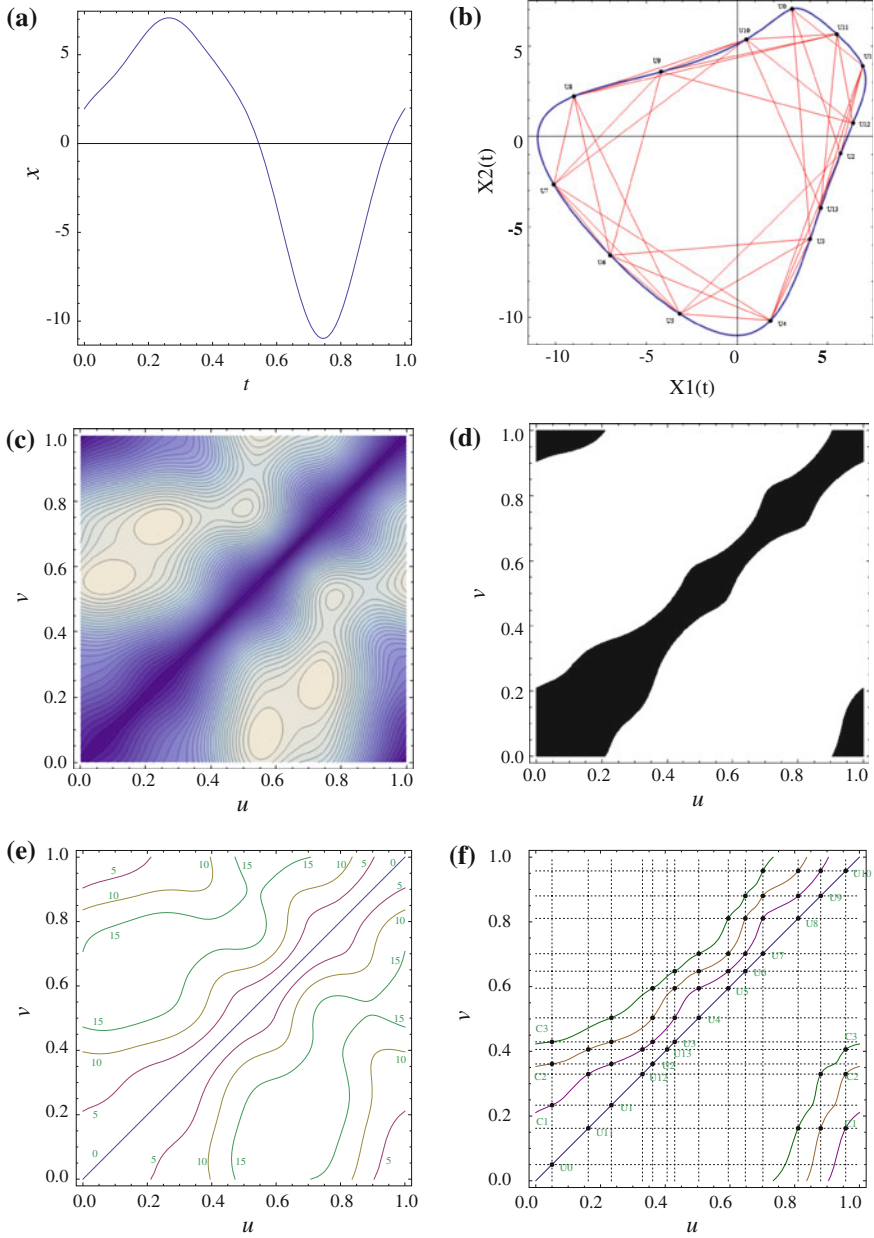
Fig. 4 **a** The zero-mean periodic signal $x(t)$ of Example 4. **b** The trajectory $X(t)$ in $\mathbb{R}^2$, the configuration of trajectory points $\mathcal{X} = \{X(u_0), \ldots, X(u_{13})\}$, and the globally rigid framework $G(\mathcal{X})$. **c** The unthresholded recurrence plot $\mathrm{URP}_X(u, v)$ for $M = 2$ and $\tau = \frac{1}{5}$. **d** The recurrence plot $\mathrm{RP}_X^5(u, v)$ for the threshold $\varepsilon = 5$. **e** The level sets (contour lines) for the values $d = 5$, $2d = 10$, $3d = 15$. **f** The curves C_1, C_2, C_3 and their points for times $t = u_0, u_1, \ldots, u_{13}$

4 Conclusions and Discussion

In Sect. 2, we used properties of rigid frameworks to explain geometrically how the information contained by a URP along a finite number of vertical lines, can be used to reconstruct the entire URP. This result holds for arbitrary trajectories $X(t)$, which need not come from a scalar signal through time-delay embedding. In Sect. 3 we presented a similar result for diagonal lines, and also for curves which coincide with or approximate contour lines. However, the proofs of those results strongly exploit periodicity of $X(t)$. The number of lines (or curves) needed to avoid loss of information in all these results is computed as $k+1$, where k equals the dimension of the space V_X. We neither claim nor conjecture that this number is minimal. In fact, especially when a continuous periodic scalar signal $x(t)$ is time-delay embedded to produce the trajectory $X(t)$, it may well be that fewer lines still contain all the information of a URP.

When a discrete-time recurrence plot is considered, the results of Sect. 2 still hold. The same goes for diagonal lines when Δt is chosen as a multiple of the sampling time which is relatively prime to the total number of measurements. The curves $C_1, \ldots, C_{k+1}$, though, are less easy to generalize to discrete-time, because they may involve time instants that are no integer multiples of the sampling time.

Regarding the information contained in a (thresholded) RP, we note that our results suggest that the information from a finite number of other curves in the URP may help to restore full information. In our opinion it does not seem likely that the choice of these curves is very critical, although convenient choices may give easier proofs. An interesting topic for further research is to investigate whether the contour lines in multi-level recurrence plots (obtained from URPs by thresholding at several levels instead of just one) may carry the full information of a URP.

In Example 3 we showed how the results of Sect. 2 can be combined with characteristics of an EEG signal to develop a novel method for artifact detection using vertical lines. Similar approaches can be investigated which involve diagonal lines or (approximate) contour plots. This theoretical study may serve as a basis to improve existing recurrence plots based methods and algorithms, and we expect it to provide new opportunities for signal analysis and feature selection.

Appendix

Proof of Lemma 1.
(1) For $X(t) \in V_X$ we have that $X(t) = \sum_{m=0}^{k} \alpha_m(t) X(t_m)$ in which the affine coordinates $\alpha_0(t), \alpha_1(t), \ldots, \alpha_k(t)$ add up to 1. For the translated trajectory

$\widetilde{X}(t) = X(t) - X(t_0)$ it then holds that: $\widetilde{X}(t) = \left(\sum_{m=0}^{k} \alpha_m(t) X(t_m)\right) - X(t_0) =$
$\left(\sum_{m=0}^{k} \alpha_m(t) X(t_m)\right) - \left(\sum_{m=0}^{k} \alpha_m(t) X(t_0)\right) = \sum_{m=1}^{k} \alpha_m(t)(X(t_m) - X(t_0)) =$
$B\alpha(t)$. This shows how the affine coordinates of $X(t)$ are related to the linear vector space coordinates of $\widetilde{X}(t)$ for the basis in the columns of B.

The matrix B has full column rank k, so the $k \times k$ Gram matrix $B^T B$ is invertible. From $\widetilde{X}(t) = B\alpha(t)$ it then follows upon premultiplication by $(B^T B)^{-1} B^T$, that $\alpha(t) = (B^T B)^{-1} B^T \widetilde{X}(t)$, which proves part (1) of the lemma.

(2) With the given definition of $A(t)$ in terms of the coordinate vector $\alpha(t)$, the right-hand side of Eq. (5) becomes: $(\alpha(u) - \alpha(v))^T B^T B \left(B^T B\right)^{-1} B^T B (\alpha(u) - \alpha(v))$
$= (\alpha(u) - \alpha(v))^T B^T B (\alpha(u) - \alpha(v)) = \|B (\alpha(u) - \alpha(v))\|^2 = \|\widetilde{X}(u) - \widetilde{X}(v)\|^2$.

(3) Since $A(t) = B^T \widetilde{X}(t)$, the entry $A_m(t)$ equals the inner product $\langle \widetilde{X}(t_m), \widetilde{X}(t) \rangle$. It is well-known that an inner product between two vectors w_1 and w_2 on a real vector space can be expressed in terms of its induced norm as $\langle w_1, w_2 \rangle = \frac{1}{2}(\|w_1 + w_2\|^2 - \|w_1\|^2 - \|w_2\|^2)$. Choosing $w_1 = \widetilde{X}(t_m)$ and $w_2 = -\widetilde{X}(t)$, and noting that $\|\widetilde{X}(t)\|^2 = \mathrm{URP}_X(t, t_0)^2$, part (3) of the lemma follows.

(4) This follows from the observation that $\left(B^T B\right)_{m,n} = \langle \widetilde{X}(t_m), \widetilde{X}(t_n) \rangle = A_m(t_n)$, where m and n can be interchanged because of symmetry. $\qquad \square$

Proof of Theorem 1.

Suppose that $(u_0, v_0) \in \mathbb{T}_a \times \mathbb{T}_a$. Then, from part (2) of Lemma 1 it follows that $\mathrm{URP}_X(u_0, v_0)$ is determined by the vectors $A(u_0)$ and $A(v_0)$, and the matrix $B^T B$. From part (3) of Lemma 1, the vector $A(u_0)$ is determined by the restriction of $\mathrm{URP}_X(u, v)$ to $\mathbb{T}_b \times \{u_0\}$. Similarly, the vector $A(v_0)$ is determined by the restriction of $\mathrm{URP}_X(u, v)$ to $\mathbb{T}_b \times \{v_0\}$. Hence, the difference $A(u_0) - A(v_0)$ is determined by the restriction of $\mathrm{URP}_X(u, v)$ to $\mathbb{T}_b \times \{u_0, v_0\}$.

From part (4) it follows that the matrix $B^T B$ is determined by the restriction of $\mathrm{URP}_X(u, v)$ to $\mathbb{T}_b \times \mathbb{T}_b$.

Together, this implies that the value of $\mathrm{URP}_X(u_0, v_0)$ is determined by the restriction of $\mathrm{URP}_X(u, v)$ to $\mathbb{T}_b \times (\mathbb{T}_b \cup \{u_0, v_0\})$. (Recall that symmetry applies to any URP.) Part (2) of the theorem now follows by letting u_0 and v_0 range over all of $\mathbb{T}_a$. Part (1) then follows by taking $\mathbb{T}_a = [0, 1)$. $\qquad \square$

Proof of Proposition 1.

Clearly, the trajectory $X(t)$ is contained in the space spanned by the vectors T_p. The dimension k of the affine space V_x is equal, by definition, to the dimension of the linear vector space obtained as $V_X - X_0$ for any point X_0 contained in V_X. Choosing $X_0 = c_0 T_0 = c_0(1, \ldots, 1)^T$, which is contained in V_X as it is the mean of all the points for one period of the periodic trajectory $X(t)$, we therefore focus of the translated trajectory $\widetilde{X}(t) = X(t) - c_0 T_0 = \sum_{p \in \mathbb{Z} \setminus \{0\}} c_p e^{2\pi p t i} T_p$. By definition of K_X, this equals $\widetilde{X}(t) = \sum_{p \in K_X} c_p e^{2\pi p t i} T_p$.

For $M \geq 2$, two vectors T_p and T_q are equal if and only if $z^p = z^q$, which holds if and only if $(p - q)\tau$ is integer. We therefore consider the equivalence relation on K_X defined by: $p \sim q$ if and only if $(p - q)\tau \in \mathbb{Z}$. Then the equivalence classes are

characterized by the fractional parts of the numbers $p\tau$, with $p \in K_X$. We now define $R_X := \{p\tau \pmod 1 \mid p \in K_X\}$ and $L := R_X/\tau \subset \mathbb{N}$. The set L is used to index these equivalence classes. For each $\ell \in L$ the corresponding equivalence class is given by $M_\ell := \{p \in K_X \mid p\tau = \ell\tau \pmod 1\}$. With this notation the set K_X can be partitioned into its equivalence classes and we may write $\widetilde{X}(t) = \sum_{\ell \in L} \left(\sum_{p \in M_\ell} c_p e^{2\pi pti} \right) T_\ell$.

First, it is noted that: (1) M_ℓ is not empty for all $\ell \in L$; (2) $c_p \neq 0$ for all $p \in M_\ell$; (3) the functions $e^{2\pi pti}$ are all independent harmonic functions on $[0, 1]$ for all $p \in \mathbb{Z}$. This proves part (1) of the proposition, and for all $\ell \in L$ we have that $\sum_{p \in M_\ell} c_p e^{2\pi pti} \not\equiv 0$ on $[0, 1]$. Second, it is observed that any selection of $j \leq M$ vectors $\{T_{\ell_1}, \ldots, T_{\ell_j}\}$ with distinct indices $\ell_1, \ldots, \ell_j \in L$, is independent (because these vectors can be joined to form the columns of a Vandermonde matrix). Hence, it follows that $\dim(V_X) = \min\{M, |L|\}$. This proves part (2) because $r = |K_X| = |L|$.

Finally, for $M = 1$ the proposition is also easily verified to hold. $\qquad \square$

References

1. Eckmann, J.P., Oliffson Kamphorst, S., Ruelle, D.: Recurrence plots of dynamical systems. Europhys. Lett. **4**(9), 973–977 (1987)
2. Marwan, N., Romano, M.C., Thiel, M., Kurths, J.: Recurrence plots for the analysis of complex systems. Phys. Rep. **438**(5), 237–329 (2007)
3. Webber, C.L., Zbilut, J.P.: Dynamical assessment of physiological systems and states using recurrence plot strategies. J. Appl. Physiol. **76**(2), 965–973 (1994)
4. Marwan, N.: How to avoid potential pitfalls in recurrence plot based data analysis. Int. J. Bifurcation Chaos **21**(04), 1003–1017 (2011)
5. Website on recurrence plots and cross recurrence plots. http://www.recurrence-plot.tk. Accessed online 1 Nov 2013 (2013)
6. Takens, F.: Detecting strange attractors in turbulence. In: Rand, D., Young, L. (eds.) Dynamical Systems and Turbulence. Lecture Notes in Mathematics, vol. 898, pp. 366–381. Springer, Berlin (1981)
7. Fraser, A.M., Swinney, H.L.: Independent coordinates for strange attractors from mutual information. Phys. Rev. A **33**(2), 1134–1140 (1986)
8. Kennel, M.B., Brown, R., Abarbanel, H.D.I.: Determining embedding dimension for phase-space reconstruction using a geometrical construction. Phys. Rev. A **45**(6), 3403–3411 (1992)
9. Sipers, A., Borm, P., Peeters, R.: On the unique reconstruction of a signal from its unthresholded recurrence plot. Phys. Lett. A **375**(24), 2309–2321 (2011)
10. Chen, Y., Yang, H.: Multiscale recurrence analysis of long-term nonlinear and nonstationary time series. Chaos, Solitons & Fractals **45**(7), 978–987 (2012)
11. McGuire, G., Azar, N.B., Shelhamer, M.: Recurrence matrices and the preservation of dynamical properties. Phys. Lett. A **237**(1), 43–47 (1997)
12. Hirata, Y., Horai, S., Aihara, K.: Reproduction of distance matrices and original time series from recurrence plots and their applications. Eur. Phys. J. Special Topics **164**(1), 13–22 (2008)
13. Jie, L., Shu-Ting, S., Jun-Chan, Z.: Comparison study of typical algorithms for reconstructing time series from the recurrence plot of dynamical systems. Chin. Phys. B **22**(1), 010–505 (2013)
14. Robinson, G., Thiel, M.: Recurrences determine the dynamics. Chaos **19**(2), 023–104 (2009)
15. Thiel, M., Romano, M.C., Kurths, J.: How much information is contained in a recurrence plot? Phys. Lett. A **330**(5), 343–349 (2004)
16. Birleanu, F.M., Candel, I., Ioana, C., Gervaise, C., Serbanescu, A., Serban, G.: A vector approach to transient signal processing. In: Information Science, Signal Processing and their Applications (ISSPA), 2012 11th International Conference on, pp. 1141–1146 (2012)

17. Birleanu, F.M., Ioana, C., Gervaise, C., Chanussot, J., Serbanescu, A., Serban, G.: On the recurrence plot analysis method behaviour under scaling transform. In: Statistical Signal Processing Workshop (SSP), 2011 IEEE, pp. 789–792 (2011)
18. Birleanu, F.M., Ioana, C., Serbanescu, A., Chanussot, J.: A time-distributed phase space histogram for detecting transient signals. In: Acoustics, Speech and Signal Processing (ICASSP), IEEE International Conference on 2011, pp. 3844–3847 (2011)
19. Facchini, A., Kantz, H., Tiezzi, E.: Recurrence plot analysis of nonstationary data: The understanding of curved patterns. Phys. Rev. E **72**(2), 021–915 (2005)
20. Gao, J., Cai, H.: On the structures and quantification of recurrence plots. Phys. Lett. A **270**(12), 75–87 (2000)
21. Alfakih, A.Y.: On dimensional rigidity of bar-and-joint frameworks. Discrete Appl. Math. **155**(10), 1244–1253 (2007)
22. Asimow, L., Roth, B.: The rigidity of graphs. Trans. Amer. Math. Soc. **245**, 279–289 (1978)
23. Jordán, T., Szabadka, Z.: Operations preserving the global rigidity of graphs and frameworks in the plane. Comput. Geom. **42**(67), 511–521 (2009)

Recent Advances in Non-stationary Signal Processing Based on the Concept of Recurrence Plot Analysis

Cornel Ioana, Angela Digulescu, Alexandru Serbanescu, Ion Candel and Florin-Marian Birleanu

Abstract This work concerns the analysis of non-stationary signals using Recurrence Plot Analysis concept. Non-stationary signals are present in real-life phenomena such as underwater mammal's vocalizations, human speech, ultrasonic monitoring, detection of electrical discharges, transients, wireless communications, etc. This is why a large number of approaches for non-stationary signal analysis are developed such as wavelet analysis, higher order statistics, or quadratic time-frequency analysis. Following the context, the methods defined around the concept of Recurrence Plot Analysis (RPA) constitute an interesting way of analyzing non-stationary signals and, particularly, the transient ones. Starting from the phase space and the recurrence matrix, new approaches [the angular distance, recurrence-based autocorrelation function (ACF), average-magnitude difference function (AMDF) and time-distributed recurrence (TDR)] are introduced in order to extract information about the non-stationary signals, specific to different applications. Comparisons with existing analysis methods are presented, proving the interest and the potential of the RPA-based approaches.

C. Ioana (✉) · A. Digulescu · I. Candel
GIPSA-lab, Grenoble Institute of Technology, Saint-Martin-d'Hères, France
e-mail: Cornel.Ioana@gipsa-lab.grenoble-inp.fr

I. Candel
e-mail: ion.Candel@gipsa-lab.grenoble-inp.fr

A. Digulescu · A. Serbanescu
Military Technical Academy, Bucharest, Romania
e-mail: adigulescu@mta.ro

A. Serbanescu
University of South-East Europe "Lumina", Bucharest, Romania
e-mail: serbalexe1@yahoo.com

F.-M. Birleanu
University of Pitesti, Pitesti, Romania

1 Introduction

Physical phenomena are naturally characterized by specific measures which progress in time. This evolution is quantified for the observer in recorded time series. Hereby, many of these recordings describe stochastic, deterministic—chaotic processes and carry information along with disturbances. Such processes can be met in weather's evolution, in speech and acoustic signal processing, for example.

Our study starts from the concept of recurrence—one main property of conservative dynamic systems [1]. For the first time in 1987, Eckmann proposed the recurrence plot (RP) as a tool describing multi-dimensional trajectories of dynamic systems [2].

Therefore, the recurrence plot analysis (RPA) concept was used in real-life applications implying deterministic-chaotic and random components. Each of these components requires a certain method to emphasize its nature. Specific structures and topologies on the RP provide a comprehensive description of dynamic process under study [3], hereby this approach is more general.

Specific characteristics of the studied system can be highlighted by the phase space representation. We can underline Lorenz's works that exploited the properties of the attractor in the weather pattern studies [4]. In *acoustic signal processing*, a current field of great interest is the study of underwater mammal behavior by processing signals and identifying vocalizations and clicks, extensively described in [5].

Another important application field is the *ultrasound signal processing* for monitoring industrial installation such as pipes, metallic structures, etc. [5]. A general framework is defined by the non-intrusive testing and measurement principles. The major problem encountered in this application is the signal's deformations that makes complex the process of parameter estimation such as time-of-flight.

The above mentioned examples represent just few real-life applications where the processing of signals, highly non-stationary, is a central part. The traditional methods are mainly based on time-frequency [6] and time-scale analysis [7]. There are a lot of contributions, in the last two decades, falling in these two broad classes of techniques. Despite of each contribution, the common element is the hypothesis on the analyzed signal (e.g. short-time stationary, in the general case of spectrogram-based processing) or on the expected time shape of the signal, which allows us to pre-define the analyzing wavelet function, for example.

In this work, we propose an alternative of non-stationary signal analysis, based on the phase space representation, defined from the signal's samples [8–14].

Compared to the wavelet-based approach that requires the definition of an appropriate wavelet function, [7, 15, 16] the RP-based representation is obtained by using only signal's samples, conferring also more flexibility and robustness.

The purpose of our work is to show how the RP-based method can be used to characterize a non-stationary signal which describes certain natural phenomena.

The work is organized as follows: the second section describes the main idea of the RPA, the third section illustrates the signal processing approach of the RPA highlighting the angular distance, as well as the vector signal processing approach. In the fourth section, we point out the results in real applications developed in our

research activity. The last part of the paper consists of conclusions and discussions on the subject.

2 Recurrence Plot Analysis and Non-stationary Signal Processing

The main idea of the RPA is to highlight recurrent states present in the analyzed time series. Let us consider the following time series:

$$x = \{x[1], x[2], \ldots, x[N]\} \tag{1}$$

Then, this time series can be represented in a phase space. Its values become the coordinates of the m-dimensional space and, consequently, the vector sample is:

$$\overrightarrow{x_i^{(w)}} = \sum_{k=1}^{m} x\left[i - \left[\frac{w-1}{2}\right] + (k-1)d\right] \overrightarrow{e_k} \tag{2}$$

where $w = 1 + (m-1)d$. If $(w-1)$ is an odd number, then $i = \overline{\left[\frac{w-1}{2}\right] + 1, N - \left[\frac{w-1}{2}\right]}$, respectively $i = \overline{\left[\frac{w-1}{2}\right] + 1, N - \left[\frac{w-1}{2}\right]} - 1$, if $(w-1)$ is an even number. m is the embedding dimension, d is the delay and $\overrightarrow{e_k}$ is the unit vector of the axes that define the phase space. The half-window $\left[\frac{w-1}{2}\right]$ centers the time index, i, in the middle of the vector sample $\overrightarrow{x_i^{(w)}}$ and it represents the a priori "memory" of the vector. According to [14], if $d = 1$, the result is a full vector sample [it contains successive samples from the recorded time series from Eq. (1)].
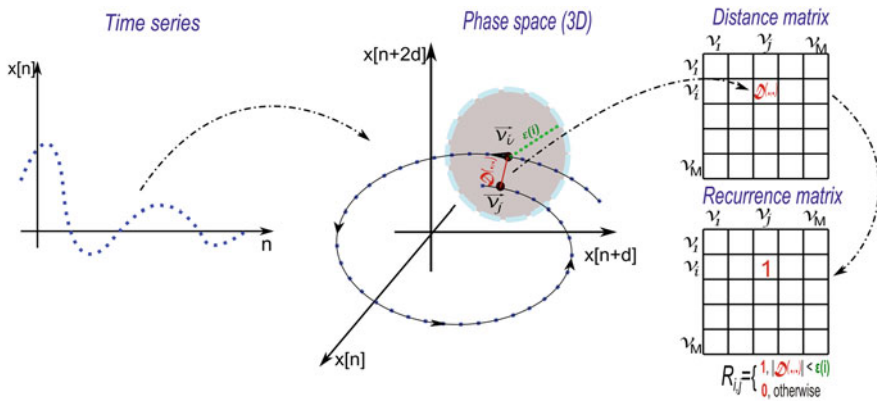

Fig. 1 Recurrence plot analysis representation

For the experiments presented in this work, the embedding dimension and the delay are chosen using the false nearest neighbor and the mutual information, respectively, [16–19]. Then the distances between the vectors in the phase space are represented on the distance matrix, Eq. (3). When compared with a threshold, the recurrence matrix is obtained, Eq. (4). A graphical representation is given in Fig. 1.

$$D_{i,j} = \mathcal{D}\left(\overrightarrow{x_i^{(w)}}, \overrightarrow{x_J^{(w)}}\right) \tag{3}$$

$$R_{i,j} = \Theta\left(\varepsilon\left(i\right) - \mathcal{D}\left(\overrightarrow{x_i^{(w)}}, \overrightarrow{x_J^{(w)}}\right)\right) \tag{4}$$

where $\mathcal{D}\left(\cdot, \cdot\right)$ is a distance applied on the vectors from the phase space (Euclidean distance [16, 20], L1 norm [17], angular distance [14], scalar dot product distance [14], etc.).

In signal processing theory, a well-known approach for transient process is the time-frequency analysis based on the wavelet transform that could provide very good results in the sense of the decomposition parsimony. If the analyzing wavelet is appropriately chosen, the wavelet-based decomposition is characterized by a reduced number of wavelet coefficients that describes the transient behavior of the signal.

The main advantage of the wavelet analysis is the multi-scale analysis [21]. This analysis indicates signal characteristics that other processing techniques could miss, such as trends, breakdowns, discontinuities, etc. While the Short Time Fourier Transform provides a constant time and frequency resolution, the wavelet analysis performs a multiresolution analysis (Fig. 2) [7, 15, 22].

Although the two methods, RPA and wavelet analysis, are based on totally different concepts (the recurrence of the system's trajectory in the phase space and the time-frequency representation, respectively), they are both able to highlight similar behaviors of a process like trends, sudden changes, discontinuities [23–30].

Several comparisons are shown between the two methods along with widely used signal processing methods (as matched filter, spectrogram, zero crossing).

The major advantage of the RPA is that it does not need any orthogonal basis or any *a priori* information about the studied system (unlike the wavelet analysis that requires the definition of the analyzing mother wavelet that must be close to parts of the signal to analyze). The method works in applications where a reference signal is not available (unlike the matched filter method) and it is more robust to noise in terms of signal detection and localization [31]. More details can be found in Sect. 4.

Next section deals with the development of signal processing methods based on the RP concept. A new distance is introduced and studied in the signal processing context.

3 Recurrence Plot Analysis in Signal Processing

The section presents our contributions in the signal analysis field using the recurrence plot context:

- The definition of the angular distance which contributes to the analysis of signals composed by time-shifted and attenuated components having the same time-shape
- The introduction of the Vector Signal Processing-based measures for more accurate detection of the transient components of the signals.

Comparisons with classical techniques are done for signals coming from some real-applications we deal with in our research.

3.1 The Angular Distance

Traditionally, the distance matrix is obtained, as indicated previously, by computing the pair-wise Euclidean distance between all points in the phase space. This distance *could not reveal recurrences in the case of signals having similar time-shifted components but with different amplitudes.* These recurrences are met in the case of multi-path environment propagated signals, where the signal arrived at the reception has multiple reflexions and attenuated/delayed versions of the source signal.

This is often the case of transient signals propagated in a multi-path environment as illustrated, in simulated conditions, in Fig. 2.
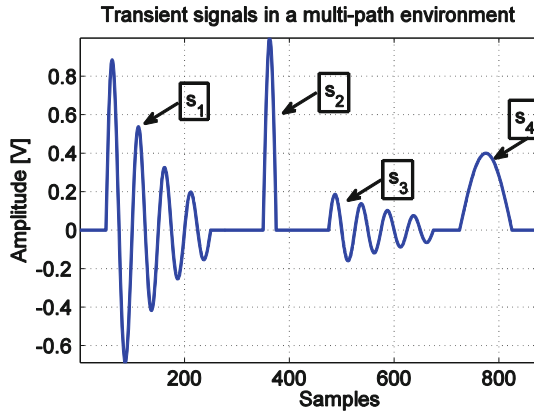

Fig. 2 Time series of transient signals in a multi-path channel; the signal s_i arrives at the receiver at different moments and its amplitude is strongly attenuated by the channel: $s_1[n] = sin\left(2\pi \frac{4}{f_s}n\right).e^{\left(-2\frac{n}{f_e}\right)}, n = \overline{1,200}; \quad s_2[n] = sin\left(2\pi \frac{4}{f_s}n\right), \quad n = \overline{1,25}; \quad s_3[n] = 0.2 \cdot sin\left(2\pi \frac{4}{f_s}n\right).e^{\left(-1.2\frac{n}{f_e}\right)}, \quad n = \overline{1,200}; \quad s_4[n] = sin\left(2\pi \frac{2}{f_s}n\right), \quad n = \overline{1,100}; \quad f_s = 200\,\text{Hz}$
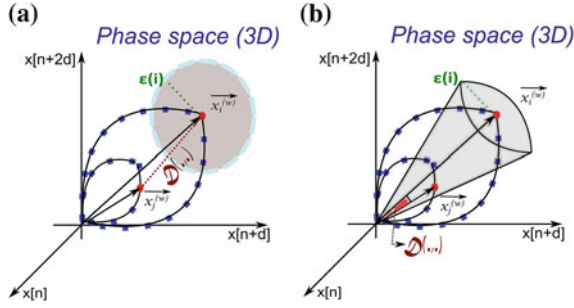
Fig. 3 The graphical representation of the Euclidean distance (**a**) and the angular distance (**b**) plotted in a 3D phase space

In order to highlight the recurrences, despite the magnitude's differences between the components, the angular distance is defined as:

$$
\mathcal{D}\left(\overrightarrow{x_i^{(w)}}, \overrightarrow{x_J^{(w)}}\right) = \arccos\left(\frac{\overrightarrow{x_i^{(w)}} . \overrightarrow{x_J^{(w)}}}{\left\|\overrightarrow{x_i^{(w)}}\right\| . \left\|\overrightarrow{x_J^{(w)}}\right\|} \right)
\tag{5}
$$

where $\overrightarrow{x_i^{(w)}} \cdot \overrightarrow{x_J^{(w)}}$ is the scalar product of the two vector samples. Using this distance, it is possible to identify the points of the trajectory placed in the solid angle and that correspond to the components with different amplitudes. Unlike the Euclidean distance (Fig. 3a), the angular distance (Fig. 3b) quantifies the aperture delimited by the position vectors $\overrightarrow{x_i^{(w)}}$ and $\overrightarrow{x_J^{(w)}}$.

Figure 3b illustrates how the points corresponding to the trajectories of two pulses with different amplitudes are located using the angular distance while in the case of Euclidian one (Fig. 3a) the two trajectories might be separated depending on the sphere parameter.

The amplitude invariance is studied at a smaller scale considering a sine wave with a linear amplitude variation. The angular distance emphasizes only the direction of the state vectors, while RPA is sensitive to this amplitude variation using the Euclidean distance. The angular distance reveals the presence of the sine wave (Fig. 4) although its amplitude varies.

The main advantage provided by this method is that the structure from the distance/recurrence matrix appears clearer and has the **same value,** independent of the magnitude's variation. RP obtained with the angular distance is potentially an *amplitude-invariant* RP, useful in practical applications.

The angular distance provides a RP representation where the phase space origin is extremely important. In real applications, this approach can be exploited in order to eliminate the drawback caused by the attenuation in multiple propagating paths. In
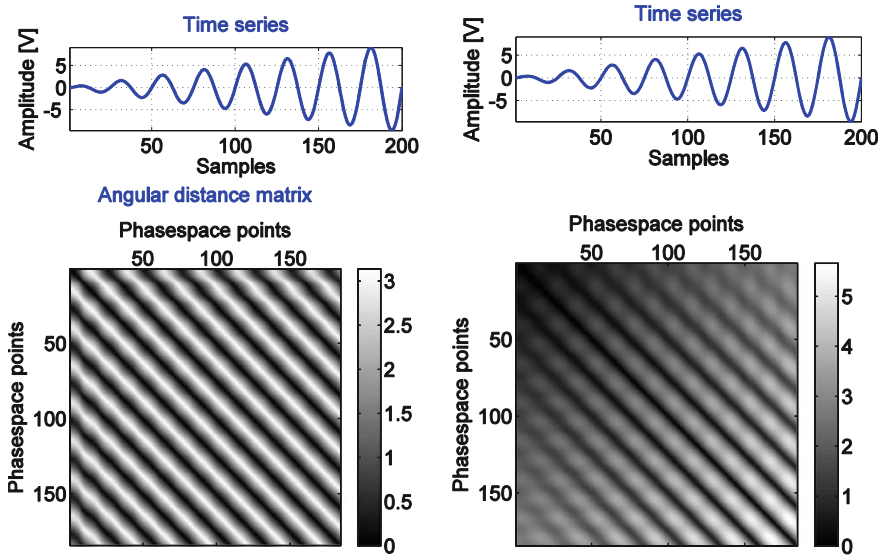
Fig. 4 The angular distance (*left side*) and the Euclidean distance (*right side*) applied on a sine wave superimposed to a linear trend, $m = 3$ and $d = 8$ ($w = 17$)
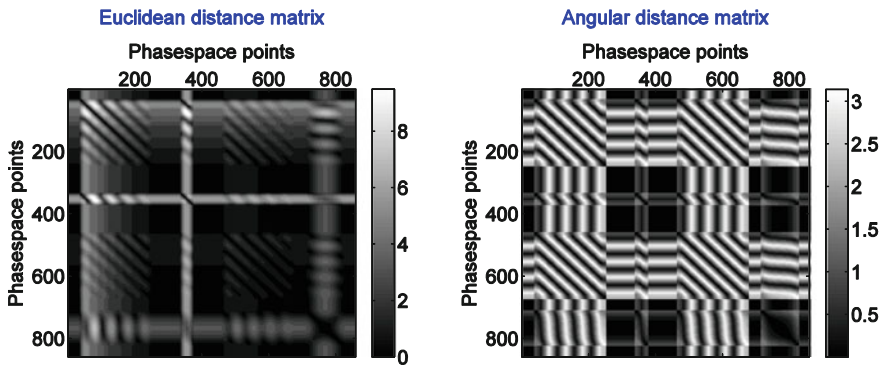

Fig. 5 The Euclidean distance (*left side*) and the angular distance (*right side*) applied on the signal propagated in a multi-path environment (Fig. 3) where $m = 3$ and $d = 8$ ($w = 17$)

such applications, presented in our work as an illustration of RPA's practical interest, the only information which counts is the time of arrival. On the other hand, the amplitude-invariance can be dramatic in other applications and it is necessary to be very careful in the decision of using the angular distance.

Figure 5 illustrates the angular distance as well as the Euclidean distance for the test signal from Fig. 2. Therefore it highlights the interest of such distance.

As a conclusion, the angular distance-based RPA provides an interesting tool for characterizing signals with similar component, but characterized by different amplitudes.

3.2 Vector Signal Processing (VeSP)

This section investigates some tools for vector signal processing defined from the RP concept.

3.2.1 Vector Signal Processing Covariance

The classical definition of the covariance of two signals x and y is:

$$C(x, y) = \frac{1}{N} \sum_{i=1}^{N} (x[i] - m_x)(y[i] - m_y) \tag{6}$$

where m_x, m_y are the mean values of the signals x and y, respectively and N is the number of samples considered for computation.

In Eq. (6), if we replace signals x and y with their vector samples defined as in (2) $\overrightarrow{x^{(w)}}$ and $\overrightarrow{y^{(w)}}$, the vector sample-based covariance is obtained [14]:

$$C^{(w)}\left(\overrightarrow{x^{(w)}}, \overrightarrow{y^{(w)}}\right) = \frac{1}{N} \sum_{i=1}^{N} \left(\overrightarrow{x_i^{(w)}} - \vec{m}_{\overrightarrow{x^{(w)}}}\right)\left(\overrightarrow{y_i^{(w)}} - \vec{m}_{\overrightarrow{y^{(w)}}}\right) \tag{7}$$

In order to have the same number of samples, N, the vector sample is zero padded so that it has the same number of samples as its corresponding time series [14].

When using two signals of different lengths, it is necessary to zero pad one signal so that the two signals, $\overrightarrow{x^{(w)}}$, respectively $\overrightarrow{y^{(w)}}$ have the same lengths and the vector sample covariance may be computed.

For simplicity reasons we consider $d = 1$.

The mean value $\vec{m}_{\overrightarrow{x^{(w)}}}$ is the average of the vectors $\overrightarrow{x^{(w)}}$ $\left(\vec{m}_{\overrightarrow{x^{(w)}}} = \frac{1}{N} \sum_{i=1}^{N} \overrightarrow{x_i^{(w)}}\right)$. Moreover, if $w = 1$, then $C^{(1)} = C$, therefore the Eq. (7) is the generalized version of Eq. (6).

This approach was proposed only for short time series, such as partial discharges (recorded in high-voltage electrical cables presenting insulation faults)where only a few samples are available, because the phenomena happen very quickly. When N is sufficiently large, then the coordinates of the mean value of the vector sample approach the mean of x, so there is no new information available.

3.2.2 Vector Signal Processing Quantiﬁcation (VeSP)

Three new measures in RPA domain [14] have been proposed using as a starting point the distance/recurrence matrix, being treated from signal processing perspective. Hereby, the recurrence-based auto-covariance function is defined as [14, 20]

$$ACF^{(w)}[n] = \sum_{i=1}^{N-n} D_{i,i+n} \tag{8}$$

$$ACF_{\varepsilon}^{(w)}[n] = \sum_{i=1}^{N-n} R_{i,i+n} \tag{9}$$

where $n = \overline{0, N-1}$, $D_{i,j}$, and $R_{i,j}$ are the distance and recurrence matrix, respectively, given in Eqs. (3) and (4). This measure quantifies the recurrence points on the diagonal lines of the distance matrix (Eq. 8) and the ε dependent recurrence matrix (Eq. 9). When $w = 1$, the $ACF^{(1)}$ function is the classical auto-covariance function.

Further, the extended version of the function is the $ACF^{(w)}$ recurrence-based average magnitude difference function, $AMDF^{(w)}$. Its definition is:

$$AMDF^{(w)}[n] = \frac{1}{N-n} \sum_{i=1}^{N-n} D_{i,i+n} \tag{10}$$

$$AMDF_{\varepsilon}^{(w)}[n] = \frac{1}{N-n} \sum_{i=1}^{N-n} R_{i,i+n} \tag{11}$$

where $n = \overline{0, N-1}$.

The $AMDF^{(w)}[n]$ function determines the mean distance from reference states and is also found in the literature as the generalized autocorrelation function or the τ- recurrence rate [16].

In terms of signal processing, one major application is the **estimation of the fundamental frequency** of a signal.

The $AMDF_{\varepsilon}^{(w)}[n]$ function was applied on a signal of 500 samples having different signal to noise ratios. The fundamental frequency was actually obtained from the fundamental period estimation, T_f. Its estimation was obtained from the time difference between two successive maximums of $AMDF_{\varepsilon}^{(w)}[n]$. The same idea can be also found in [32].

For the noisy signal from Fig. 6, the VeSP parameters are $w = 5$ and $\varepsilon = 1.2$. The fundamental frequency is obtained, from the graph of the $AMDF_{\varepsilon}^{(w)}$ function.

The second VeSP measure developed is the *dynamic range norm*. From the origin of the phase space, it is defined as:
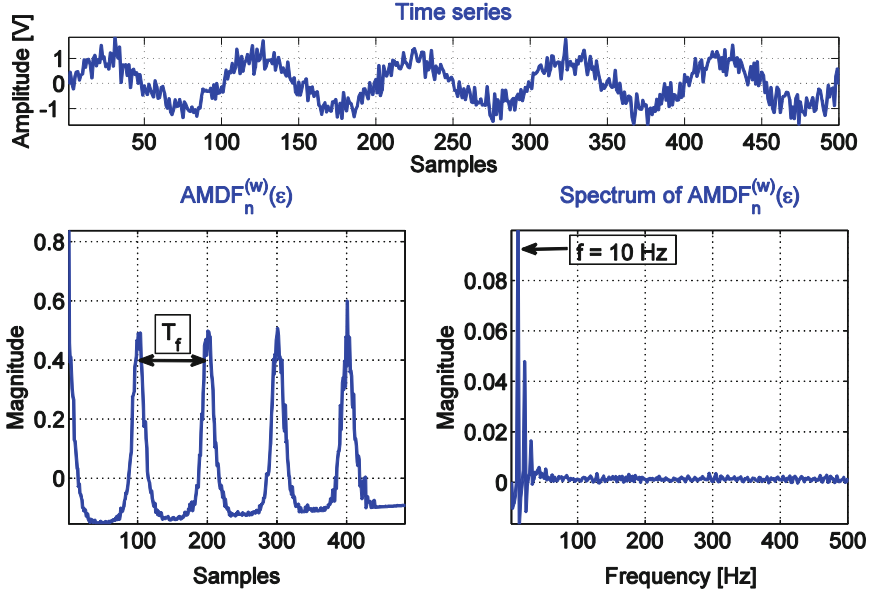
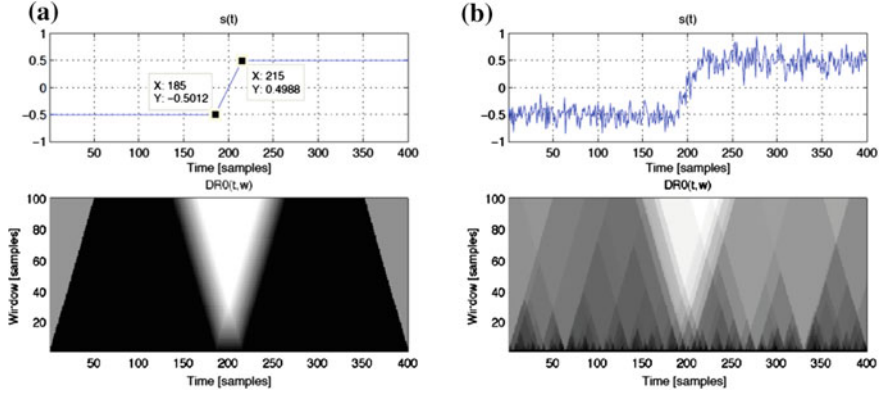**Fig. 6** VeSP AMDF applied on a narrow-band signal with a 15 *dB SNR*

Fig. 7 A noise-free signal (**a**) and its noisy version (*SNR* = 15 dB) (**b**) containing a linear transition between two steady states. The representation (t, w) is computed for each corresponding vector sample

$$DR0\,[i] = \max_k \left\{ \overrightarrow{x_t^{(w)}(k)} \right\} - \min_k \left\{ \overrightarrow{x_t^{(w)}(k)} \right\} \tag{12}$$

where $\overrightarrow{x_t^{(w)}(k)}$ is the k-th element of vector sample $\overrightarrow{x_t^{(w)}}$.

From Fig. 7, it can be observed that in terms of signal's phase changes, the dynamic range norm has a similar effect as the first order derivative. Therefore, at sudden changes, the dynamic range norm provides an impulse.

The third measure proposed is the *time distributed recurrence* and is defined as [14]:

$$TDR_\varepsilon^{(w)}[n] = \frac{1}{N}\sum_{i=1}^{N} R_{i,n} \tag{13}$$

where $n = \overline{1, N}$, N is the length of the signal and Euclidian distance is used. This approach quantifies the recurrence points from the columns of the recurrence matrix, being very useful in **transient detection applications**. This is due to the fact that sudden changes (states different from all other states of the phase space) are clearly "visible" on the recurrence/distance matrix. The corresponding vector samples have a solitary position in the phase space. Therefore, the column average changes significantly for these states.

For transient detection, we define the complementary normalized version of $TDR_\varepsilon^{(w)}[n]$:

$$\overline{TDR_\varepsilon^{(w)}(n)} = 1 - \frac{TDR_\varepsilon^{(w)}[n]}{\max\left\{TDR_n^{(w)}[n]\right\}} \tag{14}$$

Figure 8 presents the use of this measure for the detection of transient components of a signal. The synthetic signal from Fig. 9a is detected independently of the amplitude of the signal.

Moreover, when applied on a recording of an electrical arc [33], Fig. 9b shows that all the components are detected. The reflexions after the electrical arc are highlighted by the proposed function, although late ones are highly attenuated.

4 Results in Applications

The next section illustrates some real-life applications where the proposed concepts are applied. Comparisons with existing techniques are done, highlighting the practical interest of the RP-based methods.

4.1 Ultrasound Measurement

The ultrasound-based measurement is an important domain in the field of predictive surveillance of equipments. A common challenging problem encountered in this field is the estimation of the travel time between a transmitting transducer and the receiving one. In the non-destructive testing (for example, when the transmitter and the receiver are located in the same place), the propagation time multiplied with wave velocity informs about the position of a possible crack reflected by the emitted wave.
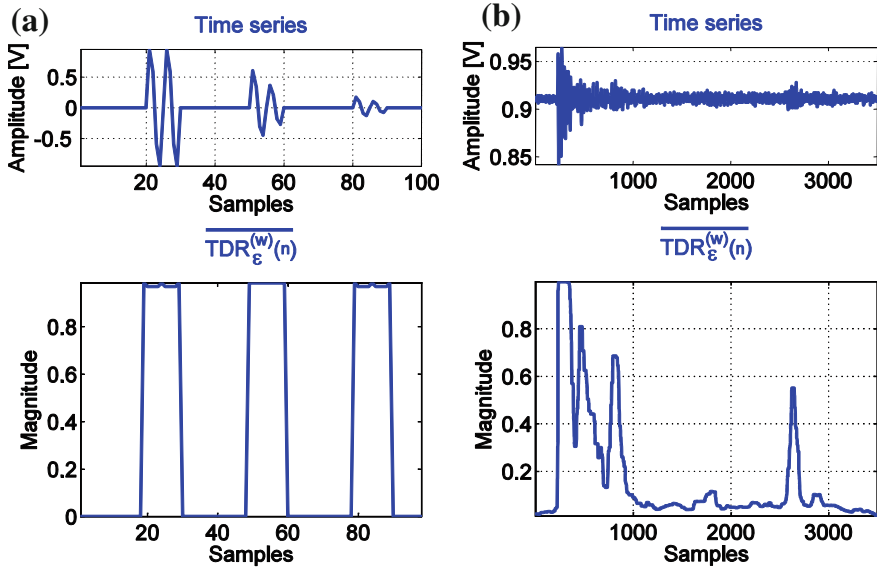
Fig. 8 Time detection curves using $\overline{TDR_\varepsilon^{(w)}}(n)$ function: **a** synthetic signal of a transient and its two reflections (each transient contains 10 samples) for $w = 17$ ($m = 3, d = 8, \varepsilon = 0.3$), **b** real signal from an electric arc recorded with an electric arc locator (the signal contains the discharge and its reflections) for $w = 31$ ($m = 4, d = 10, \varepsilon = 0.9$)
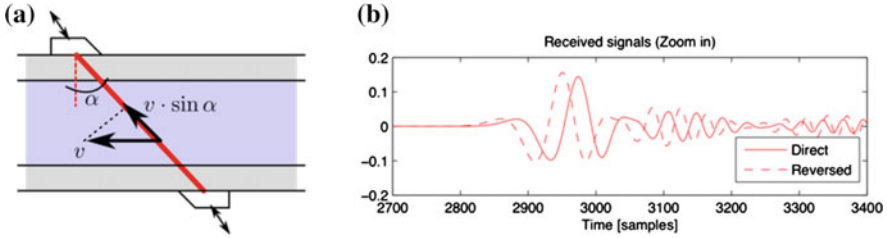

Fig. 9 Measurement configuration (**a**) and the received signals in the flow direction and counter-direction (**b**)

Another application of interest is the non-intrusive flow metering that consists of generating and receiving an acoustic signal in two ways: one—the acoustic signal is transmitted in the flow direction (Fig. 9a), second—in counter-direction [34]. Two such signals are presented in Fig. 9b.

Therefore, the difference of propagation times is $\Delta t_{propag} = t_{propag(r)} - t_{propag(d)}$ which is proportional to the flow rate [34]. The performance of flow rate metering is strongly dependent on the precision of propagation time estimation.

The envelope of the signal is classically obtained from the absolute value of the analytic signal. The transit time is estimated using the threshold [14]:

$$Th = \frac{mean\{Env\} + \max\{Env\}}{2} \qquad (15)$$

where Env is the envelope of the signal. This threshold is fixed to half value between the mean of the noise and the maximum detected value. This way of threshold selection shown practically efficiency and robustness [14].

This method, widely used by current flow metering techniques, is often affected by the inherent deformations of the envelope (due to the propagation) that influences the precision of propagation time (or time-of-flight) measurements.

As mentioned in [14], the effect of Eq. (15) is similar to the effect of the first order derivative in terms of signal's phase changes.

Figure 10 presents the results obtained using Hilbert transform and dynamic range norm. Hilbert transform was computed using the analytical signal, while the envelope was computed using Eq. (12). It can be noticed that the dynamic range norm provides a more accurate estimation of the signal's envelope. We apply on the envelopes the threshold proposed in Eq. (15). When applying different signal-to-noise ratios of real colored Gaussian noise, we succeeded to improve time estimation, therefore, the flow velocity—with at least 10 % (for 10 m/s water velocity) by using the $DR0$ measure instead of the Hilbert transform.

4.2 Monitoring Electrical Discharges

The appearances of electrical discharges in the equipments are often signs of a system which starts to develop faults. The detection and localization of the discharges sources are important operation in the field of predictive surveillance. This is the case of localization of electrical arcs present in solar panel requiring a definition of a multi sensor system, given the large perimeter of the surveillance. Localization based on the ultrasound transient signals is proposed in [33] by taking advantage of the VeSP processing of transient signals, as presented in Sect. 3.

The multi-sensor localizing system is formed of four acoustic sensors S_1, S_2, S_3 and S_4 placed in a 3D configuration as presented in Fig. 11.

Each sensor records the electrical arc coming from the photovoltaic panel. The experiments were done by placing the photovoltaic panel in the following position: $Ox = 0$, $Oy = 125$ and $Oz = -35$ cm, where O is the center of the arc locator system and the directions of the axis are presented in Fig. 11a.

In this configuration, the photovoltaic panel generated an electrical arc. All four sensors recorded the electrical arc. Then, several traditional methods (matched filtering with pre-recorded reference of an electrical arc, Wavelet, Spectrogram, Zero Crossing) were applied.

Statistical signal processing (Higher Order Statistics or Maximum Likelihood Estimation) can only detect the electrical arc (or any transient signal), but their use for localization is more problematic [35]. For the localization part, the estimation of time-of-arrival (TOA) is crucial. As shown in the following part, the TOAs are more accurately estimated from the RPA, conducting to a more precise localization.
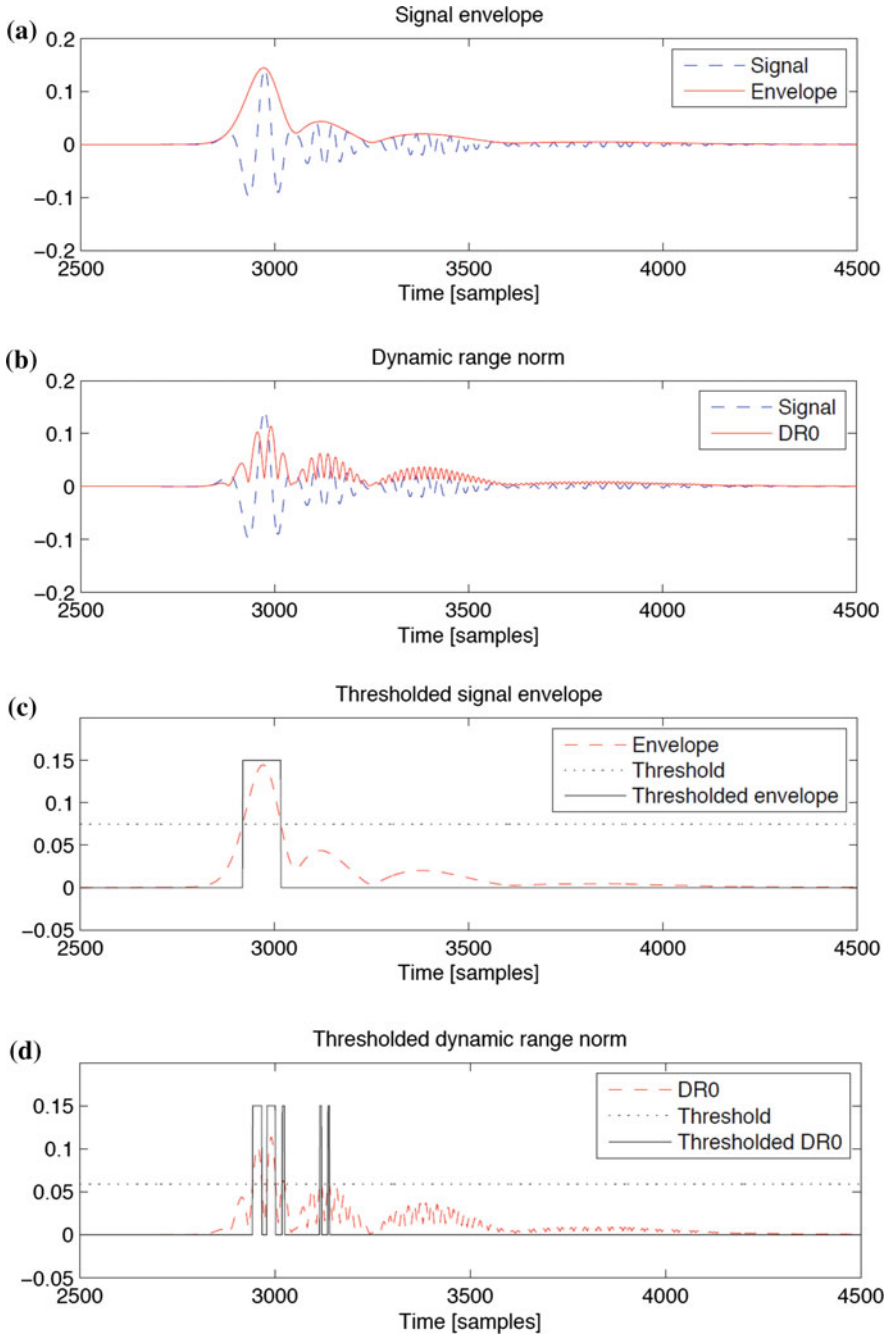
Fig. 10 Acoustic signal and the Hilbert envelope (**a**), respectively the dynamic range norm envelope (using $w = 13$ ($m = 4$, $d = 4$, $\varepsilon = 0.75$).) (**b**) and the threshold versions of the envelopes: Hilbert transform (**c**), dynamic range norm (**d**)
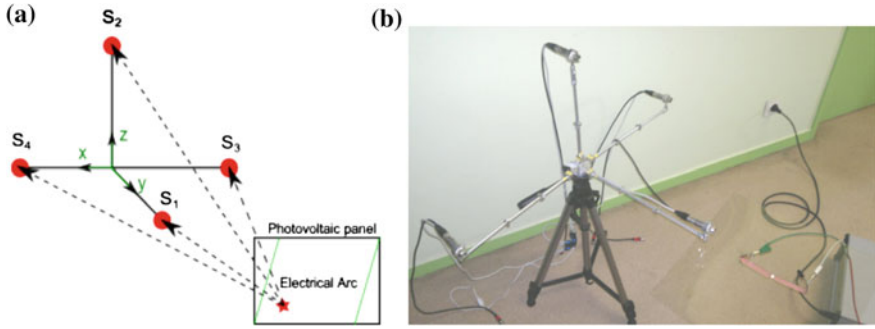
Fig. 11 The multi-sensor system for arc localization (**a**) and the experimental setup of the arc locator system (**b**)

It is obvious that each of the traditional methods manages to detect the presence of the electrical arc. For the localization part, the time of arrival of the electrical arc is determined.

The traditional methods were compared with the VeSP approach in terms of accuracy of time-of-arrival estimation.

The results for the VeSP approach were obtained using the $\overline{TDR_\varepsilon^{(w)}}(n)$ measure and they are presented in Fig. 12.

Space localization is obtained using the times of arrival at each sensor and was applied for each method. Knowing the speed of sound in the air, it is only a matter of geometry to exactly locate the source, as in Eq. (16):

$$\begin{cases} d_{S_1 P} - d_{S_2 P} = v \cdot t_{12} \\ d_{S_2 P} - d_{S_3 P} = v \cdot t_{23} \\ d_{S_3 P} - d_{S_4 P} = v \cdot t_{34} \end{cases} \tag{16}$$

where

$$d_{S_i P} = \sqrt{(x_{Si} - x_P)^2 + (y_{Si} - y_P)^2 + (z_{Si} - z_P)^2} \tag{17}$$

where $i = \overline{1,4} \cdot S_i (x_{Si}, y_{Si}, z_{Si})$. is the -th sensor of the arc locator system with its positions relative to the origin. $P(x_P, y_P, z_P)$ is the electrical arc position relative to the origin. v is the speed of sound in the air and $t_{i(i+1)} = t_i - t_{(i+1)}$, where t_i is the time of arrival of the electrical arc at sensor S_i.

Localization precision depends on the times of arrival obtained with each method and is presented in Fig. 13.

The best results, in terms of relative errors obtained from 16 experimental configurations (each of these configurations concerned around 100 trials), were obtained using the VeSP approach and the Matched Filter. Still, the latter presents the major drawback because it always needs a reference signal not available all the time.
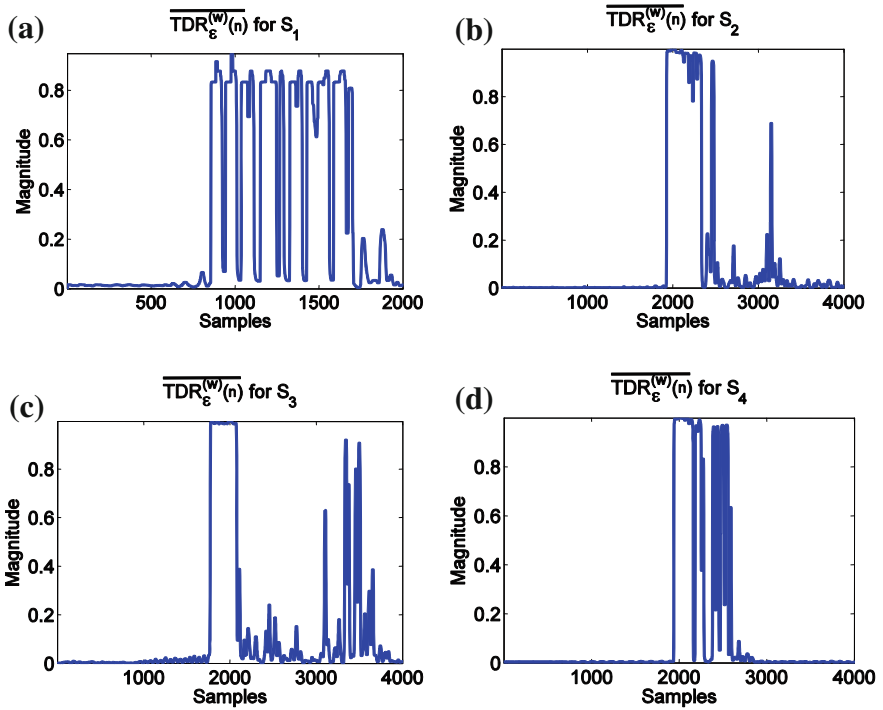
Fig. 12 The time detection curves [using $w = 17$ ($m = 3$, $d = 8$, $\varepsilon = 0.9$).] of the electrical arc recorded at each sensor: **a** the result for sensor S_1, **b** the result for sensor S_2, **c** the result for sensor S_3, a) the result for sensor S_4

It can be noticed that the VeSP approach offers more precise results than the conventional signal processing methods.

Table 1 The relative error for the localization precision obtained for each proposed method

Method	Relative error (%)
VeSP	4.8
Matched filter	5
Wavelet	10.4
Spectrogram	9
Zero crossing	9,8

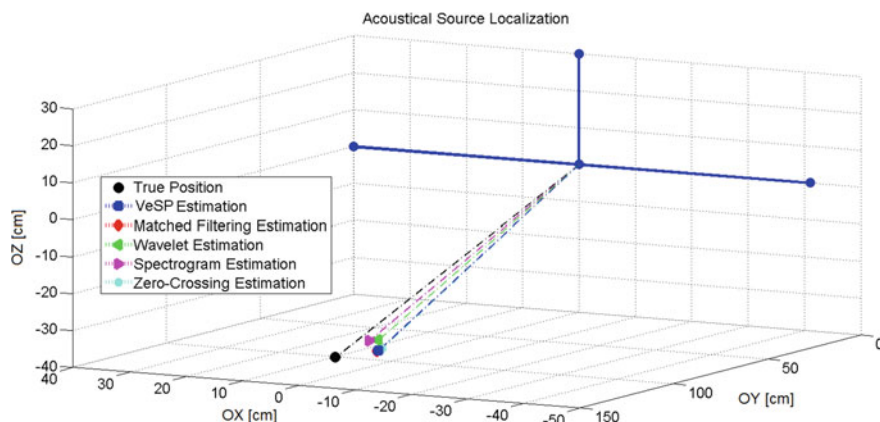**Fig. 13** The spatial localization obtained solving the geometrical system based on the times of arrival: *black*—real position of the electrical arc, *blue*—VeSP localization, *red*—Matched Filter localization, *green*—Wavelet localization, *pink*—Spectrogram localization, *cyan*—Zero Crossing localization

5 Discussion

The RP method offers new information in the analysis of non-stationary signals characterizing industrial or natural processes. When the process is driven by several parameters, many of them being hard to determine or control, the method is well suited.

According to [31], in applications where a reference signal is available, the matched filter method provides faster results with high accuracy even at a very low SNR. In this case, the RPA is also limited, as other signal analysis methods.

Another limitation of the method is given by the high number of samples contained in the recorded signal for non-stationary processes. This number depends on the sampling frequency which should be suited to the studied phenomena.

Future studies aim to use the RPA method in the context of adaptive waveform that best characterizes the physical process. As an example, the turbulence is a complex phenomena and the use of the RP method may bring new insight in this matter.

Also, we intend to implement the RPA signal processing measures in other programming languages than MATLAB which may overcome the limitations given by the increased memory demand and diminished speed computation.

6 Conclusions

This paper shows that the Recurrence Plot Analysis concept brings new tools in the world of signal processing. Through the interesting representations in the phase

space which are driven by measurements, one has new qualitative and quantitative information about the process under study.

The RP (VeSP) method proved to be flexible, allowing developing new distances and measures between the vectors from the phase space. As a central contribution, we mention the angular distance which is more powerful than the Euclidean distance, if the main interest is to characterize amplitude-varying signals. This characteristic may be very well exploited in the application of detecting transients and their reflections. This application presents a major interest in underwater environment, in high voltage cable monitoring, in radar, etc.

As we were able to demonstrate, the RP (VeSP) method is a very good alternative for detection and localization of transients in applications such as ultrasonic measurements and electrical discharge monitoring.

Future works will focus on the perspective of data-driven multi-resolution analysis and on correlating the parameters of the method with real physics phenomena. Nevertheless, this can only be done by extending the application area and validating the theory with real experiments.

References

1. Marwan, N.: A historical review of recurrence plots. Eur. Phys. J. Special Top. **164**(1), 3–12 (2008)
2. Eckmann, J.P., Kamphorst, S.O., Ruelle, D.: Recurrence plots of dynamical systems. Europhys. Lett. **5**(9), 973–977 (1987)
3. Zou, V.Y.: Exploring recurrences in quasiperiodic dynamical systems, PhD Dissertation, Universitat Potsdam (2007)
4. Sprott, J.C.: Some simple chaotic flows. Phys. Rev. Sect. E **50**(2), R647–R650 (1994)
5. Haverlock, D., Kuwavo, S., Vorlander, M.: Handbook of Signal Processing in Acoustics, pp. 1667–1833. Springer, New York (2008)
6. Cohen, L.: Time-Frequency Analysis. Prentice Hall, New Jersey (1999)
7. Mallat, S., Zhong, S.: Characterization of signals from multiscale edges. IEEE Trans. Pattern Anal. Mach. Intell. **14**(7), 710–732 (1992)
8. Fan, J., Yao, Q.: Nonlinear Time Series: Nonparametric and Parametric Methods. Springer, New York (2005)
9. Sprott, J.C.: Chaos and Time-Series Analysis. Oxford University Press, New York (2003)
10. Gao, J., Cao, Y., Gu, L., Harris, J., Principe, J.: Detection of weak transitions in signal dynamics using recurrence time statistics. Phys. Lett. A **317**, 64–72 (2003)
11. Gao, J., Cao, Y., Tung, W.W., Hu, J.: Multiscale Analysis of Complex Time Series: Integration of Chaos and Random Fractal Theory, and Beyond. Wiley, New Jersey (2007)
12. Marwan, N., Schinkel, S., Kurts, J.: Recurrence plots 25 years later—Gaining confidence in dynamic transitions. Europhys. Lett. **101**, 20007 (2013)
13. Serbanescu, A., Stanasila, O., Birleanu, F.M.: Nonlinear Analysis of Time Series. Military Technical Academy Publishing, Bucharest (2011)
14. Birleanu, F.M., Candel, I, Ioana, C., Gervaise, C., Serbanescu, A., Serban, G.: A vector approach to transient signal processing. In: The 11th Conference on Information Science, Signal Processing and their Applications, Montreal, Canada, 3–5 July 2012
15. Mallat, S.: A theory for multiresolution signal decomposition: the wavelet representation. IEEE Trans. Pattern Anal. Mach. Intell. **11**(7), 674–693 (1989)

16. Marwan, N., Romano, M.C., Thiel, M., Kurths, J.: Recurrence plots for the analysis of complex systems. Phys. Rep. **438**(5–6), 237–329 (2007)
17. Kantz, H., Schreiber, T.: Nonlinear Time Series Analysis. University Press, Cambridge (1997)
18. Thiel, M., Romano, M.C., Kurths, J., Meucci, R., Allaria, E., Arecchi, T.: Influence of observational noise on the recurrence quantification analysis. Phys. D **171**, 138–152 (2002)
19. Thiel, M., Romano, M.C., Read, P.L., Kurths, J.: Estimation of dynamical invariants without embedding by recurrence plots. Chaos **14**(2), 234–243 (2004)
20. Marwan, N., Kurths, J.: Nonlinear analysis of bivariate data with cross recurrence plots. Phys. Lett. A **302**, 299–307 (2002)
21. Misiti, M., Misiti, Y., Oppenheim, G., Poggi, J-M.: Wavelets Toolbox Users Guide, The Math-Works, Wavelet Toolbox, for use with MATLAB, 2000
22. Mallat, S.: A Wavelet Tour of Signal Processing, 2nd edn. Academic Press, New York (1999)
23. Popescu, F., Enache, F., Vizitiu, I.C., Ciotîrnae, P.: Recurrence plot analysis for characterization of appliance load signature. In: The 10th International Conference on Communications, Bucharest, Romania, 2014
24. Yang, H.: Multiscale recurrence quantification analysis of spatial cardiac vectorcardiogram (VCG) signals. IEEE Trans. Biomedical Eng. **58**(2), 339–347 (2011)
25. Chen, Y., Yang, H.: Multiscale recurrence analysis of long-term nonlinear and nonstationary time series. Chaos Solitons Fractals **45**(7), 978–987 (2012)
26. Ramirez Avila, G.M., Gapelyuk, A., Marwan, N., Stepan, H., Kurths, J., Walther, T., Wessel, N.: Classifying healthy women and preeclamptic patients from cardiovascular data using recurrence and complex network methods. Auton. Neurosci. Basic Clin. **178**(1-–2), 103–110 (2013)
27. Webber, C.L., Jr., Zbilut, J.P.: Recurrence quantification analysis of nonlinear dynamical systems. In: Riley M.A., Van Orden, G.C. (eds.) Tutorials in Contemporary Nonlinear Methods for the Behavioral Sciences Web Book, pp. 26–94, National Science Foundation (U.S.) 2005
28. Zbilut, J.P., Webber, C.L., Jr.: Recurrence quantification analysis. In: Akay, M. (ed.) Wiley Encyclopedia of Biomedical Engineering, Wiley, 2006
29. Farge, M.: Wavelet transforms and their applications to turbulence. Ann. Rev. Fluid Mech. **24**, 395–457 (1992)
30. Torrence, C., Compo, G.P.: A practical guide to wavelet analysis. Bull. Amer. Meteor. Soc. **79**, 61–78 (1998)
31. Digulescu, A., Petrut, T., Bertrand, G., Candel, I., Ioana, C., Serbanescu, A.: Advanced signal processing techniques for detection and localization of electrical arcs, In: The 10th International Conference on Communications, Bucharest, Romania, 2014
32. Zbilut, J.P., Marwan, N.: The Wiener-Khinchin theorem and recurrence quantification. Phys. Lett. A **372**(44), 6622–6626 (2008)
33. Digulescu, A., Candel, I., Dahmani, J., Deacu, D., Ioana, C., Gabriel, V.: Electric Arc Locator in Photovoltaic Power Systems using Advanced Signal Processing Techniques. Electronics in Marine, Zadar (2013)
34. Merzkirch, W., Gersten, K., Peters, F., Ram, V.V., von Lavante, E., Hans, V.: Fluid Mechanics of Flow Metering. Springer, Berlin (2005)
35. Candel, I., Digulescu, A., Ioana, C., Serbanescu, A., Sofron, E.: Optimization of partial discharge detection in high voltage cables based on advanced signal processing techniques. In: The 11th Conference on Information Science, Signal Processing and their Applications, Montreal, Canada, 3–5 July 2012

A Recurrence-Based Approach for Feature Extraction in Brain-Computer Interface Systems

Luisa F. S. Uribe, Filipe I. Fazanaro, Gabriela Castellano, Ricardo Suyama, Romis Attux, Eleri Cardozo and Diogo C. Soriano

Abstract The feature extraction stage is one of the main tasks underlying pattern recognition, and, is particularly important for designing Brain-Computer Interfaces (BCIs), i.e. structures capable of mapping brain signals in commands for external devices. Within one of the most used BCIs paradigms, that based on Steady State Visual Evoked Potentials (SSVEP), such task is classically performed in the spectral domain, albeit it does not necessarily provide the best achievable performance. The aim of this work is to use recurrence-based measures in an attempt to improve the classification performance obtained with a classical spectral approaches for a five-command SSVEP-BCI system. For both recurrence and spectral spaces, features

---

L.F.S. Uribe · R. Attux · E. Cardozo
Department of Computer Engineering and Industrial Automation (DCA/FEEC),
University of Campinas (UNICAMP), Av. Albert Einstein, 400,
Campinas, SP 13083-852, Brazil
e-mail: lsuarez@dca.fee.unicamp.br

R. Attux
e-mail: romis@dca.fee.unicamp.br

E. Cardozo
e-mail: eleri@dca.fee.unicamp.br

G. Castellano
Neurophysics Group, Deptartment of Cosmic Rays and Chronology,
Institute of Physics Gleb Wataghin (IFGW), UNICAMP, Rua Sérgio Buarque de Holanda,
777, Campinas, SP 13083-859, Brazil
e-mail: gabriela@ifi.unicamp.br

F.I. Fazanaro · R. Suyama · D.C. Soriano (✉)
Centro de Engenharia, Modelagem e Ciências Sociais Aplicadas (CECS),
Universidade Federal do ABC, Avenida dos Estados, 5001, Santo André, SP 09210-580, Brazil
e-mail: diogo.soriano@ufabc.edu.br

F.I. Fazanaro
e-mail: filipe.fazanaro@ufabc.edu.br

R. Suyama
e-mail: ricardo.suyama@ufabc.edu.br

were selected using a cluster measure defined by the Davies-Bouldin index and the classification stage was based on linear discriminant analysis. As the main result, it was found that the threshold ε of the recurrence plot, chosen so as to yield a recurrence rate of 2.5 %, defined the key discriminant feature, typically providing a mean classification error of less than 2 % when information from 4 electrodes was used. Such classification performance was significantly better than that attained using spectral features, which strongly indicates that RQA is an efficient feature extraction technique for BCI.

1 Introduction

The main objective of a Brain-Computer Interface (BCI) is to provide an alternative communication channel for human beings without using the classical biological efferent pathways. In the last decade, these systems have experienced a remarkable development due to the greater availability of low cost instrumentation and computational resources [1, 2]. In particular, the use of BCI in the context of assistive technology is very important for people suffering from stroke, spinal cord injury, degenerative disorders (e.g. amyotrophic lateral sclerosis), and any conditions that impose drastic limitations to communication and mobility [3]. Presently, it is estimated that, only in Europe, there are almost 300 thousand people with spinal cord injury (SCI), with eleven thousand new injuries occurring every year [4]. Moreover, approximately 40 % of the total population of patients with SCI are quadriplegics and it is known that loss of motor functions significantly decreases the quality of life [2].

To accomplish a rehabilitation purpose, BCI systems typically consist of well-characterized components, being signal acquisition, processing and feedback stages the main ones, as illustrated in Fig. 1. Within this general scheme, the typical approach for brain signal acquisition relies on the recording of surface EEG, being the processing and feedback stages strongly dependent on the adopted BCI paradigm [1]. The BCI paradigm refers to the process of inducing a stable electrical pattern in the brain to be detected and recognized, being finally associated with an external command. A classical example is that of task imagery, i.e. the request to perform a mental task associated with well-defined motor actions, something that can be detected in a specific cortical area (e.g. the motor cortex) and, in general, suitably classified. Another commonly employed BCI paradigm can be formulated in terms of evoked potentials, such as those present in the P300 response—a potential elicited by the process of focusing attention in events occurring with low probability—and the Steady State Visual Evoked Potentials (SSVEP) [1].

In the SSVEP paradigm, different commands (like those defining the direction of the movement of a wheel-chair) are presented to the user as visual stimuli flickering with different frequencies, and the user is requested to focus on the command that he/she wants to perform. In this case, the electrical activity of the visual cortex tends
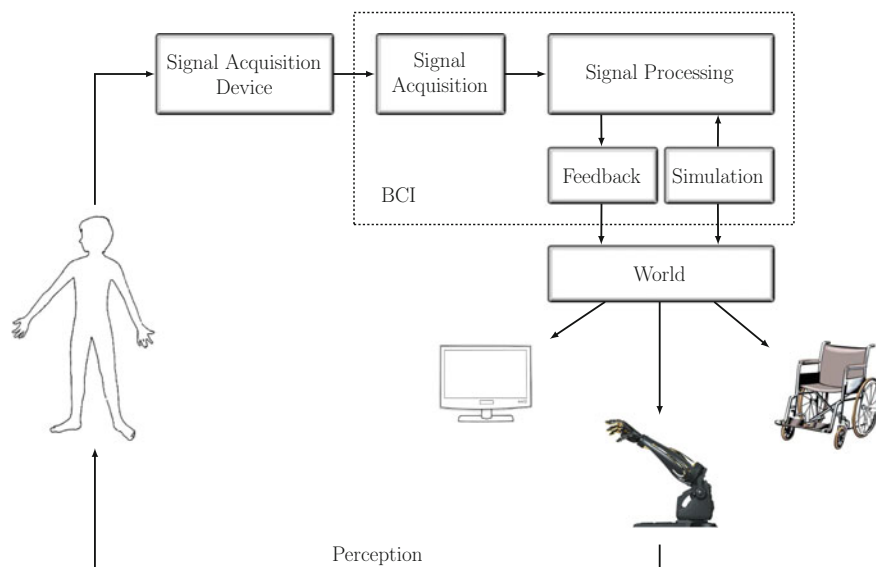
Fig. 1 A general BCI system

to synchronize with the visual stimulus chosen by the user and a simple spectral analysis can be used in order to identify the command selected by the person [5].

Once the BCI paradigm has been defined, the processing and feedback can also be specified in a more precise manner. Most works use a structure composed of feature extraction, feature selection and classification stages. These stages are essential for performing pattern recognition and classification, being thus crucial to define the external command.

Although classical spectral analysis is widely used for feature extraction in SSVEP-BCI systems, it can lead to non-optimal classification results depending on the employed visual stimulation apparatus or require a large amount of data for suitably training the classifier. In this chapter, a new recurrence-based feature extraction approach for BCI systems based on the SSVEP paradigm is presented. It is shown here that the threshold ε of the Recurrence Plot (RP), defined so as to match a specific Recurrence Rate (RR), is the key feature to separate the classes (which correspond to the commands), providing a better performance in comparison to a strategy based on spectral analysis. The results are indicative of the potential of recurrence analysis in the context of BCI, raising quite interesting application perspectives.

This work is organized as follows: Sect. 2 presents the instrumentation and the experimental procedure employed in the context of the BCI system used here. This section also briefly introduces the signal processing techniques explored for feature extraction, feature selection and classification. Section 3 exhibits the system performance (in terms of mean classification error) when the proposed recurrence-based
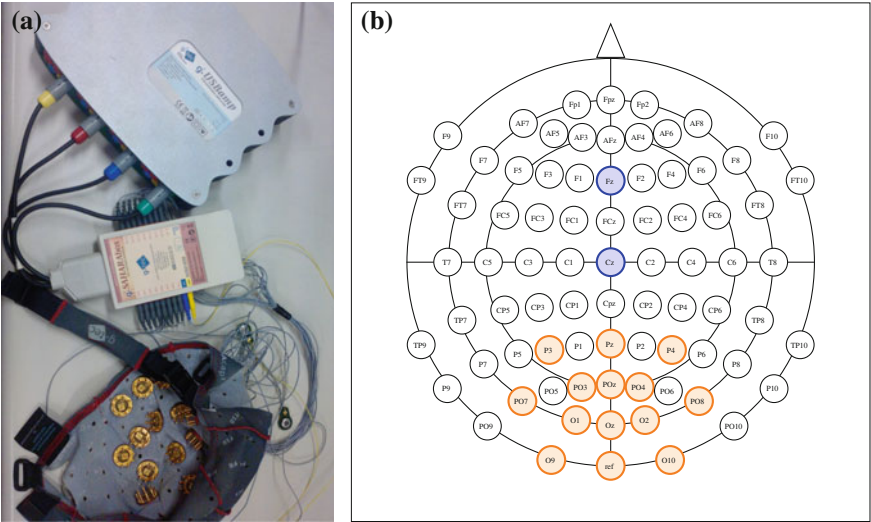
approach is employed and a comparison with different feature selection heuristics
operating in the spectral domain. Finally, this chapter is concluded with a discussion
about the developed ideas and potential extensions.

2 Methods

2.1 Experimental Setup and Experimental Procedure

In the performed experiments, the brain signals were acquired by means of surface
EEG [1], due to its simplicity and non-invasive character. For the acquisition, digiti-
zation and amplification of the EEG signals, the g.USBamp system of the g.tec com-
pany[1] was employed. This device allows the simultaneous capture of 16 channels,
with 24-bit resolution each, through a USB 2.0 connection to a desktop computer.
The device is shown in Fig. 2a.

The EEG was recorded using 16 dry electrodes with 8-pin each (the g.SAHARA
g.tec system), which are built using a special gold alloy (see Fig. 2a). These electrodes
were placed in 16 locations defined by the international 10–20 system [1], which
were chosen in accordance with the SSVEP response (i.e. emphasizing signals in the
visual cortex): Fz, Cz, Pz, Oz, PO3, PO4, O1, O2, P3, P4, Iz, POz, PO7, PO8, O9,
O10. Furthermore, two reference electrodes were placed in each mastoid. Figure 2b

Fig. 2 **a** Equipment and configuration for EEG signals capture. In **b** the *orange circles* represent
the visual cortex region and the *blue circles* define other interesting positions along the medial
longitudinal fissure

---

illustrates the cap layout, in which the letters F, T, C, P and O correspond, respectively, to the frontal, temporal, central, parietal and occipital lobes, with odd numbers used to reference the left hemisphere and even numbers the right one.

Before starting the acquisition session, it was ensured that all electrodes had impedance values below $5\,k\Omega$, which represents a common limit employed during EEG recordings. The amplifier was configured with a bandpass filter of 0.1–60 Hz and a notch filter at 60 Hz for all EEG channels, in order to cancel out DC components interference and noise. A sampling frequency of 128 Hz was used throughout all acquisitions.

In order to register the signals, the BCI2000 software[2] was employed. This software is particularly interesting due to its ability to create different experiments with multiple settings for capturing the data, which were first stored in files with a specific BCI2000 format and subsequently imported by MATLAB, in which functions from the statistical signal processing toolbox were used.

To carry out the visual stimulation, a set of four light-emitting diodes (white LEDs) was used, driven in four different frequencies, namely 13, 18, 21 and 25 Hz. These values were chosen in view of previous studies that showed strong SSVEP responses evoked in this range [5].

Three healthy subjects (ages 21, 25, 28; one woman) with no previous history of neurological diseases participated in this study. The study was approved by the ethics committee of University of Campinas, and all subjects signed an informed consent previous to data acquisition. Subjects sat on a comfortable chair placed at a distance of 0.5 m both from the LEDs and the computer screen. The same ambient light level was maintained during the execution of all experiments. Figure 3a, b show, respectively, the LED set-up and the interface used in the BCI2000 software for the execution of the experiments and for the capture of data.

For every subject, four different sessions for data acquisition were held five minutes apart from each other. The sessions comprised four separate runs interleaved by a pause of one minute. The last session had only three runs.
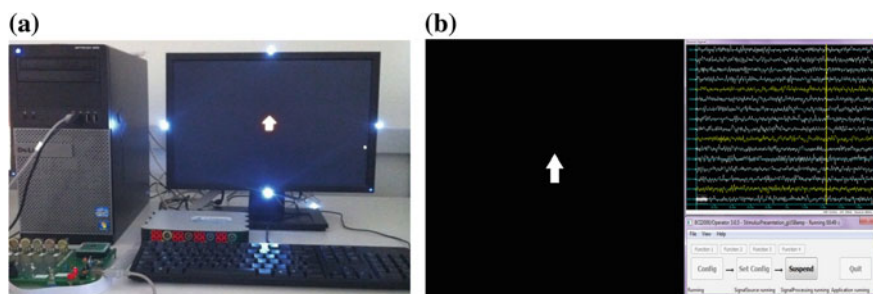

Fig. 3 **a** Visual stimulation platform used to evoke the SSVEP response. **b** Interface requesting the user to focus on a specific LED

Each run was composed of 25 trials associated with 5 different tasks (four visual stimuli plus no command). Therefore, there were a total of $15 \times 25 = 375$ trials per subject, with $375/5 = 75$ the total number of trials for each task. Subjects were instructed to stay still during every run.

Each image was continuously displayed during 6 seconds. After this period of time, the screen went blank for 1.5 s before the next image appeared. During the resting condition, the subject could rest the eyes. The pause period between each run was long enough to allow the subject to stretch and move around.

2.2 Signal Processing Techniques

After the EEG signals were acquired, a pre-processing stage took place, consisting in the normalization of each recorded time series with respect to the maximum absolute value found therein. Thereafter, feature extraction was performed with the aim of representing each trial of a given electrode in a suitable space, which, in this work, may correspond to either the recurrence or the spectral domain.

The recurrence domain is defined by Recurrence Quantification Analysis (RQA) measures obtained for a given trial. As described by [6], the classical RQA measures correspond to the percentage of determinism (DET), the entropy of the diagonals (ENTR) and the length of the longest diagonal of the map (LMAX) (excluding the main diagonal). The L-∞ norm was used for quantifying the distance between the points in the reconstructed state space, given its lower computational cost [6]. An adaptive recurrence plot was used to minimize the recurrence plot variability, thus avoiding inappropriate choices of ε and providing a better comparison between maps from different EEG electrodes. The RP parameters were defined after a preliminary analysis concerning the use of a variable threshold as reported in [7, 8]. The threshold ε of the map was defined to match a Recurrence Rate (RR) of 2.5 %—with an embedding dimension $m = 5$ and a time delay $\tau = 5$—being also employed as a feature. The DET measure was calculated for different diagonal intervals, being DET1 associated with the percentage of determinism related to diagonal lengths from 5 to 10, DET2 from 5 to 15, DET3 from 10 to 15, DET4 from 10 to 20, DET5 from 15 to 20, DET6 from 15 to 25. This partition is useful to detect deterministic sources with different characteristics [9]. In general, the diagonals obtained in the recurrence plot were small, which justifies the upper limit established by DET6.

The spectral attributes were determined using the classical Welch method for computing the Power Density Spectrum (PDS). In this approach, each trial was divided into 8 sub-blocks of identical length (with 170 points each) using a Hamming window function with 50 % superposition, i.e. with an amount of 85 overlapping points. Each block was once again divided in segments of 128 points: padding with zeros the last segment and wrapping them, the Discrete Fourier Transform (DFT) of each of the eight segments was obtained—implying in a spectral resolution of 1 Hz— and the square of its absolute value calculated, followed by the average concerning all sub-blocks. For implementation details, see [10, 11].

The feature selection stage was implemented based on the cluster measure defined by the Davies-Bouldin (DB) index [12]. This measure combines in a single expression two main relevant aspects of data clustering: the minimization of the intraclass distance and the maximization of the distance between classes, which can be mathematically described by:

$$\text{DB} = \frac{1}{M} \sum_{i=1}^{M} \max_{i \neq j} \left[\frac{\text{diam}(C_i) + \text{diam}(C_j)}{d(\mu_i, \mu_j)} \right] \tag{1}$$

where $d(\mu_i, \mu_j)$ is the distance between the centers of classes i and j, diam (C_i) is the maximum distance between all pairs of samples in class i, and M is the number of classes. Hence, low values of the DB index indicate good class discrimination, while higher values indicate less favorable scenarios. For this reason, the inverse of the DB index was employed as a rank measure (DBINV), being each class defined by the set of trials labeled with the same visual stimulus.

Finally, the classification stage was based on Linear Discriminant Analysis (LDA) [13], since it is straightforward to implement, fast to train and widespread in the BCI literature (see, for instance, [14]). In this approach, a linear combination $\mathbf{w}$ of the features $\mathbf{x}$ that better separates the classes is found, providing a decision surface in the form: $\mathbf{w}^T \mathbf{x} + c = 0$, for a threshold c. Considering two normal multivariate distributed classes with means μ_1 and μ_2 and covariance matrices C_1 and C_2, respectively, the LDA approach consists in finding the weights $\mathbf{w}$ that maximize the ratio concerning the variance between the classes and the variance within the classes:

$$S = \frac{\sigma_{between}^2}{\sigma_{within}^2} = \frac{(\mathbf{w}^T (\mu_1 - \mu_2))^2}{\mathbf{w}^T (C_1 + C_2)\mathbf{w}}. \tag{2}$$

It is possible to show that this criteria is satisfied for $\mathbf{w} \propto (C_1 + C_2)^{-1}(\mu_1 - \mu_2)$ and the threshold c is given by $\frac{1}{2}\mathbf{w}^T(\mu_1 + \mu_2)$. Once the training stage has been performed, trials with attribute vectors $\mathbf{x}$ are classified according to their position in the attribute space relative to the achieved decision hyperplane. The multi-class case was treated here analyzing all pairs of classes.

3 Results

Built in accordance with the experimental setup described in Sect. 2, Fig. 4 shows a typical DBINV map containing the main relevant features for class separation in spectral (Fig. 4a) and in recurrence-based attribute spaces (Fig. 4b), obtained for subject S1.

Some important conclusions can be drawn from the results shown in Fig. 4. For instance, it can be clearly noted that the electrode O9 was the one with best separation performance for both spectral and recurrence-based approaches for this specific
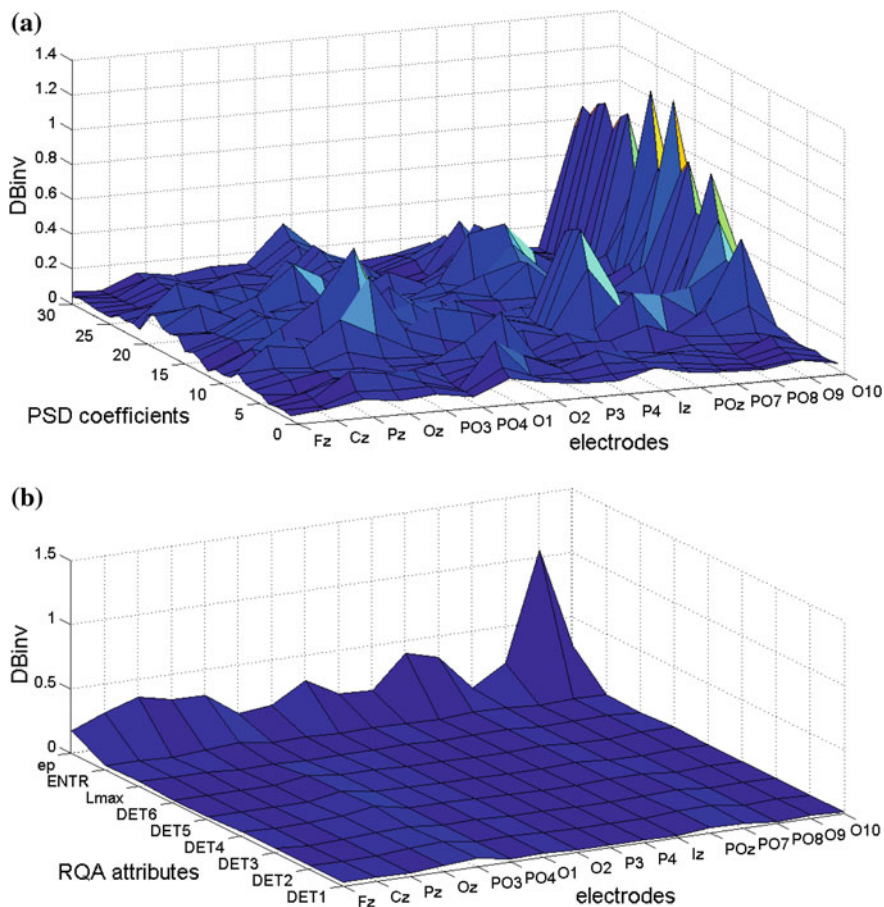
(a)

(b)

Fig. 4 Discriminant analysis using the inverse of the Davies-Bouldin index for **a** spectral and **b** recurrence attributes associated to S1. In this last figure, the threshold ε of the map is denoted by ep

subject. Effective separability was also attained with the Iz electrode in both attribute spaces. These locations completely agreed with the main cortical areas activated in SSVEP experiments, and, usually, the same promising electrode positions were identified in both attribute spaces analyzed here, despite there being a great variability concerning the achieved positions for different subjects, as commonly observed in BCI experiments.

Furthermore, Fig. 4b reveals that the threshold ε of the map was an effective attribute for separating the classes, the classical RQA measures having not reached a similar performance. This is a result observed for all subjects and probably follows from the adaptation of the recurrence plot in order to match a specific recurrence rate, a scenario that favors the adapted variable ε when comparing different recurrence patterns. The adoption of an adaptive recurrence plot is justified by the great

variability of the obtained signals, which made it difficult to find a general choice of a fixed ε for obtaining suitable recurrence plots.

Another particular RQA advantage was that the relevant features were much more concentrated—in terms of the number of attributes—in the recurrence scenario than in the spectral domain, which simplifies the automatic selection. For instance, if we consider class dispersion in the feature space, it is clear that the combination of the best PSD attributes with higher DBINV values could lead to correlated features with bad discrimination performance (Fig. 5a). On the other hand, the selection of the best PSD attributes considering different electrodes (selected by ranking the sum of all their respective PSD coefficients) can be more informative for separation (Fig. 5b). However, a clearly better separation scenario was attained in the recurrence-based attribute space as shown in Fig. 5c. In this case, note that both Fig. 5c and b used information from electrodes O9 and Iz, but class "down" (red points concentrated at the origin) was much more close to the "rest" state in the spectral domain, there also being intersections of other states in general. In fact, the classification error attained in Fig. 5b was 16.49 %, while in Fig. 5c this measure dropped to 3.81 %, i.e. 4 times
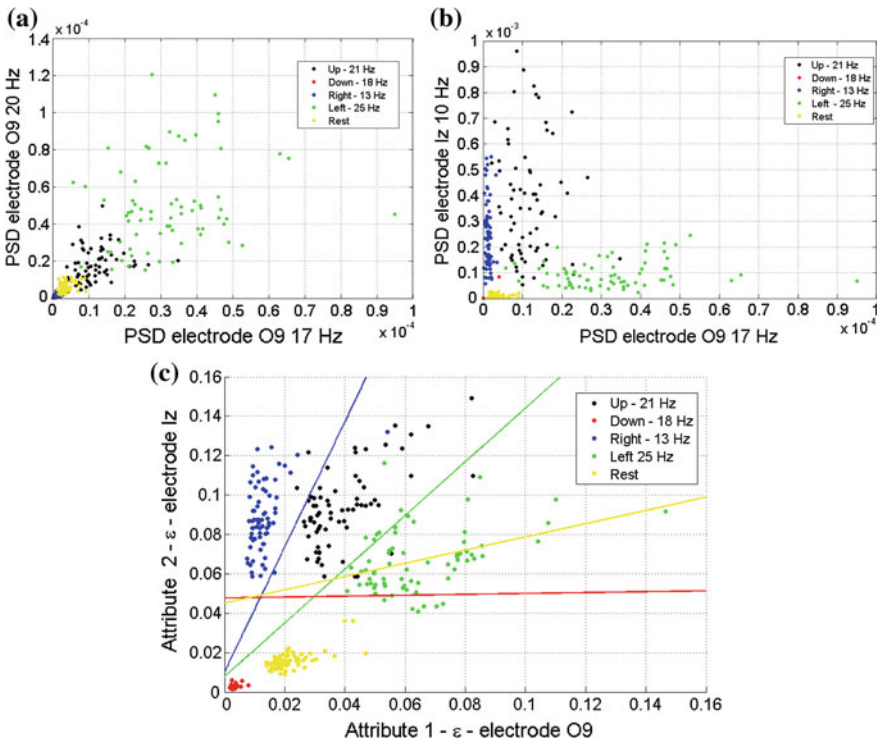

Fig. 5 Classes dispersion for **a** spectral attributes just ranked by DBINV measure; for **b** the best PSD attributes in the most promising electrodes according to DBINV value; and for **c** recurrence-based attributes domain associated to S1

lower. In this last case, the decision hyperplanes that separate class 1 ("up" state) from class i, with $i = 2, 3, 4, 5$ (in which the hyperplane color is associated with the color of the respective class), are shown, in order to illustrate the attribute space partition and that only few classification mistakes were made.

In addition to the classification performance attained here, the results described in Fig. 5 show that the recurrence analysis allowed the adoption of a simple heuristic for combining the features i.e. taking the attained ε for matching a specific recurrence rate ranked by DBINV index, while the analysis on the spectral domain would require a multi-objective optimization approach: a search that maximizes the DBINV measure, and, at the same time, minimizes the correlation between the selected attributes, which naturally poses a more complex task.

In order to investigate the classification performance in these different spaces, some simple heuristics for attribute selection were established. The first one consisted in simply taking the RQA features ranked by the DBINV index (black dots in Fig. 6). The second heuristic took the features ranked with the DBINV measure in the spectral domain (red dots in Fig. 6). The third ranked the electrodes according to the sum of the DBINV index of all frequency coefficients for that electrode and selected the PSD coefficients in the frequency of the visual stimulation (i.e. 13, 18, 21 and 25 Hz - blue dots in Fig. 6). The fourth heuristic ranked the electrodes such as in the third one and took the PSD coefficient with highest DBINV value for each electrode (green dots in Fig. 6). In all cases, the number of attributes was progressively increased and a k-fold cross-validation scheme was used to evaluate the mean classification error [13].

The evolution of the mean classification error can be observed in Fig. 6 for all subjects. It can be clearly noted that the recurrence-based attributes (specifically the threshold of the map that corresponds to the first 16 attributes) drastically dropped the classification error to lower than 10 % when 5 attributes were used and practically to 0 % with less than 8 features. In general, the performance achieved in the spectral domain was lower, with a mean classification error lower than 10 % attained only when more than 20 attributes were used in both second and third heuristics. The fourth heuristic took, progressively, the best PSD coefficients for different electrodes previously ranked, providing the better spectral scenario. Note that after using all the best coefficients of the 16 electrodes, this approach just attained a classification performance close to the recurrence scenario for S2 and a difference around 5 % for S1 and S2. In summary, using the best feature for different electrodes led to a faster convergence towards the minimal error and a better final performance in the recurrence-based attribute space.

Finally, a clear difference between the heuristics used for feature selection in the spectral domain can be also noted. Concerning heuristics 2 and 3, the free selection based on the DBINV score provided, at first, a better classification performance with a faster drop in the mean classification error, which was overcome by the selection based on the coefficients associated with the visual stimulation frequencies when few electrodes were taken into account (2 or 3 for all subjects). Interestingly, the best spectral scenario (heuristic 4) established that just the selection of the best PSD coefficient of each electrode could provide a low classification error (around 5 %) without requiring information concerning all the visual stimulation frequencies as
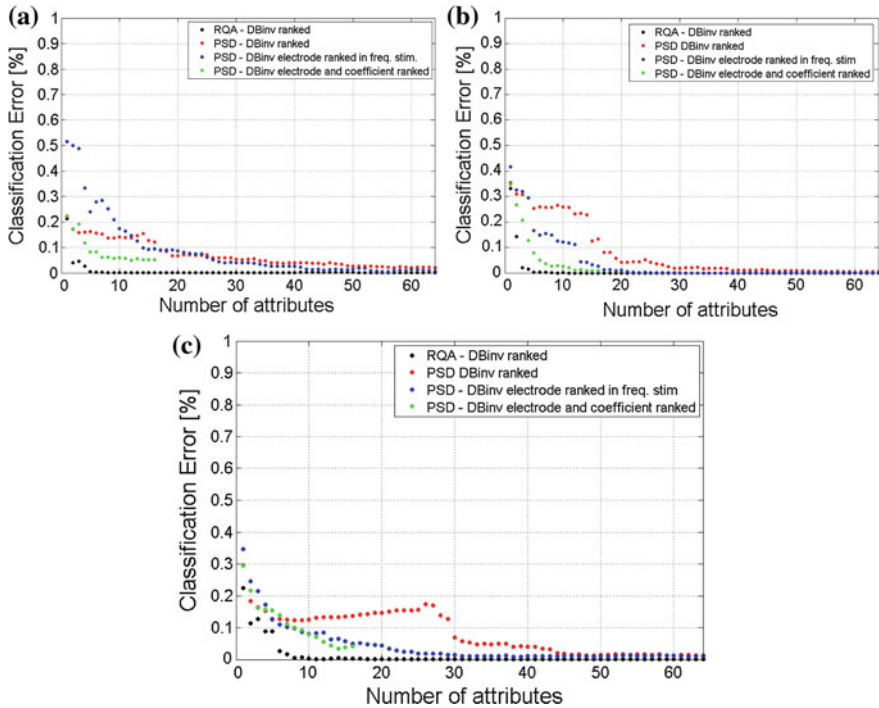
Fig. 6 Evolution of the classification error for a progressive increase in the number of attributes concerning the three aforementioned heuristics for subjects **a** 1, **b** 2 and **c** 3

commonly used in SSVEP- BCI systems. Such information could be helpful for designing BCI systems with just a few trials for training.

4 Discussion and Conclusions

In this work, the problem of efficient feature extraction for pattern recognition in SSVEP-based BCI was addressed. The obtained results clearly indicates the potential of using RQA in this task: it reached, indeed, a better performance than classical spectral analysis, commonly employed in this context. Curiously, it was found that the threshold of the recurrence plot was the key attribute to perform the class separation, which reveals the versatility of this complexity measure. In fact, if, on the one hand, the classical RQA measures are related to the diagonal structures in the RP and its generative deterministic rule [6], on the other hand, the recurrence rate is intrinsically associated with the quadratic Rényi entropy and other important information-theoretic measures can also be derived from it [6, 15].

In the present experiment, when the quadratic Rényi entropy is fixed (as a consequence of fixing the RR), the different attained recurrence plot thresholds reflect a particular metric of the recurrence structure of the signals that explain a fixed number of points. Note that this measure resembles that derived from the estimation of the correlation sum as introduced by [16] for the determination of the correlation dimension (D_2). In fact, the method used here just fixes the recurrence rate and makes use of the threshold for comparison between the different classes, instead of doing the opposite, when different thresholds define recurrence rates and a curve fit is used for obtaining D_2 in the classical approach [6, 16]. Interestingly, the procedure adopted here allowed overcoming the variability of EEG signals (and the recurrence plot drawbacks associated with it), and, at the same time, providing a better characterization of the temporal signal structure. The characterization of EEG signals in terms of the correlation dimension or nonlinear time series analysis has already been performed in the literature [17, 18], and the present work defines a particular application in the BCI context.

As a main drawback to the proposed recurrence-based approach, it can be mentioned the computational cost associated with the evaluation of an adaptive recurrence plot for this purpose, since BCI systems usually require a fast signal processing framework for real-time operation. Such limitation emphasizes the requirement for fast (dedicated) platforms for recurrence analysis, defining a natural extension to this work. The application of RQA for other BCI paradigms (e.g. motor imagery) also outlines a trend for future investigation.

References

1. Wolpaw, J., Wolpaw, E.W.: Brain-Computer Interfacing: Principles and Practice. Oxford University Press, New York (2012)
2. Wolpaw, J.R., Birbaumer, N., McFarland, D.J., Pfurtscheller, G., Vaughan, T.M.: Brain-computer interfaces for communication and control. Clin. Neurophysiol. **113**(6), 767–791 (2002). doi:10.1016/S1388-2457(02)00057-3
3. Millán, J.R., Rupp, R., Mueller-Putz, G., Murray-Smith, R., Giugliemma, C., Tangermann, M., Vidaurre, C., Cincotti, F., Kubler, A., Leeb, R., Neuper, C., Mueller, K.R., Mattia, D.: Combining brain-computer interfaces and assistive technologies: state-of-the-art and challenges. Front. Neurosci. **4**(161), 1–15 (2010). doi:10.3389/fnins.2010.00161
4. Sobani, Z.A., Quadri, S.A., Enam, S.A.: Stem cells for spinal cord regeneration: current status. Surg. Neurol. Int. **1**(1), 93 (2010). doi:10.4103/2152-7806.74240
5. Zhu, D., Bieger, J., Garcia Molina, G., Aarts, R.M.: A survey of stimulation methods used in SSVEP-based BCIs. In: Computational Intelligence and Neuroscience 2010, 702,357 (2010). doi:10.1155/2010/702357

6. Marwan, N., Romano, M.C., Thiel, M., Kurths, J.: Recurrence plots for the analysis of complex systems. Phys. Rep. **438**(5–6), 237–329 (2007). doi:10.1016/j.physrep.2006.11.001

7. Marwan, N.: How to avoid potential pitfalls in recurrence plot based data analysis. Int. J. Bifurcat. Chaos **21**(4), 1003–1017 (2011). doi:10.1142/S0218127411029008

8. Zbilut, J.P., Zaldívar-Comenges, J.M., Strozzi, F.: Recurrence quantification based Liapunov exponents for monitoring divergence in experimental data. Phys. Lett. A **297**(3–4), 173–181 (2002). doi:10.1016/S0375-9601(02)00436-X

9. Soriano, D.C., Suyama, R., Ando, R.A., Attux, R., Duarte, L.T.: Blind source separation in the context of deterministic signals. In: Eisencraft, M., Suyama, R., Attux, R. (eds.) Chaotic Signals in Digital Communications, pp. 325–348. CRC Press, Boca Raton (2013). doi:10.1201/b15473-13

10. Semmlow, J.: Signals and Systems for Bioengineers, 2nd edn. Academic Press, Amsterdam (2011)

11. Stoica, P., Moses, R.L.: Introduction to Spectral Analysis, Prentice-Hall, Upper Saddle River (1997)

12. Davies, D.L., Bouldin, D.W.: A cluster separation measure. IEEE Trans. Pattern Anal. Mach. Intell. **PAMI–1**(2), 224–227 (1979). doi:10.1109/TPAMI.1979.4766909.

13. Theodoridis, S., Koutroumbas, K.: Pattern Recognition, 2nd edn. Academic Press, New York (1999)

14. Perez, J.L.M., Cruz, A.B.: Linear discriminant analysis on brain computer interface. In: IEEE International Symposium on Intelligent Signal Processing, 2007. WISP 2007, pp. 1–6 (2007). doi:10.1109/WISP.2007.4447590

15. Prichard, D., Theiler, J.: Generalized redundancies for time series analysis. Phys. D **84**(3–4), 476–493 (1995). doi:10.1016/0167-2789(95)00041-2

16. Grassberger, P., Procaccia, I.: Measuring the strangeness of strange attractors. Phys. D **9**(1–2), 189–208 (1983). doi:10.1016/0167-2789(83)90298-1

17. Acharya, R., Faust, O., Kannathal, N., Chua, T., Laxminarayan, S.: Non-linear analysis of EEG signals at various sleep stages. Comput. Methods Programs Biomed. **80**(1), 37–45 (2005). doi:10.1016/j.cmpb.2005.06.011

18. Stam, C.J.: Nonlinear dynamical analysis of EEG and MEG: review of an emerging field. Clin. Neurophysiol. **116**(10), 2266–2301 (2005). doi:10.1016/j.clinph.2005.06.011

Response to Active Standing of Heart Beat Interval, Systolic Blood Volume and Systolic Blood Pressure: Recurrence Plot Analysis

Hortensia González, Oscar Infante and Claudia Lerma

Abstract   Recurrence quantitative analysis (RQA) indexes of beat-to-beat heart-beat interval and systolic blood pressure (SBP) have helped to understand the dynamical response to active standing. The peripheral blood volume is another variable of the cardiovascular control system with a crucial role during active standing since re-distribution of blood volume is necessary to counteract the gravity force and to provide enough blood supply to vital organs. Beat-to-beat photoplethysmographic systolic blood volume (SBV) oscillations may be useful to study the cardiovascular control if it is considered as a regulatory system with relevant local differences compared to blood pressure regulation. There are no previous reports of the SBV dynamical response to active standing. In this work we study simultaneously the dynamical response of heart-beat interval, SBP and SBV to active standing through comparison of RQA indexes evaluated during supine position and during active standing in 19 healthy volunteers. We show that in response to orthostatic stress, SBV oscillations have dynamic changes similar, but not identical, to SBP and the heart-beat interval. This suggests that these three variables are complementary for a better evaluation of the cardiovascular dynamics.

1 Introduction

The heart-beat varies after every single cycle (heartbeat, i.e. beat-to-beat), in order to adjust itself to the continuously changing living conditions that an organism must face. Although the heart possesses its own intrinsic cardiac nervous system with

H. González (✉) · O. Infante · C. Lerma
Laboratorio de Biofísica de Sistemas Excitables Facultad de Ciencias,
Universidad Nacional Autónoma de México, Av. Universidad 3000,
04510 Tlalpan, D.F., Mexico
e-mail: hortecgg@ciencias.unam.mx

O. Infante · C. Lerma
Departamento de Instrumentación Electromecánica,
Instituto Nacional de Cardiología Ignacio Chávez,
Juan Badiano 1, 14080 Tlalpan, D.F., Mexico
e-mail: infosc@cardiologia.org.mx

C. Lerma
e-mail: dr.claudialerma@gmail.com

thousands of neurons of diverse type, it has to coordinate with and integrate to the information coming from the entire body [1]. We know that this is done mainly by the autonomous nervous system (ANS) via its two subdivisions: sympathetic and parasympathetic, each of them with complementary and apparently reciprocal functions and their characteristic medium lag activation and fast inhibition. However the two branches of the ANS are not algebraically additive. Instead they interact in a dynamic fashion and either reciprocity or co-activation of both branches may occur [2]. Besides all this, there are upper coordination centers at the central nervous system, and our bodies count on long term regulatory processes like endocrine or paracrine systems; short term mechano-sensorial signals to communicate the degree of effort or total mechanical work done and demanded; and metabolic sensors that detect oxygen, glucose or ATP availability in every single cardiac cycle [2–4].

Given all the afore mentioned factors participating in heart rate regulation, it is useful to count with a well-described autonomic stress paradigm as is the change from the supine to the standing position (orthostatism), which is associated to a reduction in vagal outflow to the sinus node and with an increase in sympathetic nerves activity to compensate the sudden drop of blood pressure to the brain; the fast pressure drop produced by the blood sequestered in the limbs can be compared with a traumatic loss reducing the cardiac filling pressure [5]. Vasoconstriction reflex and increased heart rate are very important adjustments to the orthostatic stress; it has been assumed that the level of sympathetic vasomotor activity elicited in response to orthostatic stress reflects the degree of unloading of the arterial and cardiopulmonary baroreceptors. These adjustments must remain as long as the standing up position persists [5–7].

Linear heart rate variability analysis used to evaluate autonomic regulation during orthostatism is characterized by increased mean heart rate, decreased variability and mean total power in the frequencies spectrum [8]. More recently several nonlinear indexes have been evaluated in healthy subjects and in patients with different pathologies [9–11]. Besides describing nonlinear properties of the heart rate variability, clinical applications have been shown for some of them (e.g. independent prognosis of cardiac death in survivors of myocardial infarction) [8, 11]. However, rigorous application of most nonlinear time series analysis methods need long and stationary time series and their uncritical application to biological data can lead to serious misleading conclusions [12, 13]. Therefore, nonlinear methods with applicability to short and noisy data, as in the case of heart rate variability, are continuously developed with the aim of revealing non evident changes in the cardiovascular control system [14, 15]. This is the case of Recurrence Plots Analysis. Recurrence is a basic feature of many dynamical systems, including physiological ones, and it measures the repeated occurrence of a given state of the system through a quantitative recurrence analysis (RQA). The application of RQA has shown that several properties of heart rate recurrence plots are different in diabetic patients compared to healthy subjects [16], and also that several RQA indexes are sensitive to orthostatic challenge in healthy and neuropathy subjects, helping to understand the mechanism that regulate the chronotropic activity of the heart [17–20]. However, heart rate variability by itself is not enough to understand the cardiovascular regulation [21].

1.1 Systolic Blood Pressure and Systolic Blood Volume

The importance of the sympathetic nervous system in the short-term regulation of blood pressure via the modulation of peripheral vascular tone and cardiac output is well established [7]. The study of the systolic blood pressure (SBP) variability is used to assess the autonomic sympathetic regulation towards the blood vessels, and combined with heart rate it is used to evaluate the baroreflex mechanism, mainly by estimation of the baroreflex sensitivity [22]. The dynamical behavior of SBP has also been studied with nonlinear methods, including the recurrence plots analysis [23]. From the cardiovascular point of view, blood pressure is one of the main variables that the cardiovascular system is trying to keep bounded within a dynamic range that guarantees enough perfusion to all body tissues. In this sense, blood pressure can be considered as a regulated variable, while heart rate is one of the effectors that is permanently adjusted by the control system [24]. The dynamical behavior of these two variables is strongly associated by feedback loops of the cardiovascular system, for example, the negative feedback loop between blood pressure and heart rate in the baroreflex mechanism [25]. Given this association, heart rate and SBP variability are not orthogonal variables, and therefore the understanding of the cardiovascular regulation with only these two variables remains limited [26].

As a third study variable, in this work we consider the blood volume variability, evaluated by the photoplethysmographic systolic blood volume (SBV) [5, 26]. SBV is also a variable of the control system and may add relevant information regarding the cardiovascular regulation. SBV is modulated by direct influence from the sympathetic nervous system but not by the parasympathetic nervous system [7, 25–27], and other mechanisms involved, such as the baroreflex, are also relevant [26, 27]. SBV behavior has been characterized mainly by linear methods such as spectral analysis [25, 28]. However, little is known about the dynamical properties of SBV, and there are no previous studies of the recurrence plot of this variable. Considering their intricate physiological association, it is important to learn how these three physiological variables co-evolve: SBP, SBV and heart-beat interval in different physiological context; and as a first approximation we are using the recurrence plots and QRA to compare their dynamical changes during the orthostatic challenge in healthy patients.

The aim of this study was to assess the effects of active orthostatic stress as revealed by recurrence plots and RQA indexes for three relevant cardiovascular physiological outputs: heart beat interval, SBP and for the first time, SBV oscillations.

2 Methods

Nineteen healthy volunteers, age 20–40 years old were included in the study. The volunteers fulfilled the following inclusion criteria: no known history of diabetes mellitus, cardiovascular disease or any other kind of chronic or acute disease, no medication indicated, no-smokers. All subjects were asked to avoid intake of stim-

ulants such as caffeine during 12 h before the study and they gave their informed consent to participate in this study. The study protocol is in accordance with the principles outlined in the Declaration of Helsinki of 1975 (as revised in 1989), and it was approved by the Ethics Committee of the hospital (Instituto Nacional de Cardiología Ignacio Chávez, México), protocol number 12–763.

Non-invasive blood pressure recordings were obtained with a Finometer and blood volume was estimated with a photoplethysmograph during supine position and orthostatism at a sampling frequency of 200 samples per second. The pressure sensor was secured on the middle finger of the left hand, with the arm resting on a sling to reduce hand movements. A calibration was made for each person by compressive sphygmomanometry. In each body position, the recording started after 5 min of stabilization and lasted 15 min. The recordings were processed to identify SBP and SBV value of each heartbeat, and to calculate all inter beat intervals (IBI). The pertinence of using only systolic values was shown before by our group [26].

2.1 Beat Detection Process

Ad-hoc techniques were implemented by computer programs in Matlab (Mathworks, Inc) described previously [26]. Briefly, the blood pressure signal was filtered by a second derivative algorithm, it was rectified to positive values and a threshold was applied in order to find the peaks that correspond to SBP [29]. Correct identification of SBP for all heartbeats was verified manually. IBI was obtained from the time difference of SBP between consecutive heartbeats.

2.2 Systolic Blood Volume

The photoplethysmographic oscillations are associated with blood volume changes in the microvascular bed of tissue that are observed around the average blood volume [5, 26]. Since PPG pulse is not a direct quantitative measurement it is represented in arbitrary units (a.u.). We used a two LED reflectance system that has been characterized previously [30].

2.3 Recurrence Plot Construction

Recurrence plots exhibit characteristic large and small scale patterns that are caused by fundamental dynamic behavior, e.g. short diagonals lines reveal similar local evolution of different parts of the trajectory, while horizontal and vertical black lines appear when a state does not change for some time. Random processes do not exhibit

those linear structures [31, 32]. The main step for the visualization of recurrence in a time series or data set is the calculation of the N × N matrix,

$$R_{i,j} = \Theta\left(\varepsilon_i - \left\| \overrightarrow{x_i} - \overrightarrow{x_j} \right\| \right),$$

where N is the number of data, ε_i is a predefined threshold distance, $\|\cdot\|$ is a norm (e.g. the Euclidean norm), and Θ is the Heaviside function. A multidimensional state space is reconstructed from the one dimensional beat to beat time series, applying a time delay embedding method. Each point in the reconstructed phase space represents the state of the system at a given moment and is determined by m coordinates of a given embedding dimension. To obtain all these reconstructed data we used the tools developed by Norbert Marwan and colleagues, the Cross Recurrence Plot Toolbox for Matlab [available from the toolbox for complex systems (TOCSY) webpage: http://tocsy.pik-potsdam.de/crp.php].

Embedding delay was estimated with both autocorrelation function and mutual information minima without finding significant differences. Embedding dimension was estimated by means of false nearest neighbor method. Since the estimated dimension was smaller than 10 in all times series, we set the embedding dimension = 10, which is in accordance with the recommendation of Webber [33] and other references [34, 35]. The distances between individual points in the matrix corresponding to a state of the system at a given time were calculated using the option Maximum norm fixed recurrence rate ("rr") in the toolbox for auto recurrent plots [15, 31, 36].

Besides the visual inspection of recurrence plot that help to recognize different characteristics between different physiological conditions, we applied a quantitative analysis of the generated patterns (RQA). We measured the following parameters: percentage of determinism (the percentage of recurrence points forming diagonals from all recurrence points), mean diagonal length, Lmax (length of the longest diagonal line), trapping time (time in which the dynamics remains trapped in a certain state), mean length of the vertical lines, laminarity (proportion of recurrence points forming vertical or horizontal lines), Vmax (maximal verticality), T1 (recurrence time of first type) and T2 (recurrence times of second type) [31]. Specifically, T2 is able to detect very weak transitions with high accuracy, both in clean and noisy environments. T1 has the distinguished merit of being more robust to the noise level and not sensitive to the parameter changes of the algorithm [37]. Also entropy was obtained. It is defined as the Shannon information entropy of the line length distribution [38]. Shannon Entropy is related to the amount of data needed to identify a particular state of the system.

Normal distribution of RQA indexes was tested with Kolmogorov-Smirnov tests. The variables that did not satisfy the normality test were transformed by a natural logarithm. Mean values of the RQA indexes were compared between supine position and active standing with paired t tests. A p value <0.05 was considered statistically significant (ANOVA). The statistical analysis was performed using the Statistical Package for the Social Sciences (SPSS) program, version. 15.0(SPSS, Inc).

3 Results

3.1 Recurrence Plots

Figures 1 and 2 show two examples of the three underlying time series used to produce each RP of healthy volunteers in clinostatism and orthostatism: IBI, SBP and SBV. Globally they show a significant content of high frequency oscillations ("fast cycles"), combined with some oscillations of lower frequencies. In the corresponding recurrence plot during supine position, the high frequency oscillations are reflected in regularly distributed diagonal lines, parallel to the identity line. The small diagonals are tramped in well-formed squares and rectangles. The white vertical spaces correspond to slow transient changes; and it is also possible to recognize a slow drift along some time series. Some differences were found in the associated patterns to IBI, SBP and SBV in the same person. In most cases the SBP and SBV plots seem like filters of the pattern observed in the IBI plot, with less fast cycles (Figs. 1 and 2 in supine position), like a progressive smoothing effect.

In contrast, in the standing up position there is an increase in both intercalated white regions and the density of points forming square zones (laminarity). Compared to supine position, during orthostatism the time series shows a decrease in the high frequency oscillations and increase in low frequency oscillations (Figs. 1 and 2).

The corresponding recurrence plot has important qualitative changes: it still shows diagonal lines but they are less fine and more scattered than the ones observed in supine position, while more regions have white vertical spaces in correspondence with slow transient changes in the time series. With careful inspection or visual training it could be possible to know if the plots correspond to a standing up person.

3.2 Recurrence Indexes from QRA

Table 1 summarizes our findings. In response to active standing there was no change in embedding dimension of all variables, but the embedding delay of both IBI and SBV increased significantly. On IBI, active standing caused significant increment in laminarity, trapping time, recurrence time of the first type (T1) and recurrence time of the second type (T2). In SBP, the only significant changes in response to active standing were: decrease in mean diagonal length, longest diagonal length, and increase in T1. In response to active standing, SBV showed significant increase in laminarity, T1 and T2.

3.3 In Trend and Out of Trend

Looking at Table 1 it is possible to appreciate that there were three indexes with p-values that almost reached statistically significance ($0.05 < p < 0.10$). We decided to examine the individual variation of those groups of indexes: the group with sig-
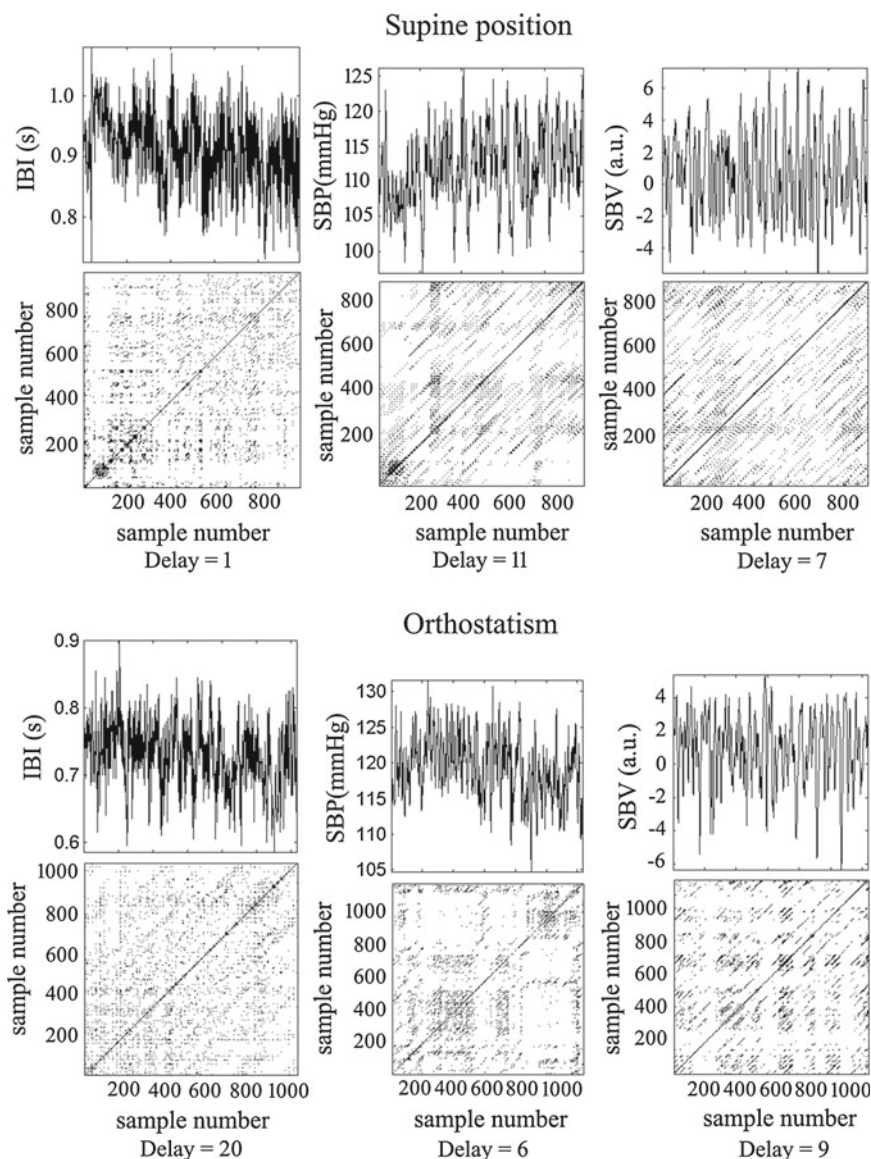
Fig. 1 Time series and recurrence plots from subject number 13. IBI= inter beat interval, SBP = systolic blood pressure, SBV= systolic blood volume. Recurrence plots parameters were: embedding dimension = 10, fixed recurrence rate = 7 %, and ad-hoc embedding delay (estimated with each corresponding auto-correlation function)

nificant differences and the group with differences almost statistically significant. Figure 3 shows examples of the first group of indexes.

We found, for example, that laminarity variation for IBI increased in response to orthostatism in 18 out of 19 subjects, although in a different extent within subjects
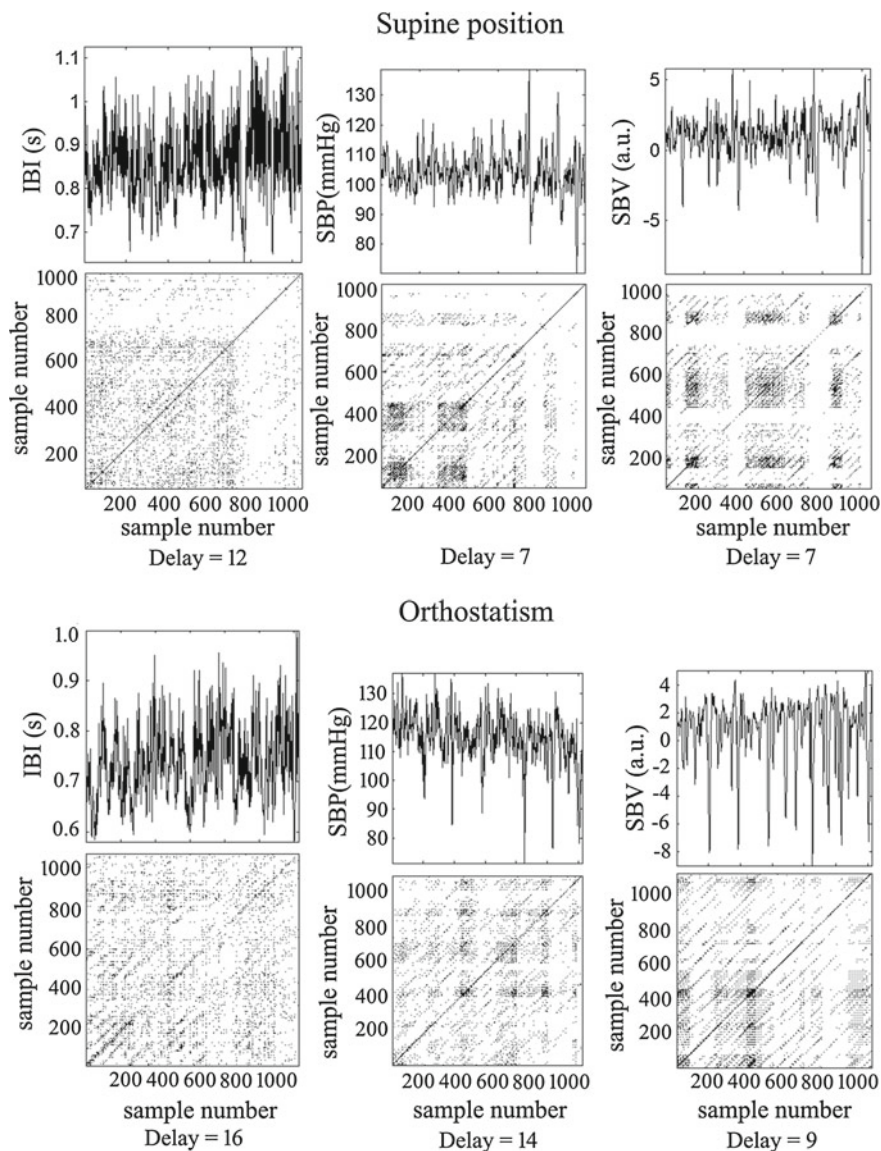
Fig. 2 Time series and recurrence plots from subject number 8. IBI = interbeat interval, SBP = systolic blood pressure, SBV = systolic blood volume oscillations. Recurrence plots parameters were: embedding dimension = 10, fixed recurrence rate = 7%, and ad-hoc embedding delay (estimated with each corresponding auto-correlation function)

(Fig. 3a). The same expected consistency was found in IBI recurrence rate which decreased during orthostatism (Fig. 3b), and in TT1of SBP and laminarity of SBV which increased during orthostatism (Fig. 3c, d). These types of consistent responses to orthostatism was observed for all other indexes with significant p-values ($p < 0.05$).

Table 1 Quantitative recurrence analysis of heart beat intervalvariability (IBI), systolic blood pressure (SBP) and systolic blood volume oscillations (SBV), evaluated from 19 healthy subjects during resting conditions (supine position) and during active standing (orthostatism)

	IBI	SBP	SBV
Supine position			
Embedding delay (heartbeats)	7 ± 5*	9 ± 3	8 ± 2*
Embedding dimension	6 ± 1**	6 ± 1	6 ± 1
Recurrence rate (%)	6.3 ± 0.4*	5.9 ± 0.4	6.4 ± 0.3**
Ln (determinism)	−0.78 ± 0.45	−0.40 ± 0.32	−0.29 ± 0.23
Mean diagonal length	3.24 ±1.67	3.72 ± 1.41*	4.23 ± 1.83
Ln (longest diagonal length)	3.14 ± 0.96	4.04 ± 0.92*	4.13 ± 0.85*
Ln (entropy)	−0.06 ± 0.56	0.27 ± 0.45**	0.38 ± 0.45
Laminarity	0.48 ± 0.12*	0.70 ± 0.13	0.79 ±0.11*
Trapping time	2.60 ± 0.32*	3.37 ± 0.82	37.2 ± 28.4
Maximal verticality	22.4 ± 12.7	33.0 ± 19.0	37.2 ± 28.4
Recurrence type of 1st type	12.0 ± 1.6*	11.5 ± 3.2*	11.7 ± 2.5*
Recurrence type of 2nd type	17.3 ± 2.6*	23.9 ± 7.5	31.1 ± 10.5*
Orthostatism			
Embedding delay (heartbeats)	14 ± 5	9 ± 4	9 ± 2
Embedding dimension	7 ± 1	6 ± 1	5 ± 1
Recurrence rate (%)	5.6 ± 0.6	6.0 ± 0.3	6.2 ± 0.2
Ln (determinism)	−0.66 ± 0.22	−0.53 ± 0.19	−0.22 ± 0.11
Mean diagonal length	2.58 ± 0.20	2.68 ± 0.36	3.72 ± 1.00
Mean diagonal length	2.58 ± 0.20	2.68 ± 0.36	3.72 ± 1.00
Ln (longest diagonal length)	2.76 ± 0.80	2.91 ± 0.77	3.62 ± 0.76
Ln (entropy)	−0.02 ± 0.20	0.04 ± 0.23	0.46 ± 0.20
Laminarity	0.67 ± 0.09	0.72 ± 0.09	0.88 ± 0.06
Trapping time	3.05 ± 0.30	3.13 ± 0.51	4.59 ± 1.23
Maximal verticality	27.8 ± 14.2	25.9 ± 15.2	48.2 ± 29.7
Recurrence type of 1st type	15.2 ± 2.9	13.7 ± 2.3	13.1 ± 2.8
Recurrence type of 2nd type	28.4 ± 6.2	28.2 ± 8.4	45.8 ± 18.9

* $p \leq 0.05$ (supine position versus orthostatism, paired t-test)
** $0.05 < p < 0.10$ (supine position versus orthostatism, paired)

On the other side, when we review the indexes with almost significantly differences like Shannon's Entropy of IBI, or determinism of SBP, we identify two or three well defined subsets of response to orthostatism within each index (Fig. 4a, b). This implies that there can be two or three types of variations in the response to orthostatism, even though they all correspond to young healthy subjects. Due to the high dispersion in the response of each index, the t-test between supine position and orthostatism did not reach a significant difference.
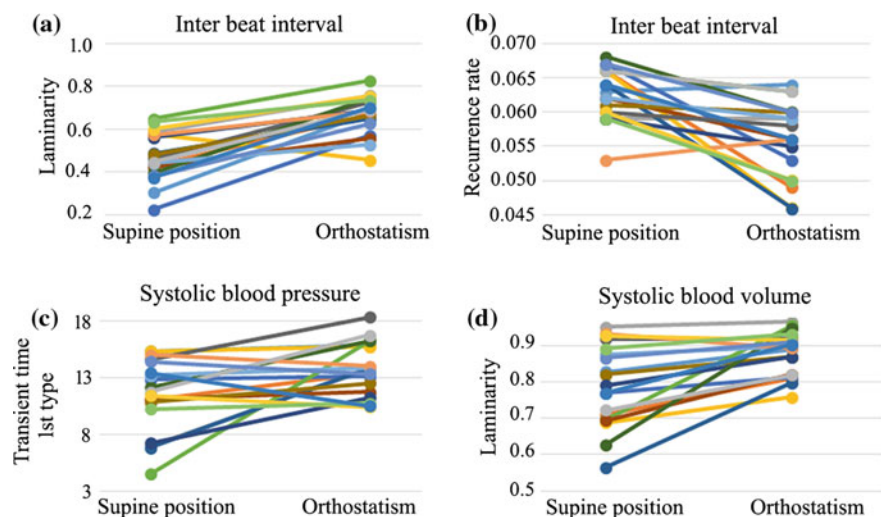
Fig. 3 Examples of quantitative recurrence plot analysis indexes with a consistent response to ortho-statism (showed as a significant paired t-test, $p < 0.05$, between supine position and orthostatism)
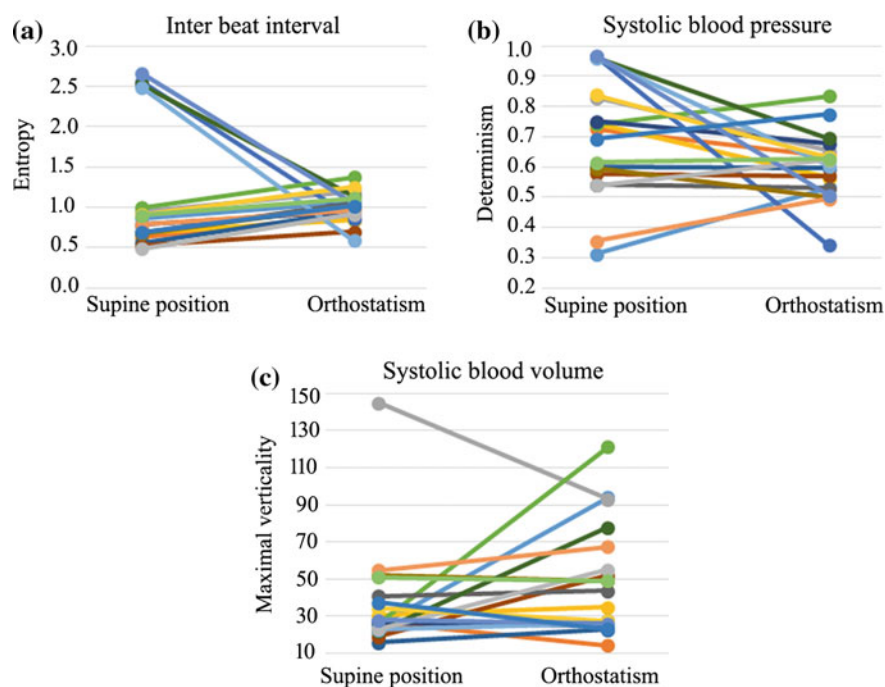

Fig. 4 Examples of quantitative recurrence plot analysis indexes with no significant changes in response to orthostatism (showed as paired t-test, $0.05 < p < 0.10$, between supine position and orthostatism)
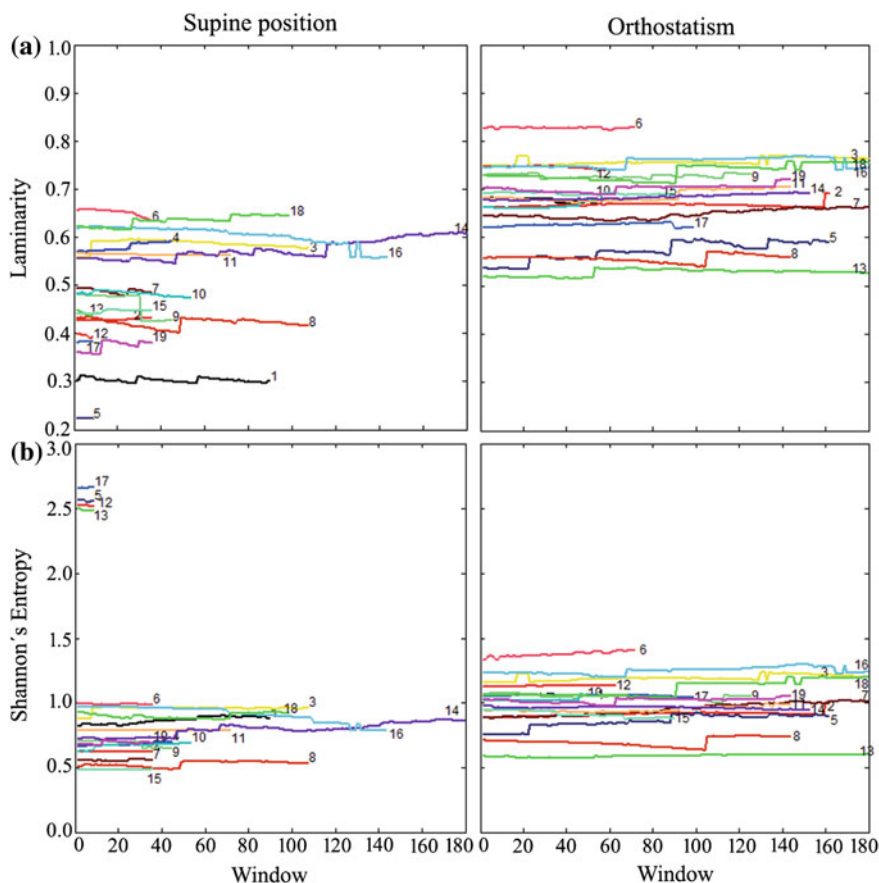
Fig. 5 Temporal variation in inter beat interval QRA indexes: **a** example of a QRA index with statistically significant difference ($p < 0.05$) between supine and orthostatism, **b** example of a QRS index with non-significant difference ($0.05 > p < 0.10$)

Another way to consider this inter-individual variation in indexes which were almost statistically different is to analyze the temporal evolution of relevant indexes in both studied conditions. Figure 5 (upper left panel) shows the temporary evolution of IBI Laminarity for the supine condition and Fig. 5 (upper right panel) for the orthostatic position.

Most of the subjects have the same type of change in their QRA index, independently of their particular trajectory, and only a few deviate from the overall trend. On the other hand, for the QRA indexes that resulted almost significant, such as the Shannon's Entropy (Fig. 5, lower panels) we found cases that markedly deviate from the overall trend. However, these cases correspond to healthy persons too.

4 Discussion

In our study the recurrence plots showed a consistent pattern of more clustering of points during orthostatism with respect to supine position. The quantitative assessment with the RQA indexes confirmed these observations of the effect of orthostatic stress in healthy subjects: IBI, SBP and SBV variability and complexity were reduced and the characteristics of their dynamics were changed by orthostatism, which is consistent with previous reports about RQA from IBI alone [19, 20], or from IBI and SBP [23].

In standing position, that represents a physiologically activated state, theRP had higher laminarity and trapping time, that is, a long permanence of the system in a particular state, with a reduction in the number of states that are visited, as can be seen for a larger proportion of white spaces. It seems that for a more activated condition (i.e. active orthostatism) the predominance of a smaller number of dynamic states is important, and therefore, the demanded physiological status is reached with a smaller set of combined adjustments.

There were similarities in the response of SBV and IBI, but the response of RQA indexes was not identical in the 3 evaluated variables. There was more parallelism in the significant QRA indexes between IBI and SBV than between IBI and SBP. This suggests that despite the known high correlation between these 3 variables, the cardiovascular control exerts different influences on them in response to active standing. Previous work with different methodology showed that during passive orthostatism, complexity of IBI decreases while complexity of SBP remained unchanged, suggesting that complexity indexes from IBI and SBP provide complimentary information [21]. Our work agrees with these ideas considering the following: (i) we observed a response to active orthostatism that is consistent with decreased complexity in several recurrence plot indexes of IBI, SBP and SBV, (ii) there were fewer indexes in SBP that changed significantly, compared to IBI, indicating that SBP have less dynamical changes in response to active standing, and (iii) several of the indexes that changed significantly in SBP were different from those that changed in IBI or SBV, which also supports the hypothesis that these 3 variables provide complementary information.

Our results also indicate an association between changes in dynamical behavior of IBI, SBP and SBV with an increased sympathetic predominance. This confirms that the autonomic modulation of the cardiovascular control responds to the orthostatic stimulus [20], but also suggests that some other mechanism, as regional vasomotor activity may have an important role. The finding can be suitable to appreciate a differential condition of the three variables in a clinical evaluation of health and disease.

Clinical considerations of decreased variability, complexity and IBI nonlinear dynamics reflected in RQA indexes has been used for detection of heart rate deregulation in various pathological conditions including chronic fatigue syndrome, hypertension, diabetes mellitus, chronic renal failure, and ventricular arrhythmia [19, 20]. One of the greatest interests of clinicians is to be able to associate the condition of

the autonomic balance, or autonomic tone, with the risk of disease or to gain some insights for therapeutics management. For example, in myocardial infarction survivors, the observation of high laminarity has been associated with an increased risk for life threatening arrhythmia [15].

Overactivity of the sympathetic nervous system is both a major early prognostic indicator for hypertension and a conspirator affecting the heart, vasculature, renin-angiotensin system and immune system. As sympathetic overactivity appears to be present before the hypertensive phenotype, its early antagonism should be considered a potential preventative measure before end organ damage becomes irreversible and hypertension becomes drug resistant [39, 40]. Therefore, having new tools to evaluate augmented sympathetic activity in health condition as those here analyzed becomes very relevant.

Another interesting aspect was to review some particular QRA indexes close to reach statistical significance; we applied to them the same methodology and data protocol; so they pose the question of considering a broader spectrum of results as corresponding to a healthy condition. Maybe it is necessary to develop a more personalized approach to distinguish between health and disease or to learn to recognize the individualized evolution to disease. As Richard Levins remarks:

> If we fail to define the problem big enough, then many important impacts on a variable come from outside the domain of the problem and are treated as "random"or"error. Contrary to common sense, big problems are often more soluble than small ones [41]

In conclusion, we have shown that in response to orthostatic stress, SBV oscillations have dynamic changes similar but not identical to SBP and IBI. This suggests that these three variables are complementary for a better evaluation of cardiovascular dynamics.

Also we discussed the convenience to develop a more personalized assessment of the physiological condition, for example the level of activity of the sympathetic nervous system based on more statistical indexes and their variances.

References

1. Armour, J.A.: Cardiac neuronal hierarchy in health and disease. Am. J. Physiol. Regul. Integr. Comp. Physiol. **287**(2), R262–R271 (2004)
2. Berntson, G.G., Cacioppo, J.T., Quigley, K.S.: Cardiac psychophysiology and autonomic space in humans: empirical perspectives and conceptual implications. Psychol. Bull. **114**(2), 296–322 (1993)
3. Akselrod, S., Gordon, D., Ubel, F.A.: Power spectrum analysis of heart rate fluctuation: a quantitative probe of beat-to-beat cardiovascular control. Science **213**(4504), 220–222 (1981)
4. Paton, J.F., Boscan, P., Pickering, A.E.: The ying and yang of cardiac autonomic. Brain Res. Rev. **49**(3), 555–565 (2005)
5. Allen, J.: Photoplethysmography and its application in clinical physiological measurement. Physiol. Meas. **28**(3), R1–R39 (2007)

6. Linder, S.P., Wendelken, S.M., Wei, E.: McGrath: Using the morphology of photoplethysmo-gram peaks to detect changes in posture. J. Clin. Monit. Comput. **20**(3), 151–158 (2006)

7. Ichinose, M., Nishiyasu, T.: Arterial baroreflex control of muscle sympathetic nerve activity under orthostatic stress in humans. Front. Physiol. **3**, 314 (2012)

8. Task force of the European Society of cardiology the North American Society of Pacing Electro-physiology, Heart Rate Variability?: Standards of Measurement, Physiological Interpretation, and Clinical Use. Circulation **93**(5):1043–1065 (1996)

9. Pikkujamsa, S.M., Makikallio, T.H., Sourander, L.B., Raiha, I.J.: Cardiac interbeat interval dynamics from childhood to senescence?: comparison of conventional and new measures based on fractals and Chaos theory. Circulation **100**(4), 393–399 (1999)

10. Lerma, C., Infante, O., Pérez-Grovas, H., José, M.V.: Poincaré plot indexes of heart rate vari-ability capture dynamic adaptations after haemodialysis in chronic renal failure patients. Clin. Physiol. Funct. Imaging **23**(2), 72–80 (2003)

11. Huikuri, H.V., Perkiömäki, J.S., Maestri, R., Pinna, G.D.: Clinical impact of evaluation of cardiovascular control by novel methods of heart rate dynamics. Philos. Trans. A. Math. Phys. Eng. Sci. **367**(1892), 1223–1238 (2009)

12. Raab, C., Wessel, N., Schirdewan, A., Kurths, J.: Large-scale dimension densities for heart rate variability analysis. Computers in Cardiology, pp. 985–988. (2005)

13. Seker, R., Saliu, S., Birand, A., Kudaiberdieva, G.: Validity test for a set of nonlinear measures for short data length with reference to short-term heart rate variability signal. J. Syst. Integr. **10**(1), 41–53 (2000)

14. Aubert, A.E., Ramaekers, D.: Neurocardiology: the benefits of irregularity. The basics of methodology, physiology and current clinical applications. Acta Cardiol. **54**(3), 107–120 (1999)

15. Marwan, N., Wessel, N., Meyerfeldt, U., Schirdewan, A., Kurths, J.: Recurrence-plot based measures of complexity and their application to heart-rate-variability data. Phys. Rev. E **66**(2), 1–8 (2002)

16. Webber, C.L.J., Zbilut, J.P.: Dynamical assessment of physiological systems and states using recurrence plot strategies. J. Appl. Physiol. **76**(2), 965–973 (1994)

17. McGuire, G., Azar, N.B., Shelhamer, M.: Recurrence matrices and the preservation of dynam-ical properties. Phys. Lett. A **237**(1), 43–47 (1997)

18. Thiel, M., Romano, M., Kurths, J.: How much information is contained in a recurrence plot? Phys. Lett. A **330**(5), 343–349 (2004)

19. Javorka, M., Trunkvalterova, Z., Tonhajzerova, I., Lazarova, Z.: Recurrences in heart rate dynamics are changed in patients with diabetes mellitus. Clin. Physiol. Funct. Imaging **28**(5), 326–331 (2008)

20. González, H., Infante, O., Pérez-Grovas, H., José, M.V., Lerma, C.: Nonlinear dynamics of heart rate variability in response to orthostatism and hemodialysis in chronic renal failure patients: Recurrence analysis approach. Med. Eng. Phys. **35**(2), 178–187 (2013)

21. Porta, A., Castiglioni, P., Di Rienzo, M., Bari, V., et al.: Short-term complexity indexes of heart period and systolic arterial pressure variabilities provide complementary information. J. Appl. Physiol. **113**(12), 1810–1820 (2012)

22. Martínez-García, P., Lerma, C., Infante, O.: Baroreflex sensitivity estimation by the sequence method with delayed signals. Clin. Auton. Res. **22**(6), 289–297 (2012)

23. Javorka, M., Turianikova, Z., Tonhajzerova, I., Javorka, K., Baumert, M.: The effect of orthosta-sis on recurrence quantification analysis of heart rate and blood pressure dynamics. Physiol. Meas. **30**(1), 29–41 (2009)

24. Russek, M.: Fisiología. Células, Órganos y Sistemas (Physiology. Cells, Organs and System). In: Muñoz-Martínez J, García X (eds) FCE México, p 500. (1988)

25. Estañol, B., Porras-Betancourt, M., Sánchez-Torres, G., Martínez-Memije, R. et al: Control neural de la circulación periférica y de la presión arterial (Neural control of peripheral circu-lation and blood pressure). Arch. Cardiol. Mex. **79**(15), 109–116 (2009)

26. Martínez-García, P., Lerma, C., Infante, O.: Relation of the baroreflex mechanism with the photoplethysmographic volume in healthy humans during orthostatism. Arch. Cardiol. Mex. **82**(2), 82–90 (2012)

27. Chan, G.S.H., Fazalbhoy, A., Birznieks, I., Macefield, V.G. et al.: Spontaneous fluctuations in the peripheral photoplethysmographic waveform: roles of arterial pressure and muscle sympathetic nerve activity. Am. J. Physiol. Heart Circ. Physiol. **302**(3), H826–H936 (2012)

28. Nitzan, M., de Boer, H., Turivnenko, S., Babchenko, A., Sapoznikov, D.: Power spectrum analysis of spontaneous fluctuations in the photoplethysmographic signal. J. Basic Clin. Physiol. Pharmacol. **5**(3–4), 269–276 (1994)

29. Infante, O., Valenzuela, F., Polo, S.: Algoritmo que utiliza la segunda derivada para identificar el complejo QRS en tiempo real (Algorithm that uses the second derivative to identify the QRS complex in real time). Rev. Méx. Ing. Bioméd **13**, 23 (1992)

30. Infante, O., Cortés, S.: Relación entre el pulso fotopletismográfico digital y la presión arterial incruenta latido a latido ante el reto ortostático (Relationship between photoplethysmographic pulse and digital noninvasive beat to beat blood pressure during the orthostatic challenge). In: Müller-Karger, C., Wong, S., La Cruz, A. (eds) IV Latin American Congress on Biomedical Engineering, Bioengineering Solutions for Latin America Health 2007 IFMBE Proceedings, vol. 8, pp. 51–55 (2008)

31. Marwan, N., Romano, C., Thiel, M., Kurths, J.: Recurrence plots for the analysis of complex systems. Phys. Rep. **438**(5–6), 237–329 (2007)

32. Marwan, N.: A historical review of recurrence plots. Eur. Phys. J. Spec. Top. **164**(1), 3–12 (2008)

33. Webber, C.L., Zbilut, J.P.: Recurrence Quantification Analysis of Nonlinear Dynamical Systems. In: Van Orden, GC., Riley, MA. (eds.) Tutorials in Contemporary Nonlinear Methods for the Behavioral Sciences, Web Book (2005)

34. Marwan, N.: How to avoid potential pitfalls in recurrence plot based data analysis. Int. J. Bifurcat. Chaos **21**(14), 1003–1017 (2011)

35. Zbilut, J.P., Webber, C.L.: Laminar recurrences, maxline, unstable singularities and biological dynamics. Eur. Phys. J. Spec. Top. **164**(1), 55–65 (2008)

36. Aguado, A., Infante, O., Lerma, C.: Recurrence plot analysis of heart rate and systolic blood pressure: a strategy for embedding parameters estimation. Paper presented at the 5th international symposium on recurrence plots, Chicago, 14–16 Aug 2013

37. Gao, J.B., Cao, Y., GuLY, H.R.: Detection of weak transitions in signal dynamics using recurrence time statistics. Phys. Lett. A **317**(1–2), 64–72 (2003)

38. Shannon, C.: A mathematical theory of communication. Bell Syst. Tech. J. **27**, pp.379–423, 623–656 (1948)

39. Fisher, J.P., Paton, J.F.R.: The sympathetic nervous system and blood pressure in humans: implications for hypertension. J. Hum. Hypertens. **26**(8), 463–475 (2012)

40. Naschitz, J.E., Rosner, I., Shaviv, N., et al.: Assessment of cardiovascular reactivity by fractal and recurrence quantification analysis of heart rate and pulse transit time. J. Hum. Hypertens. **17**(2), 111–118 (2003)

41. Levins, R.: On the threshold of complexity. Presented at Simposio Complejidad y Multidisciplina. Centro de Ciencias de la Complejidad, México, 4–6 November 2013

Recurrence Quantification Analysis as a Tool for Discrimination Among Different Dynamics Classes: The Heart Rate Variability Associated to Different Age Groups

Laurita dos Santos, Joaquim J. Barroso, Moacir F. de Godoy, Elbert E.N. Macau and Ubiratan S. Freitas

Abstract We propose a classification method based on *recurrence quantification analysis* (RQA) combined with *support vector machines* (SVM). This method combines in an effective way various quantitative descriptors to allow a refined discrimination among dynamical non linear systems that presents dynamics which are very similar to each other. To show how effective this methodology is, firstly, based on synthetic data, it is applied on time series generated from the logistic map with nearby parameter values and in the chaotic regime. Next, it is applied to human biosignals, namely, heart rate variability (HRV) time series obtained from four groups of individuals (premature newborns, full-term newborns, healthy young adults, and adults with severe coronary disease). Roughly the proposed methodology works as follows: The signals are transformed into recurrence plots (RP) and a set of RQA statistical features (recurrence rate, determinism, averaged and maximal diagonal line lengths, entropy, laminarity, trapping time, and length of longest vertical line) are extracted to form the input vector for a SVM classifier. Results show that the method discriminates groups of different ages with classification accuracy better than 75 %. Given that heart rate continuously fluctuates over time and reflects different mechanisms to maintain cardiovascular homeostasis of an individual, the results obtained may allow to draw important information on the autonomic control of circulation in normal and diseased conditions.

Keywords Recurrence quantification analysis · Heart rate variability · Different age groups

L. dos Santos
Universidade do Vale do Paraíba - UNIVAP, São José dos Campos, São Paulo, Brazil
e-mail: lauritas9@gmail.com

J.J. Barroso · E.E.N. Macau (✉)
Instituto Nacional de Pesquisas Espaciais, São José dos Campos, São Paulo, Brazil
e-mail: elbert.macau@inpe.br

M.F. de Godoy
Faculdade de Medicina de so José do Rio Preto - Famerp, São José Dos, São Paulo, Brazil

U.S. Freitas
Complexe de Recherche Interprofessionnel en Aérothermochimie - CORIA,
Université de Rouen, Rouen, France

1 Introduction

Heart rate variability (HRV) is a non-invasive measure related to the balance of the activities of sympathetic and parasympathetic divisions of the autonomic nervous system [1]. This variability is normal and indicates the heart ability to response to the environmental and physiological stimuli [2]. The balance of nervous system activities results in a nonlinear behaviour of the HRV time series. In general autonomic and parasympathetic activities attenuate with age [3], which is related with reduction of the HRV [4] (comparing the normal healthy adult and older-age adult).

There are several methods for HRV analysis [5], for example, standard linear techniques (time and frequency domain analysis) and nonlinear methods (correlation dimension analysis, largest Lyapunov exponent, central tendency measure, Poincare plot). However, none of them, from our knowledge, is regarded as universally applicable or effective for all the cases related to HRV analysis. In this study we propose a methodology that is based on the recurrence plot and recurrence quantification analysis. In recent years, recurrence plot (RP) and recurrence quantification analysis (RQA) have been applied to study different dynamics systems [6, 7], in natural science, physics [8], biological systems, and physiological processes involving heart rate variability [9–12]. Given its intrinsic discrete character, RQA is particularly suited for the analysis of HRV time series and allows for a direct quantification of the complex dynamics of heart rhythm modulation [13, 14].

RQA is a useful tool and helps to understand the variation of the autonomic nervous system over time. The major advantage of RQA and recurrence plots (RPs) over standard HRV analysis are their applicability to non stationary data and also their sensitivity to subtle changes in the cardiovascular system dynamics. These aspects enable RPs to be used in the characterization of changes in the basic cardiovascular parameters during both physiological and pathological conditions. But the analysis of HRV time series using only RQA statistics is known as not being able to provide consistent enough information to achieve a suitable classification. And our goal here is to have an effective method that allows one enough sensitivity to properly differentiate systems with very similar dynamics. This desired amplification in the discrimination sensitivity using the SVM in combination with the RQA, will be shown here in the subsequent sections. In this work, combined with SVM, we evaluated RQA measures to discriminate and identify groups of different ages, including information about the system.

2 Materials and Methods

2.1 Experimental Database

The study comprised a total of 148 tachograms divided into four groups: 26 full-term newborns (FNB) (8 days on average), 48 premature newborn (PNB) (± 27.4 days), 61 healthy young adults (HYA) (20.7 ± 1.6 years), and 61 adults in preoperative

evaluation for coronary artery bypass grafting for severe coronary disease (SCD) (58.4 ± 10.2 years). All tachograms are from databases from previous studies of Transdisciplinar Nucleus for Chaos and Complexity Study (NUTECC/Brazil) [15, 16]. There are time series with 15 min up to 1 h recording period from patients in a supine rest position without visual and sound stimulations.

The equipment used to collect signal was Polar Monitor (S810i or RS800), which has been proven [17–19] to be feasible and reliable for measuring HRV according to recognized standards [20]. At a sampling rate of 1000 Hz, this device captures successive intervals between heartbeats, namely NN, in the normal sinus rhythm (i.e., initiated by the sinoatrial node). All these studies were approved by the respective ethic committee. All NN time series were filtered to remove artifacts using an adaptive filter which takes into account the peculiarities of the signal to be analyzed [5].

2.2 Recurrence Quantification Analysis

Defined as a repeated occurrence in time of a given state of a system, recurrence is a basic attribute of many dynamical systems. It means that along the time a trajectory comes repetitively close in the state space of points previously visited. Embedding the time series in a appropriate dimensional space and then plotting in a matrix the recurrences according to a tolerance rule results a recurrence plot (RP), which is a graphical representation of the recurrences in the dynamical system. The visual features of such plots are appealing and reveal patterns not previously viewed in the original series [13].

RP represents the autocorrelation in the signal at all possible time scales. Since the diagonal marks the identity in time, long-range correlations are associated to points far from the main diagonal, whereas the elements near the principal diagonal correspond to short-range correlations. Diagonals reflect the repetitive occurrence of similar states in the system dynamics and express the similarity of system behavior in two distinct time sequences. To quantity such features, recurrence quantification analysis (RQA) has been introduced for measuring quantitative information contained in recurrence plots [21].

For instance, the density of recurrence points in a recurrence plot is defined as recurrence rate (RR), giving the probability that a specific rate will recur. Parameters based on the diagonal lines are determinism (DET, the percentage of recurrence points forming diagonals from all recurrence points), averaged diagonal line length (L), maximal diagonal line length (Lmax), and entropy (which denotes the Shannon entropy of the histogram of the lengths of diagonal segments and thus indicates the complexity of the deterministic structure of the system).

Verticals are also important structures in a RP in that they reflect the persistence of one state during some time interval. The parameters derived from vertical lines are laminarity (LAM, the proportion of recurrence points forming verticals), trapping time (TT, the mean length of vertical lines), and the maximal length of a vertical, Vmax. Low TT, LAM, and Vmax values imply high complexity in the systems

dynamics, since the state of the system stays only for a short time in a state similar to the previously occurring state. Theoretically, diagonal and vertical structures would not occur in random (stochastic) as opposed to determinist process [7].

2.3 SVM Classifier

Support Vector Machines (SVMs), developed by [22], are supervised learning techniques used for classification, regression analysis and learning tasks. Such techniques can be applied to the solution of problems related to text categorization, image analysis, and bioinformatics [23]. The main idea behind this classifier is to construct a hyperplane that maximizes the distance (so-called margin) to the nearest data points pertaining to two classes as pictured in Fig. 1.

The classifier was trained from the previously discussed dataset which, in an empirical way, was divided into the training and test sets enumerated in Table 1.
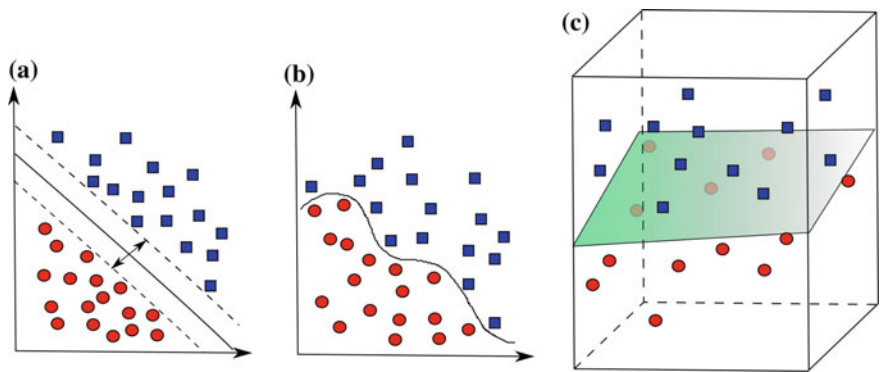

Fig. 1 Examples of separation of two classes using an SVM classifier: **a** two classes linearly separable, **b** two classes with nonlinear separation, and **c** separation achieved by a hyperplane in a high-dimensional space

Table 1 Number of training and test sets employed in the SVM classifier

Groups[a]	Training set	Test set	Total of cases for comparison
FNB (26) and PNB (48)	17 and 17	9 and 9	26 and 26
FNB (26) and HYA (61)	17 and 17	9 and 9	26 and 26
PNB (48) and HYA (61)	30 and 30	18 and 18	48 and 48
FNB (26) and SCD (61)	18 and 18	8 and 8	26 and 26
PNB (48) and SCD (61)	30 and 30	18 and 18	48 and 48
HYA (61) and SCD (61)	45 and 45	16 and 16	61 and 61

[a] *FNB* full-term newborn, *PNB* premature newborn
HYA—healthy young adult, SCD—adult with severe coronary disease

Fig. 2 Structure of the
methodology for discrimi-
nation of HRV clinical groups
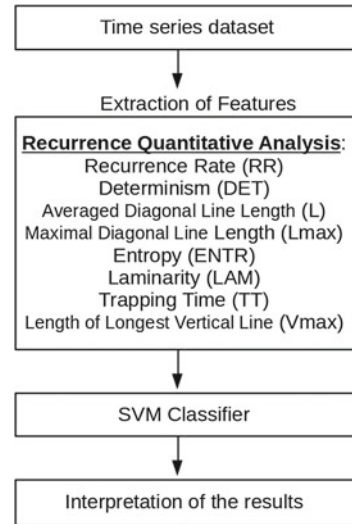
The class label (PNB, FNB, HYA, SCD) for each NN interval time series was assigned by a cardiologist.

For each time series, eight RQA features were extracted to form the input for the classification step (Fig. 2). The SVM classifier was assessed from the LIBSVM open library [23] and executed 100 times for each RQA feature for comparison between two clinical groups. Detailed information about learning and classification algorithm can be found in [22, 23]. For each execution of the code, the training and test cases were randomly selected from which was obtained the average accuracy, defined as the percentage ratio of the number of cases correctly classified to the total number of cases used for classification.

3 RQA Plus SVM: Discriminating Almost Similar Dynamics

To show the effectivity of the proposed the methodology RQA + SVM, we used the logistic map time series ($x_{n+1} = r * x_n * (1 - x_n)$) for values $r = 3.68$, $r = 3.7$ and $r = 3.9$ (see Fig. 3). For each value of the dynamic parameter r, 30 time series were generated, each one with 2,000 points (the first 200 points were discarded to allow transients to die out), with $x(0) \in [0.1, 0.8]$, and an incremental step $\Delta x(0) = 0.0241$.

For the study of the RQA measures, the RP parameters to the logistic map were selected embedding dimension ($m = 1$), delay ($\tau = 1$) and threshold radius ($\varepsilon = 0.1$). Details about these values are given in [7].

To the SVM classifier three groups are assigned (according r values: $r = 3.68$, $r = 3.7$ and $r = 3.9$). We used 21 time series for each group of the training set
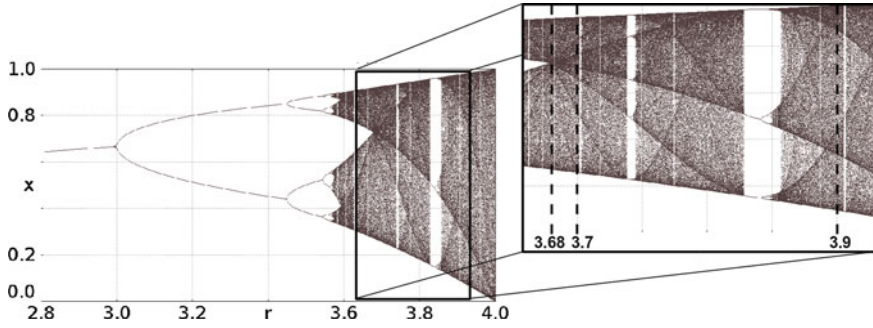
Fig. 3 Bifurcation diagram of the logistic map with a zoomed in view in the region of the *r* parameters chosen: $r = 3.68$, $r = 3.7$ and $r = 3.9$
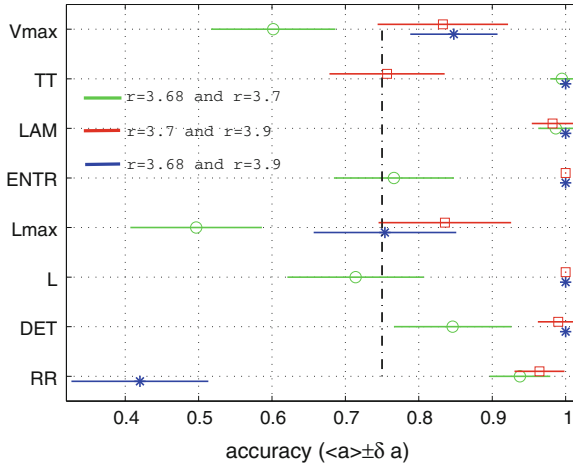

Fig. 4 Average accuracy and standard deviation ($\langle a \rangle \pm \delta a$) obtained by the SVM of the comparison between two time series groups to Logistic Map. (A) $r = 3.68$ and $r = 3.7$, (B) $r = 3.7$ and $r = 3.9$ (*red line*); $r = 3.68$ and $r = 3.9$ (*blue line*). The proper level of accuracy (75 % or higher) is indicated by points to the right of the *dashed vertical line*

and 9 to the test set. The average accuracy and standard deviation obtained by SVM are displayed in Fig. 4. In this figure an accuracy equal to 1 means that all of the cases tested (100 %) were correctly classified, while a zero value means that all cases were not properly classified. For accuracy values above the threshold of 75 %, the dynamics of the analyzed groups are considered to be similar. We can observe that for the pair of groups ($r = 3.68$, $r = 3.7$) the RQA features are more similar than the pairs of groups ($r = 3.68$, $r = 3.9$) and ($r = 3.7$, $r = 3.9$). These results demonstrate the ability of the methodology RQA + SVM to differentiate groups with almost similar dynamics.

4 Application: Using HRV to Discriminate Physiological Age

The main objective of this study was to analyze RQA measures as a tool to discriminate HRV time series recorded from different clinical groups. Typical HRV time series and RP patterns are shown in Figs. 5 and 6, from which the peculiarities of each recurrence plot and the corresponding HRV series are noticeable. For these plots and throughout the present study the RP parameters were selected as: $m = 3$, $\tau = 3$, and $\varepsilon = 8$. The choice of embedding dimension ($m = 3$) was based on results from the false nearest neighbor method [24]. We chose the minimum value for m that presented minimum percentage of false neighbors. This value was adopted for the time series analyzed, standardizing all the data set. Time delay for embedding was set at the first minimum of the mutual information function [25], since the embedded signals have the minimum overlapping information. The tolerance level, following the recommendation of [26], was selected to ensure the percentage of recurrence points lying between 0.1 and 0.2 % to obtain reliable values for the RP parameters. Detailed discussions about the RP parameters are found in [13, 14, 26].

For each group, the extracted RQA features are displayed in Figs. 7 and 8. We can notice that for the pairs of groups (SCD, HYA) and (FNB, PNB) the RQA features are similar. Then to further examine the ability of RQA features to differentiate groups of different ages we applied SVM classification.

A similar plot to those for the RQA measures (Figs. 7 and 8) is obtained when using the mean value and standard deviation of the HRV time series. We see in Fig. 9a that the groups FNB and PNB can be distinguished from the groups SCD and HYA in terms of the average values of the NN intervals. But since an NN interval gives
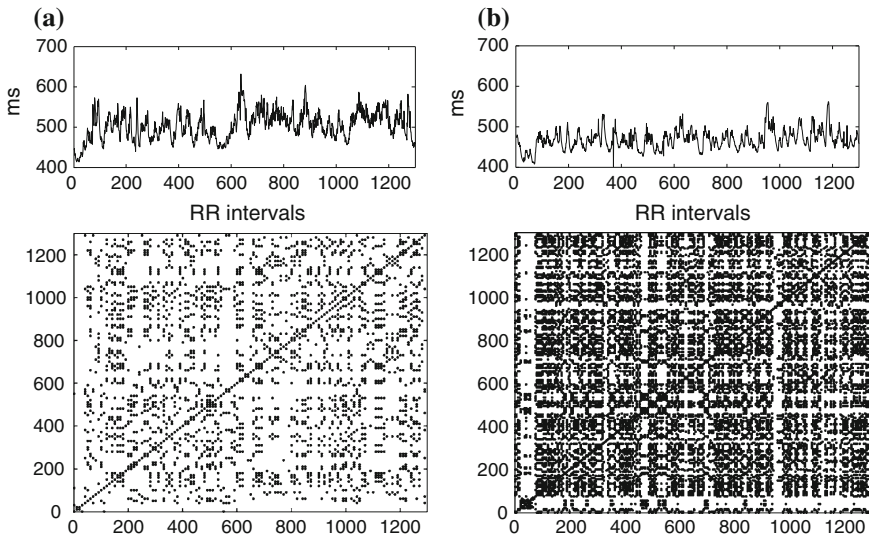

Fig. 5 Examples of NN time series and RPs for **a** FNB and **b** PNB groups (embedding dimension = 3, delay = 3 and threshold = 8)
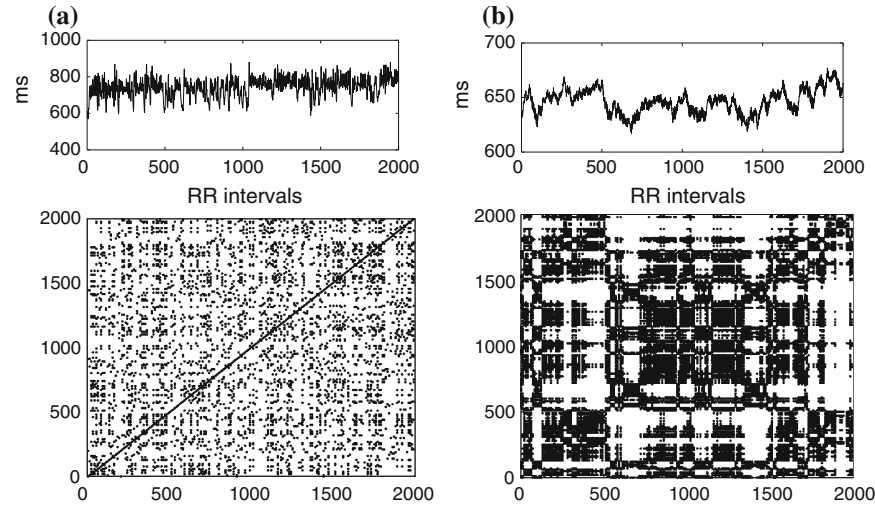
(a)

(b)

Fig. 6 Examples of NN time series and RPs for **a** HYA and **b** SCD groups (embedding dimension = 3, delay = 3 and threshold = 8). Example of RPs for each time series groups (embedding dimension = 3, delay = 3 and threshold = 8)
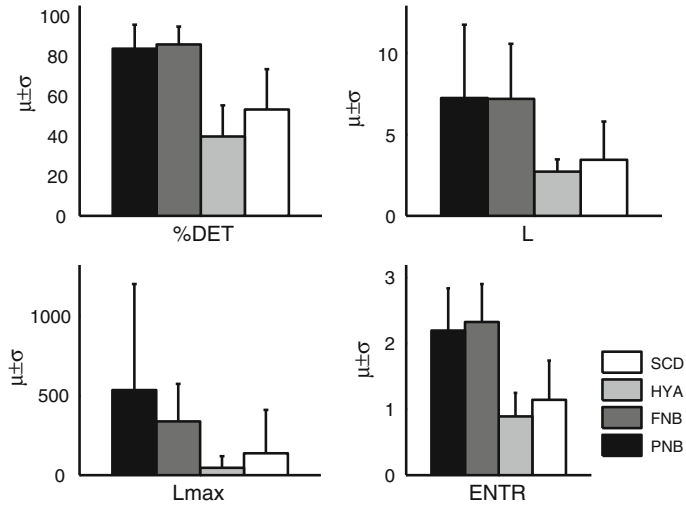

Fig. 7 Average values and standard deviation to RQA diagonal parameters for each group

(in milliseconds) the duration of a heartbeat, the values displayed in Fig. 9a are only correlated with the mean heart rate for the time series of each group. However we emphasize that the mean value of the NN interval, i.e., the heartbeat average is not enough to characterize the homeostasis of an individual, which is a dynamical process that is reflected in the heart rate variability. On the other hand, upon analyzing the
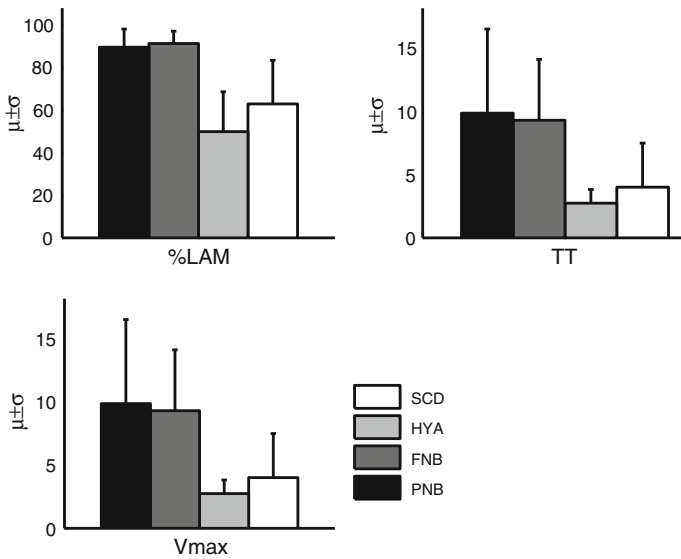
Fig. 8 Average values and standard deviations of vertical-based RQA measures for each group
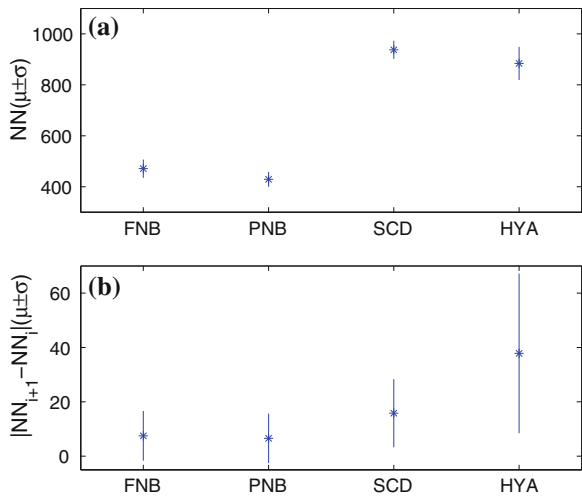
Fig. 9 Average values for the full set of HRV time series by taking for each series: **a** the NN interval and **b** the beat-to-beat NN interval variability

set of series in terms of beat-to-beat NN interval variability, the separation between groups is no longer possible as demonstrated in Fig. 9b.

The average accuracy values of RQA indexes obtained from SVM through comparison between groups of different ages are reported in Fig. 10. It is seen that RQA indices are better at distinguishing groups the larger is the age difference. In fact, for

Fig. 10 Average accuracy and standard deviation ($\langle a \rangle \pm \delta a$) obtained by SVM from the comparison between two NN intervals time series groups to RQA indexes. **a** Full-te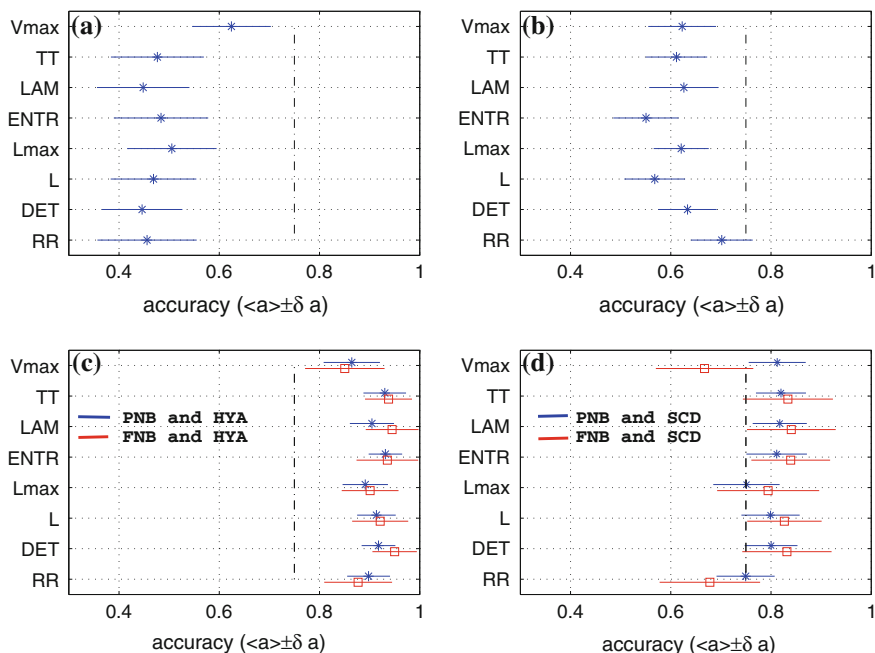rm newborn (FNB) and premature newborn (PNB), **b** healthy young adult (HYA) and adult with severe coronary disease (SCD), **c** premature newborn and healthy young adult (*red line*); full-term newborn and healthy young adult (*blue line*), **d** premature newborn and adult with severe coronary disease (*blue line*); full-term newborn and adult with severe coronary disease (*red line*)

close age difference as in Fig. 10a, b the average accuracies are restricted to 50 and 60 %, respectively. Nevertheless, this might indicate that age difference between the HYA and SCD groups is more significant than in groups FNB and PNB. In support to this conclusion, we see in Fig. 5 that the recurrence plots for the groups FNB and PNB look more similar than the RPs for the HYA and SCD groups (Fig. 6).

In addition, comparison of newborns with older individuals yields higher accuracy, namely, 80 % as demonstrated in Fig. 10d and 90 % in Fig. 10c. It is to be mentioned, however, that a larger age difference does not necessarily imply a larger accuracy, i.e., the larger accuracy in Fig. 10c is related to an age difference smaller than that in Fig. 10d.

5 Conclusion

The present study was concerned with recurrence quantification analysis (RQA) of HRV time series for groups of individuals with different ages. RQA was proven to be a powerful discriminatory tool to detect the degree of determinism of the systems

examined. Among the four groups studied, all the RQA measures (Figs. 7 and 8) were lower in the healthy young adults (HYA). Low TT, Lam, and Vmax, for instance, imply high complexity in the system's dynamics. This result is in line with the concept that high complexity is a general feature of healthy dynamics compared to pathological conditions.

We also verified that RQA measures were able to differentiate groups, with the results demonstrating that better discrimination is achieved the higher the age difference is. It was noted in Fig. 10c, d, however, that a higher age difference does not imply a higher discriminatory accuracy. The closeness of the comparison of the SCD group with the newborns (PNB and FNB) and the higher degree of dissimilarity between the HYA group and the newborns reflect the fact that the comparisons were quantified in terms of HRV, which is age dependent. This result shows that the HRV decreases with age as described in [3, 4].

Given that HRV time series reflects the complex interactions of different control loops of the cardiovascular control system, the results obtained here provide important information on the autonomic control of circulation in normal and diseased conditions. In addition, the approach discussed here permits an automatic analysis of a large number of time series, thus making the method useful in clinical sets and in epidemiological studies to analyze HRV series or other biomedical signals.

References

1. Wijngaarden, M.A., Pijl, H., van Dijk, K.W., Klaassen, E.S., Burggraaf, J.: Clin. Endocrinol. **79**, 648 (2013)
2. Kuusela, T.: Heart rate variability (HRV) signal analysis. In: Kamath, M.V., Morillo, C., Upton, A. (eds.) Methodological Aspects of Heart Rate Variability Analysis, pp. 9–40. CRC Press, Boca Raton (2013)
3. Yukishita, T., Lee, K., Kim, S., Ando Y.Y., Kobayashi, A., Shirasawa, T., Kobayashi, H.: Anti-Aging Med. **7**(8), 94 (2010)
4. Moodithaya, S., Avadhany, S.T.: J. Aging Res. **2012**(679345): 1–7 (2012)
5. dos Santos, L., Barroso, J.J., Macau, E.E.N., de Godoy, M.F.: Med. Eng. Phys. **35**, 1778 (2013)
6. Webber Jr, C.L., Zbilut, J.P.: J. Appl. Physiol. **76**, 965 (1994)
7. Marwan, N., Romano, M., Thiel, M., Kurths, J.: Phys. Rep. **438**(5–6), 237 (2007)
8. Ngamga, E., Senthilkumar, D., Prasad, A., Parmananda, P., Marwan, N., Kurths, J.: Phys. Rev. E **85**, 026217 (2012)
9. Wessel, N., Marwan, N., Meyerfeldt, U., Schirdewan, A., Kurths, J.: Lecture Notes in Computer Science **2199**(2199), 295 (2001)
10. Peng, Y., Sun, Z.: Med. Biol. Eng. Comput. **49**(1), 25 (2011)
11. Ramírez Ávila, G., Gapelyuk, A., Marwan, N., Stepan, H., Kurths, J., Walther, T., Wessel, N.: Autonomic Neuroscience: Basic and Clinical (2013)
12. Mesin, L., Monaco, A., Cattaneo, R.: BioMed Res. Int. **2013**, 420–509 (2013)
13. Zbilut, J.P., Webber Jr, C.L.: Phys. Lett. A **171**, 199 (1992)

14. Javorka, M., Trunkvalterova, Z., Tonhajzerova, I., Lazarova, Z., Javorkova, J.: Clin. Physiol. Funct. Imaging **28**(5), 326 (2008)
15. Selig, F.A., Tonolli, E.R., Godoy, M.F., da Silva, E.V.C.M.: Arq. Bras. Cardiol. **96**(6), 443 (2011)
16. Leal, J.C., Petruccic, O., de Godoy, M.F., Braile, D.M.: Interact. CardioVasc. Thorac. Surg. **14**, 22 (2012)
17. Gamelin, F.X., Berthoin, S., Bosquet, L.: Med. Sci. Sports Exerc. **38**(5), 887 (2006)
18. Vanderlei, L.C., Silva, R.A., Pastre, C.M., Azevedo, F.M., Godoy, M.F.: Braz. J. Med. Biol. Res. **41**(10), 854 (2008)
19. Nunan, D., Donovan, G., Jakovljevic, D.G., Hodges, L.D., Sandercock, G.R., Brodie, D.A.: Med. Sci. Sports Exerc. **41**(1), 243 (2009)
20. Task Force of the European Society of Cardiology the North American Society of Pacing Electrophysiology. Circulation **93**, 1043 (1996)
21. Marwan, N., Kurths, J.: Phys. Lett. A **302**, 299 (2002)
22. Cortes, C., Vapnik, V.: Mach. Learn. **20**, 273 (1995)
23. National Taiwan University, Taiwan, LIBSVM: A Library for Support Vector Machines (2012). http://www.csie.ntu.edu.tw/cjlin/libsvm/
24. Kennel, M.B., Brown, R., Abarbanel, H.D.I.: Phys. Rev. A **45**(6) (1992)
25. Fraser, A.M., Swinney, H.L.: Phys. Rev. A **33**(2) (1986)
26. Zbilut, J.P., Thomasson, N., Webber, C.L.: Med. Eng. Phys. **24**(43) (2002)

Analyzing Social Interactions: The Promises and Challenges of Using Cross Recurrence Quantification Analysis

Riccardo Fusaroli, Ivana Konvalinka and Sebastian Wallot

Abstract The scientific investigation of social interactions presents substantial challenges: interacting agents engage each other at many different levels and timescales (motor and physiological coordination, joint attention, linguistic exchanges, etc.), often making their behaviors interdependent in non-linear ways. In this paper we review the current use of Cross Recurrence Quantification Analysis (CRQA) in the analysis of social interactions, and assess its potential and challenges. We argue that the method can sensitively grasp the dynamics of human interactions, and that it has started producing valuable knowledge about them. However, much work is still necessary: more systematic analyses and interpretation of the recurrence indexes and more consistent reporting of the results, more emphasis on theory-driven studies, exploring interactions involving more than 2 agents and multiple aspects of coordination, and assessing and quantifying complementary coordinative mechanisms. These challenges are discussed and operationalized in recommendations to further develop the field.

1 Introduction

Human beings possess an impressive ability to coordinate their actions and goals—from the small scale of the dyad, all the way up to the largest scales that span social groups and societies. We coordinate while dancing [1], we excel at managing complicated traffic situations [2], we effectively share information and make important

R. Fusaroli (✉) · S. Wallot
Interacting Minds Center, Aarhus University, Aarhus, Denmark
e-mail: fusaroli@gmail.com

R. Fusaroli
Center for Semiotics, Aarhus University, Aarhus, Denmark

I. Konvalinka
Cognitive Systems, DTU Compute, Technical University of Denmark, Copenhagen, Denmark

collective decisions with colleagues and family members [3], and we even organize larger scale processes to sail massive battleships [4] and coordinate complex political systems [5]. Increasingly, the study of human cognition and behavior is focusing on the ways we interact to create such cognitive and behavioral synergies: the ways people effectively engage each other through language and actions, managing to coordinate their cognitive processes and even physiology, in order to create rapport, share information and achieve joint goals [6, 7]. Much is at stake in this enterprise, since social interactions do not only lie at the core of our private and economic well-being, but are also thought to be one of the most crucial aspects in mental health and healthy development [8].

In this article we discuss some of the crucial challenges in analyzing social interactions. Within this framework we introduce Cross Recurrence Quantification Analysis (CRQA). We systematically review the studies that have employed CRQA to analyze the unfolding of social interactions and the results they report.[1] The aim is to critically evaluate the potential of the method in assessing the quality of various interactions. Finally we discuss the challenges still to be faced and we provide recommendations to further develop the field.

2 Analyzing Social Interactions: The Challenges

When compared to the classical research paradigms in cognitive psychology, the study of human interactions presents tough methodological challenges to the cognitive scientist [9]. In an interaction there are at least two agents, most often employing several expressive modalities (e.g. words, prosody, gestures, posture, etc.) and continually influencing each other, in ways that are difficult to capture when the individual behaviors are analyzed separately [10–12]. Much of the research in social cognition has either focused on the quantification of intra-personal phenomena, or confined research to ask very basic questions, such as "how strongly aligned are the interacting agents?" [13], assuming homogeneous and stationary behavior across the whole episode of interest. This approach has produced valuable insights into human interactions: by measuring how similar the frequency of given behaviors are between interacting individuals, it has been shown that people engaged in interactions tend to imitate each other's gestures [14] and align their lexicon and syntax [15, 16].

However, interactions are more complex than that. Doing the same thing is not enough to make an effective joint decision, or to coordinate on who is going to pass through a narrow train corridor first. Much in interactions is about not doing the same thing, establishing differential roles (e.g. a leader and a follower) [17–19], complementing each other (e.g. following a question with an answer, or produc-

---

[1] The review was accomplished by searching for "cross recurrence" and "crqa" on PubMed, Google Scholar and Web of Science (on October 1st 2013) and then manually selecting the articles analyzing social interactions. We followed up on the bibliography of these articles to individuate further relevant ones. The resulting list counts 41 articles, 34 of which reporting empirical studies and the rest being reviews or method papers. To these we added 6 submitted, but not yet published papers.

ing complementary actions to better coordinate a task) [20, 21]. This is especially emphasized through the use of culturally evolved routines (e.g. how to greet, how to apologize and how to repair misunderstandings) and scripts which enable to maximize efficiency (e.g. military rules of conduct and codes for emergencies) [10, 22].

In addition, interactions tend to behave in non-stationary ways. For example, imagine the escalation inherent in a heated discussion where interlocutors keep topping each other's voice or periods of high engagement followed by disengagement in attacker-defender exchanges in sports [23]. This implies that the statistical measures of moment-to-moment interactions (such as the mean and the range of values) might vary over time, defying the assumptions of linear methods [24, 25], and poses important methodological problems for the field of quantitative interaction studies.

We introduce CRQA as a way to cope with at least some of theseissues, and show how this non-linear method has proven suitable in quantifying many non-stationary coordinative patterns across various modalities and interactions, as well as discuss the challenges that it still faces.

3 An Introduction to Cross Recurrence Quantification Analysis

CRQA was introduced by Zbilut et al. [26] as an extension of Recurrence Quantification Analysis (RQA, for a comprehensive discussion of the method, see [27]). RQA is a more articulated non-linear equivalent of auto-correlation. It reconstructs the dynamical system underlying a time-series, maps its possible states and quantifies the trajectory of the system through these states [28]. RQA thus grants quantitative indexes of how strongly patterned the behavior of a system is, which kinds of patterns are repeated and how complex/flexible the repetitionsare. CRQA could analogously be defined as a more sophisticated non-linear equivalent of cross-correlation: it quantifies the strength, but also the form and complexity of the shared dynamics of two systems. By reconstructing the possible states of the two systems and assessing the points in time in which they visit similar states, CRQA quantifies how often the two systems display similar patterns of change or movement, and how complex the structure of the entrainment between their trajectories is.

Several parameters have been suggested to articulate the structure of the coordination between two systems. Cross Recurrence Rate (RR) represents the "raw" amount of similarities between the trajectories of the two systems (the degree to which they tend to visit similar states). The structure of the similarities can be assessed along the diagonal and the vertical dimension. Diagonal structures represent periods in one time series that follow similar paths in their time-evolution to those in another time series, when aligned or shifted in time. The more closely coupled the two systems are, in terms of sharing the same paths, the more recurrences will be organized in diagonal lines. The measure that captures the rate of recurrence points forming diagonal lines is called determinism (DET) of the interaction between the two time series. The average length of the diagonal lines (L) represents the time that both systems stay attuned. The longest diagonal line on a recurrence plot (LMAX) represents the

longest uninterrupted period of time that both systems stay attuned, which serves as an indicator of stability of the coordination: for example, sensitivity to noise and external perturbations creates unstable sequences of coordination and therefore a shorter longest diagonal line. It is also possible to measure how complex the attunement between the systems is (entropy or ENTR): if the diagonal lines tend to all have the same length the attunement is very regular (low ENTR), otherwise the attunement is complex (high ENTR). Finally, by analyzing which delay maximizes recurrence (diagonal recurrence profile, or DiagProfile), it is possible to observe the direction of the coordination, that is, if there is an asymmetry with one interlocutor leading the other. Diagonal structures thus highlight shared trajectories and their properties.

As an example, we simulated a strong and consistent coupling between two oscillators (i.e. the black and red time-series) in the line plot in Fig. 1a. Immediately below, the coupling can be observed in the cross-recurrence plot in the form of very evident diagonal structures. In Fig. 1b we introduced strong white Gaussian noise, creating two time-series with less stable coupling. This is reflected in the much weaker diagonal structures (fewer recurrences organized in diagonal lines and much shorter lines) in the cross-recurrence plot.

Vertical structures in a cross-recurrence plot quantify the propensity of the trajectories to stay in the same region (i.e. repeat the same value). In particular, the percentage of recurrence points forming vertical lines (as opposed to being isolated dots) is informative of the laminarity (LAM) of the interaction, and the average length of the vertical lines (trapping time, or TT) represents the average time two trajectories stay in the same region. As an example, in Fig. 1c we display the effects of stabilizing the two time-series at two moments (the flat lines in the line plot). The permanence of the trajectories in the same region (repeating the same value) is reflected in the vertical structures in the cross-recurrence plot.

While these examples are all of continuous variables, which have initially been the main focus of CRQA analyses, recent studies have developed ways to also explore the recurrence and cross recurrence of nominal sequences. These include sequences of phonemes, words, and coded behavior, such as the presence or absence of a particular gesture, or a nod [24, 30].

CRQA thus might constitute an answer to some of the issues posed by the analysis of social interactions: It enables the analysis of the shared dynamics of two time series. It is highly sensitive to the temporal structure of the interactions and to their nonlinear trends. It can cope with a wide variety of data, thus quantifying interactions between people in a wide range of modalities. Its output is highly articulated, allowing a fine-grained understanding of the structure of the shared dynamics between two agents. In the following section we investigate these potentialities, by critically reviewing the aspects of human interactions to which the method has been applied, and the picture that the results of the analyses enable us to sketch.
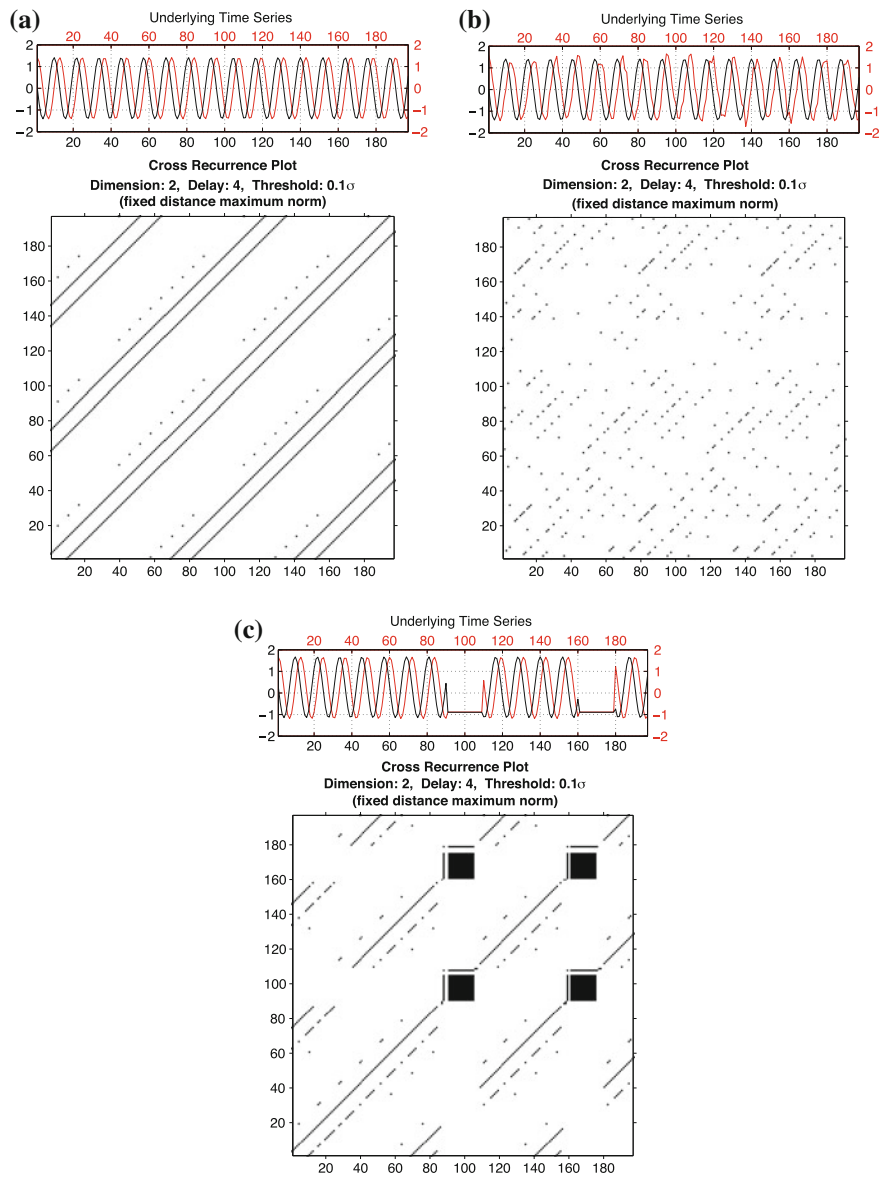
Fig. 1 Examples of diagonal and vertical recurrence structure. The plots were generated using the CRP toolbox for Matlab [29]

4 CRQA and Social Interactions: From Swinging Pendula to Conversation

A first crucial question to be answered is: can CRQA be used to assess the coupling between two systems (i.e. interpersonal coordination) at all? In other words, can it successfully assess the same dynamics assessed by other dynamical systems models, which are already widely used and very successful in capturing interpersonal phase and anti-phase synchronization [31–33]? In order to address these questions, Shockley et al. demonstrated the effectiveness of the method in assessing and quantifying coupling between two physical systems, above and beyond linear methods including cross-correlation and spectral analysis [34], by capturing shared dynamics using CRQA (quantified via both diagonal and vertical recurrence structures). It is thus no surprise that CRQA has been effectively employed to show basic synchronization phenomena between interacting agents. For example, people swinging pendula in a coordinated fashion show strong and stable coordination (high RR and LMAX, see [35]).

Given the complexity often present in any system's behaviors, it is, however, crucial that CRQA indexes are compared to an appropriate baseline, so to ensure that the degree of coordination they express is indeed due to coupling between the systems analyzed. A commonly employed baseline is the use of shuffled data, which maintains distributional properties but not the information contained in the temporal sequence of the data. In some cases, surrogate pairs are a more appropriate control condition, which consist of computing cross recurrence of time-series from mismatched pairs (e.g. matching the data from person A from pair 1 with the data from person B from pair 2). In surrogate pairs the overall individual structure is maintained, but the coupling dynamics are disrupted. The advantage of surrogate pairs is that they preserve the temporal organization of the overall event (e.g. the experimental task) as reflected in the individuals' time-series, but disrupt the actual dynamics between interacting agents. However, this control conditionis problematic in at least two cases: if the coordination analyzed involves turn-taking with alternate production of behavior of varying length (e.g. a conversation), the temporal structure of adjacent turns and the different lengths of the time-series would not be respected. A second problematic case is nominal time-series with sparse data, such as coded nodding, for which computer simulations have shown that shuffled data are a more conservative baseline [36]. Finally, a few studies have employed within pair contrasts: for example, in Ramenzoni et al. [37] the same pairs performed both interactive and non-interactive but otherwise similar tasks, with the non-interactive condition providing an ideal baseline. Analogously, Konvalinka et al. [38] compares the levels of heart rate coordination during a religious ritual with coordination before the ritual itself.

Once the sensitivity of CRQA to interpersonal coordination has been established against an appropriate baseline, the second question is: what does it add to a simpler phase analysis? CRQA is particularly useful for analyzing shared dynamics between signals that are not necessarily periodic in nature, or rather, whose periodic quali-

ties are more complex, and hence relative phase analysis is not so straightforward. CRQA has thus been applied to many different aspects of complex interpersonal coordination, which would not be easily amenable to phase analysis, ranging from physiological to motor, linguistic and even conceptual ones.

A series of studies has shown how physiological signals, such as heart rate, also coordinate between individuals. Konvalinka et al. hypothesized physiological coordination to be involved in the community consolidating effects of highly arousing rituals. They investigated a fire walking ritual in Spain, showing that heart rhythms of firewalkers were more closely matched by heart rhythms of spectators who were their relatives or friends than those of non-related spectators, during the course of the ritual (higher RR, DET, LMAX, ENTR and LAM, see [38])—despite the fact that they did not have the same behavior. Fusaroli et al., in a less dramatic setting, investigated heart rate coordination in collective Lego construction tasks [39]. Groups of five participants built Lego models of abstract notions such as "trust" and "safety" alternatively as individuals ("Build your own individual model of trust") and collectively ("As a group build a model of trust that you all agree upon"). Interpersonal heart rate coordination (RR, L and ENTR) was shown to be significantly present in all groups both during individual and collective trials against shuffled baseline. However, a contrast with surrogate pairs showed no difference in individual trials—coordination being likely driven by task constraints as all participants in all groups were doing similar things—and higher levels of coordination during collective trials—coordination being likely driven by actual interactions.Not least, coordination during collective trials was shown to grow over time.

Focusing on motor coordination, Ramenzoni et al. assigned pairs of participants an interpersonal precision task: one participant holds a circle and the other has to keep a pointer inside the circle without touching its sides [11, 37, 40]. Hand and postural movements were strongly and stably coordinated across participants (RR and LMAX higher than in a non-interactive task), and increasing the difficulty of the task with smaller circles increased the coordinative structures. Analogously, stable coordinative structures were highlighted in groups of pedestrians walking in a crowded space (higher LMAX than control conditions, see [2]), and in duos and quartets of musicians and dancers [41, 42].

Interpersonal motor coordination appears very early in development: Reddy et al. investigated the specific structures of interpersonal coordination in infants anticipating being picked up [43]. Employing a pressure mat, the researchers showed that legs and arms of the infant are significantly coordinated (higher RR) with the mother already at 2 months of age, while full-bodied coordination appears at a later stage.

Notably, all of these studies have used high recurrence as the marker of coordination. However, Wallot et al. [44] present less straightforward findings. Pairs of participants built Lego cars together, while their hand-movements and heart rates were monitored. While significant behavioral and physiological coordinative structures were found (DET), they were negatively correlated with the effectiveness of the interaction measured in terms of functionality and aesthetic appeal of the resulting cars. These results might be interpreted as an effect of task constraint: doing the same thing might be counter-productive to effective collective construction, while distrib-

uting different subtasks—a division of labor strategy implying different actions for each participant—would be a better strategy.

Motor coordination has also been observed during conversations, where language acts as a highly effective social coordination device [16, 45, 46]. For instance, pairs of participants engaged in a joint problem-solving task show high coordination (RR and LMAX) in their postural sway, even when they are not looking at each other [47, 48]. In a follow up experiment, Shockley et al. showed that postural sway coordination is mediated by two factors: interlocutors employing increasingly similar speech patterns, and actual interaction as opposed to simply repeating the same words in unison [49]. However, Richardson et al. report significant unintentional coordination (RR and LMAX) of hand-held pendula when pairs of participants solve a joint task while able to see each other, but where verbal interactions do not seem to have an effect [50]. This might be due to postural sway being a more natural part of linguistic interactions than swinging hand-held pendula.

While postural sway and hand-held pendula coordination might seem a simple byproduct of verbal coordination, or at most a facilitation of social rapport [51], other forms of coordinated behavior might have a more explicit functional role: for example, shared attention often relies on head movement and gaze coordination. It has been observed in several conversational contexts that interlocutors tend to coordinate gaze direction (high RR and low DiagProfile, [52]) and head movements (high RR, DET, L, LMAX, ENTR, LAM, TT, [53]), the latter which is mediated by dominance (higher scores for pairs with a dominant interlocutor) and gender (higher scores for women).

Gaze direction has been extensively explored in conversational scenarios by Richardson, Dale et al. The researchers recorded the speech and eye movements of one set of participants as they described pictures of six cast members of a TV sitcom. A second set of participants listened to these descriptions while looking at the same pictures. Gaze was highly coordinated between participants (RR), especially at a 2 s lag; in addition, the level of coordination correlated with the comprehension of the description [54]. When pairs of participants were asked to actively discuss pictures, the delay disappeared: they looked at the same elements at the same time [55]. In a third experiment, the researchers manipulated how much shared knowledge the participants had on the pictures to be discussed. Higher amount of shared knowledge generated higher coordination in eye movement [56]. In a final study, pairs of participants were presented with the same set of abstract shapes portrayed in different orders and they had to alternate in directing each other so that the orders would match. As the participants developed a common language to refer to these shapes, their eye-movements became increasingly coordinated at lag 0, suggesting that they sampled the world in increasingly similar and effective ways [57]. Analogously, it has been shown that eye-movement recurrence is statistically higher when anaphoric and referential expressions are used [55, 58].In other words, specific linguistic items can be used as devices to further increase coordination. These results are supported by Jermann and Nussli's study, which reports increased gaze coordination (RR) in programmers jointly analyzing code, when they are allowed to talk and/or select portions of the text for each other [59]. In other words, by developing and

implementing a shared language, participants develop effective interpersonal attention management systems [60]. These effects are not just limited to gaze or head movement coordination, but also include behavioral matching of facial expressions, nodding, touching face, chin-resting, and manual gestures. Evidence for this comes from a systematic study investigating all of these behavioral measures during a task oriented conversation, where synchronous behavior matching was found across all the parameters (RR and DiagProfile) [36].

Up to now we have discussed how language facilitates motor coordination. However, the conversation itself also becomes coordinated between interlocutors as they manage turn-taking, adapt to each other's tone and language, construct shared routines, etc. The structure of turn-taking has been analyzed in many different ways: nominal sequences of 1s (interlocutor speaking) and 0s (interlocutor being silent) [52, 53, 61, 62], employing utterance length [63, 64], or simply the sequence of interlocutors [65]. In all cases CRQA showed significant amounts of coordination (RR, cf. [52, 64]), tendency to keep attuned (DET [65]), synchronization (DiagProfile, [52, 62]) and in general diagonal and vertical recurrence structures [53, 63]. The amount of coordination has been reported to positively correlate with the experiential quality of the interaction [52, 64] and with the familiarity between interlocutors [65]. In other words, when we converse we (unsurprisingly) coordinate our utterances, this coordination is easier when we have familiar interlocutors, and the more coordinated we are the better the experience of the interaction.

From the developmental perspective, just as Reddy et al. [43] showed the coordinative adjustments in infants' movements, studies have demonstrated prosodic (fundamental frequency) coordination already from 3 months [66] and turn-taking coordination in children from at least 1 year of age [63]. However, turn-taking coordination seems to change in nature, being more rigid and repetitive (higher vertical structures) in younger children, and more flexible and extended (more prominent diagonal structure) in older ones [63]. Cognitive impairment (adults, [52]) and developmental disorders (children with autism, [62]) involve a statistically lower amount of coordination and lack of immediate responsiveness (lower RR and higher DiagProfile). However, the amount and the function of coordination cannot be so simplistic described. For example, an exploratory study on adolescents with Moebius syndrome (involving congenital facial paralysis) shows high levels of conversational coordination in pitch and speech rate (RR, DET, L, LMAX), which decrease after an intervention aimed at improving social skills [67].

A few studies have also attempted to tackle the coordination of linguistic contents. Orsucci et al. [30, 68–70] tested CRQA of more symbolic aspects of language: they analyzedtranscripts of conversations by focusing on the recurrence of sequences of 3 characters roughly corresponding to morphemes.[2] A natural conversation showed stronger coordinative patterns and attunement (RR and DET) than a clinical psychotherapy session, during which the patient's production tended to drift away from the therapist's. Dale and Spivey have investigated the coordination of syntactical

---

[2] The characters (including spaces) are converted to numbers, the embedding dimensions are set to 3, and the threshold to 0, to respect the categorical nature of the data.

patterns of words in children and caregivers engaged in naturalistic conversations (from the CHILDES corpus),reporting significant syntactic coordination (RR). While the coordination decreased as they grew up, it changed direction: initially the children followed adults, to increasingly assume leadership at later stages [71]. Louwerse et al. investigated the coordination of dialog acts (questions, answers, instructions, etc.), discourse connectives ("Alright", "ok", "hmm") and landmark descriptions in conversations where pairs of participants had to give each other instructions on how to draw a path on a map [36, 72]. Interestingly, they observed significant amounts of coordinative structures (RR and DiagProfile), which would decrease over time as the participants developed more minimal and effective ways to coordinate. However, when the difficulty of the task was increased, coordinative structures also increased.

Fusaroli et al. analyzed several aspects of linguistic coordination at once in a series of task-oriented conversations [3, 73]. They analyzed coordination in turn-taking(as sequences of 1 and 0 s), prosody (as fundamental frequency) and morphemes (as sequences of 3 characters)—and assessed it in relation to the efficacy of the conversations in enabling accurate solution of the task (a joint decision making). Pairs of participants showed consistent coordinative structures (L and ENTR)in all linguistic aspects analyzed, when compared to shuffled controls. However, the researchers argued that while CRQA quantifies the shared dynamics between participants, it might not capture other coordinative structures, for instance, complementary dynamics in which an interlocutor would share information only to be answered by the other making a decision. Little alignment would be found there due to the different prosodic and lexical patterns involved in the two distinct conversational moves, but not for lack of tight coordination. These dynamics were better captured by employing RQA on the conversation as a whole without discriminating between interlocutors, and therefore highlighting how patterned and routinized the conversation became trial after trial. In a comparative analysis, while CRQA of prosody and morphemes positively correlated with performance, RQA of all aspects (turn-taking, prosody and morphemes) consistently provided better predictors of performance, with each aspect contributing non-overlapping information [61]. In other words, the best way to capture effective coordination was to look at how routinized the interactions became, making the decision making process as standardized, quick and efficient as possible. Those routines manifested at a lexical, prosodic and pause level. CRQA was not fully able to capture these complementary dynamics, but RQA was.

Angus et al. took an even more radical approach [74–77]. Being interested in the conceptual structure of conversations they organized the words used in the corpus in conceptual clusters, according to their co-occurrences within the same speech-turns, or to pre-defined conceptual domains. They then analyzed the coordination of these conceptual clusters, defining new recurrence indexes taking into account the timescale (adjacent, mid-range, global), direction (backward and forward) and type (auto vs. cross recurrence). While still exploratory, these indexes of conceptual recurrence nicely characterized case studies including phone conversations, diagnostic interviews in clinical settings, and aircraft transcripts.

5 Challenges and Recommendations

We have shown that CRQA is suitable for analyzing many different aspects of coordination, from low-level physiological and motor synchronization, to complex joint actions and even symbolic and conceptual aspects of conversations. While several papers report case studies (11 out of 35), or limited numbers of participants, an increasing amount is scaling up the use of CRQA to statistically relevant samples (18 out of 35). The most basic indexes of recurrence—RR, DiagProfile and LMAX—have been shown sensitive to a wide range of conditions—such as gender, age, dominance, familiarity, modality of interaction and difficulty of the interaction—and to be reflected in the experience of the interaction. Other indexes—such as DET, L, ENTR, TT and LAM—are more sparsely employed, making it difficult to produce a clear picture of their relevance and meaning.

The most common result is that social interactions display higher amount and structure of recurrence than controls; however, a few isolated findings present more nuanced or even opposite findings, which seem worthy of further development and testing (cf. Challenge 2). We argue that the studies have demonstrated great promise for using CRQA to study social interactions, but that this analysis in relation to interaction is still in its birth, and we have only begun to ask many of the relevant questions. In particular we feel that the field faces 7 crucial challenges:

Challenge 1: to use CRQA when it is most appropriate and make its advantages explicit. Many researchers in psychology have shied away from applying CRQA to their data, even when working with continuous time-series that exhibit a non-linear, non-stationary structure. CRQA is a powerful but complex tool for the analysis of interaction data with an initial steep learning curve, and it has an articulated output that is often tricky to interpret. Thus, it might seem overly and unnecessarily complicated to scientists trained in more traditional methods. While it has proven capable of capturing basic periodic coordination (an important result to establish the validity of the method), for time-series that are predominantly linear in nature it might be more appropriate to use simple correlation-based analysis. Similarly, for quantifying non-linear coupling between certain periodic signals, phase analysis might be sufficient. Not by chance, recent research on basic synchronization skills in clinical populations has been conducted with analysis of phase and coupled oscillators models by authors well versed in CRQA [31, 33, 78]. While perfectly able to analyze these phenomena, CRQA gives its best on more complex and noisy data, which make it easier to justify its use. By more explicitly making CRQA one of the tools in the scientist's toolbox, arguing for its well-aimed use and showcasing its advantages over linear models for complex noisy data, it will be easier to get it accepted in mainstream research.

Challenge 2: to complement exploratory studies with theory-driven ones. This second challenge is shared with much of the investigations in social interactions. It is an informative and necessary step to explore the behavior of CRQA indexes in different coordinative contexts and on different aspects of coordination. However, such exploration should lead to theory-driven studies.

A first step in this direction is a more systematic exploration and report of indexes of cross recurrence across different types of interactions and modalities, which would be very useful in pinning down general patterns indicative of different coordination types. This could lead to the possibility of more fine-grained analyses in new contexts, where multiple CRQA indexes could be used to better assess the type of coordinative behavior—whether it is synchronized, stationary, and whether there are distinctive changes in coordinative structures throughout the interaction itself (i.e. mutual adaptation changing into leader-follower dynamics). In parallel, researchers should more consistently report their results: not only report all CRQA indexes to facilitate a more fine-grained grasping of the coordinative dynamics involved, but also effect sizes and statistical power (currently missing from the large majority of the studies reviewed). This would enable an easier planning of follow-up studies and facilitate cumulative science [79–82].

However, a more substantial step is the construction of conceptual models of coordination, which could generate hypotheses as to which recurrence indexes would be impacted by a manipulation, in which direction and, possibly, which range of effect sizes would be interesting. While RQA/CRQA has been really useful in analyzing non-linear dynamics across various modalities of human interaction, its interpretation and impact is sometimes unclear given the exploratory nature of most of these studies. For example, finding stronger coordination (i.e. higher RR, DET, LMAX) between certain motor activities of two people engaged in an interaction versus not interacting is interesting, but not particularly surprising. How can we use this information to make predictions about future behavior, about the outcome of the interaction, or for example, about the strength of rapport between two people? Some preliminary ideas are suggested by the studies reviewed, others by ongoing conceptual reflections in the field of interactions studies. For instance, a few studies seem to suggest that vertical structure and consistent delay in DiagProfile are related to simpler and more hierarchical interactions, while diagonal structures and low or alternating delay could be related to fluid, bidirectional, and flexible interactions. A second line of results questions the straightforward relation between amount and structure of recurrence and successful coordination, which is often assumed. In parallel, more conceptual studies have been developing the idea of alignment in social interactions as only one of the mechanisms at play, especially useful to initially establish the coordination and later to signal and repair problems, or even reinforce coordination if the difficulty of the task increases [83]. However, many forms of coordination include complementary dynamics, roles, and routines, which would require more nuanced analyses and could involve a decrease in recurrence diagonal structures. Thus, CRQA indexes might not increase with more fluent coordination and might not necessarily correlate with performance. This model could be used to hypothesize high presence of diagonal structures at the beginning of an interaction, which would decrease over time.

These are only initial suggestions: the study of social interactions in general needs more explicit models of coordination, and empirical investigations developed to assess and compare them [6, 10].

Challenge 3: to take into account multiple aspects of coordination at once and their interdependence. Studies like the ones performed by Louwerse [36], Fusaroli

et al. [39, 61] are promising in these respects in that they systematically investigate several aspects of coordination at once and offer the possibility to map their interconnections. Dale and Louwerse are exploring how the many coordinated aspects of interpersonal behavior highlighted in their previous study relate to each other [72]. Analogously, Fusaroli et al. are exploring the connections between speech, actions, and heart rate coordination to understand what are the means through which physiological coordination is achieved [39]. It might be expected that not all aspects of coordination behave equally: for instance, achieving high levels of shared dynamics in motor behavior might create the enough common ground to enable interlocutors to effectively diversify their linguistic behavior [36], or vice versa highly shared linguistic dynamics might make complementary actions possible [44]. In any case, multivariate analyses of the multiple aspects seem necessary to account for many aspects of coordination at once [84, 85].

This might seem at odd with the previous challenge (more theory-driven studies to complement the explorative ones). We argue that it is possible to design a theory-driven experiment, with precise hypotheses, and complement it with exploratory analyses of a wider range of coordinative aspects and CRQA indexes, which will help generate new hypotheses for further studies.

Challenge 4: to account for multiple forms of coordination: complementarity and routines. Interestingly, the studies mentioned in the previous challenge also raise additional important issues for the study of coordination and the use of CRQA: In Louwerse et al., while the recurrence rate of many behaviors tends to grow over time, it decreases for others, in particular for language. In Fusaroli et al. CRQA parameters are a much worse index of effective coordination than Recurrence Quantification Analysis of the overall conversation [61]. Several other studies have shown that complementarity (rather than symmetry in action) is crucial for facilitation of coordination, as well as action understanding [10, 11, 21, 86, 87]. For example, when trying to move a table from one room to another, two people might produce complementary movements in order to more effectively achieve this goal—one person faces away from the table, grasping it with their hands behind them, while the other grasps it with their hands in front of them, facing the table [88]. Similarly, complementarity was encountered in a study where participants moved a marble in one direction by either one participant holding her edge of the tablet while the other is lifting it or one participant lowering her edge of the tablet while the other one is lifting it [89]. A cross-recurrence plot of the hand-accelerations of participants, which was the dependent measure in this study, would either show strong cross-recurrence (when one participant would accelerate by lowering the tablet and the other one would accelerate by lifting the tablet) or weak cross-recurrence (when one would accelerate by lifting the tablet, but the other one would hold her hands still). In this case, an increase in cross recurrence structure does not equate to better coordination, but a more nuanced and task-specific understanding of coordinative structures has to be produced.

Fusaroli et al. [61] argued that in conversations and other kinds of coordination characterized by turn-taking complementarity might be captured by running RQA on pooled data from both participants: e.g. the whole conversation, without discrim-

inating between interlocutors. Unfortunately, this does not seem a viable solution for assessing complementarity in tightly coupled motor interactions, where all agents continuously produce behavior. Whether CRQA can be developed to address complementarity in interaction remains an open question.

Challenge 5: to better understand how individual behaviors affect interpersonal coordination (and viceversa). Many studies have investigated the distinctive behaviors of people with mental and developmental disorders. For instance, RQA has been effectively used to characterize the distinctive speech patterns of people with autism, schizophrenia, depression and right hemisphere damage [90–93]. However, there is no model to understand how such individual patterns impact conversations and are therefore related to the social impairment these patients experience. More investigations and methodological development are needed to build more articulated models of coordination and advance our understanding in these fields.

Challenge 6: to account for multiple time scales at play in the interaction. Social interactions include processes and phenomena happening at many time scales [94, 95]. Continuous reciprocal adaptation might be a necessity when initiating an interaction and learning to coordinate with each other. However, interacting agents might gradually stabilize conventions such as local routines and even employ socially established scripts. How do we take these numerous time-scales into account? Angus et al. have developed interesting measures of conceptual recurrence reflecting short, mid and long range coordination [74]. More general forms of multi-scale recurrence quantification analysis have only recently started to be developed, but they might be crucial in solving these issues [96–100].

Challenge 7: to analyze interactions with more than two participants. Social interaction often involves more than two participants. Most current studies split the groups in sets of dyads [38, 39] and one uses aggregative measures [2]. It is an open challenge to preserve the group dynamics. Joint recurrence, network theory and probabilistic graphical models could provide ways to do so.

While many of these challenges require conceptual and methodological development, we advance some recommendations (often applying to the study of social interactions in general, irrespective of the methods employed), which would help developing the field:

• *When possible attempt theory-driven predictions to identify relevant aspects of behavior, relevant recurrence indexes, and direction and size of the effect hypothesized.* These predictions should take into consideration the form of coordination required by the task employed: for instance a task encouraging differential roles between the participants might yield less cross recurrence and diagonal structures when effectively coordinated than ineffectively. In this case, CRQA might not be the best method to use, as it would be difficult to tell whether less recurrence is because of weaker coupling, or complementary movements. On the contrary, a task based on similar roles would imply effective coordination with high levels of diagonal structures.Also, it would be useful to specify at which time-scale one would expect shared dynamics, as initial short-term alignment might be replaced

by complementary roles and only be visible on longer time-scales as the participants switch roles.

- *Systematically use control conditions and appropriate baselines*. Since CRQA involves defining optimal parameters for each dataset (e.g. via normalizing and thresholding procedures), it is not always clear what constitutes statistically significant synchronization/coordination. Hence, appropriate control conditions should be designed, or failing that shuffled surrogates and false-pair-surrogates should be employed.

- *Support the development of a finer grasp of the coordinative structures observed by reporting analyses on all recurrence indexes and not only the most common or the significant ones*. When reporting results add a paragraph integrating the pattern of effects across the measures, which might help specifying which particular aspects of an interaction contributed to an outcome. For instance, an increase in L and LMAX could suggest that the duration of only one of many different time intervals during the interaction is crucial for the outcome, while an increase in L without a substantial increase in LMAX could be suggestive of a more systematic back-and-forth in an interaction, where a clear alternation between behaviors is crucial.If necessary, less theory-drivenanalyses and interpretationscouldbe reported in the appendixes/supplementary materials.

- *Support cumulative research and reproducibility, by calculating and reporting effect size and statistical power*. Also, when possible, apply more advanced statistical methods, such as resampling methods to RQA/CRQA parameters (jackknifing, bootstrapping) to better estimate statistical precision [101].

6 Conclusions

In general, CRQA shows great promise for better understanding of the multiple timescales and parameters underlying social interactions. Important groundwork has been performed on a wide range of interpersonal phenomena: from physiological synchronization to complex joint actions and conversations. In this paper we have delineated seven crucial challenges and suggested a few recommendations to further develop the field. We believe that cumulative and theory-driven approaches,the analysis of complementarity,and more-than-two-agent interactions are some of the main challenges CRQA is still facing in its application to the study of social interaction.

References

1. Kimmel, M.: Intersubjectivity at close quarters: how dancers of Tango Argentino use imagery for interaction and improvisation. J. Cogn. Semiot. **4**, 76–124 (2012)
2. Kiefer, A.W., et al.: Quantifying the coherence of pedestrian groups. in Cog Sci 2013, Berlin (2013)
3. Fusaroli, R., et al.: Coming to terms: an experimental quantification of the coordinative benefits of linguistic interaction. Psychol. Sci. **23**(8), 931–939 (2012)
4. Hutchins, E.: How a cockpit remembers its speeds. Cogn. Sci. **19**(3), 265–288 (1995)
5. Miller, J.H., Page, S.E.: Complex Adaptive Systems: An Introduction to Computational Models of Social Life. Princeton Studies in Complexity. Princeton University Press, Princeton (2007)
6. Dale, R., et al.: The self-organization of human interaction. Psychol. Learn. Motiv. **59**, 43–95 (2013)
7. Hasson, U., et al.: Brain-to-brain coupling: a mechanism for creating and sharing a social world. Trends Cogn. Sci. **16**(2), 114–121 (2012)
8. Steptoe, A., et al.: Social isolation, loneliness, and all-cause mortality in older men and women. PNAS **110**(15), 5797–5801 (2013)
9. Van Orden, G.C., Holden, J.G., Turvey, M.T.: Self-organization of cognitive performance. J. Exp. Psychol. Gen. **132**(3), 331 (2003)
10. Fusaroli, R., Raczaszek-Leonardi, J., Tylén, K.: Dialog as interpersonal synergy. N. Ideas Psychol. **32**, 147–157 (2014)
11. Riley, M.A., et al.: Interpersonal synergies. Frontiers Psychol. **2**, 38 (2011)
12. Konvalinka, I., Roepstorff, A.: The two-brain approach: how can mutually interacting brains teach us something about social interaction? Frontiers Human Neurosci. **6**, 1 (2012)
13. Bakeman, R., Gottman, J.: Observing Interaction: An Introduction to Sequential Analysis, 2nd edn. Cambridge University Press, Cambridge (1997)
14. Chartrand, T.L., Bargh, J.A.: The chameleon effect: the perception-behavior link and social interaction. J. Pers. Soc. Psychol. **76**(6), 893–910 (1999)
15. Pickering, M.J., Garrod, S.: Toward a mechanistic psychology of dialogue. Behav. Brain Sci. **27**(02), 169–190 (2004)
16. Fusaroli, R., Tylén, K.: Carving Language for Social Coordination: a dynamic approach Interaction studies **13**(1), 103–123 (2012)
17. Sacheli, L.M., et al.: Kinematics fingerprints of leader and follower role-taking during cooperative joint actions. Exp. Brain Res. **226**, 473–486 (2013)
18. Skewes, J., et al.: Implicit negotiation of leader-follower dynamics in an asymmetric joint aiming task. (under Revision)
19. Noy, L., Dekel, E., Alon, U.: The mirror game as a paradigm for studying the dynamics of two people improvising motion together. PNAS **108**(52), 20947–20952 (2011)
20. Sebanz, N., Bekkering, H., Knoblich, G.: Joint action: bodies and minds moving together. Trends Cogn. Sci. **10**(2), 70–76 (2006)
21. Masumoto, J., Inui, N.: Two heads are better than one: both complementary and synchronous strategies facilitate joint action. J. Neurophysiol. **109**(5), 1307–1314 (2013)
22. Mills, G.: Dialogue in joint activity: complementarity, convergence and conventionalization. N. Ideas Psychol. **32**, 158–173 (2014)
23. Vilar, L., et al.: Coordination tendencies are shaped by attacker and defender interactions with the goal and the ball in futsal. Hum. Mov. Sci. **33**, 14–24 (2014)
24. Dale, R., Warlaumont, A.S., Richardson, D.C.: Nominal cross recurrence as a generalized lag sequential analysis for behavioral streams. Int. J. Bifurcat. Chaos **21**, 1153–1161 (2011)
25. Coco, M.I., Dale, R.: Cross-recurrence quantification analysis of categorical and continuous time series: an R package. arXiv preprint arXiv:1310.0201, (2013)
26. Zbilut, J.P., Giuliani, A., Webber, C.L.: Detecting deterministic signals in exceptionally noisy environments using cross-recurrence quantification. Phys. Lett. A **246**(1), 122–128 (1998)

27. Marwan, N., et al.: Recurrence plots for the analysis of complex systems. Phys. Rep. **438**(5–6), 237–329 (2007)
28. Takens, F., Rand, D.A., Young, L.S.: Detecting Strange Attractors in Turbulence, in Dynamical Systems and Turbulence, pp. 366–381. Springer, Berlin (1981)
29. Marwan, N.: Cross recurrence plot toolbox. Available at http://tocsy.pik-potsdam.de/crp.php (2012)
30. Orsucci, F., Giuliani, A., Webber, C.: Combinatorics and synchronization in natural semiotics. Physica A: Stat. Mech. Appl. **361**(2), 665–676 (2006)
31. Isenhower, R.W., et al.: Rhythmic bimanual coordination is impaired in young children with autism spectrum disorder. Res. Autism Spectr. Disord. **6**(1), 25–31 (2012)
32. Kelso, J.A.S.: Dynamic Patterns: The Self-organization of Brain and Behavior. MIT Press, Cambridge (1995). (4 p. of plates)
33. Richardson, M.J., et al.: Rocking together: dynamics of intentional and unintentional interpersonal coordination. Hum. Mov. Sci. **26**(6), 867–891 (2007)
34. Shockley, K., et al.: Cross recurrence quantification of coupled oscillators. Phys. Lett. A **305**(1–2), 59–69 (2002)
35. Richardson, M.J., et al.: Comparing the attractor strength of intra- and interpersonal interlimb coordination using cross-recurrence analysis. Neurosci. Lett. **438**(3), 340–345 (2008)
36. Louwerse, M.M., et al.: Behavior matching in multimodal communication is synchronized. Cogn. Sci. **36**(8), 1404–1426 (2012)
37. Ramenzoni, V.C., et al.: Joint action in a cooperative precision task: nested processes of intrapersonal and interpersonal coordination. Exp. Brain Res. Experimentelle Hirnforschung. Experimentation Cerebrale **211**(3–4), 447–457 (2011)
38. Konvalinka, I., et al.: Synchronized arousal between performers and related spectators in a fire-walking ritual. PNAS **108**(20), 8514–8519 (2011)
39. Fusaroli, R., Bjørndahl, J., Tylén, K.: A Heart for Coordination: investigating speech, gesture and heart rate in a collective, creative construction task. submitted
40. Ramenzoni, V.C., et al.: Interpersonal and intrapersonal coordinative modes for joint and single task performance. Human Movement Science, 2012
41. Varni, G., et al.: Toward a real-time automated measure of empathy and dominance. In: IEEE International Conference on Computational Science and Engineering, CSE'09 (2009)
42. Varni, G., Volpe, G., Camurri, A.: A system for real-time multimodal analysis of nonverbal affective social interaction in user-centric media. IEEE Trans. Multimedia **12**(6), 576–590 (2010)
43. Reddy, V., Markova, G., Wallot, S.: Anticipatory adjustments to being picked up in infancy. PLoS ONE **8**(6), e65289 (2013)
44. Wallot, S., et al.: Division of labor as a cooperative strategy during complex joint action. submitted
45. Tylén, K., et al.: Language as a tool for interacting minds. Mind Lang. **25**(1), 3–29 (2010)
46. Clark, H.H.: Using Language. Cambridge University Press, Cambridge (1996)
47. Shockley, K., Santana, M.V., Fowler, C.A.: Mutual interpersonal postural constraints are involved in cooperative conversation. J. Exp. Psychol. Hum. Percept. Perform **29**(2), 326–332 (2003)
48. Shockley, K., Richardson, D.C., Dale, R.: Conversation and coordinative structures. Topics Cogn. Sci. **1**(2), 305–319 (2009)
49. Shockley, K., et al.: Articulatory constraints on interpersonal postural coordination. J. Exp. Psychol. Hum. Percept. Perform **33**(1), 201–208 (2007)
50. Richardson, M.J., Marsh, K.L., Schmidt, R.C.: Effects of visual and verbal interaction on unintentional interpersonal coordination. J. Exp. Psychol. Hum. Percept. Perform. **31**, 62–79 (2005)
51. Marsh, K.L., Richardson, M.J., Schmidt, R.C.: Social connection through joint action and interpersonal coordination. Topics Cogn. Sci. **1**(2), 320–339 (2009)
52. Reuzel, E., et al.: Conversational synchronization in naturally occurring settings: a recurrence-based analysis of gaze directions and speech rhythms of staff and clients with intellectual disability. J. Nonverbal Behav. **37**(4), 281–305 (2013)

53. Ashenfelter, K.T.: Simultaneous Analysis of Verbal and Nonverbal Data During Conversation| Symmetry and Turn-taking. University of Notre Dame, Indiana (2008)
54. Richardson, D.C., Dale, R.: Looking to understand: the coupling between speakers' and listeners' eye movements and its relationship to discourse comprehension. Cogn. Sci. **29**(6), 1045–1060 (2005)
55. Richardson, D.C., Dale, R., Kirkham, N.Z.: The art of conversation is coordination: common ground and the coupling of eye movements during dialogue. Psychol. Sci. **18**(5), 407–413 (2007)
56. Richardson, D.C., Dale, R., Tomlinson, J.M.: Conversation, gaze coordination, and beliefs about visual context. Cogn. Sci. **33**(8), 1468–1482 (2009)
57. Dale, R., Kirkham, N.Z., Richardson, D.C.: The dynamics of reference and shared visual attention. Front. Psychol. **2**, 355 (2011)
58. Diderichsen, P.: Cross recurrence quantification analysis of indefinite anaphora in swedish dialog. An eye-tracking pilot experiment. In: Brandial'06: Proceedings of the 10th Workshop on the Semantics and Pragmatics of Dialogue (SemDial-10), Universitätsverlag Potsdam, Germany, 11–13 September 2006
59. Jermann, P., Nüssli, M.-A.: Effects of sharing text selections on gaze cross-recurrence and interaction quality in a pair programming task. In: Proceedings of the ACM 2012 Conference on Computer Supported Cooperative Work. ACM, (2012)
60. Fusaroli, R., Gangopadhyay, N., Tylén, K.: The dialogically extended mind: making a case for language as skilful intersubjective engagement. Cogn. Syst. Res. **29–30**, 31–39 (2014)
61. Fusaroli, R., Tylén, K.: Investigating conversational dynamics:interactive alignment, interpersonal synergies, and collective task performance. (under Revision)
62. Warlaumont, A.S., et al.: Vocal interaction dynamics of children with and without autism. In: Proceedings of the 32nd Annual Conference of the Cognitive Science Society. TX: Cognitive Science Society, Austin, (2010)
63. Cox, R.F., van Dijk, M.: Microdevelopment in parent-child conversations: from global changes to flexibility. Ecol. Psychol. **25**(3), 304–315 (2013)
64. Rączaszek-Leonardi, J., et al.: Linguistic interaction as coordinative structure: Relationship between supraindividual and subjective. submitted
65. Gorman, J.C., et al.: Measuring patterns in team interaction sequences using a discrete recurrence approach. Hum. Factors: J Hum. Factors Ergon. Soc. **54**(4), 503–517 (2012)
66. Buder, E.H., et al.: Dynamic indicators of mother-infant prosodic and illocutionary coordination. In: Proceedings of the 5th International Conference on Speech Prosody, (2010)
67. Michael, J., et al.: Compensatory Strategies Enhance Rapport in Interactions Involving People with Möbius Syndrome. submitted
68. Orsucci, F., Giuliani, A., Zbilut, J.: Structure & coupling of semiotic sets. Experimental Chaos **742**, 83–93 (2004)
69. Orsucci, F., et al.: Prosody and synchronization in cognitive neuroscience. EPJ Nonlinear Biomed. Phys. **1**(1), 1–11 (2013)
70. Orsucci, F., et al.: Orthographic structuring of human speech and texts: linguistic application of recurrence quantification analysis. Arxiv preprint cmp-lg/9712010 (1997)
71. Dale, R., Spivey, M.J.: Unraveling the dyad: using recurrence analysis to explore patterns of syntactic coordination between children and caregivers in conversation. Lang. Learn. **56**(3), 391–430 (2006)
72. Dale, R., Louwerse. M.M.: Human interaction as a multimodal network structure. In: Conceptual Structures, Discourse, and Language (2013)
73. Bahrami, B., et al.: Optimally interacting minds. Science **329**, 1081–1085 (2010)
74. Angus, D., Smith, A., Wiles, J.: Human communication as coupled time series: quantifying multi-participant recurrence. IEEE Trans. Audio Speech Lang. Process. **20**, 1795–1807 (2012)
75. Angus, D., Smith, A., Wiles, J.: Conceptual recurrence plots: revealing patterns in human discourse. IEEE Trans. Visual Comput. Graphics **18**(6), 988–997 (2012)
76. Angus, D., et al.: Visualising conversation structure across time: insights into effective doctor-patient consultations. PloS ONE **7**(6), e38014 (2012)

77. Leonardi, G.: The study of language and conversation with recurrence analysis methods. Psychol. Lang. Commun. **16**(2), 165–183 (2012)
78. Marsh, K.L., et al.: Autism and social disconnection in interpersonal rocking. Frontiers Integr. Neurosci. **7**, 4 (2013)
79. Lakens, D.: Calculating and reporting effect sizes to facilitate cumulative science: a practical primer for t-tests and anovas. Frontiers Psychol. **4**, 863 (2013)
80. Dienes, Z.: Understanding Psychology as a Science : An Introduction to Scientific and Statistical Inference, p. 170. Palgrave Macmillan, New York (2008)
81. Plonsky, L.: In: Porte, G. (ed.) Replication, Meta-analysis, and Generalizability. Replication Research in Applied Linguistics. Cambridge University Press, Cambridge (2012)
82. Cumming, G.: The new statistics why and how. Psychol. Sci. **25**(1), 7–29 (2014)
83. Dale, R., et al.: Beyond synchrony: complementarity and asynchrony in joint action. In: Cognitive Science (2013)
84. Thomasson, N., Webber, C., Zbilut, J.P.: Application of recurrence quantification analysis to EEG signals. Int. J. Comput. Appl. **9**, 9–14 (2002)
85. Marwan, N., Kurths, J., Saparin, P.: Generalised recurrence plot analysis for spatial data. Phys. Lett. A **360**(4), 545–551 (2007)
86. Kokal, I., Gazzola, V., Keysers, C.: Acting together in and beyond the mirror neuron system. Neuroimage **47**(4), 2046–2056 (2009)
87. Newman-Norlund, S.E., et al.: Recipient design in tacit communication. Cognition **111**, 46–54 (2009)
88. Sebanz, N., Bekkering, H., Knoblich, G.: Joint action: bodies and minds moving together. Trends Cogn. Sci. **10**(2), 70–76 (2006)
89. Lang, M., et al.: Lost in the rhythm: the effects of rhythm on subsequent interpersonal coordination. underRevision
90. Fusaroli, R., et al.: Non-linear dynamics of speech and voice in schizophrenia. in Neurobiology of Language 2013, San Diego (2013)
91. Fusaroli, R., Bang, D., Weed, E.: Non-linear analyses of speech and prosody in asperger's syndrome. In: IMFAR 2013, San Sebastian (2013)
92. Fusaroli, R., et al.: Non-linear dynamics of voice in mental disorders. in Cog Sci 2013, Berlin (2013)
93. Weed, E., Fusaroli, R.: Prosodic production in right-hemisphere stroke patients: using temporal dynamics to characterize voice quality. in Neurobiology of Language (2013)
94. Rączaszek-Leonardi, J., Kelso, J.A.S.: Reconciling symbolic and dynamic aspects of language: toward a dynamic psycholinguistics. N. Ideas Psychol. **26**(2), 193–207 (2008)
95. Fusaroli, R., et al.: Conversation, coupling and complexity: matching scaling laws predict performance in a joint decision task. in Cog Sci 2013 (2013)
96. Chen, Y., Yang, H.: Multiscale recurrence analysis of long-term nonlinear and nonstationary time series. Chaos Solitons Fractals **45**(7), 978–987 (2012)
97. Xiang, R., et al.: Multiscale characterization of recurrence-based phase space networks constructed from time series. Chaos **22**(1), 013107 (2012)
98. Lancia, L., Avelino, H. Voigt, D.: Measuring laryngealization in running speech: interaction with contrastive tones in Yalálag Zapotec. In: Interspeech 2013. in press
99. Lancia, L., Fuchs, S., Tiede, M.: Application of concepts from cross-recurrence analysis in speech production: an overview and a comparison to other nonlinear methods. J. Speech Lang. Hearing Res. **57**, 743–757 (2013)
100. Lancia, L., Tiede, M.: A survey of methods for the analysis of the temporal evolution of speech articulator trajectories. In: Fuchs, A., et al. (eds.) Speech Planning and Dynamics, Peter Lang (2012)
101. Schinkel, S., et al.: Confidence bounds of recurrence-based complexity measures. Phys. Lett. A **373**(26), 2245–2250 (2009)

Cross-Recurrence Quantification Analysis of the Influence of Coupling Constraints on Interpersonal Coordination and Communication

Michael Tolston, Kris Ariyabuddhiphongs, Michael A. Riley and Kevin Shockley

Abstract This chapter describes a methodological strategy for studying the influence of coupling constraints on interpersonal coordination using cross-recurrence quantification analysis (CRQA). In Study 1, we investigated interpersonal coordination during conversation in virtual-reality (VR) and real-world environments. Consistent with previous studies, we found enhanced coordination when participants were talking to each other compared to when they were talking to experimenters. In doing so we also demonstrated the utility of VR in studying interpersonal coordination involved in cooperative conversation. In Study 2, we investigated the influence of mechanical coupling on interpersonal coordination and communication, in which conversing pairs were coupled mechanically (standing on the same balance board) or not (they stood on individual balance boards). We found a relationship between movement coordination and performance in a conversational task in the coupled condition, suggesting a functional link between coordination and communication. We offer these studies as methodological examples of how CRQA can be used to study the relation between interpersonal coordination and conversation.

1 Introduction

When people converse they exhibit a tendency to coordinate with their conversational partners. For example, classic studies using videotaped evaluations of dyadic interactions have shown that people are likely to nod and gesture in synchrony and reciprocation with their partners (interactional synchrony [1, 2]), and when they listen to an engaging speaker they are likely to share postural configurations with that speaker [3, 4]. In subsequent years, available technology has evolved considerably beyond the hand scoring of video tapes, creating both new possibilities and new challenges for interpersonal coordination research. For example, the movements that people produce exhibit meaningful structure at many scales of variation [5, 6], and this

M. Tolston (✉) · K. Ariyabuddhiphongs · M.A. Riley · K. Shockley
Center for Cognition, Action, & Perception, Department of Psychology,
University of Cincinnati, Cincinnati, USA
e-mail: tolstomt@gmail.com

can be captured objectively and accurately using modern motion tracking technology. The high-resolution, continuous signals afforded by this equipment yield a rich source of data for detailed analysis of interpersonal coupling. However, these types of continuous time-domain signals can present a range of challenges, including non-stationarity and irregularity, making them unsuitable for many conventional analyses that are based on assumptions of stationarity and normality. Moreover, typical summary measures, such as mean and standard deviation of individual time series statistics—statistics that work well for quantifying individual performance—are not designed to index the degree of coordination between individuals. In answer to these challenges, this chapter describes a methodological strategy for studying interpersonal coordination that attempts to overcome problems presented by complex time-series.

In subsequent sections, we demonstrate two applications of cross-recurrence quantification analysis (CRQA [7–10]), an extension of recurrence quantification analysis (RQA; [8, 11–14]), both of which are methods that are well-suited for the analysis of complex, irregular time series data. Importantly, CRQA, is especially well-suited to capture the coupling between the time-evolving dynamics of noisy, nonstationary time series data. While there are several sophisticated time series methods that may be used to analyze interpersonal coordination, including wavelet analysis [15, 16] and cross-spectral coherence [17], CRQA methods are particularly useful for studying postural sway dynamics which are notoriously irregular and non-stationary (e.g. [11]), and these methods have proven invaluable for quantifying interpersonal coordination across a range of contexts (see [18] for a recent review). In the present work, we therefore utilize CRQA to quantify interpersonal postural coordination.

Previous research using CRQA to quantify interpersonal coordination has shown that spontaneous coordination of postural sway—the continuous, low-amplitude, and complex pattern of fluctuation of the position of the body's center of mass—arises when two people engage in cooperative conversation [19–21]. Shockley et al. [19] developed an experimental paradigm that involves tracking participants' postural sway while they converse to jointly solve a find-the-differences puzzle, a task in which each participant views a picture that is similar to that viewed by the other, except for a few subtle differences which they are asked to find via conversation. When participants converse with each other to solve the task, their postural sway becomes coordinated, regardless of whether they can see each other. This postural coordination emerges from constraints imposed by the cooperative nature of the tasks which go beyond purely biomechanical constraints resulting from coordinated speech patterns [22]. In other words, postural coordination seems to reflect cognitive coordination and the intention of the participants to work together to solve the puzzle [23]. This latter idea is complemented by findings suggesting that motor behavior is causally related to the evolution of cognitive trajectories [24, 25]. Given this understanding, evaluating changes in interpersonal movement coordination may prove to be a means of detecting otherwise covert variations in cognitive alignment between conversing individuals.

The present chapter reports two experiments that used CRQA to quantify how interpersonal coordination between conversing dyads changed in response to manipulations of certain coupling parameters. A variety of factors might serve to couple the activities of two conversing individuals. In Study 1, we focused on perceptual factors that might be involved in coupling two conversants' activities using a relatively simple virtual-reality (VR) environment. Study 2 focused on factors that might play a role in coupling when individuals are mechanically linked to each other via the support surface.

In Study 1, we implemented the find-the-differences task of Shockley et al. [19] to determine whether interpersonal coordination occurs when individuals interact in a VR environment. It has been shown that direct visual access to a conversational partner may not be a necessary condition for emergent interpersonal coordination [19], though several other studies investigating rhythmic interpersonal coordination have shown that visual coupling parameters are important for interpersonal coordination [16, 26]. The consequence of the nature of visual coupling in interpersonal contexts, therefore, requires further investigation. Moreover, Study 1 is important for methodological reasons—if interpersonal coupling is equivalent in a VR setting as in a real environment, then the powerful tools of VR can be implemented to study interpersonal coordination. This is important because VR allows for manipulations that may not be possible or easy to achieve in a real environment, such as manipulating one person's movements artificially to attempt to enhance or disrupt interpersonal coordination.

In Study 2, individuals performed the same find-the-differences task while coupled mechanically (they stood on the same balance board) or not (they stood on individual balance boards). It has been shown that standing on unstable support surfaces adversely affects the stability of postural sway [27], measures of interpersonal coordination [21], and performance on cognitive tasks [28]. It is thus important to determine how biomechanical factors influence interpersonal coordination and, thus, effective communication.

2 Study One: The Influence of Informational Coupling on Interpersonal Coordination

This experiment quantified interpersonal coordination between participants who interacted in a virtual-reality (VR) environment while performing find-the-differences tasks. Our experimental design partly followed that of Shockley et al. [19] by investigating the effects on interpersonal coordination of task-partner, crossed with the additional factor of task environment. Participants performed the find-the-differences task either with each other, or with confederate task partners, but while in the presence of the other participant and his or her task partner (interpersonal coordination was only assessed between the two participants). Following Shockley et al., interpersonal coordination was measured in this study via CRQA of postural sway. We also

directly compared interpersonal coordination in VR with interpersonal coordination in the real world to determine if the overall amount of coordination, the temporal structure of the coordination, and the overall stability of the coordination were of similar magnitudes in VR and the real world.

With respect to task environment, we predicted that we would find the same patterns of coordination in both the real world and VR conditions, and that these patterns would be comparable to those that were found in the original investigation by Shockley et al. [19]. This prediction was motivated, in part, by the finding in Shockley et al. that participants did not have to see each other to coordinate with each other. Regarding the task-partner manipulation, we predicted (again following Shockley et al.) that coordination would be higher within pairs when they were discussing the pictures together rather than with confederate partners.

2.1 Method

Twenty-eight participants (14 pairs), recruited from the University of Cincinnati Psychology Department Participation Pool, took part in this IRB-approved study after giving written consent to participate. Participants received course credit in return for their participation. All participants were screened to ensure the absence of neurological and movement disorders.

Motion data were obtained using an Optotrak Certus system (Northern Digital Industries, Waterloo, Ontario, Canada) with a sampling rate of 30 Hz. Participants wore spandex bodysuits with 34 motion-tracking markers affixed to their legs, arms, and torso. They also wore running gloves with motion tracking markers affixed to the dorsal sides of the gloves. This full-body motion was projected onto the movements of virtual avatars in a custom OpenGL program. Participants wore Vissette 45 head-mounted displays (Cybermind, Maastricht, the Netherlands) with a resolution of $1,280 \times 1,024$ pixels and a transparent visor. In the VR conditions, the displays were turned on and an occluding cover was placed over the transparent visor, while in the real-world conditions the displays were turned off and the occluding covers removed.

During their conversational tasks, participants stood 195 cm apart from each other with their heels approximately shoulder-width apart, and were allowed to move their upper bodies freely. The pictures on a given trial were identical, except for 10 differences in each set. Participants were asked to find the differences by discussing the details of their pictures with one another or with their confederate partners. Different picture sets were employed for each trial. The order of picture presentation was completely randomized, with the exception of the very first picture, which was the same practice picture for all pairs.

In the real-world condition, the pictures were attached to wooden stands to the immediate left of each participant at approximately eye-level. Participants looked at the picture to the side of their partner and could not see their partner's picture on their own left. In the VR condition, the pictures were in the same relative location,

but were hi-definition digital copies of the real-world pictures (color bitmap images measuring 960 × 720 pixels). During the task, pairs were instructed to say "That's a difference" whenever they discovered, or thought they discovered, a difference. To index task performance, researchers kept track of the conversation in real time and verified the pair's self-reported performance against picture puzzles identical to those being discussed.

The environment manipulation was crossed with a task-partner manipulation, in which participants either solved the puzzles with each other or with a confederate partner. In these conditions, each confederate stood to the side of their respective partner, out of the direct line of sight of either of the participants. Confederates were instructed to record differences found and to attempt to perform as naïve participants during the trials by engaging in each conversation as if they had never seen a given picture before. The purpose of the confederate condition was to serve as a de facto control condition, in that participants were performing the same basic task but were not interacting with each other. Trials were blocked by condition and the blocks were randomized. There were four trials in each condition, plus one practice trial, yielding 17 trials per pair, each lasting 130 s.

Measures of anterior-posterior (AP) movements from the torso (the lower back) and from the front of the head were analyzed. The phase space of each time series was reconstructed using the method of delays [29] by unfolding the recorded time series into a 7-dimensional phase space using a time delay of 62 samples. For CRQA, a radius of 27 % of the mean distance separating points in the phase space was considered a recurrent point (i.e., a shared postural configuration).

Prior to CRQA, the first and last 5 s of data were truncated to remove transients. Data were then analyzed for anomalies that sometimes occur with optical motion tracking systems, which appear as very large amplitude spikes of short duration. To do this, a 14 Hz, 2nd order, high-pass Butterworth filter was applied to the data and deviations between the filter and the data that were determined to be outliers via the Grubb's outlier test were removed from the original signal. Time series were then analyzed for amount of missing data, and any trial with greater than 40 contiguous missing samples was removed from the analysis. Any missing data points in retained observations were then interpolated with a cubic spline and the signal was then filtered with a 14 Hz, 2nd-order, high-pass Butterworth filter. The marker at the torso location resulted in a large amount of lost data due to its relative positioning with respect to the camera configuration, resulting in a decreased sample for that location compared to the head.

Of the dependent measures that are available using CRQA, three were used: Percent recurrence (%REC), percent determinism (%DET), and maximum diagonal line length (LMAX). %REC is the total number of instances that two time series visit coinciding regions in their phase spaces, and in the context of human movement coordination has been shown to be a measure of global coordination that doesn't take into account the temporal patterning of the recurrent points [30, 31]. %DET is a measure of the total number of recurrent points that are located along diagonal lines, defined in the reported analyses as two contiguous recurrent points. This measure indexes the probability that a given recurrent point forms part of a recurring series, which

Table 1 Differences found in the find-the-differences tasks from Experiment 1

Task partner[a]	Real environment	Virtual environment
	M (SE)	*M (SE)*
Confederate	3.37 *(0.34)*	4.62 *(0.44)*
Participant	3.85 (1.00)	4.56 *(0.61)*

[a]$n=7$

gives insight into the structure of the coordination, since single chance recurrences lower %DET. LMAX is the longest diagonal line in the recurrence matrix—literally how long the two time series can maintain a common pattern—and is thus a measure of the stability of the observed coordination.

2.2 Results

Results from CRQA and task performance were sorted by condition and analyzed for outliers at the trial level, with any observation that was an outlier for any variable being removed from all measures obtained for that trial (e.g., if an observation was an outlier in the %REC distribution for a given condition, then that trial was removed from %REC, %DET, LMAX and task performance analyses). Data from each pair were then averaged over trials in each condition, yielding one observation per pair per condition. These reduced data were again assessed for outliers, with any observation that was an outlier for a given variable being removed for all variables, removing that pair from subsequent analyses. Data were then submitted to separate two-way within-subjects analyses of variance (ANOVAs) with environment (real or VR) and task-partner (confederate or participant) as factors.

Task performance data are presented in Table 1. There were no significant main effects of environment or task partner on task performance, nor was there an interaction of environment and task partner on task performance (all $p > 0.05$).

The CRQA variables were affected by both the environment and task partner manipulations. At the torso, there was a main effect of task partner on %REC, $F(1, 6) = 6.28$, $p = 0.046$, %DET, $F(1, 6) = 18.35$, $p = 0.005$, and LMAX, $F(1, 6) = 7.51$, $p = 0.034$, with all three being higher when participants were talking with each other than when they were talking with the confederates (see Fig. 1; an example CRQ plot is shown in Fig. 2).

With respect to head movement, we found that being immersed in the virtual environment rather than completing the task in the real world resulted in increased %REC, $F(1,11)= 10.12$, $p = 0.009$, %DET, $F(1,11) = 14.61$, $p = 0.003$, and LMAX, $F(1,11) = 11.96$, $p = 0.005$, indicating that head coordination patterns were altered by VRimmersion in a way that increased the overall similarity of the two participants' head movements as well as the shared structure and pattern stability of head movements within interacting pairs.There was also a main effect of task-partner
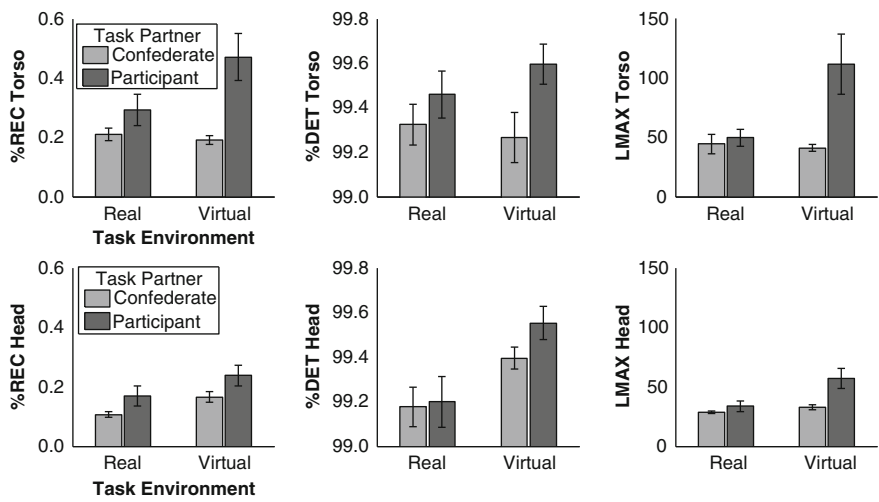
Fig. 1 Mean values from CRQ analyses of torso and head data from study one, where participants solved picture puzzles in either a real or virtual environment while working with either each other or confederate partners. Error bars represent (±) one standard error
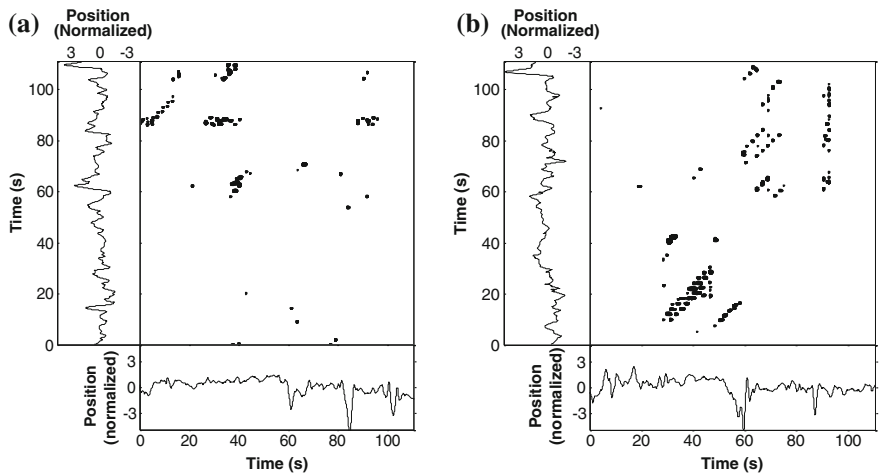

Fig. 2 CRQ plots created using torso data from a pair participating study one. **a** A trial in which the pair were conversing with confederates in VR. **b** The same pair, but data were from a trial during which the individuals were conversing with each other in VR

on LMAX measured at the head, $F(1,11) = 8.27$, $p = 0.015$—coordination patterns between participants were higher when they were talking to each other versus when they were talking to the confederates.

There was also an interaction between environment and task partner on LMAX measured at both the torso, $F(1, 6) = 7.89$, $p = 0.031$, and the head, $F(1, 11) = 5.53$, $p = 0.038$. Simple-effects analyses found no differences in LMAX of head or torso coordination when participants were talking with each other or with confederates in the real world condition (ps > 0.05), but coordination pattern stability was greater when participants were talking to each other than when talking with confederates in the VR condition for both the head, $p = 0.027$, and the torso, $p = 0.014$.

2.3 Discussion of Study One

Similar to the original findings of Shockley et al. [19], we found a main effect of task partner on %REC measured at the torso, meaning that participants shared more postural configurations when they were discussing the pictures as a pair rather than when they were separately discussing the pictures with confederate partners. We also found that task partner affected %DET and LMAX in the same manner on measurements at the torso. Thus, in line with our hypothesis, we found evidence of the influence of informational coupling via verbal communication on movement patterns using CRQA measures. This suggests that VR settings are sufficient to support interpersonal postural coordination, and, apparently, to support interpersonal cognitive coordination, given that performance of the joint find-the-differences task was equivalent across the VR and real-world conditions. This finding may have many important practical implications for using VR technologies for collaborative work and training.

Unexpectedly, we also found that when pairs were working in the VR condition their head movements exhibited greater similarity and more shared patterns than when they performed the task in the real world condition. This finding complements findings of Stoffregen et al. [20], in which participants performed the same find-the-differences task, but under different visual constraints. Those authorsevaluated the influence of target distance and target size on postural coordination crossed with the same task-partner manipulation reported here and in Shockley et al. [19]. They found that when participants were discussing closer targets or larger targets they exhibited greater shared head configurations than when they discussed targets that were farther away or smaller. Their findings, along with the present findings, show the sensitivity of interpersonal coordination to visual constraints. Specifically, the effect of the environment manipulation was more pronounced at the head, where it affected all three CRQA variables in the same direction, with enhanced coordination in the VR condition.

Additionally, we found interactions between task-partner and environment at both the head and the torso, in that when pairs discussed their pictures with each other in the VR they had a greater amount of coordination stability compared to when they conversed with confederates, but this did not hold in the real-world condition. One interpretation of these findings may be that the relatively sparse nature of the virtual environment allowed the individuals to focus more intently on the task, thereby

strengthening the stability of coordination that governed the interaction. However, prior research has also shown a differential influence of virtual and real-world conditions on visual entrainment [32], indicating that more research in this area is required. It is possible that these differences are attributable to different demands for ocular convergence and accommodation—objects in VR headsets that are projected at different distances require variations in convergence but mostly invariant accommodation, which can lead to discomfort and salient differences between VR displays and real environments [33]. However, in the current study, both the avatar and pictures were displayed at a constant distance in the VR, which likely diminishes this concern.

3 Study Two: The Influence of Mechanical Coupling on Interpersonal Coordination and Communication

Shockley et al. [23] hypothesized that postural coordination during cooperative conversations may reflect the functional organization that supports the joint goals of individuals engaged in the conversation. In other words, the postural coordination during conversation may embody coordination of cognitive process in communication. This embodiment thesis implies the mutual influence of body and cognition: Cognition or emotion alters bodily processes, and the bodily processes can also bring about change in cognition or emotion [34]. In particular, bodily coordination is not just a by-product of cognitive processes of communication, but an integral aspect of cognition that unfolds across different scales [35]. Hence, an alteration of interpersonal postural coordination should in turn influence the linguistic coordination that occurs during conversation, which in turn may influence the effectiveness of communication.

In the present study, we manipulated parameters affecting postural coordination by requiring participants to stand and balance on balance boards (long wooden boards secured atop circular dowels running along their length) while engaging in the find-the-differences conversational task described in study one. During half of the trials, both participants balanced on the same balance board (coupled condition). In the other half of the trials, participants balanced on separate balance boards (uncoupled condition; see Fig. 3).

The goal was to investigate how mechanical coupling would influence postural coordination and, ultimately, communication. During all trials, participants were able to become informationally coupled through conversation, and during half of the trials they were coupled mechanically via a shared balance board. We predicted this physical coupling should increase postural coordination above levels brought about by the informational coupling established by verbal communication alone. According to the functional organization thesis outlined above, shared postural configurations should facilitate better communication and, hence, task performance. We thusbreak predicted that when CRQA measures were higher (i.e., greater coordination), the pairs would find more differences (i.e., communication would be more effective).
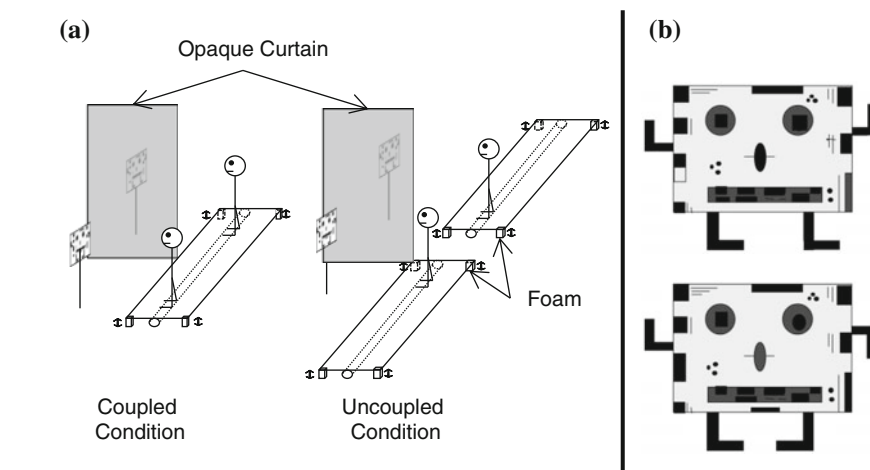
Fig. 3 An overview of the method used in study 2. **a** The positions of participants in the coupled and uncoupled conditions. An opaque curtain was hung from the ceiling to prevent participants from seeing each other's picture, and small pieces of foam were attached to each corner of the balance boards to dampen the rocking motion. **b** A pair of puzzle stimuli used in the experiment. Participants discussed their respective pictures in order to find differences while their movements and task performance were recorded

3.1 Method

Thirty-four participants (17 pairs) performed the same find-the-differences task described in Study 1. This study employed a repeated-measures design, in which individuals stood on either the same or separate balance boards, depending upon the coupling condition. Each board was made of a $60.96 \times 243.84 \times 1.90$ cm flat plywood sheet. Two 121.92 cm length dowels with 5.08 cm diameter were secured underneath the boards along their major axes in order to create a pivot point. Four $5 \times 7 \times 10.5$ cm pieces of foam were attached underneath four corners of the board with the 5×7 cm surface attached to the board. These foam pieces damped the rocking motion of the board and simplified the balancing task. Thin carpeting was secured to the top of the surface of each board to protect participants from splinters and from slipping. A picture stand for holding the find-the-differences task stimuli was placed 195 cm in front of each participant at approximately eye-level (155 cm from the floor). A black opaque curtain was hung between the two participants spanning from the board to the picture stands in order to prevent pairs from seeing both pictures, though they could still see each other in their peripheral vision. Participants were asked to actively balance the board throughout each trial, and were discouraged from simply resting their weight at a fully tilted position.

The experimental sessions consisted of a single practice trial and two blocks of four trials each of the coupled and uncoupled conditions. Each trial lasted for three minutes. The order of the blocks was randomized. In the practice trial, the same

puzzle was used for all pairs. In the remaining eight experimental trials, the order of the puzzles was randomized. In the practice trial, the dyads stood on the same balance board, each facing in the same direction, with their AP axes orthogonal to the major axis of the board, meaning that postural sway was destabilized primarily in the AP direction. Participants were positioned such that one participant stood approximately 60 cm from the left edge and the other stood the same distance from the right edge. The coupled condition was identical to the practice session, except that new puzzles were used. In the uncoupled condition, participants stood on two different balance boards, which were aligned along their major axes and positioned with their minor axes adjacent. During these trials, each participant stood about a quarter of the board length from the adjacent ends of the two boards. Hence, they were standing in at the same relative distance from one another as they were in the coupled condition.

The movements of the participant's heads and torsos were tracked at a 50 Hz sampling rate with the same motion tracking system described in study one. Task performance was also indexed in the same manner as in study one. Each sensor was attached to the back of participant's heads and torsos using elastic Velcro belts and headbands. The time series data for analyses were taken from the AP movement of the head and torso. These data were prepared in the same manner as in study one, and then submitted to CRQA using a delay of 103 samples, an embedding dimension of 7, and a radius of 27 % of the mean distance separating points in reconstructed space.

3.2 Results

A log transformation was applied to %REC and LMAX to correct positively skewed data. Extreme outlier values of CRQA in each condition were detected and removed via Tukey's method with a three interquartile range threshold. A linear mixed-effects model was employed to analyze the obtained measures [36], with conditions and trial numbers included as repeated-measure factors with an unstructured covariance structure. Additionally, CRQA measures and trial numbers (to control for potential learning effects) were used to predict task performance. These analyses were conducted separately for the coupled and uncoupled conditions. Only significant effects ($p < 0.05$) are reported.

Estimated marginal means for CRQA measures and task performance can be seen in Table 2. Analyses showed that increases in %REC of the two participants' head movements positively predicted increases in performance in the coupled condition, $t(15.83) = 6.59$, $p < 0.001$. The relation between %DET for interpersonal head movement coordination and performance showed a similar pattern, where increases in %DET predicted increases in performance in the coupled condition, $t(16.31) = 3.15$, $p = 0.006$. Finally, LMAX for interpersonal head movement coordination also positively predicted performance in the coupled condition, $t(21.60) = 3.46$, $p = 0.002$.

Table 2 Mean values of CRQA measures and differences found in the find-the-differences tasks from Experiment 2 (standard errors in parentheses)

CRQA Measure[a]	Uncoupled	Coupled
%REC[b]		
Head	0.14 *(0.02)* [−0.96 *(0.05)*]	0.14 *(0.025)* [−0.97 *(0.06)*]
Torso	0.09 *(0.01)* [−1.09 *(0.02)*]	0.12 *(0.016)*[−1.05 *(0.05)*]
%DET		
Head	99.82 *(0.02)*	99.81 *(0.02)*
Torso	99.72*(0.03)*	99.74 *(0.04)*
LMAX[b]		
Head	56.96 *(4.08)* [1.73 *(0.03)*]	60.93 *(5.30)* [1.74 *(0.03)*]
Torso	48.52 *(2.66)* [1.66 *(0.02)*]	55.87 *(5.47)* [1.70 *(0.04)*]
Differences found	6.33 (0.24)	6.34 (0.29)

[a]$n = 17$

[b]Calculations based on $\log_{10}$ transformed values in brackets

3.3 Discussion of Study 2

Contrary to our predictions, CRQA measures of coordination between participants were not greater in the coupled versus the uncoupled condition. Nonetheless, the balance board was found to moderate the relation between coordinated head movements and the effectiveness of communication (operationalized as the number of differences during the task). In the coupled condition, coordinated head movement exhibited a positive relation to the number of differences found, while no such relation was found in the uncoupled condition. It is important to note that this relation held for log-transformed values of %REC and MAXLINE, meaning that the relation was not strictly linear.

With respect to the lack of effect of coupling condition on coordination, we observe that when participants shared a board, they had to continuously compensate for each other's movements. In other words, the mechanical link between two participants may have disrupted, rather than enhanced, coordination. This is consistent with comments from several participants who said that balancing on a shared board was more difficult than balancing independently on separate boards. This is also consistent with the findings of Stoffregen et al. [21], who found that when participants were standing on an unstable rather than a stable surface, the enhanced coordination that normally occurs during conversation was absent. Additionally, interpersonal coordination has been observed to become attenuated in difficult stance conditions [37]. These observations might suggest that interpersonal coordination is a fragile phenomenon. We note that, at some level, interpersonal postural coordination surely must depend on postural stability and coordination at the *intra*-personal level, which depends in part on mechanical support. However, it might not be the case that mechanical constraints necessarily override interpersonal constraints. Instead, a variety of sources of constraint, stemming from task demands, perceptual factors, biomechanical variables,

and other sources, may interact to determine postural stability and coordination at the intrapersonal and interpersonal levels [38]. The nested relation between intrapersonal postural stability and interpersonal postural coordination is an important issue for future research.

Regarding the relation between movement coordination and task performance, one way to interpret the divergent influence between balance board conditions is that when participants were mechanically coupled, they met two simultaneously shared task demands: balancing the board together and maintaining effective communication. In that effective communication required stable visual access to the target pictures, it is likely that the tasks were functionally dependent. In this case, the positive relation between head movement coordination and task performance in the coupled condition may indicate that successful participant pairs were able to coordinate their postural movements in order to obtain the visual information necessary for ongoing problem solving during the conversational task.

4 Conclusion

The present experiments illustrate how CRQA contributes a broader robust methodology that can be used to study human interactions (see [18] for a recent review). The results of the two studies described show that manipulations of perceptual (i.e., informational) and mechanical coupling variables can influence the coordination observed between two conversing individuals, and that CRQA measures are sensitive to these changes.

With respect to perceptual coupling (Study 1), we demonstrated that visual constraints influence the coordination observed between two conversing individuals. In doing so, we also showed that virtual environments are suitable for evaluating the influence of visual information on interpersonal coordination and communication. This finding presents potential for new possibilities for manipulating visual information beyond those offered in real world contexts, which would allow finer evaluation of how visual constraints influence the movement coordination that occurs during communication. Moreover, the present results, considered along with the findings of Stoffregen et al. [20], may indicate that visual manipulations influence the coordinative structure that emerges during cooperative conversation. Specifically, both studies found that talking to a task partner enhanced interpersonal movement coordination, but only at the head (cf. Shockley et al. [19], who only found enhanced coordination at the waist). Given that gaze coordination has been shown as an index of joint attention (e.g., [39]), future studies may also be warranted to directly manipulate head coordination while tracking participants gaze patterns. This could serve to address why changes in head coordination did not influence communication in Study 1, in spite of the fact that previous studies have shown an influence of gaze coordination on effective communication [40, 41].

Finally, in Study 2, we demonstrated that manipulating movement coordination can impact effective communication, and we showed how measures obtained from

CRQA are related to this outcome. This finding is consistent with Shockley et al.'s [23] suggestion that the movement coordination observed during conversation may embody the cognitive coordination required for effective communication, and implies that the relation between coordination and communication may be bidirectional. We suggest that this finding invites a more comprehensive investigation of how movement coordination (as indexed by CRQA and other methods) influences effective communication.

References

1. Condon, W.S., Ogston, W.D.: J. Psychiatr. Res. **5**(3), 221 (1967). doi:10.1016/0022-3956(67)90004-0
2. Kendon, A.: Acta Psychol. **32**, 101 (1970). doi:10.1016/0001-6918(70)90094-6
3. Bernieri, F.J.: J. Nonverbal Behav. **12**(2), 120 (1988). doi:10.1007/BF00986930
4. LaFrance, M.: Soc. Psychol. Q. **42**(1), 66 (1979). doi:10.2307/3033875
5. Riley, M.A., Turvey, M.T.: J. Mot. Behav. **34**(2), 99 (2002). doi:10.1080/00222890209601934
6. Van Orden, G.C., Kloos, H., Wallot, S.: In philosophy of complex systems: handbook of the philosophy of science, pp. 639–682. Elsevier, Amsterdam (2011)
7. Marwan, N., Kurths, J.: Phys. Lett. A **302**(5), 299–307 (2002). doi:10.1016/S0375-9601(02)01170-2
8. Marwan, N., Romano, M.C., Thiel, M., Kurths, J.: Phys. Rep. **438**(5), 237 (2007). doi:10.1016/j.physrep.2006.11.001
9. Shockley, K., Butwill, M., Zbilut, J.P., Webber Jr, C.L.: Phys. Lett. A **305**(1), 59 (2002). doi:10.1016/S0375-9601(02)01411-1
10. Zbilut, J.P., Giuliani, A., Webber Jr, C.L.: Phys. Lett. A **246**(1), 122 (1998). doi:10.1016/S0375-9601(98)00457-5
11. Riley, M.A., Balasubramaniam, R., Turvey, M.T.: Gait Posture **9**(1), 65 (1999). doi:10.1016/S0966-6362(98)00044-7
12. Webber Jr, C.L., Zbilut, J.P.: J. Appl. Physiol. **76**(2), 965 (1994)
13. Webber Jr, C.L., Zbilut, J.P.: In Bioengineering approaches to pulmonary physiology and medicine, pp. 137–148. Plenum Press, New York (1996)
14. Webber Jr, C.L., Zbilut, J.P.: In: Tutorials in contemporary nonlinear methods for the behavioral sciences, pp. 26–94. http://www.nsf.gov/sbe/bcs/pac/nmbs/nmbs.jsp (2005)
15. Issartel, J., Marin, L., Cadopi, M.: Neurosci. Lett. **411**(3), 174 (2007). doi:10.1016/j.neulet.2006.09.086
16. Varlet, M., Marin, L., Lagarde, J., Bardy, B.G.: J. Exp. Psychol. Hum. Percept. Perform. **37**(2), 473 (2011). doi:10.1037/a0020552
17. Schmidt, R.C., Morr, S., Fitzpatrick, P., Richardson, M.J.: J. Nonverbal Behav. **36**(4), 263 (2012). doi:10.1007/s10919-012-0138-5
18. Shockley, K., Riley, M.A.: In Recurrence quantification analysis: theory and best practices, Springer, New York (in press)
19. Shockley, K., Santana, M.V., Fowler, C.A.: J. Exp. Psychol. Hum. Percept. Perform. **29**(2), 326 (2003). doi:10.1037/0096-1523.29.2.326
20. Stoffregen, T.A., Giveans, M.R., Villard, S.J., Shockley, K.: Ecol. Psychol. **25**(2), 103 (2013). doi:10.1080/10407413.2013.753806
21. Stoffregen, T.A., Giveans, M.R., Villard, S., Yank, J.R., Shockley, K.: Mot. Control **13**(4), 471 (2009)

22. Shockley, K., Baker, A.A., Richardson, M.J., Fowler, C.A.: J. Exp. Psychol. Hum. Percept. Perform. **33**(1), 201 (2007). doi:10.1037/0096-1523.33.1.201
23. Shockley, K., Richardson, D.C., Dale, R.: Top. Cogn. Sci. **1**(2), 305–319 (2009). doi:10.1111/j.1756-8765.2009.01021.x
24. Spivey, M.J., Grosjean, M., Knoblich, G.: Proc. Nat. Acad. Sci. U.S.A. **102**(29), 10393 (2005). doi:10.1073/pnas.0503903102
25. McKinstry, C., Dale, R., Spivey, M.J.: Psychol. Sci. **19**(1), 22 (2008). doi:10.1111/j.1467-9280.2008.02041.x
26. Richardson, M.J., Marsh, K.L., Isenhower, R.W., Goodman, J.R., Schmidt, R.C.: Hum. Mov. Sci. **26**(6), 867 (2007). doi:10.1016/j.humov.2007.07.002
27. Schmit, J.M., Regis, D.I., Riley, M.A.: Exp. Brain Res. **163**(3), 370 (2005). doi:10.1007/s00221-004-2185-6
28. Woollacott, M., Shumway-Cook, A.: Gait Posture **16**(1), 1 (2002). doi:10.1016/S0966-6362(01)00156-4
29. Abarbanel, H.D.I.: Anal. observed chaotic data. Springer, New York (1996)
30. Pellecchia, G.L., Shockley, K.: In: Tutorials in contemporary nonlinear methods for the behavioral sciences, pp. 95–141. http://www.nsf.gov/sbe/bcs/pac/nmbs/nmbs.jsp (2005)
31. Richardson, M.J., Schmidt, R.C., Kay, B.A.: Biol. Cybern. **96**(1), 59 (2007). doi:10.1007/s00422-006-0104-6
32. Stoffregen, T.A., Bardy, B.G., Merhi, O.A., Oullier, O.: Presence: Teleoperators Virtual Environments **13**(5), 601 (2004). doi:10.1162/1054746042545274
33. Edgar, G.K., Bex, P.J.: In Simulated and virtual realities: elements of perception, pp. 85–102. Taylor & Francis, Bristol (1995)
34. Niedenthal, P.M.: Science **316**(5827), 1002 (2007). doi:10.1126/science.1136930
35. Van Orden, G.C., Hollis, G., Wallot, S.: Front. physiol. **3**(207), 1 (2012). doi:10.3389/fphys.2012.00207
36. Baayen, R.H., Davidson, D.J., Bates, D.M.: J. Mem. Lang. **59**, 390 (2008). doi:10.1016/j.jml.2007.12.005
37. Ramenzoni, V.C., Davis, T.J., Riley, M.A., Shockley, K., Baker, A.A.: 211(3–4), 447 (2011). doi:10.1007/s00221-011-2653-8
38. Riley, M.A., Kuznetsov, N., Bonnette, S.: Sci. Motricité **74**, 518 (2011). doi:10.1051/sm/2011117
39. Grant, E.R., Spivey, M.J.: Psychol. Sci. **14**(5), 462 (2003). doi:10.1207/s15516709cog0000_29
40. Richardson, D.C., Dale, R.: Cogn. Sci. **29**(6), 1045 (2003). doi:10.1207/s15516709cog0000_29
41. Richardson, D.C., Dale, R., Kirkham, N.Z.: Psychol. Sci. **18**, 407 (2007). doi:10.1111/j.1467-9280.2007.01914.x

Recurrence Quantification as an Analysis of Temporal Coordination with Complex Signals

Charles A. Coey, Auriel Washburn and Michael J. Richardson

Abstract Ample past research demonstrates that human rhythmic behavior and rhythmic coordination reveal complex dynamics. More recently, researchers have begun to examine the dynamics of coordination with complex, fractal signals. Here, we present preliminary research investigating how recurrence quantification techniques might be applied to study temporal coordination with complex signals. Participants attempted to synchronize their rhythmic finger tapping behavior with metronomes with varying fractal scaling properties. The results demonstrated that coordination, as assessed by recurrence analyses, differed with the fractal scaling of the metronome stimulus. Overall, these results suggest that recurrence analyses may aid in understanding temporal coordination between complex systems.

1 Introduction

Human behavior is structured in both obvious and non-obvious ways. It is readily apparent when someone runs to catch a train before it leaves the station that their behavior is coordinated (i.e., non-random with respect) to the environment. But, there are more subtle layers of structure in behavior, such as the complex patterns of variation in the intervals between the runner's strides. Despite the imperceptible nature of this fine-grained structure, research shows it is an essential characteristic of human behavior and that it too might be coordinated with the environment and the behaviors of other actors.

Repeated measurements of human behavior, from simple motor performances (e.g., rhythmic finger tapping), to basic perceptual processes (e.g., visual search), to cognitive operations (e.g., choice reaction times), to attitudes and emotions (e.g., self-esteem ratings), all tend to show fractal, power-law structure. That is, the measurement series bears a dependency wherein the size of a fluctuation (S) in behavior scales as a constant power of how often fluctuations of that size occur (f), $S(f) = 1/f^\alpha$. Typically, in natural and healthy behavior, the scaling exponent (α) falls near 1,

---

C.A. Coey (✉) · A. Washburn · M.J. Richardson
Department of Psychology, University of Cincinnati, Cincinnati, OH, USA
e-mail: coeyca@mail.uc.edu

indicating an inverse proportionality between the size and frequency of fluctuations which is scale free, much like geometric fractal objects. Changing the frequency by a constant amount results in a constant change in power regardless of the exact frequencies examined [1]. Unlike a truly random, 'white noise' signal ($\alpha = 0$), such 'pink noise' scaling involves a dynamic pattern of variation in which successive observations are not independent of one another. Instead, pink noise is said to be 'persistent' and entails long-range correlation such that observations are positively correlated over considerable lengths of time. Interestingly, many research projects have shown that experimental manipulations, and other psychologically-relevant factors, can reliably alter this scaling and shift α toward random variation or even further toward an 'anti-persistent', 'blue noise' pattern of fluctuation ($\alpha = -1$).[1]

More recently, several research projects have found that the scaling properties of two interacting systems tend to match one another (e.g., [2–6]). Remarkably, this 'complexity matching' effect seems to only be partially accounted for by tight coordination at the immediate timescale. That is, although the scaling exponents of the two systems are highly correlated, the two series are not strongly synchronized with each other. These findings naturally have led to questions as to the form of the temporal coordination underlying complexity matching [3, 7, 8]. How exactly can two systems, interacting through an exchange of energy or information, match one another's 'global', fractal structure without strong, 'local' synchronization?

Further investigation of complexity matching critically depends on techniques to assess the nature and degree of coordination between two behavioral series. Most recently, researchers have begun to explore techniques capable of capturing both short- and long-range dependencies, as well as the scaling relations defining the co-variation of two series [5, 6]. Here, we present some preliminary research investigating how cross-recurrence quantification analysis (CRQA) may aid in understanding temporal coordination between two complex systems. CRQA is a highly-articulated technique that provides analysis of how two signals co-evolve through the same abstract phase space over the entire span of measurement. CRQA also provides an abundance of (albeit potentially redundant) information about the coordination of the two series in its various outcome measures. For these reasons, we thought CRQA might serve as an advantageous compliment to the other techniques employed as analyses of the complexity matching phenomenon. It is important to note at the outset, however, that these recurrence analyses *do not* assess the complexity (i.e., power-law scaling) of behavior (see [9] for an analogous argument). Rather, these analyses quantify aspects of the *variability* of behavior in phase space. Although the complexity and variability of behavioral signals are likely related in empirical data, the outcomes of the recurrence analyses may not be taken to speak to complexity directly.

---

[1] There are ample resources available for those readers interested in the details of fractal analyses [1, 10, 11] and the current theoretical debates [12–14].

2 The Experiment

The current study was conducted as a pilot experiment in a larger project designed to investigate complexity matching in finger tapping behavior. We first sought to determine if complexity matching was present when participants tapped to recordings of other participants' tapping behavior, as the extant research either had individual participants coordinate with mathematically-generated stimuli [4] or had two participants interact in real time under bi-directional coupling conditions [3]. Thus, we recorded tapping behavior from an initial sample of participants under different experimental conditions, and then used these series as metronome stimuli for a second sample of participants.

More specifically, in our initial sample, we had participants undergo two trials of tapping behavior. In the first trial, participants performed a continuation task in which they synchronized to a 500 Hz (2 bps) metronome for a short period (10 s), and then attempted to maintain that tapping interval after the metronome was discontinued. In the second trial, participants performed a synchronization task in which they simply synchronized their taps to the metronome for the entire trial. The inter-tap interval (ITI) series from both trials were submitted to two fractal analyses. Consistent with the past research on fractal scaling in tapping behavior (see [15]), both fractal analyses showed the ITI series tended toward persistent, 'pink' scaling during continuation tapping ($\alpha \approx 0.75$) and toward anti-persistent, 'blue' scaling in synchronization tapping ($\alpha \approx -0.60$).

From this initial sample, we selected a set of 11 series to serve as metronome stimuli for our second sample of participants. It is important to note that only the variation in the onset of taps was retained in the inter-onset interval (IOI) of the resulting metronomes. All variation in the length of the taps was eliminated by equalizing the duration of each tone in the resulting metronome series. Five series from the synchronization condition formed a set of 'blue' metronomes ranging from strong ($\alpha = -0.80$) to mild ($\alpha = -0.41$) anti-persistent structure. Six series from the continuation condition served as 'pink' metronomes ranging from strong ($\alpha = 1.06$) to mild ($\alpha = 0.41$) persistent structure. Participants in the second sample also completed continuation and synchronization trials. During synchronization, however, they heard 1 of the 11 fractal metronomes. We collected 33 participants, with 3 in each of these 11 possible metronome conditions.

The design of this experiment allowed us to investigate the extent to which the recurrence analysis can capture the dynamics underlying temporal coordination with complex stimuli. Specifically, we examined if auto-recurrence quantification analysis (RQA) would suggest different dynamics in the participants ITI series as a function of the metronome type (i.e., pink vs blue), whether these differences in recurrence actually did (albeit indirectly) reflect the complexity of the ITI series (as assessed by fractal analyses), and what cross-recurrence analysis between the ITI and IOI series might suggest as to the nature of the coordination between the participant and metronome systems.

3 The Results

We have tried to provide sufficient detail here about the specifics of the many analyses we conducted, but there are a number of technical points that have been omitted due to the limited available space. Where possible, we have provided references for the reader interested in learning more about these analyses.

3.1 Fractal Scaling and Complexity Matching

As a first step, we thought it necessary to demonstrate the complexity matching phenomenon was present in our series. To this end, we used two standard fractal analyses; power spectral density (PSD) and detrended fluctuation analysis (DFA). The outcomes of these techniques are generally equivalent, but as they do operate in different ways [16] we used both to corroborate our results.[2] The outcome of PSD is the scaling exponent (α) as described above, but DFA instead outputs Hurst exponents (H). To directly compare these two analyses we rescaled the Hurst exponents (where $2(H − 0.5) = \alpha$; see [17]). In keeping with standard practice, every ITI series was integrated prior to submission to DFA (see [1, 6]).

It is also important to note that, at this stage, the participants' ITI series were initially treated separately from the metronome IOI series. That is, the ITI series, from both the continuation and synchronization conditions, first underwent several pre-processing steps (e.g., outlier removal, linear detrending). The final processed series were submitted to fractal analysis and their scaling exponents compared across tapping conditions and to the scaling of the metronome IOI series.

In general, PSD and DFA showed the same pattern of results. Just as in the first phase of the study, ITI series during continuation tapping revealed persistent, pink noise scaling and showed a marked decrease in α during synchronization. Here though, there were also significant interactions (PSD: $p = 0.001$, $\eta_{p2} = 0.28$; DFA: $p = 0.013$, $\eta_{p2} = 0.18$) between the blue and pink metronome groups across the tapping conditions (Fig. 1). Whereas the blue metronome group showed a large decrease in α from continuation to synchronization (PSD: $p = 0.001$, $d = 1.10$; DFA: $p = 0.002$, $d = 0.96$), the decrease in α for the pink metronome group was marginally significant at best (PSD: $p = 0.079$, $d = 0.44$; DFA: $p = 0.122$, $d = 0.38$).[3]

---

[2] These two fractal analyses are frequently used in studies of human behavioral data, but there are also maximum-likelihood techniques that are superior for verifying actual power-law scaling (see [18, 19]).

[3] The primary difference between the two analyses is that, although both indicate the ITI series of participants synchronized with blue metronomes to be near-random on average ($\alpha \approx 0$), PSD estimated α in the remaining conditions to be substantially greater than DFA ($\alpha \approx 0.7$ versus 0.5). This difference, however, likely has little bearing on the further analyses described below.
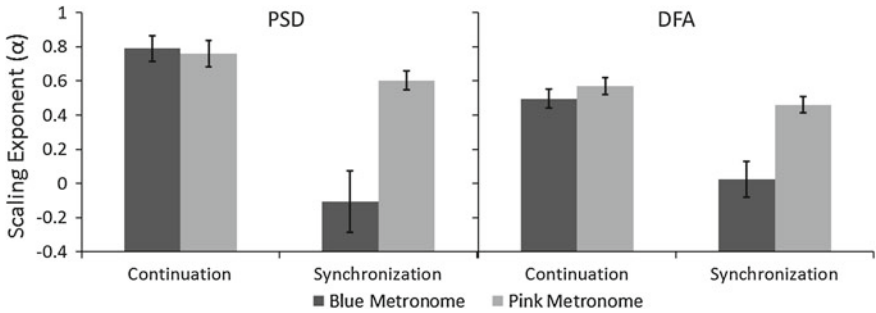
Fig. 1 Scaling exponents as a function of tapping condition and metronome group as estimated by power spectral density (*left*) and detrended fluctuation analysis (*right*)
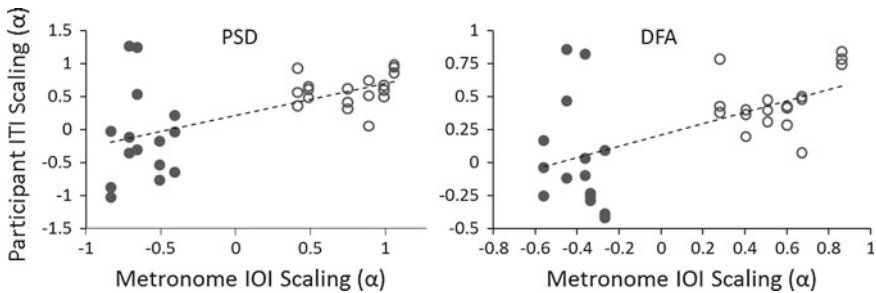

Fig. 2 Scatterplots for the relationship between participant ITI and metronome IOI scaling exponents for both power spectral density (*left*) and detrended fluctuation analysis (*right*) techniques. *Blue* metronomes are indicated by filled-in *circles* and *pink* metronomes by empty *circles*

Consistent with past research on complexity matching, we wanted to examine the correlation between the scaling of the participants' ITI series and the metronomes' IOI series. Simple correlations did reveal a moderate positive relationship for both PSD ($r = 0.58$, $p < 0.0005$) and DFA ($r = 0.57$, $p < 0.0005$). Interestingly, there seemed to be far greater variance in the participants' ITI scaling for the blue metronomes than for the pink metronomes (see Fig. 2). Given this heteroscedasticity, and the non-independence of observations sharing the same metronome stimulus, these correlations may not be the ideal statistical test for these data. Nonetheless, these results do suggest a considerable degree of complexity matching was present in our tapping task.

In order to examine the temporal coordination dynamics related to this complexity matching effect, we turned to the recurrence quantification techniques. Prior to submitting participant ITI and metronome IOI series to cross-recurrence analysis, however, we chose to examine the ITI series with auto-recurrence analysis in hope of relating recurrence outcomes (concerning variation within phase space) to the complexity of the series (as revealed by the fractal analyses).

3.2 Recurrence Quantification Analysis and Fractal Scaling

Recently many researchers have employed both recurrence quantification and fractal analyses [20–24]. Some have noted apparent associations between the results of the two methods [25]. Others have determined that the optimal models for classifying certain pathological conditions combine the outcomes of both methods [26–29]. Nonetheless, there has been relatively little exploration of the relationship between these two analyses in empirical data. With regard to the current study, validating that differences in recurrence measures actually are related to the complexity of the series is an important step, as many artifacts can influence recurrence analyses (see [30, 31]).

To begin, we performed auto-recurrence quantification analysis (RQA) on the very same participant ITI and metronome IOI series that we submitted to the two fractal analyses. As with the fractal techniques, there are several technical details that must be considered in preparing RQA (see [24, 32–34]). Most importantly, some preliminary analyses must be conducted in order to determine a few, critical parameter settings (i.e., delay, embedding dimension, radius). We followed the standard protocol in choosing these parameters (average mutual information, false nearest neighbors). It is also important to note that we used the integrated series (as submitted to DFA) in both the preliminary calculations and in the RQA. The preliminary steps suggested a delay of 25, an embedding dimension of 3, and a radius of 10 % the mean distance between points. We used these parameters and examined four of the possible outcomes from RQA: the total percent recurrence (REC), mean line length (MLL), percent determinism (DET), and entropy (ENT). We chose these four outcomes as they are relatively standard in analyses of human behavior, and ultimately to capture different (albeit highly interrelated) aspects of coordination between participant and metronome in the cross-recurrence analysis. In particular, REC was intended to capture the overall 'amount' of coordination, MLL and DET to capture the 'stability' of periods of coordination, and ENT to capture the 'homogeneity' in the periods of coordination.

Overall, all of the RQA outcomes revealed the same general pattern as found in the fractal analyses. That is, there was a very large decrease in all the outcomes from continuation to synchronization for those in the blue metronome group, and little to no decrease for those in the pink metronome group. One notable difference between the RQA outcomes is that REC and MLL showed sizable differences between the two metronome groups in the continuation conditions, whereas these group differences were not evident in DET and ENT (Fig. 3). As this effect was absent in the two fractal analyses, this finding suggested that DET and ENT might be more strongly related to the fractal scaling of the tapping behavior.

The convergence of the RQA results with those of the fractal analyses was also evident on a case-by-case basis. To this point, we calculated difference scores across the continuation and synchronization conditions, for each outcome variable, for every participant. We then computed correlations between the two difference variables for the fractal analyses (PSD-shift; DFA-shift) with the four difference variables
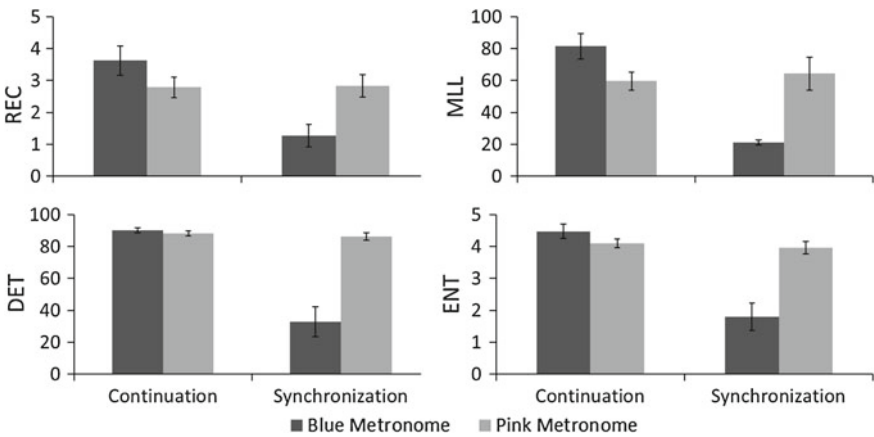
Fig. 3 Percent recurrence (*top left*), mean line length (*top right*), percent determinism (*bottom left*), and entropy (*bottom right*) as a function of tapping condition and metronome group

for the RQA outcomes (REC-shift; MLL-shift; DET-shift; ENT-shift). These tests all revealed a strong relationship ($0.72 \leq$ all r's ≤ 0.90, all p's < 0.0001) between the shift in fractal scaling and in the recurrence outcomes across the two tapping conditions. As before, the DET and ENT ($r \approx 0.85$) outcomes seemed to be more strongly related to the fractal scaling than REC and MLL ($r \approx 0.75$).

To more fully understand the relation between the complexity (fractal scaling) of the tapping behavior and the dynamic structure revealed by recurrence analysis, we also examined the ITI dynamics as embedded in phase space. To illustrate, we chose two example series from each metronome group (see Fig. 4). The difference between the series was not readily apparent 'by eye' in the raw ITI series. In fact, the series had similar overall variability (Blue: $SD = 9.48$; Pink: $SD = 10.74$), but the structure of that variability over time was very different between the two series (Blue: $\alpha = -0.03$; Pink: $\alpha = 0.75$). The long-term, coherent trends entailed in the persistent structure of the pink series, when cumulatively summed, led to much greater variability than the near-random blue series. This structure also translated into the trajectory of the series through phase space. Not only did the pink series show much greater variability, but also a more coherent (less 'noisy') trajectory through phase space. Thus, the differences in complexity revealed by the fractal analyses did reliably translate into differences in the dynamics assessed by RQA. The pink series accordingly yielded larger recurrence outcomes (REC $= 1.88$, MLL $= 58.90$, DET $= 89.19$, ENT $= 4.16$) than did the blue series (REC $= 0.71$, MLL $= 6.50$, DET $= 26.69$, ENT $= 1.62$).

Collectively, these analyses suggested that the recurrence outcomes did capture the different dynamics in the tapping behavior, particularly DET and ENT. Again, this is not to imply that the recurrence technique assesses the complexity of these series directly, but only that there was a reliable mapping between the two analysis techniques for the tapping behavior under study. Thus, we proceeded to the
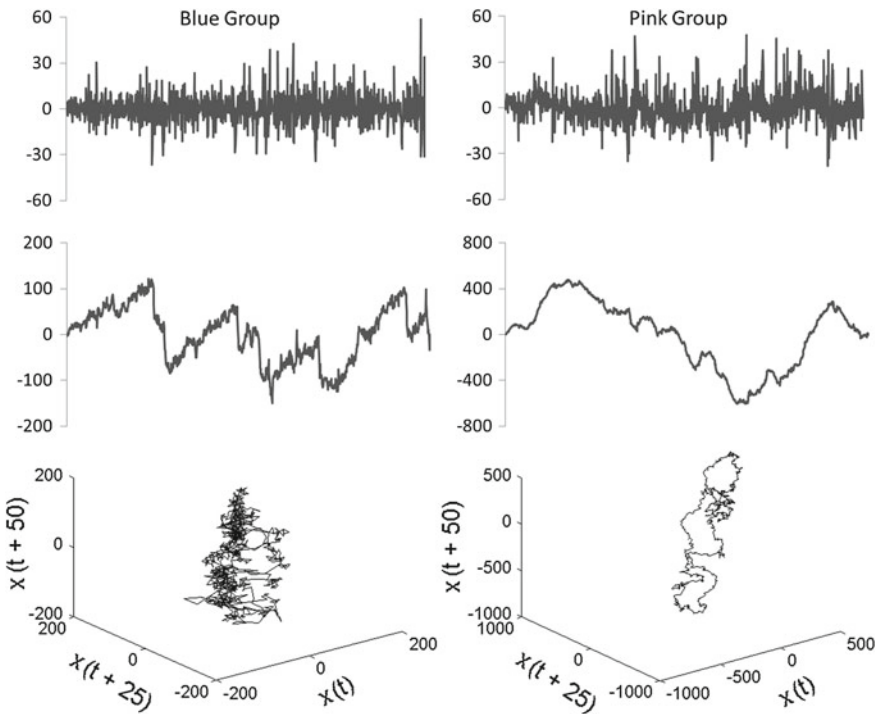
Fig. 4 Raw ITI series (*top row*), integrated series (*middle row*), and phase space trajectories (*bottom row*) for an example series from the *blue* and *pink* group. Note, although the scale is the same for the two raw series, it differs dramatically for the integrated series and the phase space

cross- recurrence analysis to examine the shared dynamical structure (i.e., coordination) between the participants' ITI series and the metronome IOI series.

3.3 Cross-Recurrence and Temporal Coordination

It was, in principle, possible to simply submit the ITI and IOI series as they were to cross-recurrence quantification analysis (CRQA) by embedding both series in the same phase space. As noted above, however, this would have ignored the fact that the participant and metronome time series were initially treated separately. That is, the participant ITI series were pre-processed by a set of criteria that did not need to be applied to the metronome IOI series. The result was that there was no guarantee that, for a given trial, the 100th ITI in the participant series actually corresponded in real time to the 100th IOI in the metronome series. So, we utilized a different pre-processing procedure for the series submitted to CRQA. We paired each tap to its nearest metronome beat and eliminated any extraneous observations (i.e., taps for which the nearest metronome beat was nearer to another tap). The ITI and IOI series were

calculated from these tap-beat paired series, respectively. Finally, the ITI series went through all the same pre-processing steps as before, and in cases where a particular ITI was to be eliminated (e.g., met outlier criteria) the paired IOI was also eliminated.

We conducted a number of preliminary analyses to ensure that this alternate method of pre-processing the data did not substantially alter the previous findings. The scaling exponents defining these new series were strongly correlated with the original scaling exponents (PSD: $r=0.98$, $p < 0.0001$; DFA: $r=0.97$, $p < 0.0001$) and there were small differences in exact values on average (PSD: 0.01; DFA: 0.002). As before, we also found strong correlations between the fractal scaling of these new ITI series and the accompanying IOI series for both PSD ($r=0.69$, $p<0.0001$) and DFA ($r=0.67$, $p<0.0001$). These findings showed that the fractal scaling and complexity matching revealed in the original analyses did not change for this new processing method, and so we proceeded to CRQA.[4] From our initial findings, we were most interested in DET and ENT. We did also examine REC and MLL, however, and the results were generally consistent with those of DET and ENT.

There were a number of possible analyses to assess the relationship between these CRQA outcomes and the degree of complexity matching. As seen above, one common method of assessing complexity matching is to simply correlate the scaling exponents of two time series. We knew from the preliminary tests that the scaling exponents from the participant and metronome were strongly correlated, but we also tested whether the two metronome groups differed in their degree of complexity matching. The blue metronome group showed weaker correlations (PSD: $r=0.31$, $p=0.27$; DFA: $r=-0.10$, $p=0.72$) than did the pink metronome group (PSD: $r=0.49$, $p=0.04$; DFA, $r=0.52$, $p=0.03$). Moreover, the raw difference in the participant and metronome scaling exponents was greater for the blue metronome (PSD: $M = 0.47$, $SD=0.58$; DFA: $M=0.39$, $SD=0.38$) than the pink metronome (PSD: $M=-0.18$, $SD=0.24$; DFA: $M=-0.09$, $SD=0.21$). Interestingly, these group differences are also apparent in the CRQA outcomes. The blue metronome group showed substantially lower DET ($M=9.74$, $SD=8.11$) and ENT ($M=0.77$, $SD=0.11$) than did the pink metronome group (DET: $M=86.42$, $SD=11.03$; ENT: $M=4.37$, $SD= 1.16$). As above, these results suggested a reliable mapping between the CRQA outcomes and the complexity matching revealed by the two fractal analyses.

Although the relation between CRQA and the fractal methods held at the scale of group differences, we also wanted to consider a finer-grained scale. To do so, we calculated the absolute value of the difference between the scaling exponents for the participants and the metronome as a rudimentary 'complexity match' score. These scores showed generally significant correlations with the CRQA outcomes both for PSD (DET: $r=-0.37$, $p=0.04$; ENT: $r=-0.32$, $p=0.07$) and for DFA (DET: $r = -0.46$, $p=0.01$; ENT: $r=-0.43$, $p=0.01$), which suggested that greater differences between the scaling exponents of participant and metronome were associated with lower DET and ENT.

---

[4] Preliminary examination of the new ITI series suggested that the same parameter settings for delay (25), embedding dimension (3), and radius (10 % of the mean distance). Every series was also Z-scored prior to CRQA to ensure both series were on a standard scale.
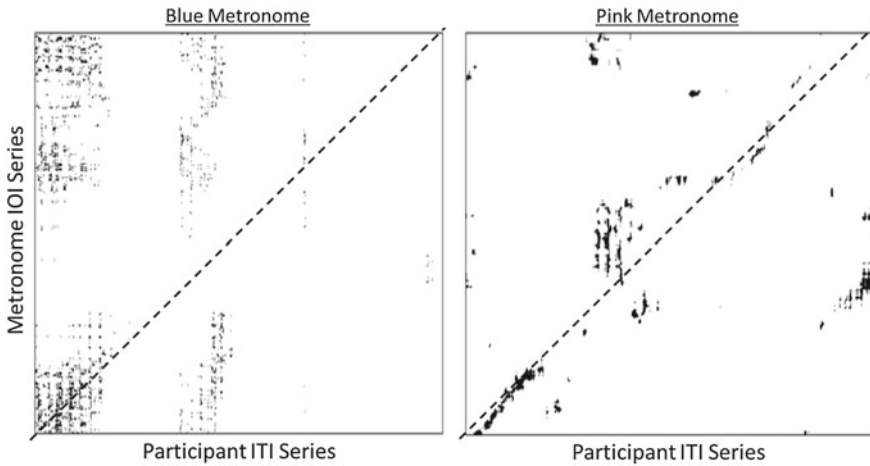
Fig. 5 Two example CR plots from the *blue* (*left*) and *pink* (*right*) metronome conditions. These plots reflect cases with near equal percent recurrence, but the plot for the *pink* metronome case reveals greater structure in the coordination between the participant and metronome

Collectively, these analyses suggested that the shared structure assessed by CRQA outcomes and the cross-recurrence (CR) plots might provide insight as to the nature of the coordination defining complexity matching. The two plots above (Fig. 5) represent two trials, one from each of the different metronome groups. These two cases are interesting because they are comparable in terms of their overall recurrence (Blue: REC = 1.32; Pink: REC = 1.27), but very different in the measures of the *structure* of that recurrence (Blue: DET = 28.13, ENT = 1.53; Pink: DET = 79.74, ENT = 3.30). This difference in the behavioral structure shared between the participant and the metronome is apparent in the CR plots.

Interestingly, the two instances reflected in these CR plots also are comparable in terms of their 'complexity matching' (i.e., simple difference in scaling exponents). That is, in both the blue and pink metronome case, the difference between the scaling of the participant ITI series and metronome IOI series was relatively small (PSD, α-difference ≈ 0.21; DFA, α-difference ≈ 0.14). This finding suggests that although coordination with a blue signal might yield 'bluer' behavior, and a pink signal to 'pinker' behavior, the actual *coordination* between signal and behavior might differ considerably. Specifically, coordination (i.e., instances of recurrence) with a blue metronome seemed to be less 'stable' (lower MLL and DET) and to be more homogeneous (lower ENT). Hence, these findings suggest that beyond the discussion of whether the complexity matching phenomenon is driven by local coordination there are questions as to the dynamical structure of that coordination.

As before, a fuller appreciation of these effects can be gained by examination of the dynamics as embedded in phase space. The participant ITI series and the metronome IOI series for the two example cases presented in the above CR plots are shown above (Fig. 6). Again, the long-term trends entailed in the pink noise pattern
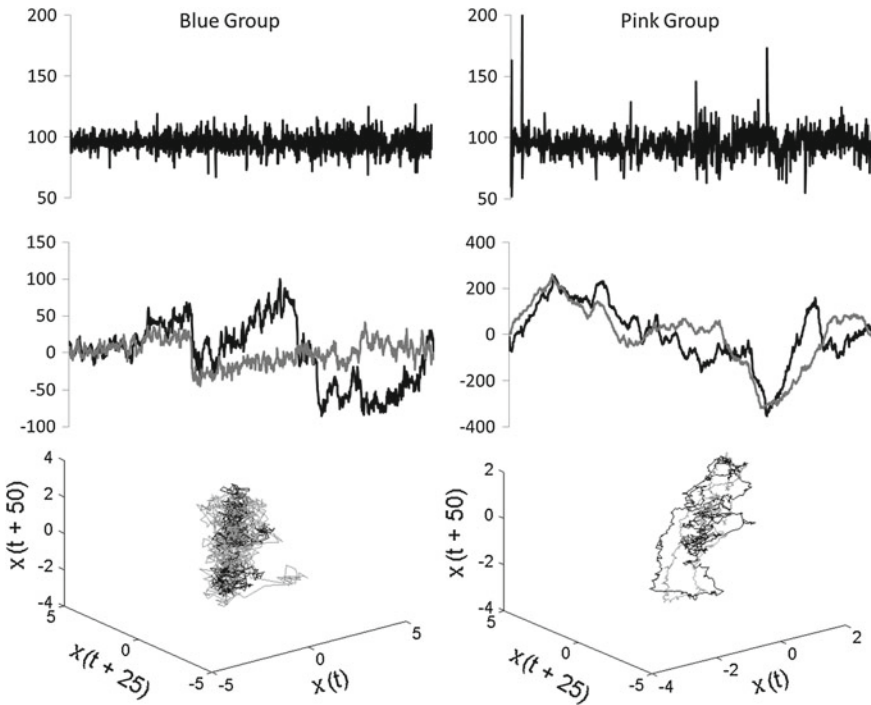
Fig. 6 The raw ITI series (*outliers included*) for the series portrayed in the example CR plots (*top row*), the pre-processed, integrated participant ITI (*black*) and metronome IOI (*grey*) series (*middle row*), and the Z-scored ITI and IOI series embedded in phase space (*bottom row*)

of variation yielded a more coherent trajectory through the phase space. With respect to coordination, these more coherent trajectories yielded to greater structure in cross-recurrence for the pink metronome group. That is, the ITI and IOI series tended to 'move together' through the phase space for longer periods, which ultimately led to longer lines of recurrence (MLL), more recurrent points on lines (DET), and a more heterogeneous distribution of line lengths (ENT).

4 Conclusion

The results of the current experiment suggest that the structure of the coordination between two complex systems might itself be characteristically different under different conditions. Although these findings do propose an interesting new idea, it is important to remember that these results are preliminary and that further testing and validation are imperative. We thus acknowledge some of the limitations of the current work below and suggest some directions for future research.

First and foremost, there is some question as to how precisely the outcomes of CRQA map onto the dynamical structure revealed by fractal analysis. Again, the

recurrence techniques do not directly quantify the same complexity of a signal (i.e., power-law scaling) as fractal methods. As stated before, recurrence analyses are more readily understood as capturing the variability in phase space associated with the fundamental dynamics. Our analyses demonstrate that this variability does indeed reflect the complexity in our measured behavior, although generally complexity cannot be inferred from variability alone (see [9]). One must be mindful of this distinction when interpreting what the outcomes of recurrence techniques mean with respect to the complexity of a behavior.

Secondly, though the results of this introductory study are encouraging, further research is required to validate the use of CRQA to assess the coordination driving complexity matching. For instance, even within the context of finger tapping tasks, a more controlled and thorough study should be conducted to replicate these initial results, and a series of careful surrogate analyses should be run to substantiate the data from the experimental conditions. Moreover, these analyses should be applied to instances of complexity matching in different behavioral tasks to assess whether this use of CRQA can be reliably generalized.

Lastly, CRQA should be carefully compared to other possible analyses of the complexity matching phenomenon. For instance, joint recurrence analysis [24, 32] has several potential advantages in comparison to CRQA, and should be evaluated as an alternative. Similarly, recent research has explored detrended cross-correlation analysis in study of complexity matching [6], and these two techniques should be compared to ensure CRQA provides unique and helpful information.

Despite these limitations, we contend that recurrence techniques remain a viable option for researching the dynamics of temporal coordination underlying the complexity matching effect. First, recurrence analysis is a sensitive analysis with several different outcomes, each of which can provide information as to different aspects of coordination. Second, recurrence analysis is a flexible technique and it readily treats time series of different lengths, even those considerably shorter than those acceptable for fractal analysis. Third, there are several potential avenues within recurrence methods yet to be explored. Information concerning fractal scaling and complexity matching might be available in other quantifiable aspects of the recurrence plots, or in examination of the phase space itself. We do hope that future research will continue to survey this rich technique.

References

1. Eke, A., Herman, P., Bassingthwaighte, J., Raymond, G., Percival, D., Cannon, M., Balla, I., Ikrenyi, C.: Physiological time series: distinguishing fractal noises from motions. Pflügers Arch. **439**, 403–415 (2000)

2. Abney, D.H., Paxton, A., Kello, C.T., Dale, R.: Complexity matching in dyadic interaction. In: Davis, T., Passos, P., Dicks, M., Weast-Knapp, J.A. (eds.) Studies in Perception and Action XII. Proceedings from the Seventeenth International Conference on Perception and Action, Taylor & Francis (2013)
3. Marmelat, V., Delignières, D.: Strong anticipation: complexity matching in interpersonal coordination. Exp. Brain Res. **222**, 137–148 (2012)
4. Stephen, D.G., Stepp, N., Dixon, J.A., Turvey, M.T.: Strong anticipation: sensitivity to long-range correlations in synchronization behavior. Phys. A **387**, 5271–5278 (2008)
5. Torre, K., Varlet, M., Marmelat, V.: Predicting the biological variability of environmental rhythms: weak or strong anticipation for sensorimotor synchronization? Brain Cogn. **83**, 342–350 (2013)
6. Delignières, D., Marmelat, V.: Strong anticipation and long-range cross-correlation: application of detrended cross-correlation analysis to human behavioral data. Phys. A **394**, 47–60 (2014)
7. Stepp, N., Turvey, M.T.: On strong anticipation. Cogn. Syst. Res. **11**, 148–164 (2010)
8. West, B.J., Geneston, E.L., Grigolini, P.: Maximizing information exchange between complex networks. Phys. Rep. **468**, 1–99 (2008)
9. Goldberger, A.L., Peng, C.K., Lipsitz, L.A.: What is physiologic complexity and how does it change with aging and disease? Neurobiol. Aging **23**, 23–26 (2002)
10. Delignières, D., Ramdani, S., Lemoine, L., Torre, K., Fortes, M., Ninot, G.: Fractal analyses for 'short' time series: a re-assessment of classical methods. J. Math. Psychol. **50**, 525–544 (2006)
11. Holden, J.G.: Gauging the fractal dimension of response times from cognitive tasks. Tutorials in contemporary nonlinear methods for behavioral scientists: A webbook tutorial. Available via www.nsf.gov/sbe/bcs/pac/nmbs/nmbs.jsp (2005). Accessed 20 Nov 2013
12. Diniz, A., Wijnants, M.L., Torre, K., Barreiros, J., Crato, N., Bosman, A.M., Hasselman, F., Cox, R.F., Van Orden, G.C., Delignières, D.: Contemporary theories of 1/f noise in motor control. Hum. Mov. Sci. **30**, 889–905 (2011)
13. Torre, K., Wagenmakers, E.J.: Theories and models for 1/fβ noise in human movement science. Hum. Mov. Sci. **28**, 297–318 (2009)
14. Van Orden, G.C., Kloos, H., Wallot, S.: Living in the pink: intentionality, wellbeing, and complexity. In: Hooker, C. (ed.) Philosophy of Complex Systems: Handbook of the Philosophy of Science, pp. 629–674. Elsevier, Great Britain (2011)
15. Torre, K., Delignières, D.: Unraveling the finding of 1/f β noise in self-paced and synchronized tapping: a unifying mechanistic model. Biol. Cybern. **99**, 159–170 (2008)
16. Delignières, D., Marmelat, V.: Theoretical and Methodological Issues in Serial Correlation Analysis. In: Richardson, M.J., Riley, M.A., Shockley, K. (eds.) Progress in motor control, pp. 127–148. Springer, New York (2013)
17. Peng, C.K., Havlin, S., Stanley, H.E., Goldberger, A.L.: Quantification of scaling exponents and crossover phenomena in nonstationary heartbeat time series. Chaos **5**, 82–87 (1995)
18. Bauke, H.: Parameter estimation for power-law distributions by maximum likelihood methods. Eur. Phys. J. B **58**, 167–173 (2007)
19. Clauset, A., Shalizi, C.R., Newman, M.E.: Power-law distributions in empirical data. SIAM Rev. **51**, 661–703 (2009)
20. Conte, E., Khrennikov, A., Zbilut, JP.: New possible properties of atomic nuclei indicat ed by nonlinear methods: fractal and recurrence quantifications analysis. Available via http://www.arxiv.org/abs/0704.0903 (2007). Accessed 20 Nov 2013
21. Conte, E., Zbilut, J.P.: Evidence of low dimensional chaos in glow curves of thermoluminescence. Available via http://www.arxiv.org/abs/0812.0932 (2008). Accessed 20 Nov 2013
22. Sarkar, A., Barat, P.: Effect of meditation on scaling behavior and complexity of human heart rate variability. Fractals **16**, 199–208 (2008)
23. Subha, D.P., Joseph, P.K., Acharya, R., Lim, C.M.: EEG signal analysis: a survey. J. Med. Syst. **34**, 195–212 (2010)
24. Webber, C.L.: Recurrence quantification of fractal structures. Front. Physiol. **3**, (2012). doi:10.3389/fphys.2012.00382

25. Masugi, M.: Applying a recurrence plot scheme to analyze non-stationary transition patterns of IP-network traffic. Commun. Nonlinear Sci. **14**, 1418–1430 (2009)
26. Little, M.A., McSharry, P.E., Roberts, S.J., Costello, D.A., Moroz, I.M.: Exploiting nonlinear recurrence and fractal scaling properties for voice disorder detection. BioMed. Eng. Online **6**, 23–42 (2007)
27. Naschitz, J.E., Sabo, E., Naschitz, S., Rosner, I., Rozenbaum, M., Priselac, R.M., Gaitini, L., Zukerman, E., Yeshurun, D.: Fractal analysis and recurrence quantification analysis of heart rate and pulse transit time for diagnosing chronic fatigue syndrome. Clin. Auton. Res. **12**, 264–272 (2002)
28. Naschitz, J.E., Itzhak, R., Shaviv, N., Khorshidi, I., Sundick, S., Isseroff, H., Fields, M., Priselac, R.M., Yeshurun, D., Sabo, E.: Assessment of cardiovascular reactivity by fractal and recurrence quantification analysis of heart rate and pulse transit time. J. Hum. Hypertens. **17**, 111–118 (2003)
29. Naschitz, J.E., Michael, R., Fields, M., Enis, S., Manor, H., Dreyfuss, D., Peck, S., Peck, E.R., Babich, J.P., Mintz, E.P., Sabo, E., Slobodin, G., Rozner, I.: Cardiovascular reactivity in fibromyalgia: evidence for pathogenic heterogeneity. J. Rheumatol. **32**, 335–339 (2005)
30. Marwan, N., Kurths, J.: Line structures in recurrence plots. Phys. Lett. A **336**, 349–357 (2005)
31. Marwan, N.: How to avoid potential pitfalls in recurrence plot based data analysis. Int. J. Bifurcat. Chaos **21**, 1003–1017 (2011)
32. Marwan, N., Romano, C.M., Thiel, M., Kurths, J.: Recurrence plots for the analysis of complex systems. Phys. Rep. **438**, 237–329 (2007)
33. Webber, C.L., Zbilut, J.P.: Recurrence quantification analysis of nonlinear dynamical systems. Tutorials in contemporary nonlinear methods for behavioral scientists: A webbook tutorial. Available via http://www.nsf.gov/sbe/bcs/pac/nmbs/nmbs.jsp (2005). Accessed 20 Nov 2013
34. Webber, C.L., Zbilut, J.P.: Recurrence quantifications: feature extractions from recurrence plots. Int. J. Bifurcat. Chaos **17**, 3467–3475 (2007)

Synchronicity Assessment Using a Non-parametric Dynamic Dissimilarity Measure

Patrick Crowley and Christopher Trombley

Abstract In this paper, we introduce a non-parametric dynamic dissimilarity measure (DDM) of synchronicity based on recurrence plots, which is particularly suited to use in small samples. The measure attempts to capture the dissimilarity of the topology of the dynamics of time series, based on an epoch analysis of the cumulative sums of data series. The measure is applied to US State macroeconomic data and is used to assess how synchronous US State business cycle variables are with US aggregates.

1 Introduction

Social scientists often refer to variables as being synchronized if they exhibit co-movement. But generally co-movement in social science is measured from a long term perspective, using relatively large datasets, and employing simple measures such as maximal windowed correlations to indicate synchronization, or more complex techniques such as cointegration and concordance measures from factor models (see [1, 2]), if data permits. Otherwise, if only small samples are available, then most social scientists resort to simple correlations as a measure of synchronicity. Macroeconomic researchers in particular are typically faced with small data sets (relative to those found in natural and environmental sciences) and so more often than not, when these conditions arise they appeal to regression analysis or basic correlation to assess synchronization.

Macroeconomists in particular are also concerned specifically with the synchronization of business cycles (the boom and bust cycles that are a stylized fact in economics), and so are particularly focused on correlations of economic growth patterns across countries or regions as a way of measuring economic integration across

P. Crowley (✉) · C. Trombley
College of Business, Texas A&M University, Corpus Christi, TX, USA
e-mail: patrick.crowley@tamucc.edu

C. Trombley
Department of Mathematics, Texas A&M University, Corpus Christi, TX, USA

regions or geographic areas that have some facet of economic policy in common (such as a common currency). But when applying synchronization measures economists often face major problems in interpreting these measures (such as with accounting for lag or lead effects), and also the distributional assumptions of these measures might not be appropriate.

In this study we therefore introduce a simple non-parametric dynamic dissimilarity measure (DDM) that can be applied to economic and other data series to overcome some of the issues encountered when using small datasets. We present this DDM for assessing synchronization, which is derived from recurrence plot techniques, as a relatively simple approach particularly suited to small sample stochastic empirical data. In the paper, for illustrative purposes, we apply this technique to US State macroeconomic data.

The paper is organized as follows: Sect. 2 presents two different ways of assessing the degree of synchronization with small data samples, while Sect. 3 looks at an application using the methodology employed in this study. Section 4 then concludes.

2 Measurement of Synchronization

The topic of synchronization is vast, with probably the best reference on the subject being [3], which details the myriad forms of synchronization in nonlinear science. In this section we first explore the cross-recurrence methodology for synchronicity detection, and then we introduce the new measure, both of which are specifically applied to small sample measurement of synchronization.

2.1 Cross-Recurrence Methodology for Synchronicity Detection

The first measure of synchronization presented here is based on recurrence plots. Recurrence plot analysis is now over 20 years old (see [4] for the first contemporary application) and the quantification of these plots is much more recent (see [5, 6]) but the notion of recurrence has a much longer pedigree in mathematics (see [7]). Recurrence plots first originated from work done in mathematics and physics but now has a considerable following in a variety of fields.[1] There are several excellent introductions available to RQA and recurrence plots, not least those by [8, 9]. There are very few papers that apply recurrence plot techniques to macroeconomic issues, the notable exceptions being [10–13].

In terms of the mathematical background, a recurrence plot is calculated from a phase space trajectory, that can be reconstructed using Takens' embedding theorem (see [14]). However, here we simplify the usual exposition of recurrence plots and

---

[1] Norbert Marwan's website catalogues all the articles published using recurrence plots and RQA, and is a veritable mine of information on this topic. See http://www.recurrence-plot.tk.

consider just the dynamics of the raw data x_i $(i = 1, \ldots, N)$. To derive the recurrence features of the series then every point in the series x_i is tested to see whether it is close to another point, i.e., the distance $D_{i,j}$ between these two points i and j

$$D_{i,j}(x, y) = \|x_i - y_j\| \tag{1}$$

is less than a specified threshold ε. In this case the value one (a black dot in the recurrence point) is assigned to this point in a $k \times k$-array (the auto-recurrence plot):

$$R_{i,j} = \Theta(\varepsilon - D_{i,j}(x, x)) \tag{2}$$

where x_i and y_i in (Eq. 1) are two series such that $x = y$ in the auto-recurrence case, and ε is the predefined "threshold" and Θ is the Heaviside function. Following [15] the cross recurrence plot is defined by considering two different time series x and y:

$$CR_{i,j} = \Theta(\varepsilon - D_{i,j}(x, y)) \tag{3}$$

where in this instance x_i and y_j in (Eq. 1) are two series such that $x \neq y$. This gives a thresholded cross recurrence matrix $CR_{i,j}$ which, dependent on the value of ε contains either 0s (the white areas in the plots) or 1s (the black areas in the plots).

In an auto-recurrence plot, the main diagonal is always present, as every point in the series is identical to the same point in the series, so there will always be a diagonal line (1's down the main diagonal of the thresholded $R_{i,j}$ matrix), once all points in the series are considered. In the cross recurrence plot if line-like patterns that correspond to diagonal lines on the leading diagonal in the recurrence plot appear, the two series are identical, but this is obviously a special case. If line-like patterns that correspond to diagonal lines in the recurrence plot appear in other parts of the cross-recurrence plot, it implies similar dynamics, but these implying short lived periods of synchronization or phasing of the two cycles. This line, if it can be identified, is termed the "line of synchronization" or LOS [15]. These observations also hold when not applying the thresholding but using the distance matrix (Eq. 1) itself (instead of lines we consider then the line-like patterns formed by the lowest distance values in the matrix).

Next, complexity measures can be derived to characterize the cross-dynamics of a given series. For two series these will be characterized as diagonal lines (not necessarily on the main diagonal), which demonstrate similar dynamics maybe at different points in time. Following [16] the distributions of the diagonal line lengths can be written as $P_t(l)$ for each diagonal parallel to the main diagonal, where $t = 0$ denotes the main diagonal, $t > 0$ denotes diagonals above the main diagonal (a lead) and $t < 0$ denotes diagonals below the main diagonal (a lagged dynamic). RQA was initiated by [5] and has now been introduced into mainstream physics through the study of nonlinear dynamics. A good summary is available in [9].

The starting point in this paper is the analysis conducted in [12] with cross recurrence plots. Here we take the example of the real Gross State Product (GSP) growth rate for Texas and the real GDP growth rate for the US, and display the unthresholded
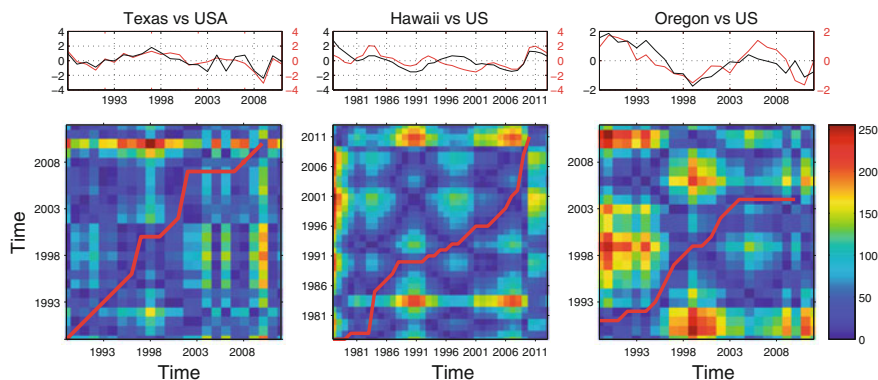
Fig. 1 (*Left*) Cross recurrence plot of Real GDP growth for Texas versus US. (*Middle*) Cross recurrence plot of GDPPI inflation for Oregon versus US. (*Right*) Cross recurrence plot of the unemployment rate for Hawaii versus US

version in Fig. 1(left). These data series are annual (that is all that is available by State in the US), so that there are only 25 observations available for the analysis. In the upper part of the figure the data is reproduced, and in the lower part of the figure the color scale denotes the distance between the two series with red denoting a small distance up to blue areas which denote large distances. Any diagonal lines in the plot indicate the synchronous dynamics in both series with a diagonal going up from the lower left to the upper right being the "line of identity" (LOI). In other words if there was just a red line going diagonally through the plot this would indicate identical series. If an unthresholded plot is used, the line of synchronous movements, otherwise termed the LOS, can be plotted using a search algorithm (see [15, 17]) to detect the best path through the plot. The LOS thus indicates coincident synchronicity and it is apparent that this is fairly consistent in the first part of the period in question in Fig. 1(left). Synchronicity though appears to break down in the late part of the cycle leading up to the 2001 recession, but once the recession hits (observations 13–15 in red in the upper figure), synchronicity is restored. In the growth period of the last business cycle, there doesn't appear to be a great amount of synchronization in growth until the most recent downturn hits in 2008, and then for the remainder of the period in question the two series are highly synchronous and convergent again. This is also shown by a return of the LOS to the leading diagonal in the cross recurrence plot. These results are consistent with the finding that synchronous behaviour in economic growth nearly always occurs during the recessionary period of the business cycle, but occurs much less frequently during the growth phase of the business cycle.[2]

Further examples are given for different US States for the other variables used in this study. Figure 1(middle) shows the cross recurrence plot for Oregon for GSPPI (Gross State Product Price Index) inflation measure against the US GDPPI (GDP Price Index) inflation measure. This particular State was chosen because of its relative

---

[2] Crowley and Schultz [19] have termed this phenomena "intermittent synchronicity".

asynchronous dynamic with the US. Here the LOS is much less obvious in the cross recurrence plot, and the algorithm that chooses the LOS doesn't appear to detect any consistent synchronicity beyond roughly 2004 onwards.

Lastly, we produce the cross recurrence plot for Hawaii against the US for the unemployment rate in Fig. 1(right). Hawaii does not seem to have been particularly synchronous with the rest of the US until the most recent business cycle from 2002 to present. Nevertheless there does seem to have been a variable lag synchronous effect at work throughout the 1990 s and this is detected by the algorithm generating the LOS. Note as well that the movements in the two unemployment rates are similar from 2003 onwards, but the LOS cannot jump in the CRP so that it reflects this high degree of concurrent synchronization.

So in the context of employing traditional cross recurrence plots to analyze synchronicity in economics, there are several issues, and these are:

(a) that economic series are stochastic in nature, so that synchronicity might be detected only at certain points in time;
(b) that the cross recurrence plot LOS measure is only designed to detect similar dynamic movements in variables due to time scaling, rather than similar patterns of directional dynamics in stochastic time series (see [15]); and
(c) that cross recurrence plots also incorporate an analysis of convergence, which is not the focus here.

Although recurrence quantification analysis does account for (a) above, we wish to focus in solely on the degree of synchronicity, so we wish to abstract from (c) and place the spotlight on (b), so as to concern ourselves only with directional dynamics.

2.2 A Small Sample Measure of Synchronization Based on Dynamic dissimilarity

We next introduce a measure of synchronization based on a dynamic dissimilarity measure (DDM), by focusing on the similarity of the dynamics by taking the distance measure between the cumulative sum of any two series, and seeing how this varies through time within an epoch analysis framework.

Each time series is first transformed into a stationary growth rate (e.g. by log first differencing real GDP to obtain economic growth rates) or stationary source variables are used (such as unemployment rates), and then a cumulative summation variable of this stationary variable is created:

$$X_i = \sum_{j=1}^{i} (\log x_j - \log x_{j-1}) \tag{4}$$

We refer to these modified time-series, X_i, as cumulative unsigned summation (CUS) series. Distance matrices, $D_{i,j}$ for each CUS series are then created using the standard

Euclidean distance metric as described in [8] and this operation is identical to (Eq. 1). To evaluate the dissimilarity between two time series, we then perform an epoch (moving window) analysis with a three sample window incremented one sample at a time, where in the bivariate case $D1_{i,j}$ denotes the epoch window for X_i containing NN values of $D_{i,j}$ for the epoch window of size $N \times N$. For each epoch the DDM is computed by taking the difference between the paired values in the epochs from each time series, which for the bivariate case we denote as $D1_{i,j}$ and $D2_{i,j}$:

$$E_{i,j} = |D1_{i,j} - D2_{i,j}| \tag{5}$$

where $E_{i,j}$ represents the differenced epoch window for the first series etc., and i, j are the time points in a particular epoch. Note that for example in the case where $N = 3$: (i) the dynamics included in the comparison can range over 4 periods, as each point in itself can represent a change in the distance matrix; (ii) the $E_{i,j}$ matrix incorporates both lead and lag dynamics as it includes off-diagonal elements as well; and (iii) that the range in values for $E_{i,j}$ is from 0 to $\max\{D1_{i,j}, D2_{i,j}\}$. A value of $E_{i,j} = 0$ clearly denotes complete synchronization between the two series.

Finally we take the average value of the components of $E_{i,j}$:

$$DDM = \frac{\sum_{i,j=1}^{N} E_{i,j}}{N^2} \tag{6}$$

to obtain a DDM which represents the total dissimilarity between $D1$ and $D2$ for a particular epoch. This process can be done for a single variable against another variable (as is shown above) to create a synchronicity-proxy or can be repeated for each possible pair of time series so as to create a "super" dissimilarity matrix for all variables by epoch. In the latter case, the dissimilarity matrix at each time step is then averaged to estimate the total dissimilarity between members of the set for a particular temporal window. The final product is then a one dimensional time series representing the synchronization in dynamic between members of a set with smaller values indicating greater synchronicity.

Once the absolute differences have been evaluated for a set of variables they can also be plotted to show the "within-group" average level of dissimilarity between all the members of the group.

To summarize then, the methodology is as follows:

  (i) Cumulate all the (signed or unsigned) series;
 (ii) Form a distance matrix $D_{i,j}$ for the cumulative series by calculating the distance of every point from every other point, then squaring, sum and square root;
(iii) Now form an epoch window over the set of cumulative distance measures $D_{i,j}$ which we label as matrix $D1_{i,j}$;
(iv) Now subtract the matrix $D2_{i,j}$ from the equivalent matrix $D1_{i,j}$ to form another matrix, $E_{i,j}$;
 (v) Average the values of $E_{i,j}$ to obtain a dynamic dissimilarity/synchronicity measure between the two series.

Although the method described above is similar to the approach described in [18] for finding optimal lag or lead structures, the present method is not concerned with lead or lag structures but is solely concerned with using the general approach to construct a non-parametric measure of synchronicity. This DDM described here was first applied by [19] to EU data to show how signed macroeconomic synchronicity between European Union member states is intermittent, and in this paper we use an unsigned (Euclidean distance) measure as a means of assessing synchronicity in small samples.

3 Application to US State Macroeconomic Data

3.1 Background

Given the longevity of the US monetary union, which is partly due to the fact that the monetary union was part of the political union that took place at the same time in 1776, one would expect a high degree of economic convergence between its constituent parts. The reason for this expectation is that policies enacted at the federal level, most notably fiscal and monetary policy, should have provided a common component which could be found across all 50 states.[3]

Of course being part of an economic and monetary union could also generate specific industry dynamics which give rise to agglomeration effects, and hence faster growth in a specific location (for example technology in relation to Silicon Valley in California, or banking and securities in relation to New York), but if these location effects are spread fairly evenly across the country, then these effects will likely not overpower the impact of federal policies at the State level. At the same time, similar regional characteristics might come into play here as certain industries (such as agricultural industries) might dominate regionally, giving a higher degree of regional co-movement.

This clearly merits some exploration, given that the US has long been regarded as an optimal currency area (OCA).[4] But why is this the case? Obviously the fiscal record of each US State government is not a significant factor as it would be in the European Union, as most US States have enacted balanced budget amendments so relatively little debt is issued compared with Gross State Product (GSP) (California is a recent exception to this, as was New York State back in the 1980s). Several papers

---

[3] Of course fiscal policy enacted by Congress can be aimed at a particular set of States (for example disaster relief after a hurricane), or its impact might incidentally give greater benefits to a specific state (for example defense spending in relation to the Californian economy). Similarly monetary policy that benefits financial institutions might have a greater impact on those regions of the country that have a greater concentration of financial industry (such as New York and Illinois).

[4] There is little research as to the nature of the US monetary union in terms of its macroeconomic characteristics. This is partly due to the severe data limitations on availability of State macroeconomic data.

have established that the US can be regarded as an optimal currency area not only because of the convergence in many macroeconomic measures, but also because of the perceived synchronization between most US States and macroeconomic measures for the country as a whole (see [20] for an example in relation to globalization and in particular an unpublished paper by [21]). Of course the major policy measures are taken at the Federal level, not only by Congress through US fiscal policy but also there is the Federal Reserve (Fed) monetary policy. Not only this, but also if there are regional shocks which depress certain States, there is a relatively high degree of labor mobility due to a high degree of linguistic and cultural homogeneity. Thus most economists view the major criteria for being a single currency area as largely met in the US (usually for counter-factual reasons given the longevity of the arrangement), and therefore because of the common monetary policy one might expect a high correlation of business cycle variable movements between the participants of the US monetary union. This is the basic thesis for the application presented in this application, which explores the nature of the co-movement in growth and other business cycle variables.

3.2 Business Cycles and OCA Theory

The standard tool used in economic literature to evaluate the adequacy of a monetary union is the OCA theory, originated by [22, 23], with refinements by [24] and [25]. The OCA theory compares the benefits and costs to countries participating in a currency area. Benefits include lower transaction costs, price stabilization, improved efficiency of resource allocation, and increased access to product, factor, and financial markets. The main cost, however, is the country's loss of sovereignty to maintain national monetary and exchange rate policies. Both costs and benefits depend on the nature of exogenous shocks affecting potential member countries and the speed with which they adjust to them. The costs tend to be lower (higher) if shocks are symmetric (asymmetric) and market mechanisms are quick (slow) to restore equilibrium after the shock. Nonetheless, the existence of heterogeneities across countries does not necessarily imply that monetary integration cannot be achieved. This follows from the endogeneity argument—originally proposed by [26], which suggests that countries become more similar when they form a monetary union.

The synchronicity in movement of economic growth rates is economically important for 2 underlying reasons:

1. the more globalized the world becomes, the more likely that trade and financial flows will cause greater "synchronization" in growth rates between countries—known in the literature as the "international business cycle"; and
2. for collections of administrative entities that use the same currency (such as the US dollar, the Canadian dollar and the euro area member states of the European Union), similar movements in economic growth rates can either indicate

(i) *ex-ante* the suitability for adopting the same monetary policy (the optimal currency area (OCA) theory[5]); or

(ii) *ex-post*, the fact that monetary policy has been a factor in making these countries have similar patterns of growth (the endogenous OCA theory).

There has long been recognition of the propagation phenomenon of business cycles between countries (the main mechnanisms being trade and capital flows). The main indicator of this propagation is the synchronicity of turning points in business cycles (noted by [27, 28] in the real business cycle literature) but what is not recognized here is that the economic growth dynamic between these turning points (usually the recessions or peaks of business cycles) can be radically different between countries or in this case, US States. This observation has given rise to the notion and study of growth cycles in the context of the dynamic of economic growth between these turning points (see [29, 30]). From an empirical perspective there have been some efforts to empirically extract cycles for measurement and comparison across countries using frequency domain techniques (see [31–33]) but only limited research has been conducted in this area.

In the US, as the US dollar has been the adopted currency of the US for so long (despite the private printing of notes in the 19th century), according to the theory it should clearly be an OCA *ex-post*, and indeed many studies have shows that the majority of US States do exhibit high correlations in growth dynamics, but some research has indicated that the geographic extremes of the country (Hawaii, Alaska and Florida in particular) do exhibit some independent growth dynamics. Little research has been done in this vein in terms of analysis of US State business cycle synchronicity using measures other than conventional correlation measures.

Only in the last decade has the question been asked as to whether increased-break business cycle synchronization is driven more by global or regional factors, and whether this has changed over time. Research by [34] first noted that cyclical convergence was much more a global rather than a regional phenomenon, but more recently, using spectral analysis [35] showed that the convergence at lower frequencies was due to common cycles, in other words globalization. In the latter study though [35] only used the US, UK and the euro area to assess this, so this could have been due to anomalies associated with the UK situation rather than being a general result. [20] provides strong evidence in support of the conventional wisdom that rising global integration over time, through either trade or foreign direct investment flows, raises a state economy's business cycle correlation with the world economy. Interestingly openness to trade and investment promotes greater business cycle synchronization within regional US economies than with the rest of the world. If our results mirror those found by [20], then we should expect to find that there is a trend to greater synchronization between US State data over time.

To summarize, we are assessing whether the similarity in business cycle variables (economic growth, inflation and unemployment) changes over time, and whether the variance in synchronicity between States and the US aggregate has changed through time.

---

[5] The original and seminal contribution here was made by [22].

3.3 Data

There is very little purely macroeconomic data available by US State, but we select
three variables directly related to the business cycle, namely:

3.3.1 Economic Growth

Here we measure economic growth at time t, as g_t, by taking the real Gross State
Product (GSP) at time t, y_t, and transforming it by taking natural log first differences
as follows:

$$g_t = \ln(y_t) - \ln(y_{t-1}) \tag{7}$$

Unfortunately this dataset is only available from 1987, so once log first differences
are taken, the data runs from 1988 to 2011, giving 23 datapoints. The data is sourced
from the Bureau of Economic Analysis (BEA). Data was available by State and for
the US as a whole.

A sample of these economic growth rates is plotted. Figure 2 shows the data for
the States in one particular region—notably the BEA Southwest region, comprising
Arizona, New Mexico, Texas and Oklahoma.

Figure 2 (left) shows that even with specific geographical regions of the US, growth
rates at any point in time can be quite different, but that in general the turning points
in the business cycle (most notably the 2008–2010 US recession) are synchronized.
Even so, it is clear that Arizona had a much deeper recession than Texas did, which
was likely due to the fallout from the housing market collapse, where Arizona had
much more highly inflated prices than Texas.

Synchronization in growth rates might be expected to be much less coordinated in
more geographically dispersed parts of the country though, most notably in Alaska
and Hawaii, so in Fig. 2 (right) we plot the growth in real GSP for Alaska, Hawaii,
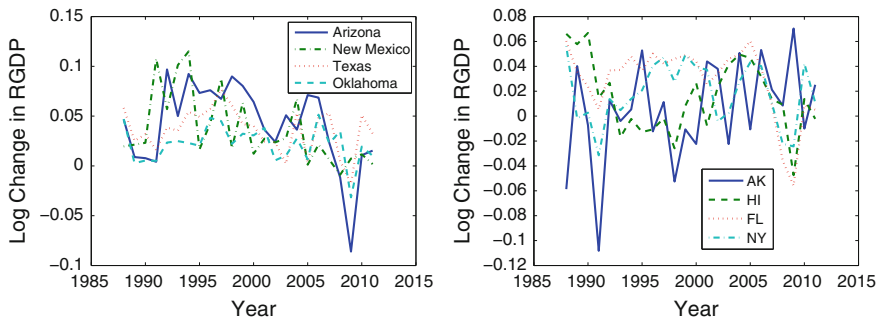
Fig. 2 (*Left*) Real GDP growth rate for South West US States. (*Right*) Geographically dispersed
US State GSP growth

Florida and New York (New York is selected to represent a highly synchronized US state).

Interestingly Alaska appears not to have been affected by the recent economic downturn until several years later, and to a much smaller extent whilst Hawaii appears to have been affected with a lag, but as severely as Florida. In the growth period there appears to be little synchronization in growth during this period with large 2 year cycles in Alaska, and smaller growth cycles in other States.

As economic growth is considered to be an important measure of the health of the economy, we also reproduce the figures from the BEA which show the latest levels of growth in individual states in Appendix A.

3.3.2 Inflation

Here this is proxied by the GSP deflator, as a Consumer Price Index (CPI) is only available for urban areas, and so does not cover all States, and even when there is a major urban center in a specific State, it might not reflect prices for the whole of a larger State. Once again the natural log first difference is taken (to create the equivalent of an inflation rate), and also the data is similarly sourced from the BEA[6] and contains just 23 datapoints. This dataset had to be derived from BEA data on real GSP and nominal GSP.

Figure 3 (left) shows the data for the Southwestern US States, and Fig. 3 (right) shows the data for the Far Western US States. In Fig. 3(left) the inflation data for New Mexico, Texas and Oklahoma are fairly synchronized in the last growth phase after the 2001 recession, and move very closely together into a deflationary period during the recent downturn from 2007–2009, before rebounding in 2010. Arizona however does not appear to follow the trend of the other 3 States—although inflation slows in the late part of the last decade, there is actually a slight pickup in inflation going into the recession, followed by a fall in inflation as there is a pickup in inflation elsewhere in the region. In the Far West region of the US, Fig. 3 (right) shows that the States concerned exhibit a very narrow range of inflation rates in the early part of the period, but the range of inflation rates widens out in the late 1990s with inflation highest in Nevada and lowest in Oregon. There appears to have been greater synchronicity in inflation during the most recent downturn, although Oregon appears to have experienced lower inflation rates than the other 3 States throughout the period.

3.3.3 Unemployment

This is taken as the usual definition of the unemployment rate, i.e., the number of unemployed divided by the labor force. This is available from 1976 onwards, both

---

[6] Two series had to be spliced together to create this series. Details are available from the author on request.
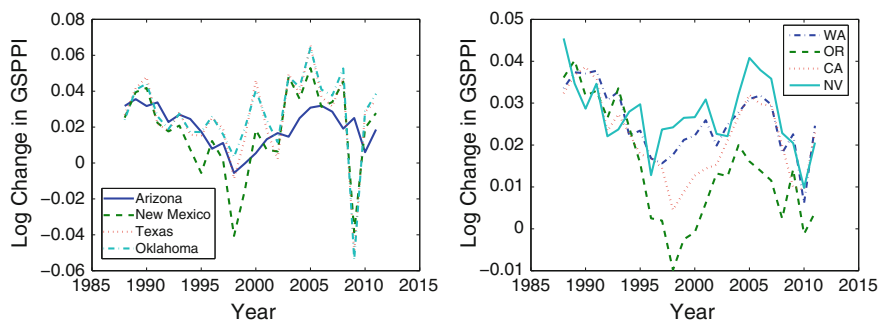
Fig. 3 (*Left*) GSPPI inflation for Southwestern US States. (*Right*) GSPPI inflation for Far West US States

monthly and annually from the Bureau of Labor Statistics. Two versions of this series are used in the analysis—one that uses the full data span available and the other which uses only the data from 1988 to 2011 so as to be comparable with the economic growth and inflation variables detailed above.

Unemployment is usually viewed as a lagging indicator when referencing the business cycle, and in Fig. 4 (left) for the Southwestern US States, this appears to be very much the case. Unemployment magnitudes are, however, different accross the region with unemployment rates peaking at around 7 % in Oklahoma but at over 10 % in Arizona. One of the worst parts of the country to be hit by large increases in unemployment rates was the Great Lakes region, and the relevant unemployment rates are shown in Fig. 4 (right). Perhaps the most interesting aspect of this figure is the fact that for all these US States the unemployment rates were higher in the early 1980s recession than in the most recent economic downturn. Once again, the movement in the unemployment rates is fairly well synchronized across all the States.
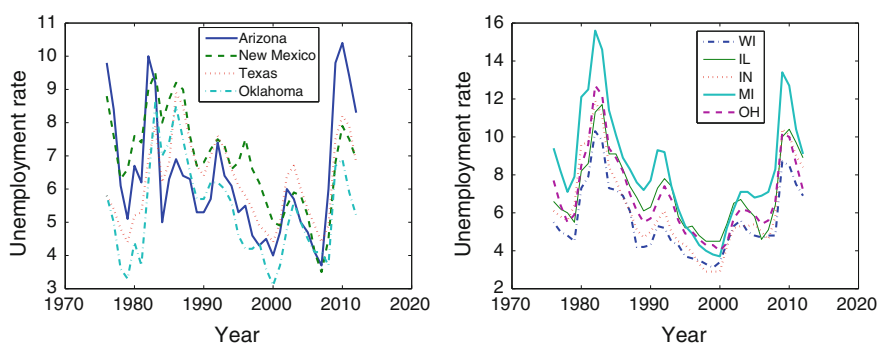
Fig. 4 (*Left*) Unemployment rate for Southwestern US States. (*Right*) Unemployment rates for the Great Lakes US States

3.4 Results

Results here are presented for each US State vs the US aggregate. An alternative approach which is currently being explored is to look at intra-State synchronicity and then average these over all States or a collection of States (e.g. for a specific geographical BEA region).

3.4.1 Economic Growth

In this section we review the results of applying the technique above to US state economic growth data, which we plot by BEA region. As shown in appendix A there are 8 BEA regions. As some US states are extremely large relative to the rest of the US, we construct aggregates for each State for real GDP such that the aggregate represents [US real GDP—State i GDP] and then conduct the dissimilarity exercise on the State vs this aggregate. For purposes of statistical testing, we use the 95 % confidence limit on the actual distribution of States.

In Figs. 5 and 6 we display the results by State collected by BEA region In Fig. 5 (left) it is noticeable that Oregon and Hawaii track into the shaded (significant) area in the figure denoting significant asynchronicity with the US as a whole. Another feature of all these figures relating to real GDP growth is the fact that most of the US states clearly had similar dynamics going through the last major economic downturn in 2008 (this represents the window centred on 2008, so covers 2007–2009), but that there are some notable exceptions. So for example in 2008, in Fig. 5e North Dakota appears to have been an exception, and did not experience the same recessionary dynamics that the rest of the country faced, and also Virginia in Fig. 6b and Wyoming in Fig. 5f appear to have faced somewhat different growth dynamics during the recession. Overall, for the period as a whole there appears to have been a slight increase in synchronicity in growth (as measured by the fall in dissimilarity), which mirrors the results of [20].

In Fig. 7 (left) both the mean dissimilarity and the standard deviation of the DDM are plotted. The results clearly confirm the increase in synchronicity documented earlier, and a small fall in standard deviation.

The kernel estimate of the PDF is given in Fig. 7 (right). The 95 % confidence interval under the null hypothesis of similar dynamics is shown in the figure and is at 0.2102.

As a robustness check on the qualitative results obtained above, we repeat the exercise in Appendix B for personal income over a longer time period and using quarterly data. The qualitative results are similar although not identical, but that is not surprising as personal income is a nominal variable and also it is only one component of GDP.
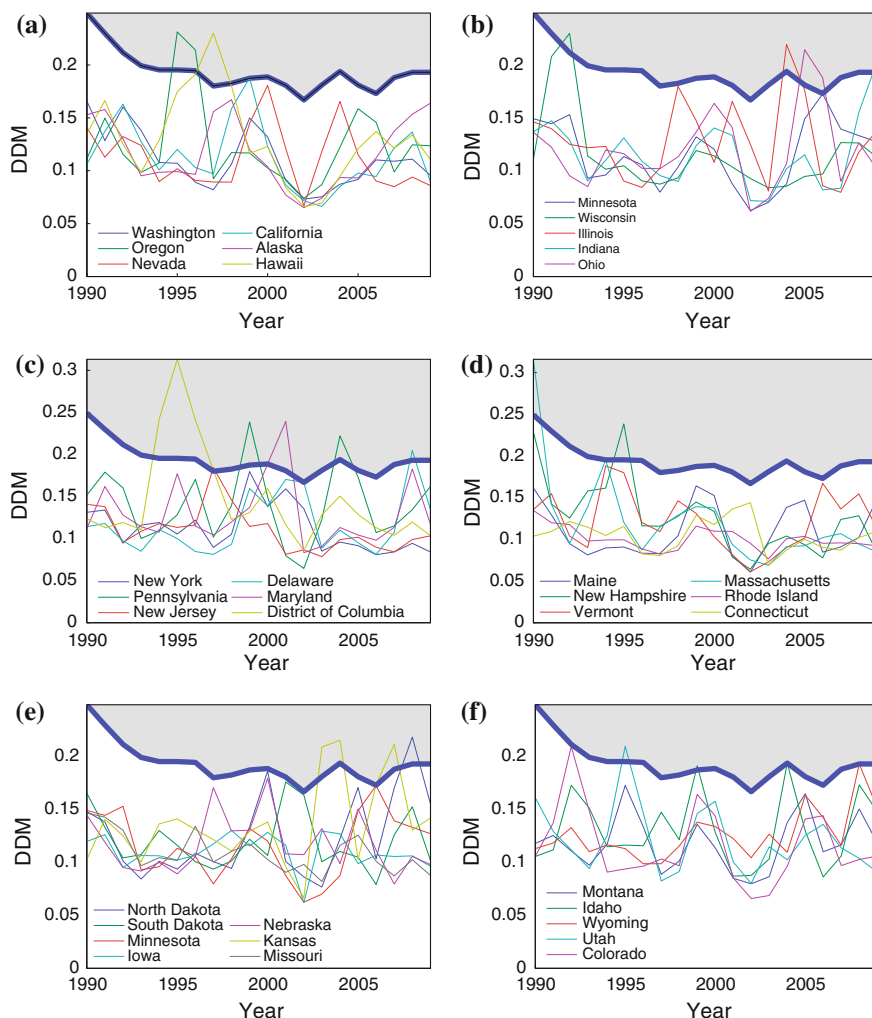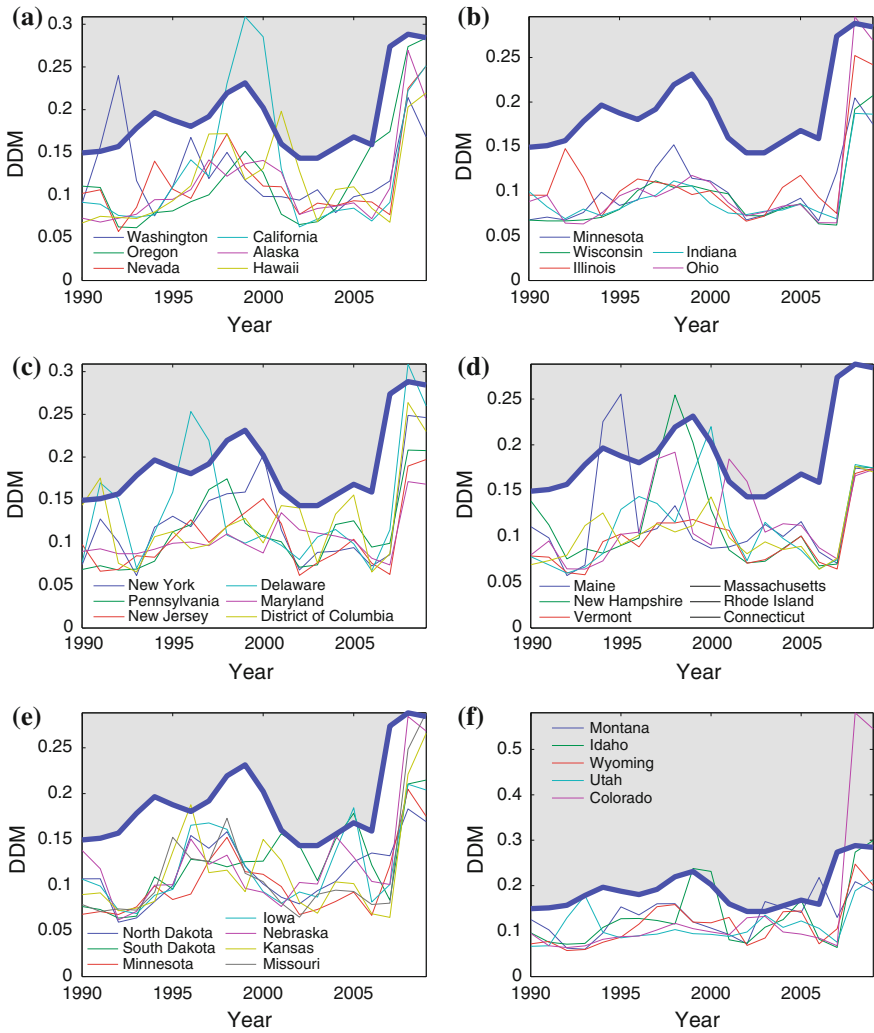
Fig. 5 Real GSP growth of **a** Far West State. **b** Great Lakes State. **c** Mid East State. **d** New England State. **e** Plains State. **f** Rocky Mountain State versus US national aggregate

3.4.2 Inflation

In this section we repeat the exercise conducted above but instead for the growth in the real GSP deflator, which is derived from simple calculations using published estimates of state real GSP and state nominal GSP.

Figures 8 and 9 show the dissimilarity plots for the real GDP deflator variable. Here the pattern is a little different, with a clear divergence in GDP deflator growth rates in the 2007–2009 downturn, so noticeably at the 2008 mid-point. Clearly the
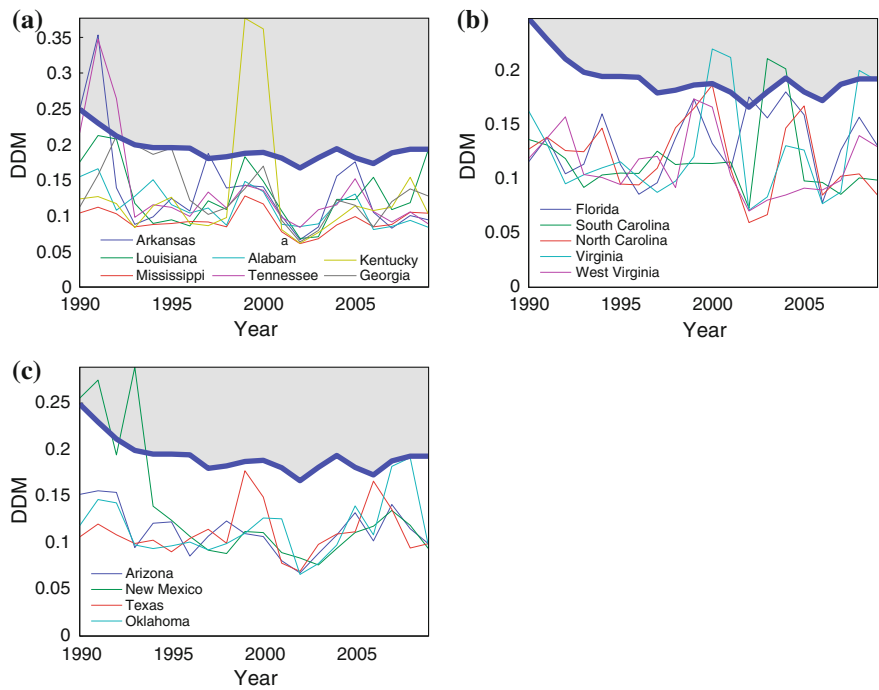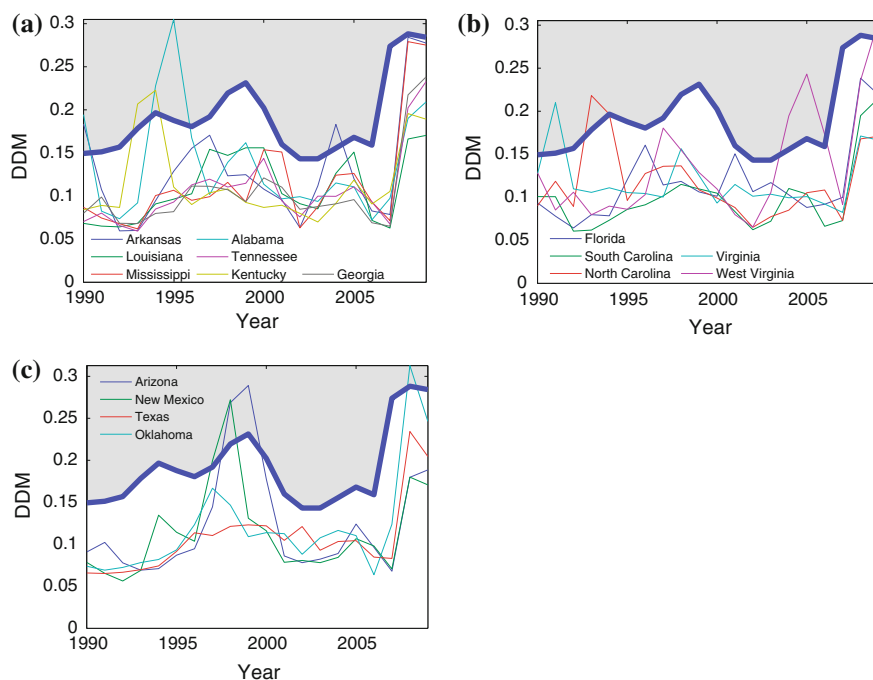
Fig. 6 Real GSP growth of **a** South East State. **b** South East State. **c** South West State versus US national aggregate
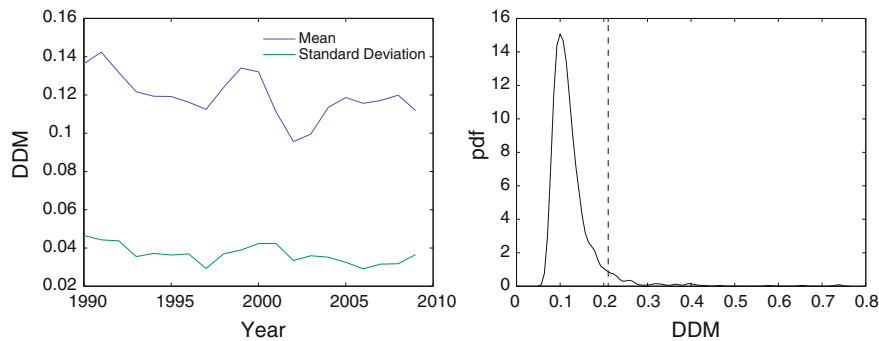
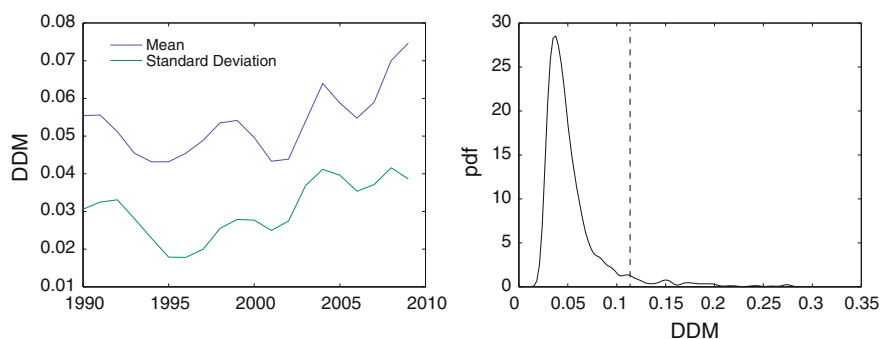**Fig. 7** (*Left*) Mean and standard deviation of dissimilarity measure for real GSP growth versus US aggregate. (*Right*) Kernel density estimation for US real GDP growth synchronization measure

distribution of different inflation dynamics widens out on entering the recession but is more convergent coming out of the recession in 2009. Oregon, Delaware, Ohio and West Virginia appear to have had quite different dynamics from other states during the last recession. The general trend in synchronicity though is definitely towards

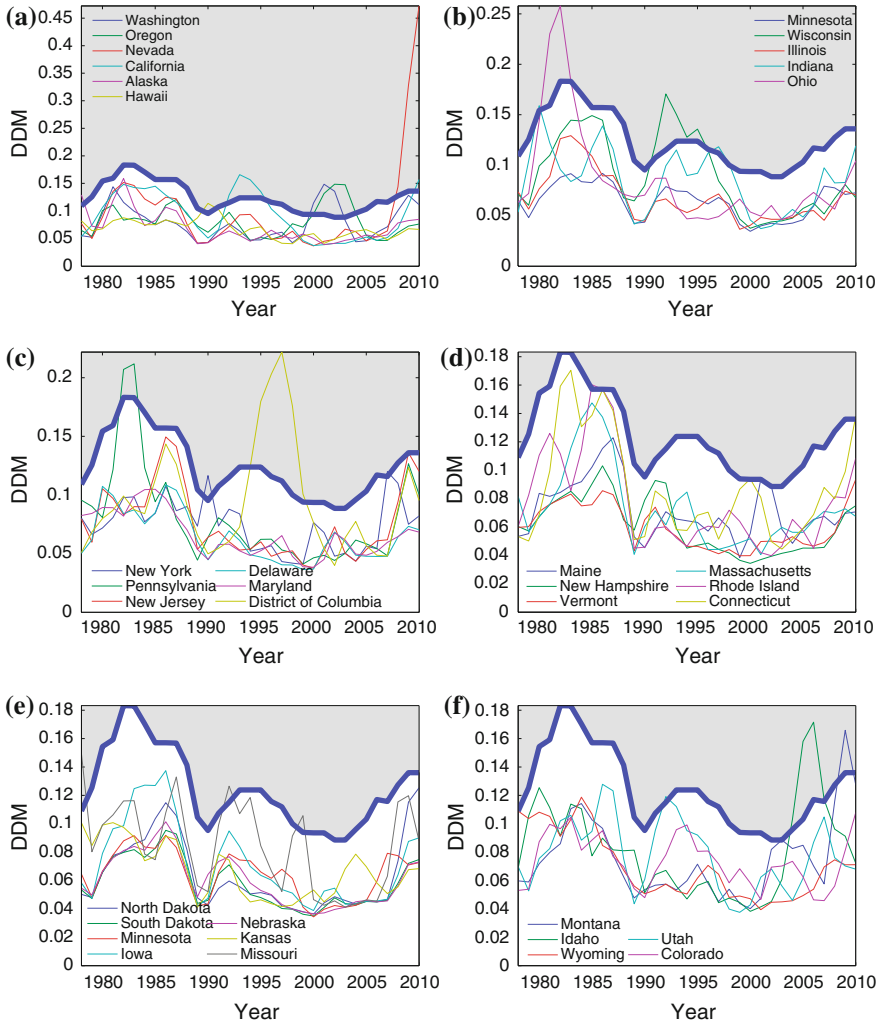**Fig. 8** Real GSP deflator growth of **a** Far West State. **b** Great Lakes State. **c** Mid East State. **d** New England State. **e** Plains State. **f** Rocky Mountain State versus US national aggregate

less synchronization during the last downturn and recovery and likely is related to the differing experiences of States to the housing boom and bust before and during the last recession.

The mean and standard deviation of the DDM are plotted by year in Fig. 10 (left). There has been a clear decrease in synchronization after 2000, and in fact greater variation in levels of synchronicity since 1995. This greater dispersion could reflect a widening gap between the States which contain major urban areas, and those which

Fig. 9 Real GSP deflator growth of **a** South East State. **b** South East State. **c** South West State versus US national aggregate

Fig. 10 (*Left*) Mean and standard deviation of dissimilarity measure for inflation vs US aggregate. (*Right*) Kernel density estimation for US GSPPI growth synchronization measure

are still mostly rural, in terms of their housing markets and also in terms of a general widening in the cost of living between these two types of States.

The estimate of the kernel density function is provided in Fig. 10 (right). The 95 % confidence interval under the null hypothesis of similar dynamics is shown in the figure and is at 0.1137, indicating a greater degree of similarity in inflation dynamics between US States than for economic growth.

Fig. 11 Unemployment rates of **a** Far West State. **b** Great Lakes State. **c** Mid East State. **d** New England State. **e** Plains State. **f** Rocky Mountain State versus US national aggregate

3.4.3 Unemployment

Here we use unemployment rates as defined by the Bureau of Labor Statistics (BLS) as the basis for creating dissimilarity indices by State.

In Figs. 11 and 12 we present the same synchronization exercise for the State unemployment rates against the US rate. Here the dynamics of unemployment across the states have been quite similar, in the sense of there being a falling degree of synchronicity going into 3 of the 4 past recessions, but a rising degree of synchronicity coming out of these recessions (with the notable exception of the 2001 recession).
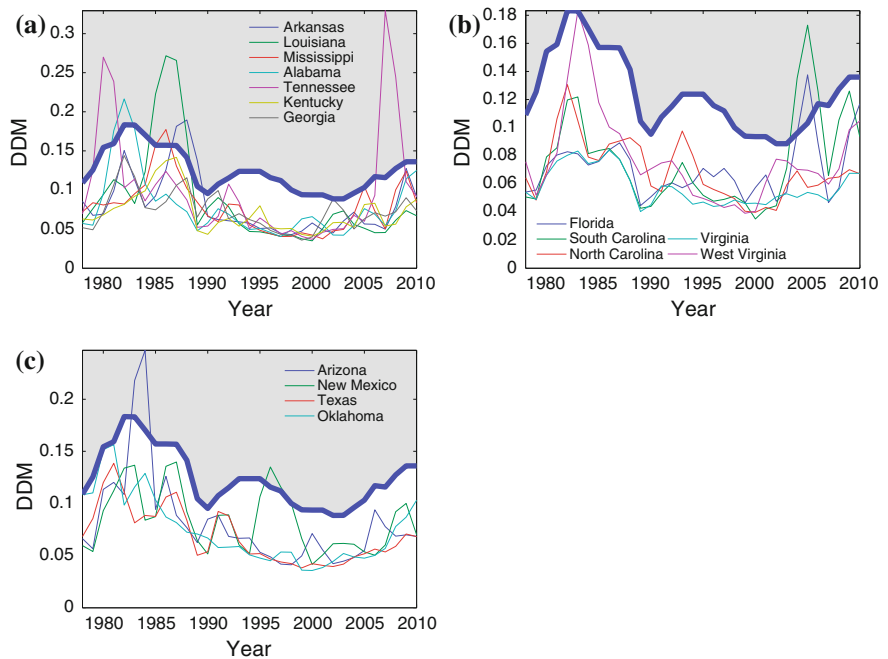
Fig. 12 Unemployment rates of **a** South East State. **b** South East State. **c** South West State versus US national aggregate

What is noticeable here though is that the general trend was, up until the last recession, an increase in synchronicity of unemployment rates. Also it is noteworthy that the spike in dissimilarity during the last downturn in economic growth was not as high as for the recession of 1982–1983. In Fig. 13 (left) the mean and standard deviation of the DDM are now plotted, and show a decrease in synchronicity since 2000, with
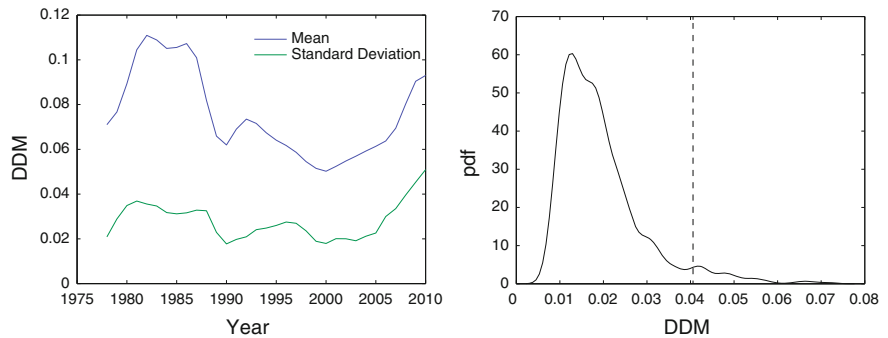
Fig. 13 (*Left*) Mean and standard deviation of dissimilarity measure for unemployment rate versus US aggregate. (*Right*) Kernel density estimation for US unemployment rate synchronization measure

the mean dissimilarity rising during the 2000s and then accelerating upwards going into the last recession. The standard deviation plot seems to have been on a slow decline up until 2005, when the dispersion of unemployment rate synchronicities appears to have widened. This is an unexpected result, as the popular perception is that unemployment generally in the US was highly synchronized between US States during the economic boom of the mid-2000s.

Once again, the kernel density estimate for the pdf of the dissimilarity measure is shown in Fig. 13 (right) and the 95 % confidence interval under the null hypothesis of similar dynamics is shown in the figure and is at 0.0406, which signifies much greater synchronization than for either economic growth or inflation. As the unemployment rate is the ratio of two large stock variables, and economic growth is the rate of change of a flow variable, this greater dynamic conformity with the unemployment rate is to be expected.

4 Conclusions

The main purpose of this paper is to present a measure of time series synchronicity, that is particularly suited to small samples, and is derived from the recurrence plot approach. The measure is non-parametric, is not dependent on stationarity of data and is fully flexible in terms of encompassing specified lead and lag dynamics. The measure was successfully applied to the evaluation of synchronicity in an example of macroeconomic data for US States compared with the US aggregate. In the latter case we have used the measure as a means of detecting whether synchronicity in macroeconomic variables measured at the US State level occurs consistently through time, and whether there are certain US states that are less synchronous with the US on aggregate than others.

Our findings are that the measure shows the time-varying level of synchronicity for a small dataset consisting of US State macroeconomic variables. In the latter case, although regions are fairly well grouped together in terms of similar economic dynamics, there are some notable differences within regions, whereby states like Alaska, which is geographically part of the Far West region, nevertheless seems to have a rather different business cycle from the rest of the country. The results indicate that synchronicity has been on upward trend for real GDP growth and on a downward trend for the unemployment rate, but that there has been little change in synchronicity of inflation rates. Our results also confirmed the long-standing finding that growth synchronicity among the US states seems to be at its highest when entering a recession, and least similar when exiting a recession.

In terms of future research, one of the uses of this methodology that would be informative in the sphere of economics[7] would be to test whether being in a monetary union causes greater macroeconomic synchronicity in business cycle variables—this would require data on similar variables for other monetary unions and then data from

---

[7] We acknowledge one of the reviewers of this paper for suggesting this approach.

a collection of countries that are not part of monetary unions to act as a control group. In terms of the methodology itself, future research could also employ varying epoch window sizes (with more temporally disaggregated data) to test if the results are robust to such changes, and if so whether an optimal window size could be derived.

Appendix A: BEA regions

Here we duplicate the most recent results from the BEA for real GSP growth. In Fig. 14 the real GDP by State is given for 2012. As can be seen, the 8 BEA regions do not correspond to the 12 Federal Reserve districts,

Figure 15 also shows the economic growth dynamic following the last economic downturn by BEA region. Clearly the Southwest has had the largest rebound, and the New England area has had only a moderate rebound since the last recession.
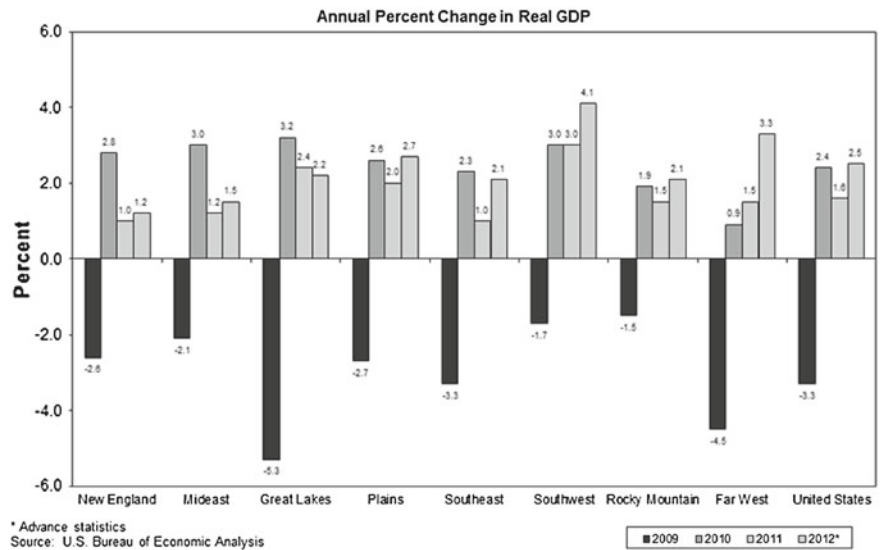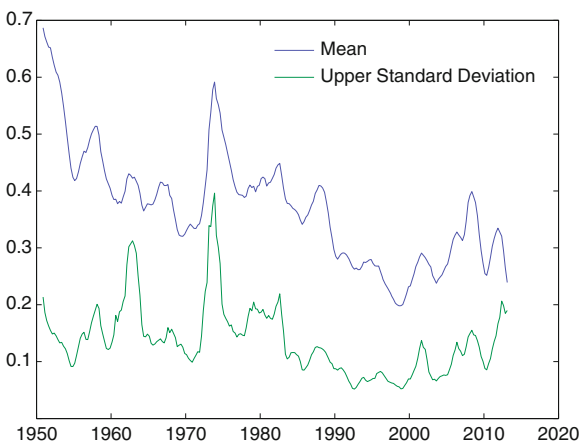

Fig. 14 Real GSP growth by US State for 2012
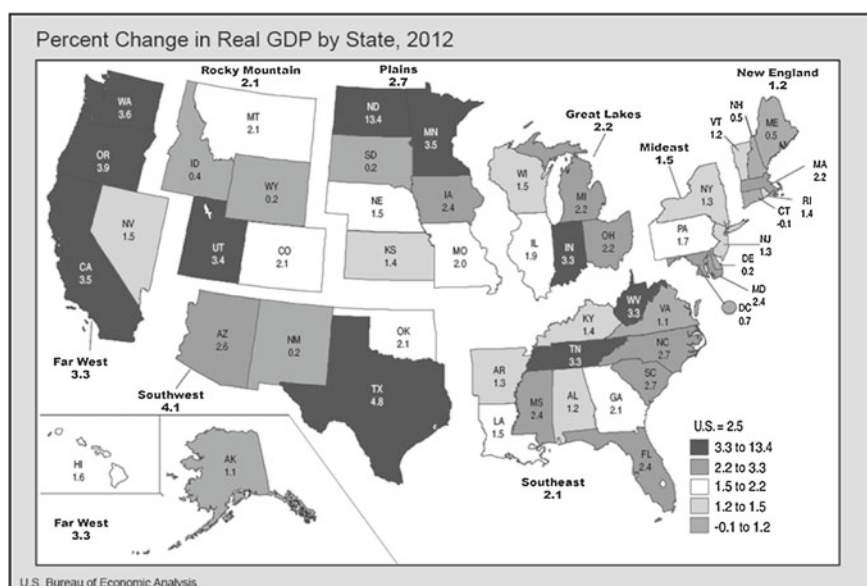
Fig. 15 Economic growth dynamic by BEA region

Fig. 16 Mean and standard deviation of dissimilarity measure for personal income versus US aggregate

Appendix B: Personal Income

Here, as a robustness check for our results as applied to US State macroeconomic data, we report the results of an identical exercise, except with personal income (sourced from the BEA) by State which contains quarterly data from 1950. We use a 12 quarter epoch window, which is equivalent to the 3 year window used with the annual data for real GDP growth. Figure 16 shows the mean and standard deviations for the dissimilarity metric. Once again, the trend in the mean is downwards, with

an uptick on both entering and exiting the last recession—this is a difference with the real GDP measure, which only showed an increase on exiting the recession. On exiting the recession, the standard deviation also increases.

References

1. Moneta, F., Ruffer, R.: Business cycle synchronization in east asia. ECB Working paper No. 671 http://www.ecb.europa.eu/pub/pdf/scpwps/ecbwp671.pdf (2006)
2. Gogas, P., Kothroulas, G.: Two speed europe and business cycle synchronization in the european union: The effectect of the common currency. Munich Personal RePEc Archive, Paper 13909 http://mpra.ub.uni-muenchen.de/13909 (2009)
3. Pikovsky, A., Rosenblum, M., Kurths, J.: Synchronization: A Universal Concept in Nonlinear Sciences. Cambridge Nonlinear Science, vol. 12. Cambridge University Press, Cambridge (2001)
4. Eckmann, J.P., Oliffson Kamphorst, S., Ruelle, D.: Europhys. Lett. **4**(9), 973 (1987)
5. Zbilut, J., Webber Jr, C.: Phys. Lett. A **171**, 199 (1992)
6. Webber, C.J., Zbilut, J.: J. Appl. Physiol. **76**, 965 (1994)
7. Feller, W.: An Introduction to Probability Theory and its Applications. Wiley, New York (1950)
8. Marwan, N., Romano, C., Thiel, M., Kurths, J.: Phys. Rep. **438**, 237 (2007)
9. Webber, Jr. C., Zbilut. J.: Recurrence quantification analysis of nonlinear dynamical systems. National Science Foundation, Chapter 2, Methods for the Behavioral Sciences, Riley, M., Van Orden, G. (eds.) available at www.nsf.gov/sbe/bcs/pac/nmbs/nmbs.jsp. Washington DC, USA (2005)
10. Zbilut, J.: In Economics: Complex Windows, Salzano, M., Kirman, A. (eds.) pp. 91–104, Springer, Milan (2005)
11. Kyrtsou, C., Vorlow, C.: Complex Dynamics in Macroeconomics: A Novel Approach. Springer, New York (2005)
12. Crowley, P.: Eur. Phys. J. **164**, 67 (2008)
13. Goswami, B., Ambika, G., Marwan, N., Kurths, J.: Phys. A **391**, 4364 (2012). doi:10.1016/j.physa.2012.04.018
14. Takens, F.: Lecture Notes in Mathematics: Dynamical Systems and Turbulence. In: Rand, D., Young, L.S. (eds.) Detecting Strange Attractors in Turbulence, pp. 366–381. Springer, Berlin (1981)
15. Marwan, N., Thiel, M., Nowaczyk, N.: Nonlinear Process. Geophys. **9**, 325 (2002)
16. Marwan, N., Kurths, J.: Phys. Lett. A **302**, 299 (2002)
17. Zolotova, N.V., Ponyavin, D.I., Marwan, N., Kurths, J.: Astron. Astrophys. **505**, 197 (2009). doi:10.1051/0004-6361/200811430
18. Sornette, D., Zhou, W.X.: Quant. Financ. **5**(6), 577 (2005)
19. Crowley, P., Schultz, A.: Int. J. Bifurcat. Chaos **21**, 1215 (2011)
20. Lee, J.: J. Int. Global Econ. Studies **3**(1), 41 (2010)
21. Leiva-Leon, D.: Monitoring synchronization of regional recessions: A markov-switching network approach. The Twelfth Annual Missouri Economics Conference, St Louis Federal Reserve website. (2012). http://research.stlouisfed.org/conferences/moconf/2012/Leiva-Leon_Danilo.pdf
22. Mundell, R.: Am. Econ. Rev. **51**, 509 (1961)
23. McKinnon, R.: Am. Econ. Rev. **53**, 717 (1963)
24. Kenen, P.: In monetary problems of the international economy, Mundell, R., Swoboda, A. (eds.) pp. 41–60. University of Chicago Press, Chicago (1969)
25. Krugman, P.: Geography and Trade. MIT Press, Cambridge (1991)
26. Frankel, J., Rose, A.: Eur. Econ. Rev. **41**(3), 753 (1997)
27. Backus, D., Kehoe, P.: Am. Econ. Rev. **82**, 864 (1992)

28. Backus, D., Kehoe, P.: F. Kydland. In: Cooley, F. (ed.) Frontiers of Businss Cycle Research, pp. 331–356. Princeton University Press, Princeton (1995)
29. Kontolemis, Z.: Economica **64**(255), 441 (1997)
30. Zarnowitz, V., Ozyildirim, A.: Time series decomposition and measurement of business cycles, trends and growth cycles. Working Paper 8736, NBER, Cambridge, MA, USA (2002)
31. Gallegati, M., Gallegati, M.: Stud. Nonlinear Dyn. Econometrics **11**(3), 1435 (2007)
32. Crowley, P., Lee, J.: Decomposing the co-movement of the business cycle: A time-frequency analysis of growth rates in the euro area. Discussion paper 12/2005. Bank of Finland, Helsinki, Finland (2005)
33. Crivellini, M., Gallegati, M., Gallegati, M., Palestrini, A.: Industrial output fluctuations in developed countries: A time-scale decomposition analysis. Working Papers and Studies: Papers from the 4th Eurostat and DGFin colloquium modern tools for business cycle analysis, European Commission, Brussels, Belgium (2004)
34. Stock, J., Watson, M.: J. Eur. Econ. Assoc. **3**(5), 968 (2005)
35. Hughes Hallett, A., Richter, C.: Int. J. Finance Econ. **11**, 177 (2006)

Understanding the Interrelationship Between Commodity and Stock Indices Daily Movement Using ACE and Recurrence Analysis

Kousik Guhathakurta, Norbert Marwan, Basabi Bhattacharya and A. Roy Chowdhury

Abstract   The relationship between the temporal evolution of the commodity market and the stock market has long term implications for policy makers, and particularly in the case of emerging markets, the economy as a whole. We analyze the complex dynamics of the daily variation of two indices of stock and commodity exchange respectively of India. To understand whether there is any difference between emerging markets and developed markets in terms of a dynamic correlation between the two market indices, we also examine the complex dynamics of stock and commodity indices of the US market. We compare the daily variation of the commodity and stock prices in the two countries separately. For this purpose we have considered commodity India along with Dow Jones Industrial Average (DJIA) and Dow Jones-AIG Commodity (DJ-AIGCI) indices for stock and commodities, USA, from June 2005 to August 2008. To analyse the dynamics of the time variation of the indices we use a set of analytical methods based on recurrence plots. Our studies show that the dynamics of the Indian stock and commodity exchanges have a lagged correlation while those of US market have a lead correlation and a weaker correlation.

K. Guhathakurta (✉)
Indian Institute of Management Kozhikode, IIMK Campus,
Kozhikode 673570, Kerala, India
e-mail: kousikg@iimk.ac.in

N. Marwan
Potsdam Institute for Climate Impact Research (PIK),
P.O. Box 60 12 03, 14412 Potsdam, Germany

B. Bhattacharya
Department of Economics, Jadavpur University, Kolkata 700032, India

A.R. Chowdhury
Department of Physics, Jadavpur University, Kolkata 700032, India

1 Introduction

The relationship between the temporal evolution of the commodity market and the stock market is of utmost importance for investors and other market participants. It has long term implications for policy makers, and particularly in the case of emerging markets, the economy as a whole. The history of commodity markets dates back much more than that of the stock market. Traditionally, commodity markets had been primarily consumption markets with some investment opportunities as opposed to the stock market which is an investment market only. The commodity as an option of financial investment and an alternative to traditional assets, had always been attractive because of its ability to add to diversification benefits. However, the majority of investments in commodity markets took place in over the counter markets as opposed to the exchange traded stock markets. The dynamics of the two markets were, therefore, governed by different characteristics. This fact coupled with the lack of consistent and reliable data from the over-the-counter markets has made reliable studies of the interrelationship between the dynamics of the two markets difficult, especially in emerging markets like India where exchange based spot and derivatives trading of commodities is relatively new. But with the evolution of the exchange based trading of commodity spot and derivatives markets it is now possible to study and capture the complex dynamics of both stock and commodity markets and compare their interrelationship. In a recent work by Reddy and Sebastin, the dynamics of information transfer among the commodity spot, commodity derivatives, and stock markets in India are studied, using the information theoretic concept of entropy, which captures complex relationships as well [1].

In spite of having a long history of derivatives trading in commodity markets, the history of exchange traded commodity futures trading in India is rather short. The first commodity trading exchange of India Multi-commodity exchange (MCX) started operating from November 2003. However, since then there has been a phenomenal growth in volume and turnover in this exchange. From a mere 9 million Indian rupees in 2004 the trading volume has increased to over 1 billion Indian rupees in 2013. By 2008 it had already grown by up to 438 million Indian rupees. This growth is not unique to the commodity sector; stock market volume has also continued its growth during the same period. The market capitalisation of the National stock exchange grew from 8.63 trillion to 21.23 trillion Indian rupees between 2003 and 2008. This concurrent growth is of importance from the investment portfolio perspective as the inclusion of commodities adds depth and diversification to the portfolio.

The importance of this study, therefore, lies in investigating the utility of the commodity as a diversification tool. Under normal circumstances, we would expect the correlation between the stock and commodity markets to be low. Only then can commodities be used as an avenue for diversification. But in India, we may expect a different scenario. If we look at traditional investment practices in India, people tend to invest a constant proportion of their portfolios in gold. Thus, when investment goes up, both commodity prices and stock prices will rise, due to the increased complementary demand for these assets. Recently, with the introduction

of commodity futures, oil has also taken an important position in the Indian portfolio (incidentally, in 2007, 28 % of the trading volume of commodity futures in MCX was contributed by gold, while 56 % was contributed by crude oil). We would thus expect a different relationship to exist between the stock and commodity markets in India when compared to some other developed economy like that of the USA.

The complex dynamics of two investment markets is best understood by analyzing a time series representing the price movement of the respective markets using tools of nonlinear dynamics. Keeping this in mind we analyze the movement of the daily close value of two indices of stock and commodity exchange, respectively, of India. To understand whether there is any difference between emerging markets and developed markets in terms of the dynamic correlation between the two market indices, we compare it with the US market. We use a set of methods based on maximal correlation [2] and recurrence plots [3, 4].

A simple cross-correlation study based on Pearson correlation measures could indicate a degree of correlation between the time series under study. To start with, we will compute the Pearson correlation for both US and Indian markets. Despite the true nature of the dynamics, this linear approach might yield some initial interesting results in a first order approximation. However, in order to get deeper insights we have to consider potential nonlinear properties, because there is ample empirical evidence against the assumption of simple linear dynamics in economics. Theoretically, there is no reason to believe that economic systems must be intrinsically linear (cp. [5–7]). Empirically, a great number of studies show that financial time series exhibit nonlinear dependencies (cp. [8–16]). Hence, "A natural frontier for financial econometrics is the modelling of nonlinear phenomena" [6]. Testing for nonlinearity has become popular in the financial econometrics literature in recent years, though the focus is on financial markets of developed countries. In principle, testing for nonlinearity can be viewed as a general test of model adequacy for linear models [17] and it has been argued that if the underlying generating process for a time series is nonlinear in nature, then it would be inappropriate to employ linear methods. For instance, most of the widely applied statistical tests like the unit root or stationary tests, the Granger causality test, and the cointegration test are all built on the basis of a linear autoregressive model. [18, 19], among others, illustrated that the adoption of linear stationarity tests are inappropriate in detecting mean reversion if the true data generating process is in fact a stationary nonlinear process. On the other hand, the Monte Carlo simulation evidence in [20] indicated that the standard linear cointegration framework presents a mis-specification problem when the true nature of the adjustment process is nonlinear and the speed of adjustment varies with the magnitude of the disequilibrium. Thus, if the underlying process of a time series is indeed nonlinear in nature, we would have to resort to empirical methods the like non-parametric cointegration test due to [20], nonlinear stationarity tests [19, 21, 22], and nonlinear causality tests [23].

This requires the application of alternative methods over and above simple Pearson correlation measure to understand the degree of nonlinear correlation between the time series. We used the alternating conditional expectation algorithm (ACE) to test the correlation between the time series [24]. The ACE algorithm showed that

the functional form of the data sets under examination are clearly nonlinear. This encouraged us to use nonlinear methods to study the interrelationship between the time series. This also motivated us to go for a study of the entire time evolution of the time series to understand whether they co-evolve or not, by using the cross recurrence plot and recurrence quantification analysis [3, 4], which has already been successfully applied to financial and economic data [16, 25, 26]. Recent extensions in recurrence network analysis allow us to estimate topological dimensions from time series like the transitivity dimensions [27]. Motivated by this, we construct the transitivity dimensions of the two markets and see whether topological measures reinforce our findings in recurrence analysis.

The structure of the paper is as follows. In Sect. 2, we briefly describe the source and nature of the data. In Sect. 3 we discuss all the tests performed, giving the background theory of our analysis before commenting upon the results. In Sect. 4 we perform the comparative analysis of the results of our tests. Finally we summarise our conclusions in Sect. 5.

2 Data

Our analysis is based on daily time series of the S and P CNX NIFTY (NIFTY) and MCX-COMDEX (commodity) index of India as well as Dow Jones Industrial Average (DJIA) stock index and Dow Jones-AIG Commodity Index (DJ-AIGCI) of USA (Fig. 1). From the respective exchange web sites (www.nseindia.com, www.mcxindia.com, www.djaverages.com, www.nasdaq.com/symbol/ucd) historical data respectively for NIFTY, NCX, DJIA and DJ-AIGCI have been collected for the period from June 2005 to August 2008 (both months inclusive). Considering this time period, the sub-prime period is not completely excluded from the analysis. The initial few months when the first shock affected the market are still included, but the long period of global recession after this initial period are not. The idea was to capture the beginning of the stock market crash and see whether the commodity market was reacting in a correlated manner. Our purpose was to understand whether there is anything endogenously different in the two markets. The S and P CNX Nifty is a well-diversified 50 stock index (traded in the National Stock Exchange, India) accounting for 25 sectors of the Indian economy. MCX-COMDEX is a composite futures index comprising of commodity futures of diversified sectors traded in MCX India. MCX-COMDEX is based on futures prices of 15 different commodities, comprising of three sub-indices which represent the major sector groupings in commodity trading: metals, energy, and agricultural products. DJIA is a composite index computed from stock prices of 30 largest and most widely held public companies in the USA. DJ-AIGCI is a composite index composed of future contracts on 19 physical commodities traded on US exchanges.

For our analysis, we have used the z-score of the original index time series, i.e., we have normalized all time series to have a mean of zero and standard deviation of one (no log change or change data used).
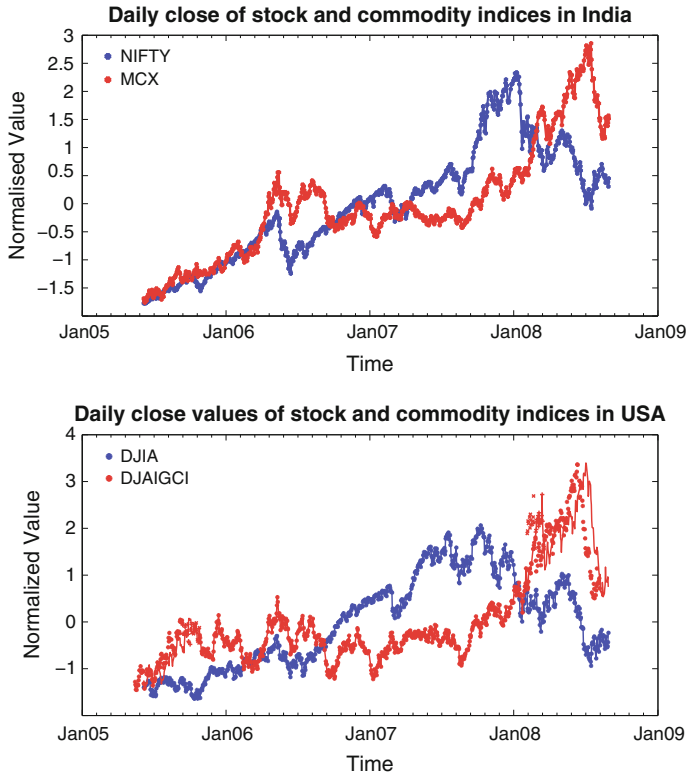
Fig. 1 Normalized values of daily close of NIFTY and MCX-COMDEX (*top*), as well as of daily close of DJIA and DJ-AIGCI (*bottom*)

3 Background of Examinations

3.1 Alternating Conditional Expectation (ACE) Algorithm and Maximum Correlation Function (MCF)

The ACE algorithm [24] estimates the transformations $\Phi(x)$ and $\Theta(y)$ giving rise to the maximal multiple correlation of a response y and a set of predictor variables x:

$$MC = \frac{\langle \Phi(x)\Theta(y) \rangle}{\sqrt{\langle \Phi^2(x) \rangle \langle \Theta^2(y) \rangle}} \overset{!}{=} \max. \tag{1}$$

These real-valued measurable mean-zero functions $\Theta(y)$ and $\Phi(x)$ (with $\overset{!}{=}$ max meaning that the correlation is maximal for the found $\Theta(y)$ and $\Phi(x)$) are then called

optimal transformations, and *MC* is called *maximal correlation*. A study of these transformations can give the insight into the relationships between these variables.

To calculate the optimal transformations, we have used an adaptive partitioning algorithm as described in [2]. The ACE and MCF functions of the CRP toolbox [28] use this algorithm except for two differences:

1. The output is not normalized with respect to the mean values of the optimal transformations, so the mean values may not necessarily be zero.
2. The data are rank ordered before the calculation of the optimal transformations. This leads to a simpler computation of conditional expectation values.

The algorithm (but not the particular subroutine of estimating the conditional expectation values) is described in [2, 29, 30].

Although this algorithm is meant for exploring whether there is a relationship between response and predictor variables, we have used the stock and commodity index data as if a predictive relationship exists between them, and then found whether in such a case the programme detects a correlation or not.

3.2 Recurrence Analysis

Natural processes can have a distinct recurrent behavior (e.g., Milankovich cycles, El Niño phenomenon, extreme flooding events, epileptic seizures). Recurrence of states $\mathbf{x_i} \in \mathbb{R}^m$ (with m the dimension of the phase space), in the meaning that states are arbitrary close after some time, is a fundamental property of deterministic dynamical systems.

Eckmann et al. have introduced a tool which visualizes the recurrence of states $\mathbf{x}_i$ in phase space [3]: the recurrence plot. A recurrence plot (RP) is a visualisation of state- space dynamics that shows all those times at which a state of the dynamical system recurs:

$$R_{i,j} = \Theta(\varepsilon - \parallel \mathbf{x}_i - \mathbf{x}_j \parallel), \quad \mathbf{x}_i \in \mathbb{R}^m, \quad i, j = 1, \ldots, N, \tag{2}$$

where $\mathbf{R}$ is the recurrence matrix, N is the number of considered states x_i, ε is a threshold distance, $\parallel \cdot \parallel$ a norm, and $\Theta(\cdot)$ the Heaviside function. A recurrence of a state at time i at a different time j is, thus, marked within a two-dimensional squared matrix with ones and zeros. Both axes of the recurrence matrix are time axes. This representation is called recurrence plot (RP). RPs has shown to be useful for analysing short and non-stationary data [4].

In our study we apply the RP in order to reveal the characteristics of the dynamics of the economic time series under investigation. For an economic time series, the patterns over time tell us whether the series is disrupted, non-stationary or nonlinear in nature. By comparing RPs of two economic time series we can visually infer whether the dynamical systems governing the time series are similar, or not.

3.2.1 Embedding Parameters

If only one observable is available, the phase space can be reconstructed using time-delay embedding [4]. Thus, we need to choose an appropriate value for the time delay d and the embedding dimension m. Several methods have been developed to best estimate m and d. Frequently used methods are the Average Mutual Information Function (AMI) for the time delay [31] and the False Nearest Neighbors (FNN) method for the embedding dimension [32]. As for the embedding delay, we chose such a value where the mutual information has its first minimum or changes its scaling behavior, and for the embedding dimension, we use such a value for m where the number of false nearest neighbours in the phase space vanishes.

3.2.2 Structures in Recurrence Plots

The initial purpose of RPs was the visual inspection of recurrences of phase space trajectories. The view on RPs gives hints about the time evolution of these trajectories. RPs exhibit characteristic large scale *typology* and small scale patterns (*texture*). The typology offers a global impression which can be characterized as homogeneous, periodic, drift, and disrupted [4]. Small scale structures are single dots, diagonal lines as well as vertical and horizontal lines (the combination of vertical and horizontal lines obviously forms rectangular clusters of recurrence points). For a recurrence analysis, the diagonal and vertical line structures are important.

A diagonal line $R_{i+k,j+k} = 1$ (for $k = 1, \ldots, l$, where l is the length of the diagonal line) occurs when a segment of the trajectory runs parallel to another segment, i.e., the trajectory visits the same region of the phase space at different times. The length of this diagonal line is determined by the duration of such similar local evolution of the trajectory segments and can give an idea about its divergence behavior, i.e., the faster the trajectory segments diverge, the shorter are the diagonal lines.

A vertical (horizontal) line $R_{i,j+k} = 1$ (for $k = 1, \ldots, v$, where v is the length of the vertical line) marks a time length in which a state does not change or changes very slowly. It seems, that the state is trapped for some time. This is a typical behavior of laminar states (intermittency).

These small scale structures are the base of a quantitative analysis of the RPs.

Though the visual interpretation of RPs requires some experience, their quantification offers a more objective way for the investigation of the considered system. A detailed discussion on the application and interpretation of RPs and the various structures in a RP can be found in [4].

3.2.3 Cross Recurrence Plot

The cross recurrence plot (CRP) is a bivariate extension of the RP and was introduced to analyze the similarity and synchronization of the states of two different dynamical systems [33]. Suppose we have two dynamical systems, each one represented by the

trajectories $\mathbf{x}_i$ and $\mathbf{y}_i$ in a d-dimensional phase space. Analogously to the RP, Eq. (2), the corresponding cross recurrence matrix is defined by

$$CR_{i,j}^{\mathbf{x},\mathbf{y}}(\varepsilon) = \Theta(\varepsilon - \|\mathbf{x}_i - \mathbf{y}_i\|), \quad i = 1, \ldots, N, \quad j = 1, \ldots, M \qquad (3)$$

where the length of the trajectories of $\mathbf{x}_i$ and $\mathbf{y}_i$ are not required to be equal, and hence the matrix **CR** is not necessarily square. Note that both systems are represented in the same phase space, because a CRP looks for those times when a state of the first system recurs to one of the other system. If the embedding parameters are estimated from both time series, but are not equal, the higher embedding should be chosen. However, the data under consideration should be from a comparable process (physically the same). Here, we consider the different markets as physically very similar. Moreover, we do not compare a specific variable (like trading volume of a specific good) from these markets but a generalized index value. This additionally supports our consideration of using physically similar variables in our application. For a detailed discussion on RPs and CRPs we refer to [4, 33].

The CRP of two identical trajectories coincides with the RP of one of the trajectories and contains the main diagonal or *line of identity* (LOI). However, if the trajectories are not equal or their evolution happens on different time scales, the LOI will be somewhat displaced, disrupted or bowed and is called *line of synchronisation* (LOS).

For our analysis, we use the CRPs to visually inspect the interrelationship between the two economic time series under investigation. By looking at the pattern, i.e., the LOS, we can infer whether the two systems are completely uncorrelated or a relationship exists between them with some lead or lag. If the LOS is shifted to the right then we can conclude that there is a delayed relationship between the two time series. The other possible bivariate extension of RPs, the joint recurrence plot, is not applicable here because it tests for simultaneous recurrences, but we are also interested in changes of time scales. The potential of recurrence plot based approaches for analyzing financial and economics data was shown in [16, 25, 26].

3.3 Quantification of Recurrence Plots

A quantification of recurrence plots (Recurrence Quantification Analysis, RQA) was developed in order to distinguish between different appearances of RPs [34, 35]. Measures which base on diagonal structures are able to find chaos-order transitions, whereas measures based on vertical (horizontal) structures are able to find chaos-chaos transitions (laminar phases) [4].

Using the histogram of diagonal line lengths (see Sect. 3.2.2), we define the fraction of recurrence points forming diagonal lines as a measure called *determinism DET*,

$$DET = \frac{\sum_{l=l_{\min}}^{N} l\,P(l)}{\sum_{l=1}^{N} l\,P(l)}, \tag{4}$$

where $P(l)$ is the histogram of the diagonal lines of exactly length l, and $l_{\min}$ is a minimal length a diagonal structure should have to be counted as a line. Processes with uncorrelated or weakly correlated, stochastic or irregular chaotic behaviour cause none or very short diagonals, hence, small DET. In contrast, regular deterministic processes lead to longer diagonals and less isolated recurrence points, resulting in higher values of DET. This measure can also be interpreted as characterizing the predictability of the system.

The *average diagonal line length*

$$L = \frac{\sum_{l=l_{\min}}^{N} l\,P(l)}{\sum_{l=l_{\min}}^{N} P(l)} \tag{5}$$

gives the average time that two segments of the trajectory are close to each other, and can be interpreted as the mean prediction time.

Analogously to the definition of the determinism in Eq. (4), we can use the histogram of the vertical lines of exactly length v, and define the fraction of recurrence points forming vertical structures in the RP as the *laminarity LAM*

$$LAM = \frac{\sum_{v=v_{min}}^{N} v\,P(v)}{\sum_{v=1}^{N} v\,P(v)}. \tag{6}$$

The computation of *LAM* is realized for those v that exceed a minimum length v_{min} in order to decrease the influence of the tangential motion (time-continuous systems that are discretized with sufficiently high sampling rate and an appropriately large threshold ε result in a large amount of recurrences coming from succeeding states $\mathbf{x}_i, \mathbf{x}_{i+1}, \mathbf{x}_{i+2}, \ldots$). *LAM* represents the occurrence of laminar states in the system without describing the length of these laminar phases. In particular, *LAM* decreases if the RP consists of more isolated recurrence points than vertical structures.

The average length of vertical structures is given by

$$TT = \frac{\sum_{v=v_{min}}^{N} v\,P(v)}{\sum_{v=v_{min}}^{N} P(v)}, \tag{7}$$

and is called *trapping time*. As in the case of *LAM*, the computation of *TT* requires the consideration of a minimal length v_{min} as well. The trapping time estimates the mean time that the system will abide at a specific state, i.e., how long the state will be trapped.

Both *LAM* and *TT* have been proven to be useful for describing the dynamics of discrete systems and studying chaos-chaos transitions. RQA consists of further measures which are not used in this study. RQA as the whole is a very powerful

technique for quantifying differences in the dynamics of complex systems and has meanwhile found numerous applications, e.g., in astrophysics, biology, engineering, geo- and life sciences, or protein research [35].

Recent developments combined recurrence analysis with the complex network approach [36, 37]. By considering the recurrence plot $\mathbf{R}$ as the adjacency matrix of a network $\mathbf{A} = \mathbf{R} - \mathbb{1}$, several measures from complex networks statistics can be applied and used as alternative measures of complexity characterizing the geometrical properties of the phase space trajectory. For example, the *transitivity coefficient*,

$$\mathscr{T} = \frac{\sum_{i,j,k=1}^{N} A_{j,k} A_{i,j} A_{i,k}}{\sum_{i,j,k=1}^{N} A_{i,j} A_{i,k} (1 - \delta_{j,k})}, \tag{8}$$

measuring the fraction of closed triangles in the network, is a good measure to distinguish regular from irregular dynamics [38]. Based on geometric considerations, $\mathscr{T}$ can be used to construct a dimensionality measure, the *transitivity dimension*,

$$D_{\mathscr{T}} = \frac{\log \mathscr{T}}{\log(3/4)}, \tag{9}$$

providing a theoretically understandable measure for complexity, as more complex/irregular behaviour belongs to higher dimensional dynamics than periodic/regular behavior [39].

RQA measures can be computed in moving windows along the main diagonal (sub-RPs). This allows us to study their time dependence and can be used for the detection of transitions. Yet, one key question in empirical research concerns the confidence bounds of the calculated RQA measures. Schinkel et al. have suggested a bootstrap method to estimate the confidence of the RQA measures [40]. This method is based on the bootstrapping of line structures from the RP (or the sub-RP), allowing to estimate an empirical test distribution of all of the used RQA measures. We have used 95 % confidence level for the statistical evaluation of these measures.

The measures *DET*, *LAM*, *L*, and *TT* are not used as absolute indices of the dynamic state (i.e., chaotic, random, laminar, etc.). Instead we will consider their relative movement over time when comparing the two systems,i.e., the stock market index and commodity market index. By comparing their movement, we try to detect whether they move concurrently or absolutely independent of each other.

All analysis was performed by using the *Cross Recurrence Plot Toolbox*, Version 5.15 (R28.4) 21-Jul-2009 (http://tocsy.pik-potsdam.de).

4 Results

First, we compute the Pearson correlation for the two markets separately. We find that the correlation between DJIA and DJ-AIGCI indices were much lower (0.23) as compared to that between NIFTY and MCX (0.62). Next we proceed with the

nonlinear analysis in order to get further details of the nature of correlation. We have calculated the MCF for a maximal lag of 20 days (the length of the boxcar window was 11). For the calculation of the CRPs, the important parameters are embedding dimension and time delay. If the embedding parameters are estimated from both time series, but are not equal, the higher embedding was chosen [4]. Using the methods mentioned in Sect. 3.2.1, we got the same parameters for both Indian data sets, i.e., we found an embedding dimension of 5 and a time delay of 4. For the US data set we used the same embedding parameters because those were the higher embedding parameters amongst the two time series, viz., the DJIA time series. We used the CRP and maximum norm method for finding out the neighbours of the plot. For the RQA we used the same embedding parameters and a threshold parameter of 0.1, kept the bootstrapping sample size at 500, used a 95 % level of confidence. The used window size was 100 days and step size was 10 days.

4.1 ACE and Maximum Correlation Function

A close look at the ACE and MCF results of Nifty and MCX time series (Fig. 2), and those of DJ-AIGCI and DJI, respectively (Fig. 3), reveals a clear difference in the two markets. The optimal transformations for Nifty and MCX time series are a monotonous function, with a linear part for low values (Fig. 2). In contrast, the optimal transformations for DJ-AIGCI and DJI reveal a non-monotonous and
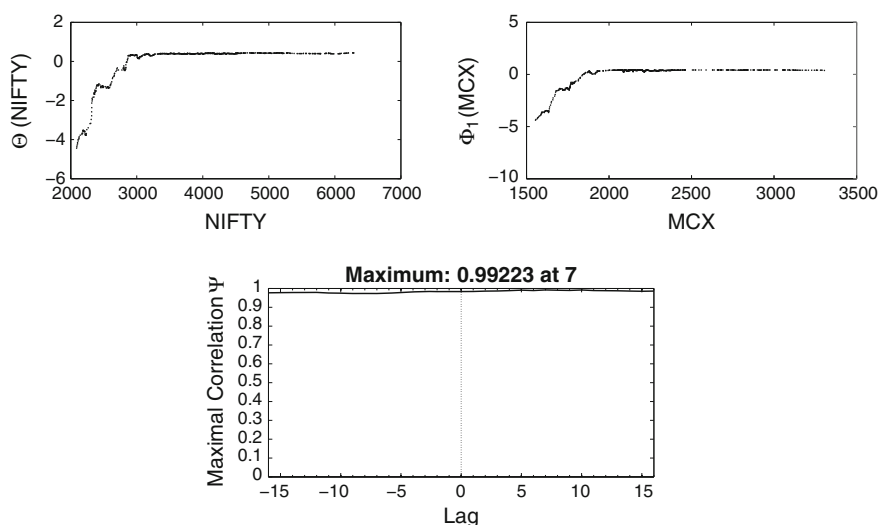

Fig. 2 Optimal transformations for NIFTY and MCX-COMDEX (*top*). Maximal correlation function for NIFTY and MCX-COMDEX (*bottom*) with rather constant value of 0.99, indicating a high level of nonlinear correlation
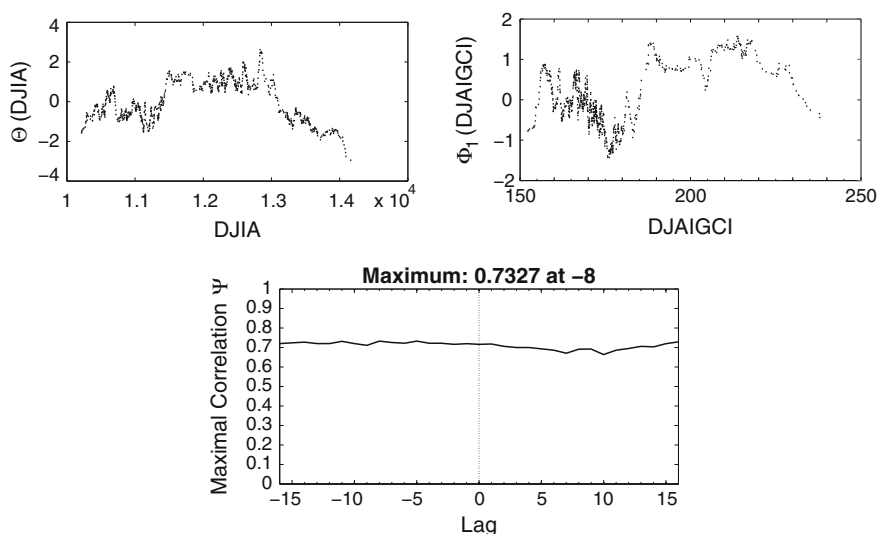
Fig. 3 Optimal transformations for DJIA and DJ-AIGCI (*top*). Maximal correlation function for DJIA and DJ-AIGCI (*bottom*) with rather constant value of 0.73, indicating a rather law correlation in the US markets ("low" from the view point of the maximal correlation)

strongly nonlinear function (Fig. 3). For a lag of seven days, we found a maximum correlation of 0.98 for Nifty and MCX-COMDEX, while for the DJIA and DJ-AIGCI the maximum correlation is only 0.70, at a lead of eight days. These results suggest a simpler relationship between the commodity exchange index and stock exchange index of India, which is also confirmed by its strong correlation, whereas the US market is much more complex and unpredictable, i.e., much weaker correlation in the US market (as the maximum correlation is significant only for very high values, i.e., larger than 0.95). This points towards a greater interrelation within the Indian markets. In India the lagged relationship suggests the commodity market follows the stock market. Since the maximum correlation in the US is not significant we are not too concerned about the nature of such correlation, i.e., lead or lag.

Next we look for a lagged maximal correlation (MCF). We have found a maximum in the MCF at lag 7 for the stock and commodity market in India (Fig. 3). This suggests a delayed relationship between the markets. The low (non-significant) values of MCF for the US market do not allow a conclusion about delayed relationships (Fig. 4).

We now proceed with the recurrence analysis of the data set to capture the relative changes of the dynamics of the respective indices as also to find out the interrelationship between the indices.
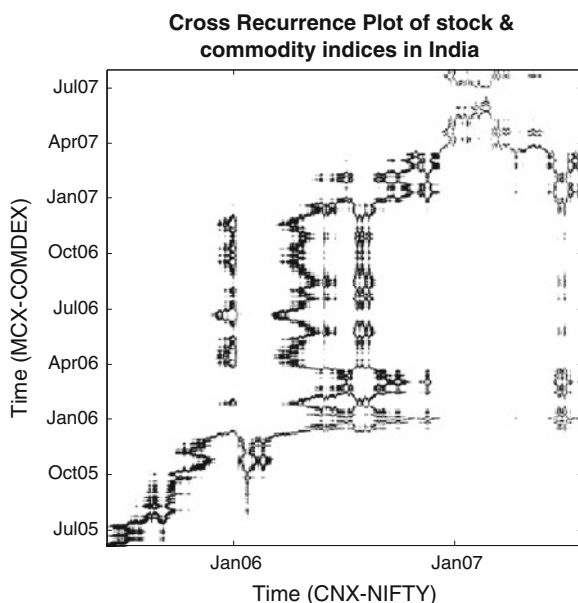
**Cross Recurrence Plot of stock &
commodity indices in India**

Fig. 4 Cross Recurrence Plot of time series representing daily close values of the stock market index CNX-NIFTY and commodity market index MCX-COMDEX in India

4.2 Cross Recurrence Plot

The CRP of NIFTY and MCX-COMDEX reveal a pattern which suggests a relationship between these two indices for India (Fig. 4). The pattern indicates partly a co-evolution of the two time series, as indicated by the connected structure of low values in the CRP, which we consider to be the LOS. The shifting of the LOS is an indication of a lagged relationship. The LOS is changing with time, suggesting that the relationship between the stock and commodity markets is not constant. The CRP contains two disruptions at May 2006 and January 2008 which correspond to stock market crashes.

In contrast, the CRP of the DJIA and DJ-AIGCI does not show a well connected structure of low distance values, which could be interpreted as a LOS (Fig. 5). Only between March 2007 and January 2008, some lagged relationship seems to be apparent. This suggests a weaker relationship between the NIFTY and MCX-COMDEX what is in line with the correlation results.
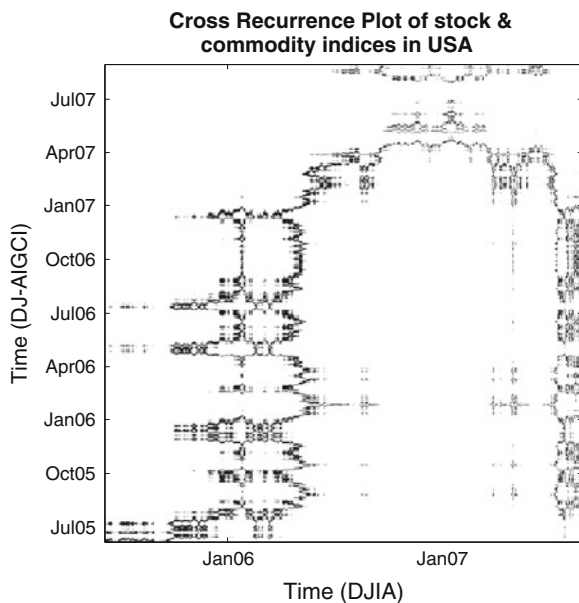
**Cross Recurrence Plot of stock &
commodity indices in USA**

Fig. 5 Cross Recurrence Plot of time series representing daily close values of the stock market index DJIA and commodity market index DJ-AIGCI in the USA

4.3 Recurrence Quantification Analysis

Next we compare the time variation of the RQA measures in order to check for similar dynamics. The variations of the *DET*, *L*, *LAM*, and *TT* values of the index data reveal changes between different dynamics, e.g., from more predictable to less predictable (DET). Such dynamical changes in the NIFTY data are well concurrent to that of the MCX-COMDEX data but with a small lag (Fig. 6). The values, though not identical in absolute terms, are increasing and decreasing in a similar fashion, except during March 2008, where the two time series appear to be out of sync. This means that the respective change of states of the two systems, i.e., the corresponding markets' dynamics, is closely related to each other. If one looks carefully at the DET values, one will notice that the DET values for both NIFTY and MCX are almost concurrent during July 2005 to October 2006, and also June 2007 onwards. We also find similar regime specific behaviour in other RQA variables as well. The concurrence departs in 2006 after a crash in the stock markets and again reappears when the market rebounds. We can infer that the stock market crash affects the two markets differently, with the commodity market recovering faster than the stock market, therefore leading to the departure of the concurrence.

The values of *DET*, *L*, *LAM*, and *TT* of the DJ-AIGCI and DJI data reveal a much less synchronised variation of the dynamical properties than in the Indian markets (Fig. 7). There are more epochs when the two values are out of sync or even negatively

Fig. 6 *DET*, *L*, *LAM*, and *TT* values with 95 % confidence limits for time series representing daily close values of the stock market index CNX-NIFTY and commodity market index MCX-COMDEX in India. The values reveal changes between different dynamics like degree of predictability. We can see how the two indices are concurrently changing in their dynamics except for March 2008
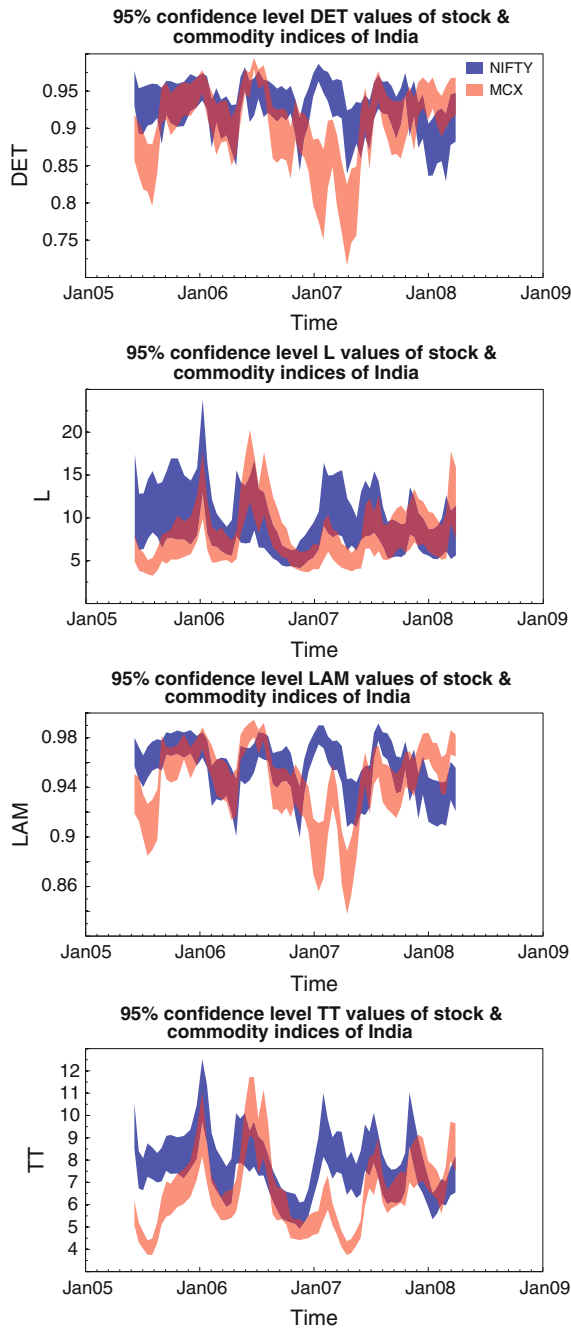

95% confidence level DET values of stock & commodity indices of India

95% confidence level L values of stock & commodity indices of India

95% confidence level LAM values of stock & commodity indices of India

95% confidence level TT values of stock & commodity indices of India

Fig. 7 *DET*, *L*, *LAM*, and *TT* values with 95 % confidence limits for time series representing daily close values of the stock market index DJIA and commodity market index DJ-AIGCI in USA. The values show that the US indices are significantly different in their dynamical properties
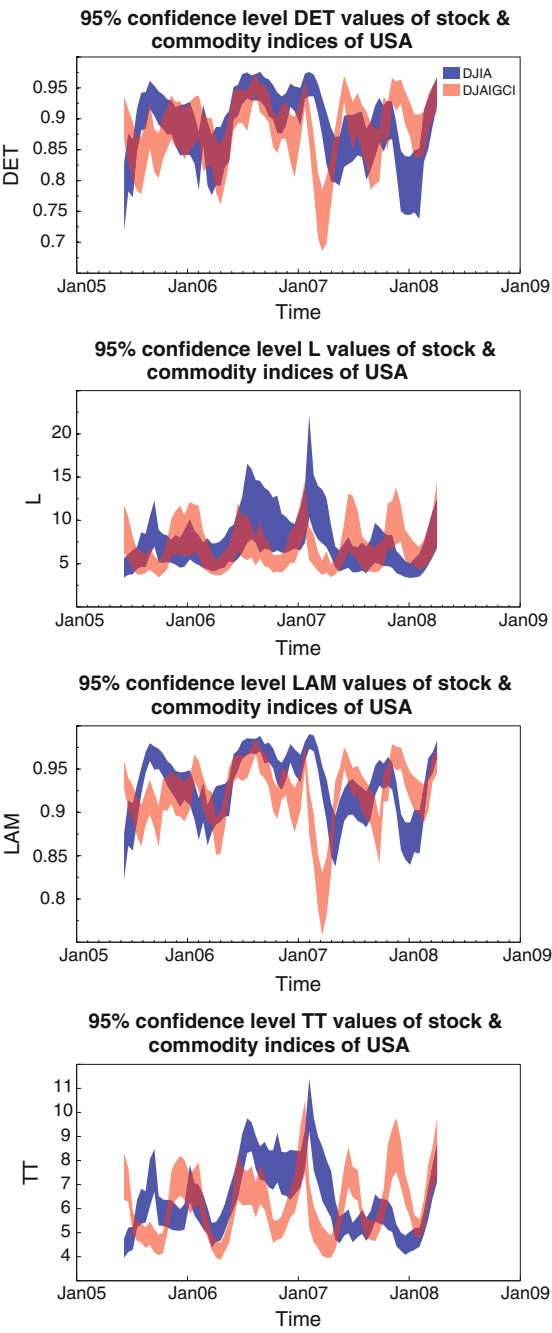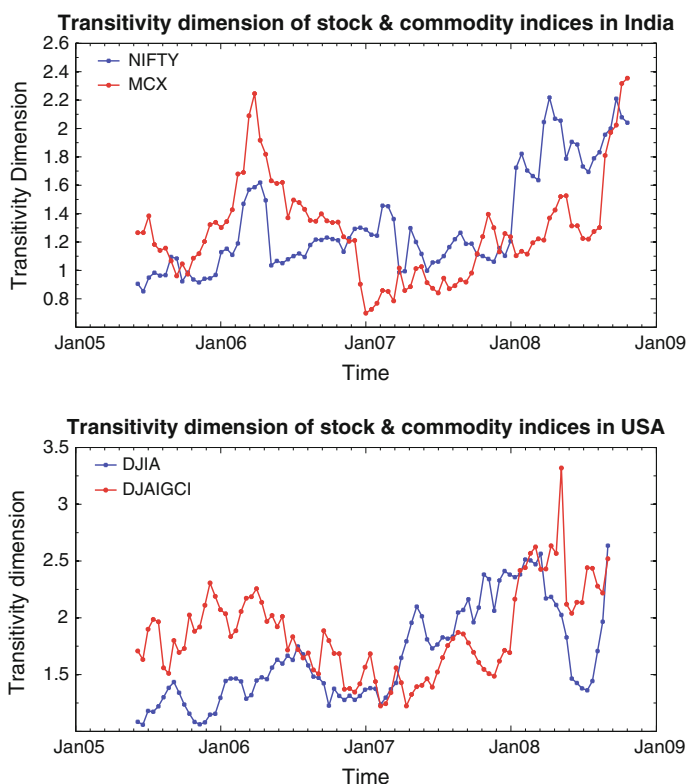
Fig. 8 Transitivity Dimensions of the commodity and stock market indices

correlated. This suggests a weaker link between the dynamics of the two markets and a significant difference in the predictability of the stock and commodity markets. Pearson correlation between the RQA values of NIFTY and MCX ranges between 0.25 and 0.55, while for DJIA and DJ-AIDCI we find correlation between 0.05 and 0.1 only. These findings corroborate our conclusions on the closer interrelation between the Indian exchanges than the US exchanges.

We conclude our analysis by comparing the transitivity dimension of the chaotic dynamics of the two markets. We find two epochs of higher transitivity dimension of the daily close of MCX, one between June 2005 and November 2006 and another after July 2008, with a decrease between November 2006 and July 2008, coinciding with a similar evolution of the close values of NIFTY, the stock market index of India (Fig. 8). The evolution of the transitivity dimensions of daily close of DJIA, the US stock market index, and of DJAIGCI, the US commodity market index, are not as similar as for the Indian counterpart, although we find a decrease between October 2006 and January 2008. In comparison to the Indian markets, the higher values of transitivity dimension in the US indices indicate a more complex/ irregular dynamics.

5 Conclusions

In the research presented, we have compared the variability of stock and commodity markets in India and US and found clear differences between the Indian and the US market behavior. We have used a nonlinear approach to measure correlation based on the alternating conditional expectation (ACE) algorithm and maximum correlation function (MCF). We found that the correlation between the Indian Markets is much stronger than in the US. While the maximal correlation between the stock and commodity markets in India is quite high, the correlation between the US stock and commodity markets is low and negligible. The relationship for the Indian markets is lagged by seven days. Furthermore, we have applied the recurrence plot analysis to look at different aspects of the dynamics. Based on cross recurrence plots, we found distortions in the link between the stock and commodity markets during stock market crashes and when the relationship between the stock and commodity markets is changing or diverging (in terms of lags). The recurrence quantification analysis (RQA) suggested a concurrence between the Indian stock and commodity markets in terms of coinciding predictability while these markets in the US were mostly out of sync. These findings are supported by transitivity dimension which reflects the changes between regular and complex market behavior, which coincides in the Indian markets, but is more divergent in the US markets.

From these findings we can infer that the Indian and the US markets behave differently. In India both markets are probably linked by external factors, like global market behavior, which influences the economic state of India in all sectors, i.e., in stock exchange and commodity markets in a similar way. There is a long tradition in India of investing in metals, particularly gold, in the form of ornaments and jewellry. Such dependance on commodities as a constant source of hedging has created an investment psychology that could have driven the Indian investors to invest a fixed proportion of their wealth always in commodity futures. This has resulted in concurrent investments in stock and commodity leading to stronger correlation. One reason for the lagged relationship could be that after every initial boom in the stock market, investors start piling up a portion of their wealth in commodity and vice versa. In India, since people have routes to diversify in commodity markets through informal channels like ornaments and utensils, they may treat the commodity futures exchange as an alternative to the informal market. That is why they seem to invest in both stock and exchange traded commodities concurrently.

Globally two commodities, namely oil and gold, play important roles in portfolio management. In the case of gold we already see that the Indian market has reasons to behave differently than US market. We can also find from investment trends that oil also, rather than the entire commodity futures, has a similar place in the investment portfolios of India, which means that whenever investment goes up, it goes up almost simultaneously both in stock and commodity markets. Finally, it may be inferred that exchange traded commodities may not be a useful diversification avenue for investors

in India as yet. However, the exchange traded commodity market is relatively new in India. The dynamics will probably undergo a change with time as the market in India further develops.

References

1. Reddy, Y.V., Sebastin, A.: J Altern. Investments **11**, 85 (2009). doi:10.3905/JAI.2009.11.3.085
2. Voss, H., Kurths, J.: Phys. Lett. A **234**(5), 336 (1997)
3. Eckmann, J.P., Kamphorst, S.O., Rullelle, D.: Europhys. Lett. **5**, 973 (1987). doi:10.1209/0295-5075/4/9/004
4. Marwan, N., Romano, M.C., Thiel, M., Kurths, J.: Phys. Rep. **438**(5–6), 237 (2007). doi:10.1016/j.physrep.2006.11.001
5. Pesaran, M., Potter, S.: Nonlinear Dynamics, Chaos and Econometrics. Wiley, New York (1993)
6. Campbell, J., Lo, A., MacKinlay, A.: The Econometrics of Financial Markets. Princeton University Press, Princeton (1997)
7. Barnett, W.A., Jungeilges, J.A., Gallant, A., Kaplan, D.T., Hinich, M.J., Jensen, M.J.: A single-blind controlled competition among tests for nonlinearity and chaos. J Econom. **82**(1), 157–192 (2000). doi:10.1016/S0304-4076(97)00081-X
8. Hsieh, D.A.: J. Bus. **62**, 339 (1989). doi:10.1086/296466
9. Hsieh, D.A.: J. Finance **46**, 1839 (1991). doi:10.2307/2328575
10. Scheinkman, J., LeBaron, B.: J. Bus. **62**, 311 (1989)
11. Abhyankar, A., Copeland, L.S., Wong, W.: Econ. J. **105**, 864 (1995)
12. Steurer, E.: Neural Networks in the Capital Markets. Wiley, New York (1995)
13. Brooks, C.: Appl. Financ. Econ. **6**(4), 307 (1996)
14. Barkoulas, J., Travlos, N.: Appl. Financ. Econ. **8**, 231 (1998). doi:10.1080/096031098332998
15. Opong, K.K., Mulholland, G., Fox, A.F., Farahmand, K.: J. Empir. Finance **6**(3), 267 (1999)
16. Goswami, B., Ambika, G., Marwan, N., Kurths, J.: Phys. A **391**, 4364 (2012). doi:10.1016/j.physa.2012.04.018
17. Hinich, M., Patterson, D.: Economic complexity: chaos, sunspots, bubblesand nonlinearity. In: Barnett W., Geweke J., Shell K. (eds.) International Symposium in Economic Theory and Econometrics, pp. 383–409. Cambridge University Press, Cambridge (1989)
18. Taylor, M., Peel, D.: J. Int. Money Finance **19**, 33 (2000)
19. Sarno, L.: Appl. Econ. Lett. **7**, 285 (2000)
20. Bierens, H.J.: J. Econom. **77**, 379 (1997). doi:10.1016/S0304-4076(96)01820-9
21. Chortareas, G., Kapetanios, G., Shin, Y.: Econ. Lett. **77**, 411 (2002)
22. Kapetanios, G., Shinn, Y., Snell, A.: J. Econom. **112**, 359 (2003)
23. Baek, E., Brock, W.: Working Paper. Iowa State University and University of Wisconsin at Madison (1992)
24. Breiman, L., Friedman, J.H.: J. Am. Stat. Assoc. **80**(391), 580 (1985)
25. Crowley, P.M.: Eur. Phys J. - Special Topics **164**(1), 67 (2008). doi:10.1140/epjst/e2008-00835-3
26. Crowley, P.M., Schultz, A.: Int. J. Bifurcat. Chaos **21**(4), 1215 (2011). doi:10.1142/S0218127411028957
27. Donner, R.V., Small, M., Donges, J.F., Marwan, N., Zou, Y., Xiang, R., Kurths, J.: Int. J. Bifurcat. Chaos **21**(4), 1019 (2011). doi:10.1142/S0218127411029021
28. Cross Recurrence Plot Toolbox. http://tocsy.pikpotsdam.de 21-Jul-2009
29. Voss, H.U., Kolodner, P., Abel, M., Kurths, J.: Phys. Rev. Lett. **83**(17), 3422 (1999)
30. Voss, H., Kurths, J.: Chaos Solitons Fractals **10**(4), 805 (1999)
31. Fraser, A., Swinney, H.: Phys. Rev. A **33**, 1134 (1986)
32. Kennel, M., Brown, R., Abarbanel, H.: Phys. Rev. A **45**, 3403 (1992). doi:10.1103/PhysRevA.45.3403

33. Marwan, N., Kurths, J.: Phys. Lett. A **302**(5–60), 299 (2002)
34. Zbilut, J.P., Webber Jr, C.L.: Phys. Lett. A **171**(3–4), 199 (1992). doi:10.1016/0375-9601(92)90426-M
35. Marwan, N.: Eur. Phys. J. - Special Topics **164**(1), 3 (2008)
36. Marwan, N., Donges, J.F., Zou, Y., Donner, R.V., Kurths, J.: Phys. Lett. A **373**(46), 4246 (2009). doi:10.1016/j.physleta.2009.09.042
37. Donner, R.V., Zou, Y., Donges, J.F., Marwan, N., Kurths, J.: New J. Phys. **12**(3), 033025 (2010). doi:10.1088/1367-2630/12/3/033025
38. Zou, Y., Donner, R.V., Donges, J.F., Marwan, N., Kurths, J.: Chaos **20**(4), 043130 (2010). doi:10.1063/1.3523304
39. Donner, R.V., Heitzig, J., Donges, J.F., Zou, Y., Marwan, N., Kurths, J.: Eur. Phys. J. B **84**, 653 (2011). doi:10.1140/epjb/e2011-10899-1
40. Schinkel, S., Dimigen, O., Marwan, N., Kurths, J.: Phys. Lett. A **373**, 2245 (2009). doi:10.1016/j.physleta.2009.04.045